AN IMPROVED TECHNIQUE FOR THE EXFOLIATION OF GRAPHENE NANOSHEETS
AND
UTILIZATION OF THEIR NANOCOMPOSITES AS FUEL CELL ELECTRODES

by

BURCU SANER OKAN

Submitted to the Graduate School of Engineering and Natural Sciences
in partial fulfillment of the requirements for the degree of
Doctor of Philosophy

Sabancı University
Spring 2011

**AN IMPROVED TECHNIQUE FOR THE EXFOLIATION OF
GRAPHENE NANOSHEETS
AND
UTILIZATION OF THEIR NANOCOMPOSITES
AS FUEL CELL ELECTRODES**

APPROVED BY

Prof. Dr. Yuda Yürüm
(Thesis Supervisor)

Prof. Dr. Nurcan Baç

Prof. Dr. Ahmet Oral

Asst. Prof. Dr. Selmiye Alkan Gürsel

Asst. Prof. Dr. Fevzi Çakmak Cebeci

DATE OF APPROVAL: 27/07/11

To the memory of my beloved grandfather and grandmother

Asım & Fadile SANER

To my beloved husband

Reşit Yiğit OKAN

AN IMPROVED TECHNIQUE FOR THE EXFOLIATION OF
GRAPHENE NANOSHEETS
AND
UTILIZATION OF THEIR NANOCOMPOSITES
AS FUEL CELL ELECTRODES

Burcu SANER OKAN

Materials Science and Engineering, Ph.D. Dissertation, 2011

Thesis Supervisor: Prof. Dr. Yuda Yürüm

Keywords: Graphene nanosheets, graphite oxide, nanocomposites, fuel cell electrode

ABSTRACT

Graphene nanosheets (GNS) were separated from graphite by an improved, safer and mild method including the steps of oxidation, thermal expansion, ultrasonic treatment and chemical reduction. With this method, the layers in the graphite material were exfoliated, and high-quality GNS were produced with higher yields. Scanning Electron Microscopy (SEM) images exhibited that GNS can exist by being rippled rather than completely flat in a free standing state. The mild procedure applied was capable of reducing the average number of graphene sheets from an average value of 86 in the raw graphite to 9 in GNS. Raman spectroscopy analysis confirmed the significant reduction in size of the in-plane sp^2 domains of GNS obtained after the reduction of graphite oxide (GO). BET measurements by nitrogen adsorption technique showed that the surface area of GNS was 507 m^2/g. The electrical conductivity of GNS was measured as 3.96 S/cm by the four-probe method.

As the oxidation time was increased from 50 min to 10 days, stacking height of graphene sheets decreased and thus the number of graphene layers decreased. The variations in interplanar spacings, layer number, and percent crystallinity as a function of oxidation time indicated how stepwise chemical procedure influenced the

morphology of graphite. The percent crystallinity of GO sheets decreased down to 2% due to the change of stacking order between graphene layers and the random destruction of graphitic structure after oxidation process.

For the production of advanced type of catalyst support materials, the distinguished properties of GNS were combined with the structural properties of conducting polypyrrole (PPy) by the proposed simple and low-cost fabrication technique. A precise tuning of electrical conductivity and thermal stability was also achieved by controlling the polymer thickness of randomly dispersed GO sheets and GNS by a layer-by-layer polymer coating. However, non-uniform polymer dispersion on the surface of expanded GO occurred due to the removal of oxygen functional groups on the surface during thermal expansion of GO sheets.

The shortest and most effective impregnation technique of Pt catalysts on the surface of GO, expanded GO and GNS based composites was achieved by a sonication process of 2 hrs. The C/O ratios of GO, expanded GO and GNS were measured as 2.3, 6.0, and 3.2, respectively. The characterization results showed that the presence of oxygen surface groups and the amount of PPy in nanocomposites favored the Pt dispersion and hindered the aggregation of Pt particles on the support surface. As GO content increased three times larger than the amount of PPy in nanocomposite, size distribution of catalyst particles was decreased into the range of 9 nm to 16 nm.

Finally, novel fuel cell electrodes made of GO, GNS and their nanocomposites were fabricated in the form of thin-films by applying drop-casting method. Then, the performance of the prepared membrane electrode assemblies was tested in a single fuel cell. Comparably better fuel cell performance was obtained when GO sheet was used as the cathode electrode due to the large amount of oxygen surface groups on the surface of GO sheets.

GRAFEN NANOTABAKALARININ AYIRILMASI İÇİN GELİŞTİRİLMİŞ YÖNTEM

VE

GRAFEN NANOKOMPOZİTLERİNİN YAKIT PİLİ ELEKTROTU OLARAK KULLANIMI

Burcu SANER OKAN

Malzeme Bilimi ve Mühendisliği, Doktora Tezi, 2011

Tez Danışmanı: Prof. Dr. Yuda Yürüm

Anahtar kelimeler: Grafen nanotabakalar, grafit oksit, nanokompozitler, yakıt pili elektrotu

ÖZET

Grafen nanotabakalar, kimyasal oksitleme, termal genleşme, ultrasonik işlem ve kimyasal indirgeme aşamalarını içeren geliştirilmiş, güvenli ve kolay bir teknikle grafitten ayırılmıştır. Bu teknik sayesinde, grafitin yapısındaki grafen tababakalarının sayıları azaltılmış, iyi kalitede ve yüksek miktarlarda grafen nanotabakalar elde edilmiştir. Taramalı elektron mikroskop (SEM) görüntüleri grafen nanotabakalarının daha çok buruşuk bir yapıda bulunduklarının göstermiştir. Bu yöntem sayesinde yapısında yaklaşık 86 adet grafen takabası bulunan grafit, grafen sayısı ortalama olarak yaklaşık 9 olan grafen nanotabakalara indirgenmiştir. Raman spektroskopisi spektrumları grafit oksitin indirgenmesinden elde edilen grafen nanotabakalarının düzlemsel sp^2 bölgelerinin (domain) büyüklüklerinde önemli ölçüde azalma olduğunu göstermiştir. Azot adsorpsiyon tekniği ile yapılan BET çalışmaları ile grafen nanotabakalarının yüzey alanı 507 m^2/g olarak bulunmuştur. Grafen nanotabakalarının 4-nokta-iletkenlik cihazı ile ölçülen elektrik iletkenliği 3.96 S/cm olarak bulunmuştur.

Oksitleme süresi 50 dakikadan 10 güne kadar çıkartıldığında grafen tabakalarının istiflenme yükseliği azalmıştır ve böylece grafen tabakalarının sayısı da azalmıştır. Oksidasyon süresine göre düzlemlerarası mesafe, tabaka sayısı ve kristalleşme

oranındaki değişiklikler kimyasal sürecin grafitin yapısını nasıl etkilediğini göstermiştir. Oksitleme işleminden sonra grafitik yapının dağınık bir şekilde bozulması ve grafen tabakaları arasındaki istiflenme düzeninin değişmesinden dolayı grafit oksit tabakalarının kristalleşme oranı %2'ye kadar düşmüştür.

Geliştirilmiş katalizör destek malzemesi üretimi için önerilen kolay ve düşük maliyetteki üretim yöntemi ile grafen nanotabakaların olağanüstü özellikleri iletken polimer polipirolün yapısal özellikleri ile birleştirilmiştir. Kompozitlerin elektrik iletkenliği ve termal dayanıklılığı, tabaka tabaka polimerle kaplanmış dağınık halde bulunan grafit oksitin ve grafen nanotabakalarının kalınlıklarına göre başarılı bir şekilde kontrol edilebilmiştir. Ancak, grafit oksite uygulanan termal işlemle yüzeydeki oksijenli fonksiyonel grupların ortadan kaldırılmasından dolayı genleşmiş grafit oksitin yüzeyinde homojen bir şekilde polimer dağılımı gözlenmemiştir.

Grafit oksit ve grafen tabakalarının yüzeylerine Pt yükleme işlemi ultrasonik banyo içerisinde 2 saatte gerçekleştirilmiştir. Grafit oksit, genleşmiş grafit oksit ve grafen nanotabakalarının C/O oranları sırasıyla 2.3, 6.0 ve 3.2 olarak hesaplanmıştır. Karakterizasyon sonuçları yüzeydeki oksijenli fonksiyonel grupların ve nanokompozitin yapısındaki polipirol miktarının yüzeyde platin dağılımını arttırıp platinlerin öbekleşmesini engellediğini göstermiştir. Nanokompozitteki grafit oksit miktarı polipirol miktarının 3 katına çıkartıldığında ise katalizör partiküllerinin büyüklük dağılımı 9 nm ile 16 nm arasına düşmüştür.

Son olarak, damlatarak kaplama yöntemi ile ince film halinde grafit oksit, grafen nanotabakalar ve bunların nanokompozitlerinden yapılmış yeni yakıt pili elektrotları üretilmiştir. Sonra, hazırlanan membran elektrot bileşkelerinin dayanıklıkları yakıt pili içerisinde test edilmiştir. Grafit oksit katot elektrodu olarak kullanıldığında yakıt pilinin performansının kıyasla daha iyi olduğu görülmüştür. Bu da grafit oksitin yüzeyinde yüksek miktarda bulunan oksijenli fonksiyonel gruplardan kaynaklanmaktadır.

ACKNOWLEDGEMENTS

TABLE OF CONTENTS

LIST OF FIGURES

LIST OF TABLES

LIST OF ABBREVIATIONS

AFC	:	Alkaline Fuel Cells
AFM	:	Atomic Force Microscopy
ARPES	:	Angle-Resolved Photoemission Spectroscopy
BET	:	Brunauer–Emmett–Teller
CB	:	Conduction Band
CNTs	:	Carbon Nanotubes
CNFs	:	Carbon Nanofibers
CVD	:	Chemical Vapor Deposition
Eg	:	Bandgap
EG	:	Expanded Graphite
FWHM	:	Full Width Half Maxima
GDL	:	Gas Diffusion Layer
GIC	:	Graphite Intercalated Compound
GNRs	:	Graphene Nanoribbons
GNS	:	Graphene Nanosheets
GNPs	:	Graphite Nanoplatelets
GO	:	Graphite Oxide
6H	:	Hexagonal
HOPG	:	Highly Oriented Pyrolytic Graphite
hr	:	Hour
MEA	:	Membrane Electrode Assembly
MCFC	:	Molten Carbonate Fuel Cells
PAFC	:	Phosphoric Acid Fuel Cells
PEM	:	Proton Exchange Membrane
PEMFC	:	Polymer Electrolyte Membrane Fuel Cells
PPy	:	Polypyrrole
Pt	:	Platinum

Py	:	Pyrrole
SEM	:	Scanning Electron Microscopy
SiC	:	Silicon Carbide
SOFC	:	Solid Oxide Fuel Cells
STM	:	Scanning Tunneling Microscope
TEM	:	Transmission Electron Microscope
TGA	:	Thermal Gravimetric Analyzer
UHV	:	Ultrahigh Vacuum
VB	:	Valence Band
XPS	:	X-Ray Photoelectron Spectroscopy
XRD	:	X-Ray Diffraction
2D	:	Two-dimensional

CHAPTER 1. INTRODUCTION

Graphene has attracted great interest due to its unique electronic, thermal, and mechanical properties, resulting from its two-dimensional (2D) structure, and to its potential applications like microchips, chemical sensing instruments, biosensors, energy storage devices and other innovations. The first graphene sheets were obtained by extracting monolayer from the three-dimensional graphite using a technique called micromechanical cleavage in 2004 [1].

With the appropriate surface treatments, single graphene sheets can be separated from the graphite material and the layer-to-layer distance can be extended [2, 3]. There are numerous old methods for the graphite modifications to reduce the number of graphene layers in graphitic structure [4-6]. One of the applicable methods is the graphite oxidation in order to reduce the strong bonding between sheets in graphite and to receive monolayer graphene sheet. The structure of graphite oxide (GO) resembles graphite but only difference is that the sp^3 hybridization in carbon atoms and thus the individual layers are considerably bent [7]. Furthermore, GO is thermally unstable material which can be pyrolyzed at high temperatures due to the existence of the oxygen functional groups [8]. After heat treatment, the crystal lattice planes of graphite flakes are extended and this leads to the formation of expanded graphite called "worm-like" or accordion structure [3, 9].

Fuel cells are clean, compact and modular energy generation devices that generate electricity by a chemical reaction between a fuel and an oxidant. Polymer electrolyte membrane fuel cell (PEMFC) offers several advantages for both mobile and stationary applications yet it is necessary to develop low cost and more efficient PEMFCs. The heart of the PEMFC is the membrane electrode assembly (MEA) composed of a proton exchange membrane sandwiched between two porous gas diffusion electrodes. These

electrodes are made up of a catalyst support material, gas diffusion layer and a catalyst layer.

Catalyst has a crucial effect on both the cost, performance and durability of PEMFCs. At this point, graphene can be a promising candidate as catalyst support material for PEMFCs due to its outstanding mechanical, structural, and electronic properties. Herein, the support material becomes significant to get high catalytic performance of catalysts by lower catalyst loadings [10].

The incorporation of graphene and its derivatives into polymer matrix can enlarge the surface area by π-π stacking with polymer hosts [11] and provide high conductivity [12]. Therefore, the combination of characteristic properties makes graphene sheets a promising candidate for the fabrication of advanced type of electrode materials to be utilized in fuel cell applications. Novel geometric structure of graphene can control the transport directions of gases, water, protons and electrons in PEMFCs [13].

In the present work, we presented an improved, safer and mild method for the exfoliation of graphene sheets from graphite to be used in fuel cells. The major aim in the proposed method is to reduce the number of layers in the graphite material and to produce large quantities of graphene bundles to be used as catalyst support in PEMFCs. Moreover, for the fabrication of novel fuel cell electrodes, polypyrrole (PPy) was first coated on partially oxidized GO sheets and graphene nanosheets (GNS) by *in situ* polymerization of pyrrole (Py) with different feed ratios of Py and sheets. Among the various conducting materials, PPy has taken special attention due to its relatively easy processability, electrical conductivity, and environmental stability [14]. By applying different deposition techniques, we proposed a shorter and more effective deposition technique for maximum catalyst dispersion. Then, the electrodes in the form of thin-films composites electrodes were prepared successfully by drop-casting method. Finally, the performances of electrodes were tested in a single fuel cell.

CHAPTER 2. STATE-OF-THE-ART

2.1. Graphene

Graphite is a layered material and is formed by a number of two-dimensional (2D) graphene crystals weakly coupled together. Graphene, the world's thinnest sheet – only a single atom thick – has a great potential to provide a new way in energy, computing and medical research [15].

In the first part of Chapter 2, physical and chemical properties of graphene and its synthesis techniques were investigated in details.

2.1.1. Physical and Chemical Properties of Graphene

Graphene is the flat monolayer of carbon atoms in sp^2 hybridization. Ideal graphene contains only six membered rings. Structural defects in graphene cause the formation of five and seven membered rings and thus the flat surface becomes rippled. The novel structure of graphene is the center stage for all the calculations on graphite, carbon nanotubes (CNTs) and fullerenes. The first graphene sheets were obtained by extracting monolayer sheets from the three-dimensional graphite using a technique called micromechanical cleavage in 2004 [1]. The important property of graphene is its stability at ambient conditions: it can exist by being rippled rather than completely flat in a free-standing state [16].

A single finite size graphite sheet, graphene, can have two typical conformations: a chair-like conformer with hydrogen atoms alternating on both sides of the plane (called a zigzag) and a boat-flake conformer with hydrogen atoms alternating in pairs

(called an armchair) [17] (Figure 2.1). Graphene nanoribbons (GNRs), with a zigzag or armchair configuration, show different electrical properties; the zigzag GNRs are metallic, while armchair GNRs can be either metallic or semiconductor.

(a)

(b)
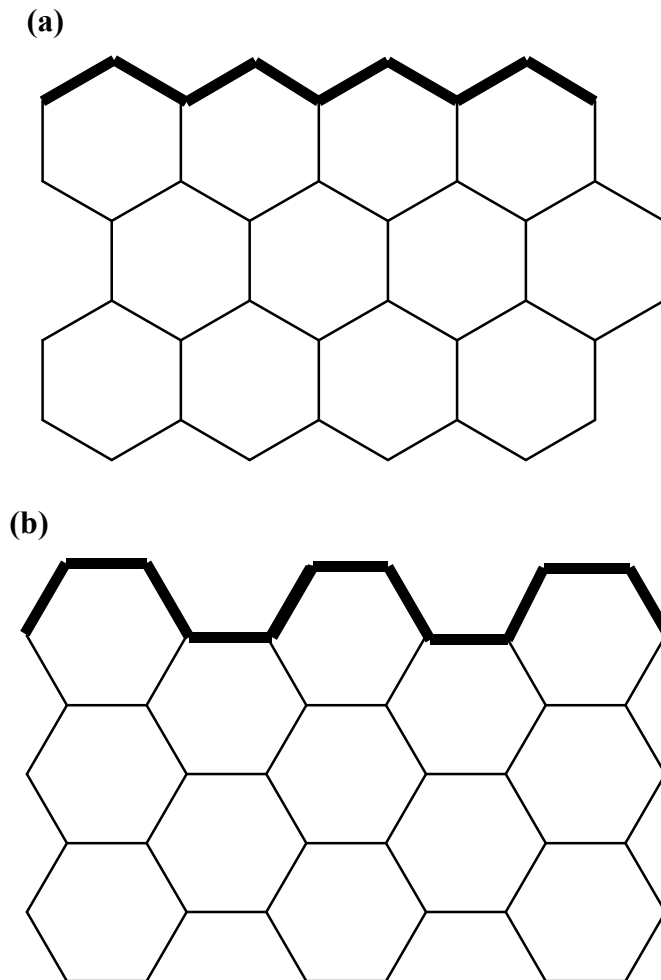
Figure 2.1. (a) Zigzag and **(b)** armchair edges in graphene.

Graphene has high mechanical, thermal and chemical stability due to the strong covalent bonds between carbon atoms. It is one of the strongest materials per unit weight with a theoretical Young's modulus of 1060 GPa [18] and also conducts electricity through the p-electron cloud resulting in numerous applications with great potential for quantum electronics [19, 20]. Graphene sheet has extraordinarily high electron mobility at room temperature with the experimentally reported value of > 15,000 $cm^2V^{-1}s^{-1}$ [1]. The major physical properties of monolayer graphene sheet are shown in Table 2.1.

Table 2.1.

Physical properties of monolayer graphene sheet at room temperature

C–C bond length in monolayer graphene, nm	0.142	[21]
Specific surface area, m^2/g	≈ 2630	[15]
Electron mobility, $cm^2/(V\ s)$	$\approx 1.5 \times 10^4$	[1]
Young's modulus, TPa	≈ 1	[18]
Thermal conductivity, W/(m K)	$\approx 5.1 \times 10^3$	[22]

Bi-layer graphene and few-layer graphene have 2 layers and 3 to 10 layers, respectively. In bi- and few-layer graphene, C atoms can be stacked in three modes: hexagonal or AA stacking, Bernal or AB stacking and rhombohedral or ABC stacking (Figure 2.2). Bi-layer graphene can act as a gapless semiconductor. On the other hand, few-layer graphene sheets become more metallic as the number of graphene layers increases [23]. Few-layer graphene sheets can be functionalized by several solvents and thus can be soluble in organic solvents (carbon tetrachloride-CCl_4, dichloromethane-DCM) by amide functionalization [24] and become water soluble by oxidation with acids (H_2SO_4 and HNO_3) [25].
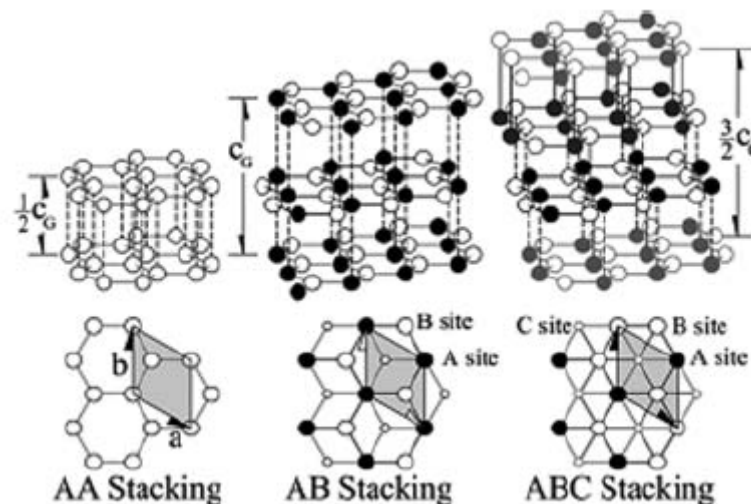
Figure 2.2. Stacking modes of graphene layers

2.1.2. Graphene Synthesis Techniques

In the last decades, several methods were published for the production of graphene sheets. These methods can be categorized into four main groups: micromechanical cleavage, chemical exfoliation, epitaxial growth on SiC and other subtrates, and chemical vapor deposition technique.

2.1.2.1. Exfoliation and Micromechanical Cleavage

Graphite consists of graphene layers in a hexagonal arrangement bonded together by weak van der Waals forces, with a covalent bond length of each carbon bonded to three neighbouring atoms as 1.42 Å and the distance between planes as 3.35 Å. Exfoliation (a simple and repeated peeling method) and cleavage processes require mechanical or chemical energy to break these week forces between layers and separate out individual graphene sheets. Novoselov *et al.* [1] obtained graphene layers using the scotch tape method. In this method, a commercially available highly oriented pyrolytic graphite (HOPG) sheet of 1 mm thickness was exposed to dry etching in oxygen plasma to make many 5 μm deep mesas (of area 0.4 to 4 mm^2). This was put on a photoresist and baked to stick the mesas to the photoresist. After the discovery of graphene, many researchers have developed new techniques for the production of graphene. For instance, Bouchiat *et al.* [26] modified Novoselov's scotch tape technique and produced large (~10 μm) and flat graphene flakes by manipulating the substrate bonding of HOPG on Si substrate and controlled exfoliation. Then, Balan *et al.* [27] exfoliated mm-sized single and few-layer graphene by bonding bulk graphite on borosilicate glass. These types of exfoliation techniques have significant potential on large-scale production to be used in graphene-based electronic devices. On the other hand, these micromechanical exfoliation techniques suffer from low throughput, and poor quality and limited graphene production.

2.1.2.2. Chemical Exfoliation of Graphite Oxide, Graphite Intercalation Compounds, and Expanded Graphite

Chemical modifications of graphene sheets influence the electronic properties and alter the magnetic properties of graphene. In order to obtain graphene sheets by chemical methods, graphite is generally used as a starting material. There are three main types of modified graphite which are mostly preferred in chemical exfoliation: graphite oxide (GO), graphite intercalation compounds (GICs) and expanded graphite (EG).

a. Graphite Oxide

There are numerous attempts in the literature to produce monolayer graphene sheets by the treatment of graphite. The first work was conducted by Brodie in 1859 and GO was prepared by repeated treatment of Ceylon graphite with an oxidation mixture consisting of potassium chlorate and fuming nitric acid [4]. Then, in 1898, Staudenmaier produced GO by the oxidation of graphite in concentrated sulfuric acid and nitric acid with potassium chlorate [5]. However, this method was time consuming and hazardous. Hummers and Offeman found a rapid and safer method for the preparation of GO and in this method graphite was oxidized in water free mixture of sulfuric acid, sodium nitrate and potassium permanganate [6]. Hummers and Offeman summarized the functional groups in the structure of GO and estimated the amount of GO sheets (mmol/100 g) using the analytical methods outlined in Table 2.2.

Table 2.2.

Functional groups in GO [6]

Functional group	Method of estimation	Number in mmol/100 g
Carboxyl groups	Reaction with PCl_5, Neutralization of $NaHCO_3$, Esterification with CH_3OH	80-130
Hydroxyl groups, total	Neutralization of C_2H_5ONa, Hydrogen content after careful drying	1000
Enol groups	Neutralization of NaOH, Reaction with CH_2N_2	450
Ether groups	Difference in oxygen content	1100
Double bonds	Difference between functional groups and carbon atoms	700

The structure of GO resembles graphite: the only difference is that the sp^3 hybridization in carbon atoms indicates that the individual layers are considerably bent [7]. A typical GO structure is shown in Figure 2.3.
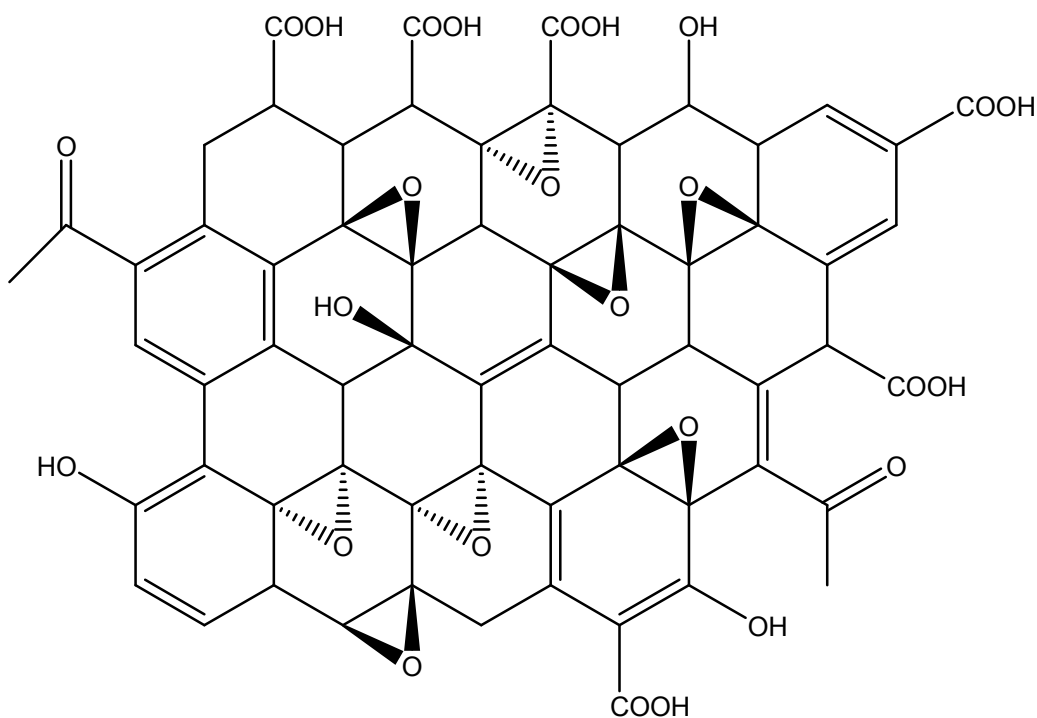
Figure 2.3. Structure of GO.

Homogeneous colloidal suspensions of graphene oxide in aqueous solvents can be attained by simple sonication of GO [28] because GO can be directly exfoliated in water due to its hydrophilic property [29] Furthermore, water molecules are strongly bound to the basal plane of GO through hydrogen bonding interactions with the oxygen in the epoxides of the GO, Figure 2.4 [30].
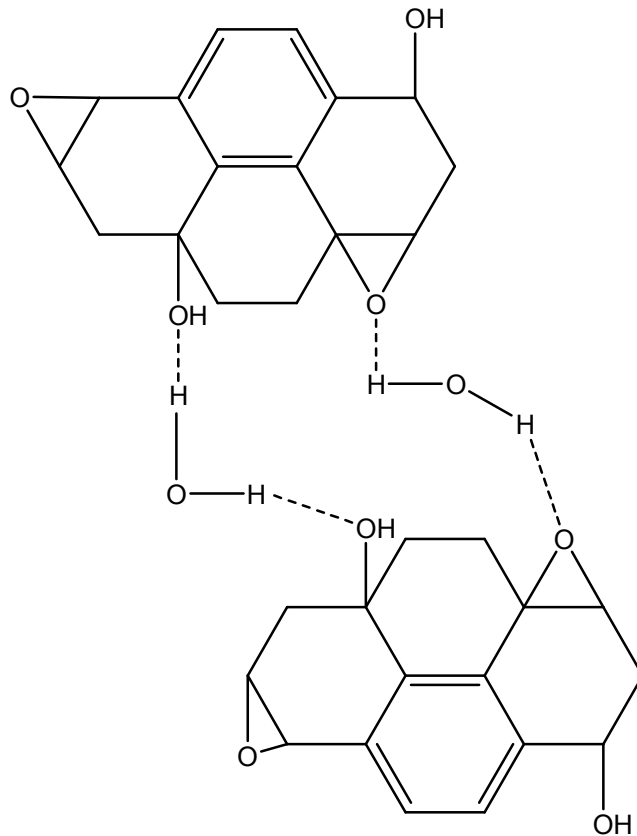
Figure 2.4. Proposed hydrogen bonding network formed between oxygen functionality on GO and water.

GO can also be directly dissolved in some polar solvents such as ethylene glycol, dimethyl formamide (DMF), 1-methyl-2-pyrrolidinone (NMP) and tetrahydrofuran (THF) [28]. When GO is treated by isocyanate groups, produced isocyanate-modified graphene oxide sheets are well dispersed in polar aprotic solvents [31]. The treatment of isocyanate with hydoroxyl and carboxyl groups on the surface and edge of graphene sheets leads to the formation of carbamate and amide functional groups [31].

Wu *et al.* [32] used five different graphites (highly-oriented pyrolytic graphite, natural flake graphite, kish graphite, flake graphite powder and artificial graphite) to

tune the number of graphene layers after oxidation and exfoliation processes. They stated that the smaller the lateral size and the lower the crystallinity of the starting graphite, the fewer the number of graphene layers obtained.

McAllister *et al.* [2] synthesized the functionalized graphene sheets by thermal expansion of graphite and investigated the exfoliation mechanism in details. According to their work, exfoliation occurs just after the decomposition rate of the epoxy and hydroxyl groups in GO reaches the diffusion rate of the evolved gases and this causes sufficient pressure to break forces keeping the graphene layers together. These functionalized graphene sheets are also easily dispersed in solvents by ultrasonication.

Ultrasonic treatment is a widely used method for the homogeneous dispersion of GO sheets in aqueous solutions and organic solvents [2, 31]. In order to separate graphene sheets, GO must be reduced and thus oxygen containing groups can be removed and the system of C=C bonds can be restored. The reduction process is performed by using strong reductants which remove oxygen containing functional groups. These are hydrazine, dimethylhydrazine, hydroquinone, and $NaBH_4$ [33]. After reduction and heating processes, graphene sheets are separated. Figure 2.5 schematically illustrates graphene separation by chemical exfoliation including oxidation, sonication and reduction steps.
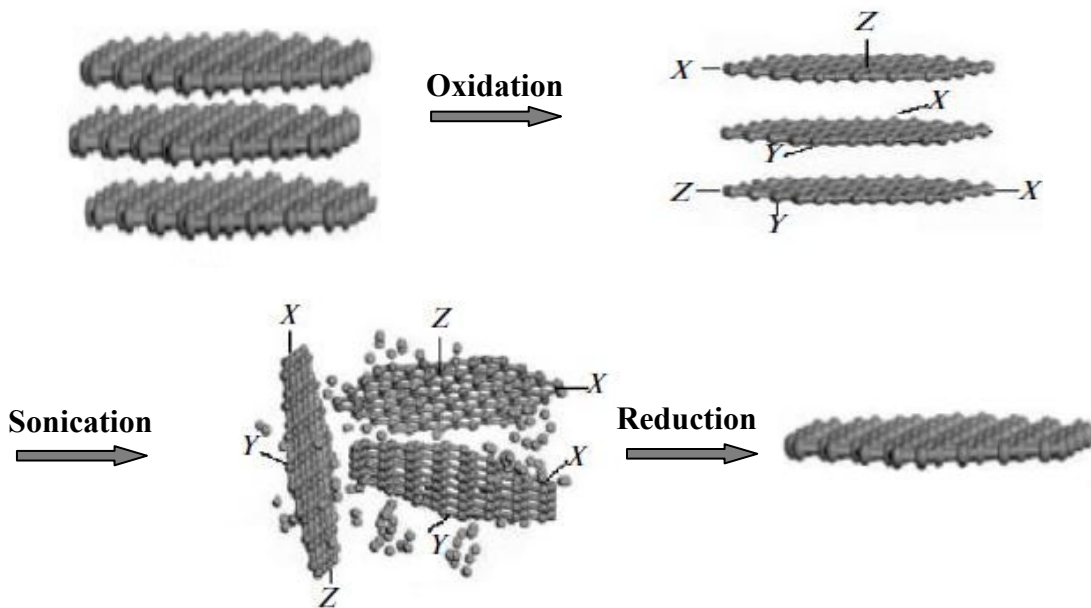
Figure 2.5. Schematic representation of graphene production by oxidation, sonication and reduction processes (X, Y, and Z are oxygen containing functional groups).

b. Graphite Intercalation Compounds

Graphite includes graphene sheets stacked along the c-axis in a staggered array denoted as ABAB....Certain atoms and molecules lead to swelling and an increase in weight. These atoms and molecules are alkali metals, alkaline earth metals, rare earth elements, halogens, metal halides, metal oxides and acids called intercalates which diffuse through layers and extend the inter-planar spacing. The products consisted of intercalates and host molecules are called graphite intercalated compounds (GICs). The intercalation process conducts by a charge-transfer between the intercalates and graphene sheets. GICs are categorized regarding the direction of electron transfer: donor GIC and acceptor GIC [34]. In donor GICs, the intercalate donates electrons to the graphene layer during the intercalation process. In acceptor GICs, compounds form because of the electron transfer in the opposite direction. Therefore, alkali metals provide the formation of donor-type GICs whereas inorganic acids or metal chlorides leads to the intercalates of acceptor-type GICs [34].

The Daumas−Herold domain model explains the staging phenomena stemming from phases with ordered arrangements of occupied and unoccupied galleries [35]. Figure 2.6 exhibits the schematic representation of stage 1, 2 and 3 GICs in the Daumas-Herold domain model. In this figure, each intercalate layer is separated by a certain number of graphene sheets and the stage number n changes by the number of graphene sheets between which adjacent intercalate layers are sandwiched.
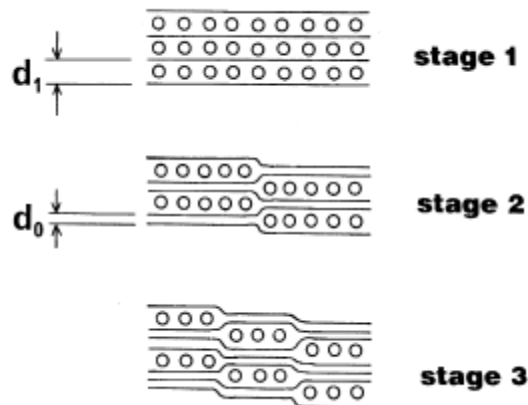
Figure 2.6. Stage 1, 2 and 3 GICs in the Daumas-Herold Model: (—) graphene sheets and (O) intercalates.

Intercalation techniques can be divided into three main groups: intercalation from vapour phase, intercalation from a liquid phase and electrochemical intercalation. For the separation of graphene nanosheets (GNS), generally intercalation in the liquid phase is preferred. For instance, Li $et\ al.$ [36] synthesized GICs with $CuCl_2$-$FeCl_3$-H_2SO_4 via a hydrothermal treatment at 150^oC and exfoliation method. After the intercalation process, they extended the inter-planar spacing along the c-axis direction from 0.34 nm to about 0.47 nm.

When graphene layers are oxidized, anions intercalate between the layers and expand the stacking height. During oxidation, stage 1 is the most highly oxidized phase where intercalate forms interlayer galleries between graphene sheets, stage 2 has alternate galleries, stage 3 has every third gallery occupied, etc. Lerner and Yan [37] prepared a new type oxidized GICs by using three perfluorinated alkylsulfonate anions, $C_{10}F_{21}SO_3^-$, $C_2F_5OC_2F_4SO_3^-$ and $C_2F_5(C_6F_{10})SO_3^-$. They obtained pure 2 stage by chemical oxidation of graphite with K_2MnF_6 in a solution including hydrofluoric and nitric acids for 72 hrs.

Prud'homme $et\ al.$ [38] intercalated GO sheets by diaminoalkanes and tailored interplanar spacings in the range of 0.8-1.0 nm by changing the size of the intercalant from $(CH_2)_4$ to $(CH_2)_{10}$. Their results showed that the intercalants are in a disordered state, with an important contribution from the gauche conformer.

Li $et\ al.$ [39] produced ultra-smooth GNRs by combining thermal exfoliation of expandable graphite with chemomechanical breaking of the resulting graphene sheets by sonication.

c. Expanded Graphite

Expanded graphite (EG) is a well-known material obtained from intercalated graphite exposed to a thermal shock. Thermal shock causes the vaporization of the intercalants and the expansion of the crystal lattice of planes of graphite flakes, and worm-like or vermicular-type structures are obtained at the end of the process. Furthermore, rapid heating of GO sheets results in superheating and volatilization of the

intercalants, embedded solvent, such as water, and the evolution of gas, such as CO_2, from chemical decomposition of oxygen containing species in the GO sheets [40]. Furthermore, EG consists of graphene layers in a hexagonal arrangement bonded together by weak van der Waals forces. Sonication process causes to break these bonds and leads to the formation of graphitic nanoplatelets (GNPs) [41].

EG is a loose and porous material and its pore sizes range from 10 nm to 10 mm (Figure 2.7) [9]. Zhu *et al.* [42] mixed natural graphite with a mixture of concentrated sulfuric acid and hydrogen peroxide and heated GIC between 200-1000°C for the decomposition of intercalating acids. Then, worm-like EG was sonicated and centrifugated in 1-methyl-2-pyrrolidinone (NMP) to obtain mono- or few-layer graphene sheets.
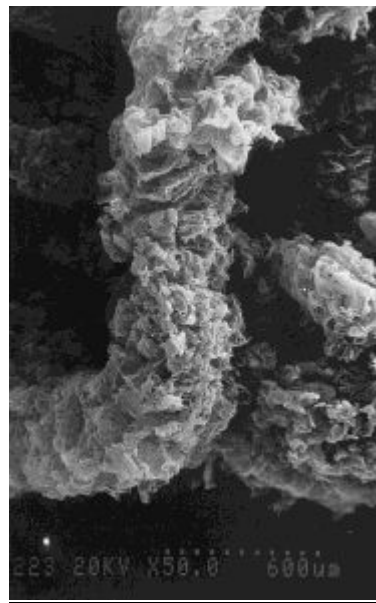
Figure 2.7. SEM image of EG.

There have been several attempts for the production of EG filled polymer nanocomposites to strengthen thermal, electrical and mechanical properties of polymers. Chen *et al.* [43] prepared polymer/graphite conducting composites using EG by a process of *in situ* polymerization. They demonstrated how the conductivity of composites can be changed in the presence of EG.

2.1.2.3. Epitaxial Growth on SiC and Other Substrates

Monolayer graphene on the graphite-silicon carbide (SiC) interface has remarkable 2D electron gas properties, including long phase coherence lengths (even at relatively high temperatures) and elastic scattering lengths measured by the micrometer-scale sample geometry [44]. Epitaxial graphene is multilayered, unlike exfoliated graphite which has only one layer. Epitaxial graphene contains stacked, non-interacting graphene sheets [45].

The fabrication of epitaxial growth on diced (3 mm by 4 mm) commercial SiC wafers has several steps which are (i) hydrogen etching, (ii) vacuum graphitization (iii) application of metal contacts, (iv) electron beam patterning and development (v) oxygen plasma etch and (vi) wire bonding [44].

Rollings *et al.* [46] obtained nearly one graphene sheets through the thermal decomposition of hexagonal (6H) SiC crystals. The process and characterization were performed in ultrahigh vacuum (UHV) conditions. Rollings's group also demonstrated the first quantative characterization of the number of graphene layers using core level x-ray photoelectron spectroscopy (XPS) and the first constant-energy electron density maps near Fermi energy using high-resolution angle-resolved photoemission spectroscopy (ARPES).

Berger *et al.* [19] obtained ultrathin epitaxial graphite films including three graphene sheets on the 6H-SiC surface through thermal decomposition. Scanning tunneling microscope (STM) image was also shown as evidence for the epitaxial growth (Figure 2.8).
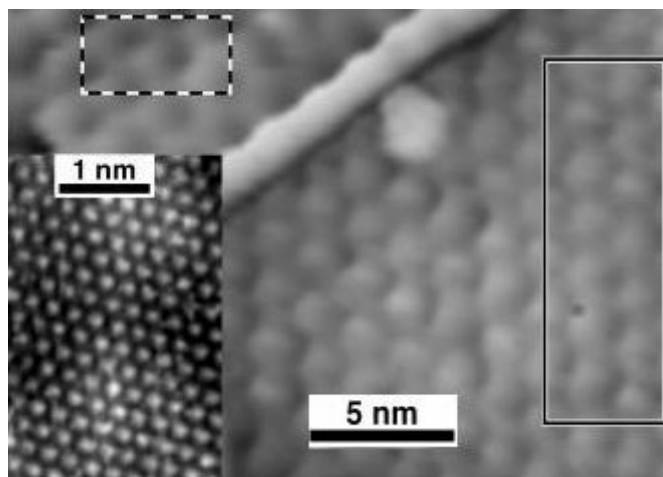
Figure 2.8. STM image of surface region of graphite/SiC (0001) after heating at 1400°C about 8 min [19].

2.1.2.4. Chemical Vapor Deposition Technique

Recently, chemical vapor deposition (CVD) technique is a promising method for the synthesis of large-scale graphene. Micromechanical cleavage of graphite produces very small graphene films and the chemical reduction of exfoliated graphite oxide produces a large-amount of graphene. There are two commonly used CVD techniques which are thermal CVD and plasma enhanced CVD techniques.

a. Thermal Chemical Vapor Deposition Technique

The thermal CVD of hydrocarbons over metal catalysts (Ni, Cu, Co, Pt, Ir) has been an effective technique for the production of graphene sheets. Several researchers have conducted the experiments that demonstrated the patterned growth of graphene using catalyst patterns in CVD, in which graphene growth just takes place on the surface of catalyst patterns, resulting in graphene patterns. Camara *et al.* [47] presented selective epitaxial growth of few layers graphene on a pre-patterned SiC substrate. In this method, they sputtered a thin aluminum nitride layer on top of a monocrystalline SiC substrate, then patterned it with e-beam lithography and wet etching. Wang *et al.* [48] demonstrated the first large-scale synthesis of few-layered sheets of graphene by

the thermal CVD of methane (CH$_4$) over cobalt (Co) supported on magnesium oxide (MgO) at 1000°C in a gas flow of argon (Ar).

Instead of metal catalysts, templates are used for the production of monolayer graphene. Template CVD is a technique widely-used to fabricate various nanomaterials with controllable morphologies. For instance, Wei *et al.* [49] proposed controllable and scalable synthesis of graphene by using ZnS ribbons as the template in the CVD growth of graphene with CH$_4$ as the carbon source. They obtained graphene ribbons with well-defined shapes on the surface of the Si substrate after the removal of ZnS by acid treatment.

b. Plasma Enhanced Chemical Vapor Deposition Technique

The first work on the synthesis of single- to few-layer graphene by plasma enhanced CVD was published in 2004 [50]. A radio frequency plasma enhanced CVD system was used to produce graphene sheets on several substrates (Si, W, Mo, Zr, Ti, Hf, Nb, Ta, Cr, 304 stainless steel, SiO$_2$, Al$_2$O$_3$), without any special surface preparation operation or catalyst deposition.

Lee *et al.* [51] synthesized a high quality of graphene sheets including 1- or 2-3-layers on stainless steel substrates at 500°C by micro-wave plasma CVD in an atmosphere of CH$_4$/H$_2$ mixture.

2.1.2.5. Lithography Etching

This technique is widely used in microelectronics and graphene devices to produce controllably etch graphene sheets into desired patterns. In 2004, Geim *et al.* fabricated graphene patterns by lithography etching (Figure 2.9), which was used in devices to explain the electric field-effect behavior of graphene [1]. The first step in this technique placed a large area graphene sheet on the substrate by micromechanical clevage. In the second step, the resist is patterned on the graphene by photo or electron beam lithography, which serves as the mask to protect graphene underneath against

etching. In the final step, an oxidative plasma etching of graphene occurs on the area without a mask, and a graphene pattern is revealed after the removal of the resist.
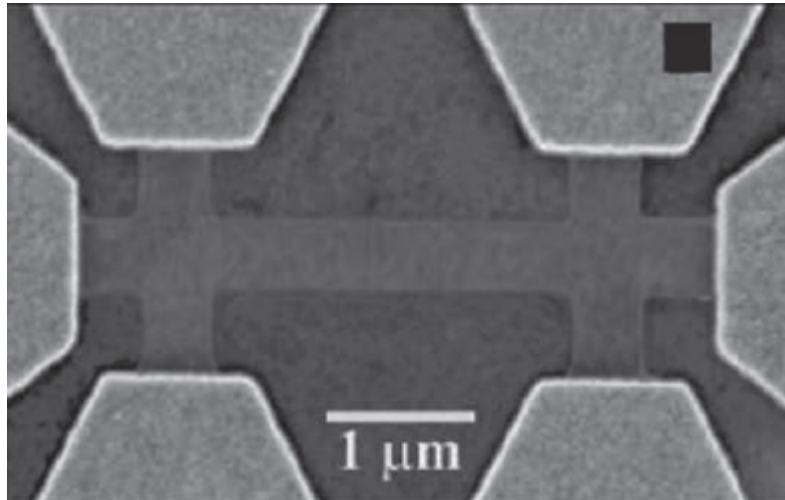
Figure 2.9. SEM image of a graphene field-effect transistor [1].

With lithography etching, different shapes of graphene (GNRs, graphene nanochannels, and graphene nanowires) can be produced. For instance, Han *et al.* [52] produced GNRs with well-defined widths ranging from 10 nm to 100 nm by this technique. In another work, Bai *et al.* [53] aligned silicon nanowires on top of graphene sheets, which protected the underlying graphene layer from oxygen plasma etching during the removal of the nanowire masks by sonication. Their technique can be used to produce GNRs with variable widths down to the sub-10-nm range.

2.1.3. Raman Spectroscopy of Graphene

Raman spectroscopy is a quick and accurate technique to determine the number of graphene layers and the change of the material's crystal structure after chemical treatments [54]. There are four remarkable peaks in the Raman spectrum of graphite: the G line around 1580 cm^{-1}, the G' line (the overtone of the G line) around 3248 cm^{-1}, the D line around 1360 cm^{-1} and the D' line (the overtone of the D line) around 2700 cm^{-1}. The intensity of the D line depends on the amount of the disorderness of the graphitic materials and its position shifts regarding to incident laser excitation energies [54]. As each layer is separated from the graphitic structure, the intensity of the G peak decreases

and the peak shifts towards higher wave numbers. In Figure 2.10, the G peak intensity of single-layer graphene is relatively lower than double-layer graphene. Ferrari *et al.* [55] showed that Raman spectroscopy could be used to discriminate the quality of graphene and to determine the number of graphene layers in the structure by the shape, width, and position of the D' peak.
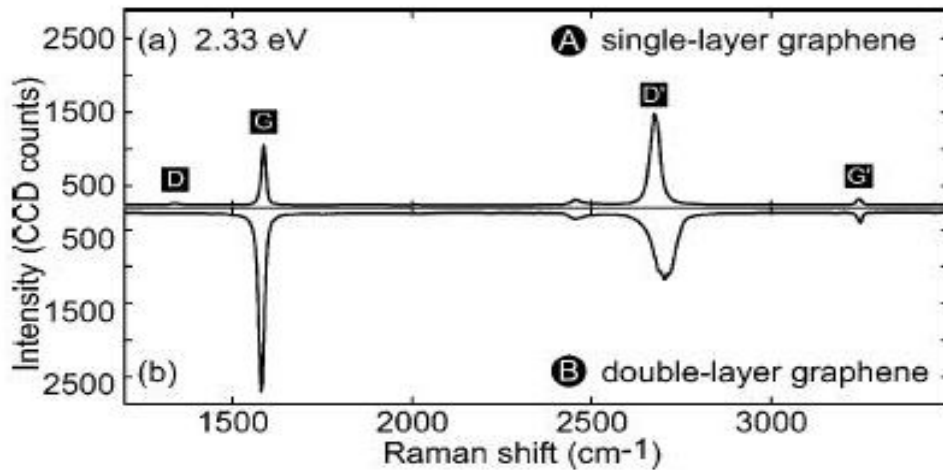
Figure 2.10. Raman spectra of **(a)** single- and **(b)** double-layer graphene [54].

In Figure 2.11, the D' band becomes broader and blueshifted when the graphene thickness increases from single-layer to multi-layer [56]. Also, G band becomes more intense as the number of graphene layers increases. The width of the D' peak splits into different subpeaks by changing the number of graphene layers [57].
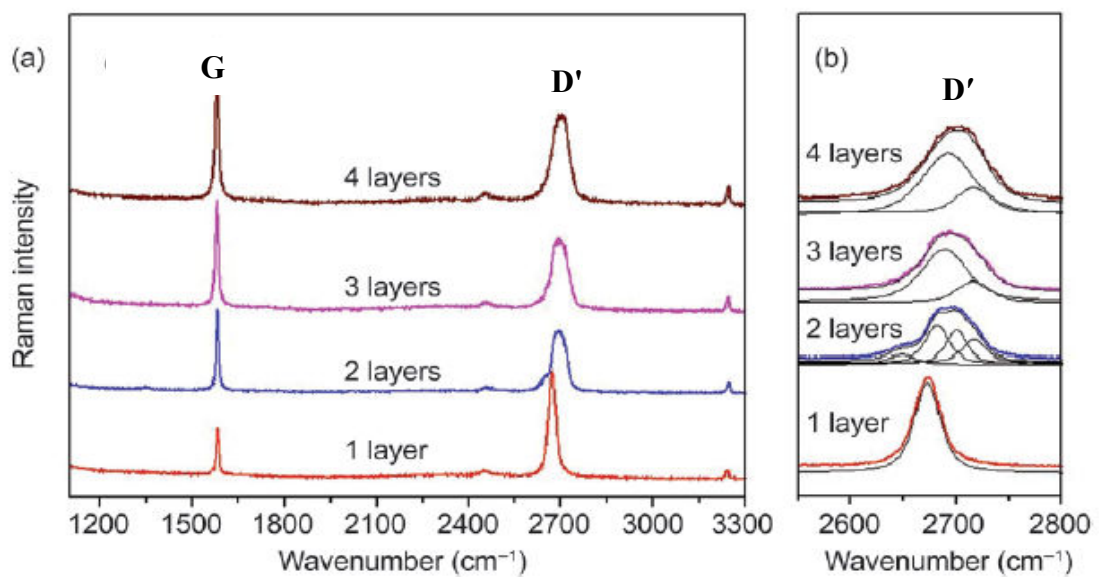
Figure 2.11. (a) Raman spectra of graphene with 1, 2, 3, and 4 layers **(b)** the enlarged D' band regions with curve fitting [56].

The structural change from graphite to GNS could be observed by the intensity ratio of the D and G bands, I_D/I_G. This ratio varied inversely with the size of the crystalline grains or interdefect distance and this was also used to estimate the amount of defects [57].

2.2. Utilization of Graphene Nanosheets in Fuel Cells

In the previous part of Chapter 2, the properties of graphene and its synthesis techniques were mentioned. In this part, utilization of graphene nanosheets (GNS) in fuel cell applications was examined.

Novel nanostructured carbon materials (carbon nanofibers, carbon nanotubes and graphene) have generated intense interest as catalyst supports in PEMFCs due to their unique structures and properties [58, 59]. However, the main drawbacks of these materials are high cost and mass production. At this point, GNS can serve as the promising catalyst support because of its low-cost and large-scale production. In addition, free standing graphene sheets have large surface area, high thermal and electrical conductivity, and high mobility of charge carriers [28]. According to Saner *et al.* [3], few graphene layers provide effective surface area to improve metal-support interaction. Authors proposed a mild chemical exfoliation method for the reduction of layer number in graphitic structure and the production in large quantities of GNS in order to utilize multiple GNS as the catalyst support materials in fuel cells. Rao *et al.* [60] demonstrated that graphene could be a good candidate as an electrode in supercapacitors because the specific capacitance of the exfoliated graphene in the aqueous electrolyte was better than activated carbons and carbon nanotubes. In another work, Ruoff *et al.* [15] showed that chemically modified graphene was incorporated into ultracapacitor test electrodes in order to increase the energy density of the packaged ultracapacitor by increasing the electrode thickness and eliminating additives.

Researchers have found new methods to enhance the dispersion of graphite nanosheets in a polymer matrix. One of them in these methods the dispersion of graphite nanosheets in polymer matrix during in situ polymerization of monomer using sonicated expanded graphite during sonication (Figure 2.12) [61]. This method provides much higher conductive composites than the other composites obtained by conventional methods.
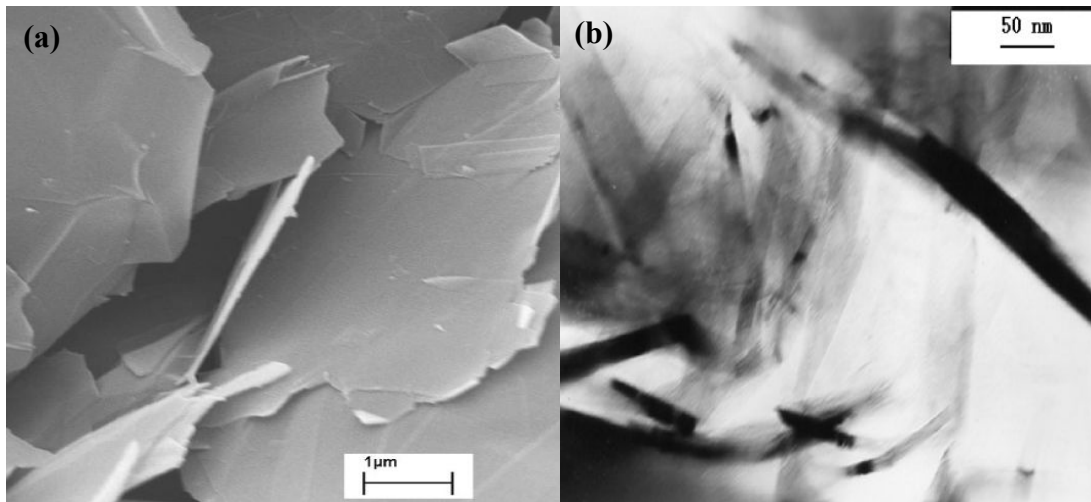
Figure 2.12. (a) SEM image of sonicated expanded graphite **(b)** TEM image of graphite nanosheet particles lying inside the polymer matrix separately [61].

2.2.1. Fuel Cells

Fuel cell is clean, compact and modular energy generation device that has the potential to revolutionalize the production of electricity and thermal energy. In fuel cells, hydrogen is used as a source of fuel. Typical fuel cell includes two electrodes sandwiched around an electrolyte. Oxygen passes over one electrode and hydrogen over the other, generating electricity, water and heat (Figure 2.13). Hydrogen is available in a mixture with other gases (such as CO_2, N_2, CO), or in hydrocarbons such as natural gas, CH_4, or even in liquid hydrocarbons such as methanol (CH_3OH).
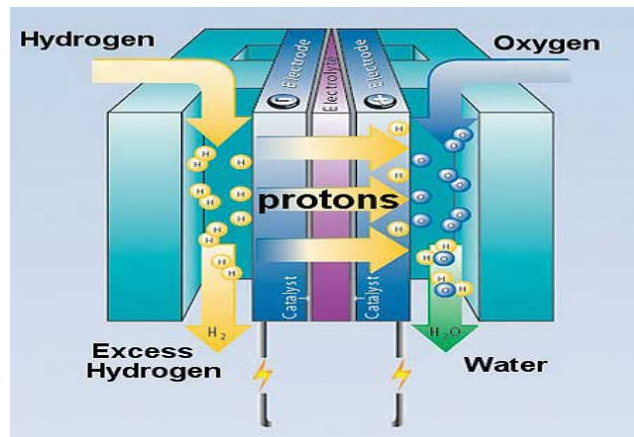
Figure 2.13. Schematic representation of fuel cell.

Sir William Grove was the pioneer of fuel cell technology who performed experiments on the electrolysis of water in 1839 [62]. Afterwards, Francis T. Bacon started to work on practical fuel cells in 1937, and he developed a 5 kW fuel cell by the end of 1950s. Then, NASA decided to use fuel cells as power sources in Gemini and Apollo spacecrafts.

United Technologies Corporation's UTC Power subsidiary was the first company to manufacture and commercialize a large, stationary fuel cell system for use as a co-generation power plant in hospitals, universities and large office buildings.

A fuel cell operates like a battery. Both have an electrolyte, and a positively charged anode and a negatively charged cathode, and they generate DC electricity by conversion of chemical energy via redox reactions at the anode and cathode. However, there are some differences between a battery and a fuel cell. One is that a fuel cell requires a constant supply of fuel and oxidant to produce electricity. Another difference is that the electrodes in a fuel cell do not undergo chemical changes.

There are many advantages of fuel cells listed as followings:

i.   high efficiency conversion (maximum 80%)
ii.   high power density
iii. environmentally friendly, its main byproduct is water, when comparing to numerous harmful pollutants created by fossil fuels
iv.   a long lasting alternative to a limited fossil fuel supply

21

v. construction in various sizes, weights and power levels (e.g. household appliances, automobiles)

Fuel cells are usually more efficient than combustion engines because fuel cells can produce electricity directly from chemical energy. In contrast to batteries, fuel cells provide easy scaling between power changed by the fuel cell size and capacity measured by the fuel cell reservoir size. Fuel cells offer higher energy densities compared to batteries and can be quickly recharged by refueling.

2.2.1.1. Types of Fuel Cells

There are different types of fuel cells depending on the kind of electrolyte used and the operation temperature as follow [63]:

- Polymer electrolyte membrane or proton exchange membrane fuel cells (PEMFC) use a proton conductive polymer as the electrolyte (e.g. perfluorosulfonated acid polymer). These fuel cells operate at temperatures between $60^{\circ}C$ and $80^{\circ}C$.
- Alkaline fuel cells (AFC) use a solution of potassium hydroxide (KOH) in water as the electrolyte. These fuel cells operate at temperatures between $100^{\circ}C$ and $250^{\circ}C$.
- Phosphoric acid fuel cells (PAFC) use concentrated phosphoric acid (~100%) as the electrolyte. Operating temperatures are between $150^{\circ}C$ and $220^{\circ}C$.
- Molten carbonate fuel cells (MCFC) have the electrolyte consisted of a mixture of alkali (Li, Na, K) carbonates, which is suspended in a ceramic matrix of $LiAlO_2$. Operating temperatures are between $600^{\circ}C$ and $700^{\circ}C$. At these temperatures, the carbonates form a highly conductive molten salt, with carbonate ions providing ionic conduction.
- Solid oxide fuel cells (SOFC) use a solid, nonporous metal oxide, typically Y_2O_3-stabilized ZrO_2 as the electrolyte. Operating temperatures change from $800^{\circ}C$ to $1000^{\circ}C$.

The operation conditions and properties of all five fuel cell types are summarized in Table 2.3 [64]. Consequently, among these fuel cells, PEMFC is attracting great attention owing to its great potential in transportation, residential and portable applications.

Table 2.3.

Characteristics of major fuel cells and their operation conditions [64]

	PEMFC	PAFC	AFC	MCFC	SOFC
Electrolyte	Polymer membrane	Liquid H_3PO_4 (immobilized)	Liquid KOH (immobilized)	Molten carbonate	Ceramic
Charge Carrier	H^+	H^+	OH^-	CO_3^{2-}	O^{2-}
Operating Temperature	80^oC	200^oC	$60-220^oC$	650^oC	$600-1000^oC$
Catalyst	Platinum	Platinum	Platinum	Nickel	Perovskites (ceramic)
Cell Components	Carbon based	Carbon based	Carbon based	Stainless steel	Ceramic based
Fuel cell compatibility	H_2, methanol	H_2	H_2	H_2, CH_4	H_2, CH_4, CO

2.2.1.2. Polymer Electrolyte Membrane Fuel Cells

PEMFCs deliver high power density which provides low weight, low cost and low volume. The idea of using a proton-conducting ion exchange membrane as solid polymer electrolyte in a fuel cell was first demonstrated by Grupp [65]. The most important breakthrough was the development of perfluorinated cation exchange membrane (Nafion®, DuPont, USA) by Grot, which extend the life time of fuel cell to several thousands of hours at operation temperatures lower than 100^oC [66, 67].

Electrochemical reactions take place at the surface of the catalyst at the interface between the electrolyte and membrane. During reaction, each hydrogen atom includes one electron and one proton. While protons travel through the membrane, electrons travel through electrically conductive electrodes, current collectors and the outside

circuit. Water is obtained at the end of the reaction and drive out of the cell with excess flow of oxygen.

The basic fuel cell reations are:

$$H_2 \rightarrow 2H^+ + 2e^- \qquad \text{(anode side)}$$

$$1/2O_2 + 2H^+ + 2e^- \rightarrow H_2O \qquad \text{(cathode side)}$$

$$H_2 + 1/2O_2 \rightarrow H_2O \qquad \text{(overall)}$$
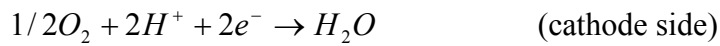
PEMFCs can be used in several application areas due to their wide range power generation. The application areas of PEMFCs according to the level of power are shown in Table 2.4 [68].

Table 2.4.

PEMFC applications according to power levels [68]

Level of power	Application area
> 1 MW	Local distributed power station
100 kW-1 MW	Large transportation vehicles (naval ships, submarines, buses); small portable power station; small stationary power station
10 kW-100 kW	Transportation vehicles (cars and mid-size buses); backup power for mid-size communication station; small power station
1 kW-10 kW	Transportation vehicles (motorcycles, utility vehicles, cars, yachts); several portable power devices used for field working; underwater platform; backup power; uninterruptible power; residential power system
100 W-1 kW	Simple riding devices (bicycles, scooters, wheelchairs); backpack power; power for exhibition or demo; UPS for small services, terminals and computers
10 W-100 W	Portable power for emergency working power supply and military equipment; battery replacements; lighting; signal light power
< 10 W	Small portable power device; cell phone

There are still problems for the commercialization of fuel cell due to the technical barriers such as on board storage, infrastructure for hydrogen fuel cell and the fuel cell system and its durability. Durability can be explained as the maximum life time of fuel cell system with no more than 10% loss in efficiency at the end of life. The main contaminants of PEMFCs are carbon monoxide, carbon dioxide, and the hydrocarbon fuel. Therefore, fuel cell life time decreased because of several failure modes mentioned in Table 2.5 [69].

Table 2.5.

Major failure modes of different components of PEMFCs [69]

Component	Failure modes	Causes
Membrane	Mechanical degradation	Mechanical stress due to the non-uniform press pressure; inadequate humidification or penetration of the catalyst particles; fluoride losss
	Thermal degradation	Thermal stress; drying of membrane
	Chemical/Electrochemical degradation	Trace metal contamination (foreign cations such as Ca^{+2}, Fe^{+3}, Cu^{+2}, Na^{+}, K^{+}, and Mg^{+2}); radical attack (e.g. peroxy and hydroperoxy)
Catalyst/Catalyst Layer	Loss of activation;	Sintering or dealloying of electrocatalyst;
	Conductivity loss;	Corrosion of electrocatalyst support;
	Decrease in mass transport rate of reactants;	Mechanical stress;
	Loss of reformate tolerance;	Contamination;
	Decrease in control of water management	Change in hydrophobicity of materials due to nafion and PTFE dissolution
Gas Diffusion Layer	Decrease in mass transport;	Degradation of backing material;
	Conductivity loss;	Mechanical stress (e.g. freeze/thaw cycle)
	Decrease in control of water management	Corrosion; change in hydrophobicity of materials

Consequently, several internal and external factors affect the performance of a PEMFC, such as fuel cell design and assembly, degradation of materials, operational conditions (temperature and pressure), and impurities or contaminants [69].

2.2.1.3. Main Fuel Cell Components

The main components of a fuel cell are an ion conducting electrolyte, a cathode (positive electrode), and an anode (negative electrode), as shown schematically in Figure 2.14. In PEMFC, a membrane as the electrolyte sandwiched between an anode (negative electrode) and a cathode (positive electrode). These three components are often called membrane electrode assembly (MEA), or simply a single fuel cell.
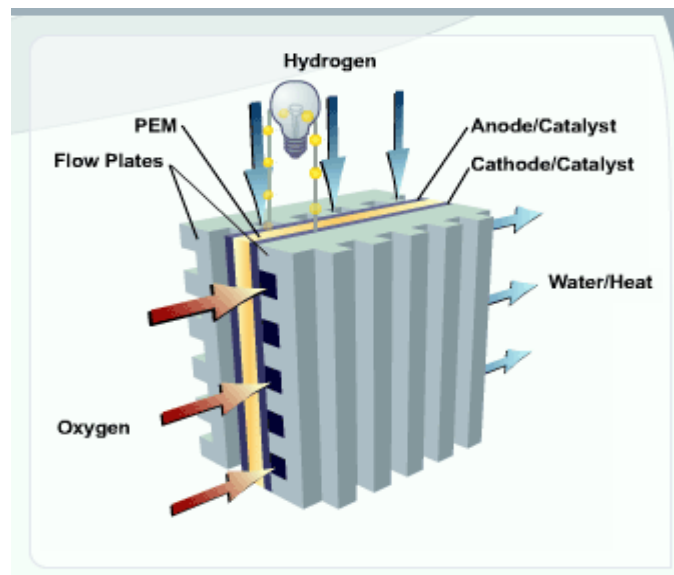
Figure 2.14. A typical PEMFC.

a. Membrane

A fuel cell membrane should have ideal physical characteristics for a PEMFC, high proton conductivity, good thermal stability, adequate mechanical strength and exceptional chemical stability [70]. The membranes of PEMFCs are made up of perfluorocarbon-sulfonic acid ionomer. The best commercial membranes are Nafion® (DuPont, USA), Flemion® (Asahi Glass, Japan) and Aciplex® (Asahi Kasei, Japan), and

composite membranes made up of a Teflon-like components such as the membrane made by W.L. Gore and Associates. However, these commercial membranes are expensive and make PEMFCs economically unattractive in several applications. These membranes are expensive because of the complex fluorine chemistry involved in the production. Therefore, the main focus of ongoing research is to decrease the cost and improve the performance of the cell [71-75].

There are some characteristic properties of membrane that affects the performance of fuel cells directly: proton conductivity, water uptake, water transport and gas permeation. The proton conductivity of proton exchange membrane (PEM) relies on the membrane structure and its water content. The water content is explained as grams of water per gram of polymer dry weight. Water uptake causes the membrane swelling and alters its dimension stability and mechanical strength. Proton conductivity is the critical property for polymer electrolytes utilized in fuel cells. High conductivity is required in order to reduce the ohmic overpotential loss. Water uptake and ion exchange capacity are two significant parameters that affect proton conductivity [76]. Membrane transport properties are highly water dependent, and thus small amount of water leads to the anode side of the membrane to dry out and lose conductivity [77]. Therefore, the membrane is a major component in the water balance. Furhermore, the membrane should be impermeable to the reacting gases to prevent the mixing of these gases prior to the electrochemical reaction.

b. Electrode

A fuel cell electrode is a thin catalyst layer sandwiched between the ion-conducting membrane and porous, electrically conductive substrate. An effective electrode is one that properly balances the transport processes required for fuel cell operations [78]. The three required transport processes are the transport of

  i. protons from the membrane to the catalyst;
 ii. electrons from the current collector to the catalyst through the gas diffusion layer (GDL);
iii. the reactant and product gases to and from the catalyst layer and the gas channels.

27

GDL must be able to conduct electricity and be water permeable because GDL is a key component of the electrode, providing hydrogen and oxygen fuel to them whereas collecting electrons generated and discharging water produced at the membrane. Therefore, there are several requirements for an ideal GDL which the diffusion of the gaseous reactants effectively into the catalyst layers, high in-plane and through-plane electronic conductivity, uniform surface for good electrical contact, and proper hydrophobicity for water management in each function. GDL has three important functions which are

   i.   the diffusion of gases through gas diffusion layer from flow channel to catalyst

   ii.   the removal of water in order to prevent flooding

  iii.   keep some water on surface to keep conductivity through PEM.

Electrode designs are changed by the structure and fabrication of the catalyst layer. Therefore, catalyst support materials have great influence on the cost, performance and the durability of PEMFCs. The ideal support materials should provide high dispersion, utilization, activity, and stability for the catalyst especially platinum (Pt) [78-80]. Pt is the most common catalyst in PEMFCs for both oxidation and reduction reactions. Carbon black has been extensively used as a catalyst support for Pt in PEMFCs. However, alternatives to carbon black are still needed to enhance catalyst utilization and reduce the cost.

c. Membrane Electrode Assembly

The heart of the PEMFCs is the membrane electrode assembly (MEA) composed of a proton exchange membrane sandwiched between two porous gas diffusion electrodes. These electrodes are made up of a catalyst support material or gas diffusion layer and a catalyst layer.

The thickness of the membrane in the MEA depends on the type of membrane and the thickness of catalyst layer. Thus, the thickness of catalyst layer relies on the amount of deposited Pt in each electrode. For catalyst layers including about 0.15 mg Pt/cm^2,

the thickness of the catalyst layer is approximately 10 μm. When the total thickness of MEA is adjusted as 200 μm, fuel cell can generate more than half an ampere of current for every square centimeter of assembly area at a voltage of 0.7 volts. However, this only occurs when all engineering components constructed properly like backing layers, flow fields, and current collectors.

2.2.2. Catalyst Support Materials

One possible limiting factor for the commercialization of PEMFCs is the cost of the catalyst materials and the relatively high resistivity of the isotropic carbon support. In current PEMFCs, carbon black is used as a catalyst support. However, the carbon black catalyst support corrodes too rapidly, especially under transient load and on/off operation conditions [81].

2.2.2.1. The Importance of Catalyst

In fuel cells, a catalyst promotes hydrogen molecules to split into hydrogen atoms and then, at the membrane, each atom splits into a proton and an electron. Noble metals (Pt, Ru or Pt-Ru alloys) deposited on high surface area carbon materials are significant electrochemical catalysts for PEMFCs. Catalytic activity relies on the size and dispersion of the metal nanoparticles on the support as well as metal-support interactions [82].

In PEMFCs, Pt is one of the best electrocatalysts for the four-electron reduction of oxygen to water in acidic environments due to its lowest overpotentials and highest stability [83]. However, Pt is quiet expensive so this becomes a major problem in the production cost. Researchers focus on the catalyst supports in order to reduce the Pt-loading but it is not easy to sustain the catalyst performance if Pt loading is decreased [84]. At this point, the proper interaction between the catalyst and support material should be provided (Figure 2.15). Carbon black is the most common catalytic support having good electronic conductivity, high surface area, good electrochemical

performance and stability in acidic environments. However, new types of support materials having high surface area are required for low catalyst loadings to decrease the cost.
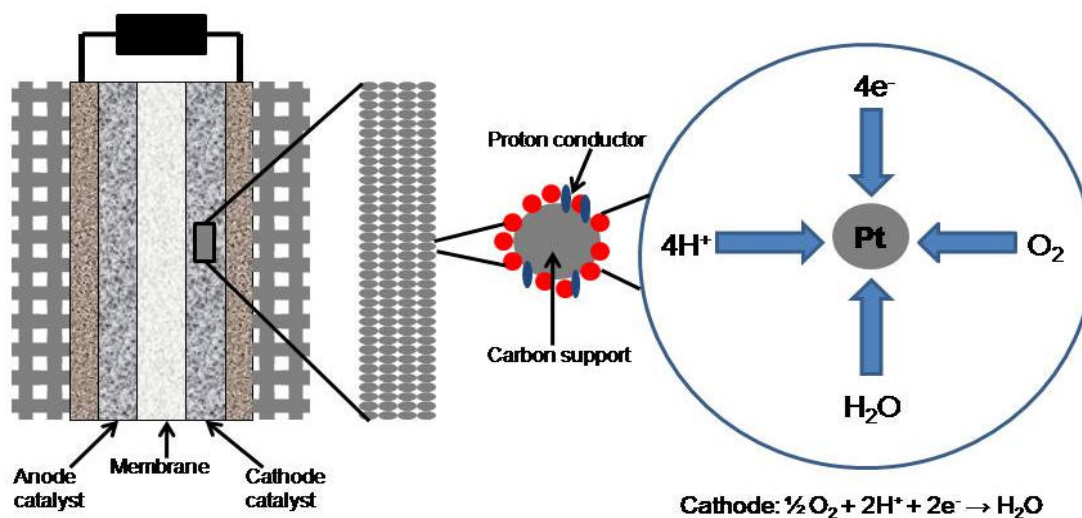
Figure 2.15. Schematic representation of the interaction between catalyst and carbon support.

Pt dispersion enlarges with increasing of oxygen surface functional groups and these oxygen groups provide fine metal dispersion because of the porous structure of supports [85]. There are two common chemical methods to synthesize carbon supported fuel cell catalysts, impregnation method [86] and colloidal method [87]. The impregnation method is more advantageous since the metal is only decorated within the pore structure of the carbon [84]. In impregnation method, a solution of metal salts is prepared and mixed with the carbon support. The resulting mixture is dried to remove the solvent and then chemical reduction and heat treatment is applied to give the desired form of the catalyst.

2.2.2.2. Ideal Catalyst Support Materials

The size of catalyst particles and the distance between the particles on support affect the surface area of electrocatalyst and catalytic activity [88]. In the PEMFC

systems, metal-support interaction has a significant influence on the growth, the structure, and the dispersion of platinum particles on the carbon supports, thus improving the catalytic properties and the stability of Pt nanoparticles [84].

An ideal carbon support should possess the following characteristics [89]:

i.   high surface area to deposit nanosized Pt catalysts, thus increasing the reaction sites for electrochemical reaction,

ii.   exhibit sufficient electrode porosity for the mass transport of reactants to the active sites and removal of products at demanding high current densities,

iii.   stable under cathode environment, where it is subjected to a high potential (> 0.85 V vs reversible hydrogen electrode), high acidity (low pH< 1), high humidity (relative humidity, RH 80%), and high temperature (60–90°C)

iv.   should possess very good electrical properties ($\sigma >0.8$ S cm^{-1}) to move the electrons produced at the anode via an external circuit to the active sites at the cathode, where air/oxygen along with the protons conducted through the membrane from the anode is reduced to water.

Long-term durability is a main obstacle in fuel cells due to loss of electrochemical surface area, carbon corrosion, etc. At this point, new discovered catalyst supports can be good candidates in order to prevent the corrosion of catalysts. These materials must be appropriately stable at low pH and high potential, in contact with the polymer membrane and under exposure to hydrogen gas and oxygen at temperatures up to 120°C. Furthermore, corrosion of the catalyst carbon support is one of the important drawbacks affecting electrocatalyst and catalyst layer durability. Carbon monoxide binds strongly to platinum catalysts at temperatures below 150°C, which decrease available sites for hydrogen chemisorption and electro-oxidation.

2.2.2.3. Novel Nanostructured Carbons as Catalyst Supports

Catalyst support materials show great influence on the cost, performance and the durability of PEMFCs. A suitable catalyst support must be stable in acidic media, and

also have good electronic conductivity, and high specific surface area. The durability of the catalyst is relied on its support.

In fuel cells, carbon black is usually utilized as the supporting material for Pt due to its high surface area and low cost. Nevertheless, carbon black has some performance and stability issues under fuel cell operation. The carbon black-based catalyst support has two common problems: (i) due to its dense structure and significant mass transfer limitations [90]; (ii) due to its easy electrochemical oxidation into surface oxides (especially CO_2 at the cathode in fuel cells). These problems lead to a very low Pt utilization. Currently, instead of carbon black, carbons with different nanostructures like carbon nanotubes (CNTs) and carbon nanofibers (CNFs) have been studied extensively [91, 92]. However, in contrast to porous carbons or CNTs, GNS have larger specific surface area, better electrical conductivity, and more flexible structure, which make graphene sheets appropriate for fuel cell applications [93].

The growth, the structure, the dispersion and size of metal catalysts on support materials affect the catalytic activity and durability. In PEMFCs, in both cathode and anode sides, low loading Pt and platinum alloys with supported carbon having large surface area are extensively used to reduce the cost.

Catalyst supports for PEMFCs are categorized in two main groups:

I. **Primary catalyst supports:** nanostructured carbon materials (CNFs, CNTs, graphitic materials (graphene, expanded graphite)), mesoporous carbons and conductive diamonds

II. **Secondary catalyst supports:** conductive oxides (indium tin oxide (ITO), TiO_x, WO_x, IrO_2, Tin oxide (SnO_2)). Oxides are used to enhance the characteristic properties of primary support material and can also be used as independent support materials.

CNFs (diameter range 3–100 nm and length range 0.1–1000 mm) often called carbon filaments or filamentous carbon have potential applications in energy storage, polymer reinforcements and catalyst supports [94]. There are three types of CNFs

shown in Figure 2.16: platelet-CNF (CNF-P), tubular-CNF (CNF-T) and herringbone-CNF (also called fishbone-CNF). Like CNTs, CNF can be produced over metal catalysts by CVD techniques. CNFs provide high dispersion of Pt nanoparticles due to their high surface area and unique structures [95]. Bessel *et al.* [95] deposited Pt particles on three types of CNFs by using incipient wetness method. Their results showed that 5 wt% Pt catalysts can be deposited on 'platelet' and 'ribbon' CNFs whereas 25 wt% Pt particles dispersed on Vulcan carbon.
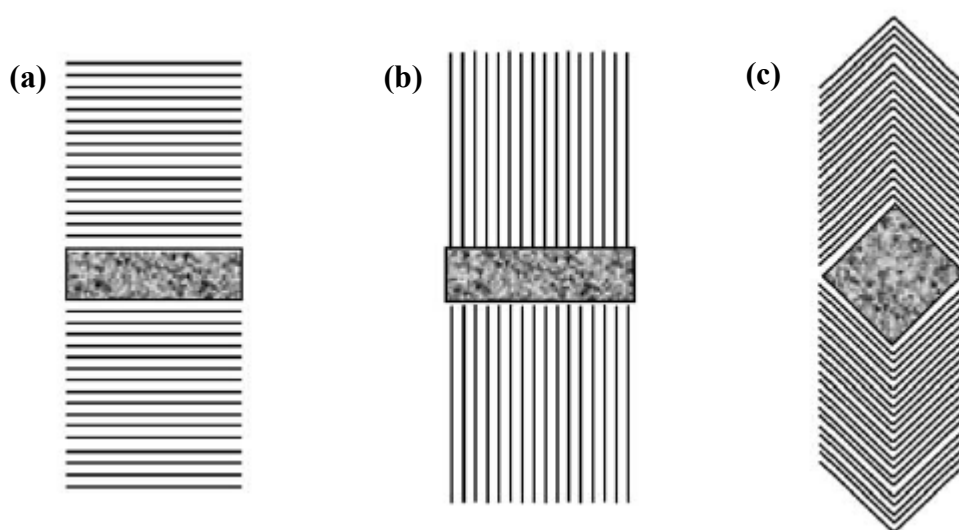
Figure 2.16. Schematic representations of three types of CNFs **(a)** CNF-P, **(b)** CNF-R and **(c)** CNF-H.

CNTs were first discovered by Iijima at the NEC laboratory in 1991 [96]. CNTs can be categorized into single-walled CNTs (1-3 nm diameter) and multi-walled CNTs (10-100 nm diameter) (Figure 2.17). Among several synthetic routes for the production of CNTs, the CVD route is mainly favored because of its scalability and potentially low cost [97]. In CVD technique, the catalytic metal nanoparticles are often coated onto a solid support in order to prevent sintering at high growth temperatures (600 to 1000°C). Widely used supports include silica (SiO_2), alumina (Al_2O_3), titania (TiO_2) or magnesium oxide (MgO) due to their chemical inertness and high-temperature resistance.
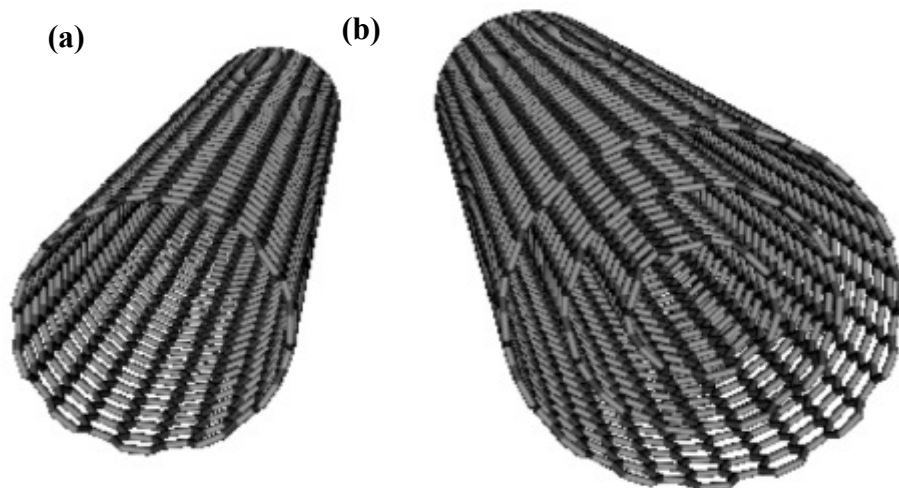
Figure 2.17. Schematic representations of **(a)** single-walled CNT and **(b)** multi-walled CNTs.

The common obstacle in CNTs and CNFs as catalyst support is to control the size and distribution of Pt nanoparticles. Surface treatment of carbon nanostructures affects the dispersion and size distribution of Pt catalyst particles on the surface. For instance, the oxidative treatment of the carbon surface causes the formation of surface acidic sites and the destruction of surface basic sites. In consequence of oxidation process, the aromatic conjugate ring system of graphene sheet surface can be modified and CNTs can be functionalized with functional groups such as hydroxyl (-OH), carboxyl (-COOH), and carbonyl (-C=O) [98]. These surface functional groups serve as metal-anchoring sites to facilate metal nuclei formation and electrocatalysts deposition.

The chemical interaction between catalyst metal ions with functionalized CNT surface could be proposed as following equation:

$$CNT\text{-}COOH + M^+X^- \rightarrow CNT\text{-}COO^-M^+ + HX$$
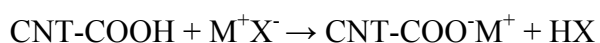
where the carboxylic group on the CNT surface exchanges a proton with a metal ion (M^+). Rajalakshmi *et al.* [99] demonstrated that the particle size of Pt might be correlated with the oxidation degree of CNTs, indicating that the efficient deposition of Pt particles is because of the strong interaction between metal salt precursor and the surface oxygen functional groups.

The properties, applications and future directions of catalyst supports summarized in Table 2.6 [10].

Table 2.6.

Electrocatalyst supports for PEMFCs: properties, preferred applications, future directions [10]

Support materials	Properties	Application	Future directions
CNT/CNF	sp^2 carbon, medium/high surface area, high conductivity, high durability	Anode and cathode	Nanostructure optimization, doping strategy.
Mesoporous carbon	sp^2/sp^3 carbon, high surface area	Anode and cathode	Conductivity and durability improvement, doping strategy.
Conductive diamond	sp^3 carbon, high stability, low surface area and low conductivity	Cathode preferred	Conductivity and surface area, nanodiamonds, doping.
SnO_x/ITO	Semiconductor/conductor, low surface area and conductivity, high durability	Anode and cathode	Conductivity, chemical composition, surface area.
Ti_xO_y	Semiconductor/conductor/proton conductor, low surface area, high durability	Anode and cathode	Conductivity (e^- & H^+), chemical composition, surface area, nanocomposite, doping.
WO_x	Semiconductor/proton conductor, low surface area	Anode and cathode	Conductivity (e^- & H^+), durability, chemical composition, surface area, doping.
WC/WC_2	Pt-like catalytic properties, synergistic effect	Anode preferred	Durability, surface area.

2.2.2.4. Conducting Polymers as Catalyst Supports

Conducting polymers have high conductivity, and are lightweight, inexpensive, flexible, airstable and environmentally friendly but the major obstacle of conducting polymers as an electrode material is the degradation during cycling because of the volume change of the polymer due to the insertion/deinsertion of counter ions [100]. Conducting polymers provide conductive through a conjugated bond system along the polymer backbone. Conducting polymers have partially crystalline or partially amorphous structures and thus they contained both delocalized and localized states. The delocalization of π electrons relies on the extent of disorder, interchain interactions, etc. The disorder and induced localization have a significant influence on the metal-insulator interaction and transport properties of conducting polymers. Furthermore, the structure of polyconjugated chain, interchain interaction, disorder and doping level affect the stability of charge carriers (solitons, polarons, bipolarons, and free carriers in doped conducting polymers).

In 1958, Natta firstly synthesized polyacetylene as a black powder by bubbling acetylene gas through a titanium/trialkyl aluminum catalyst solution while stirring. In 1971, Shirakawa synthesized polyacetylene films on the metal surface using Ti(OBu)$_4$-Et$_3$Al known as the Ziegler-Natta catalyst by a mild method. After the discovery of polyacetlyene, various conjugated polymers have been produced. There are two major synthesis techniques: chemical oxidation of the monomer and electrochemical oxidation of the monomer [101]. Figure 2.18 shows the chemical structures of commonly used conducting polymers.
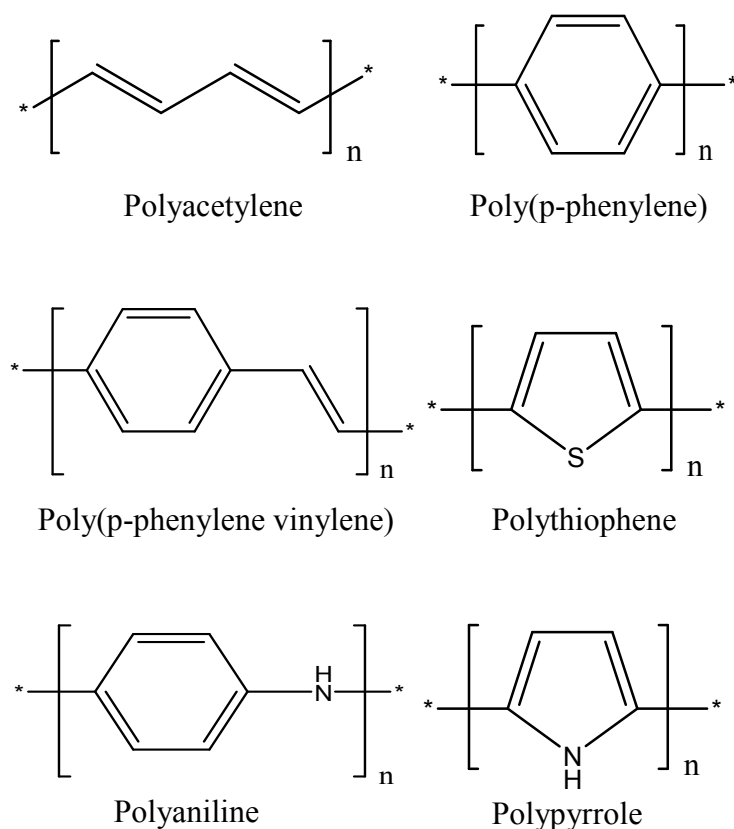
Figure 2.18. Chemical structures of widely used conducting polymers.

The doping process is performed by chemical or electro-chemical oxidation (p-type doping) or reduction (n-type doping) of a polymer. The doping leads to the formation of different charge carriers which are polarons, bipolarons, solitons, and free carriers. The polaron–bipolaron model is extensively used for the explanation of electrochromic and electrochemical behavior of conducting polymers. Polaron and bipolaron states are directly related to the intermediary energy levels that placed in the electronic band gap region of the polymer due to oxidation [102]. A charge associated with a boundary or domain wall is called a soliton since it has the properties of a solitary wave which can propagate without deformation and dissipation [103]. The amount of polarons, bipolarons, and/or solitons increases with the doping level.

Band theory can clearly explain the electrical properties of conducting polymers. Polymer having a crystalline structure can interact with all its neighbors to form electronic bands. The highest occupied electronic levels constitute the valence band (VB) and the lowest unoccupied levels, the conduction band (CB). The width of the

forbidden band, or bandgap (Eg), between the VB and CB tailors the intrinsic electrical properties of the material.

In conducting polymers, the motion of delocalized electrons occurs through conjugated arrangements but the electron hopping mechanism is expected to be operative between chains (interchain conduction) and defects. The electron transfer mechanism occurs by the movement of electrons through overlapping and unoccupied electronic energy states.

Among the various conducting materials, polypyrrole (PPy) has taken special attention because of its relatively easy processability, electrical conductivity, and stability in the oxidized states [14]. PPy shows a greater degree of flexibility in electrochemical processing than most of conducting polymers, and thus PPy is widely used as a supercapacitor or battery electrode [101].

PPy can be synthesized in two ways: chemical synthesis and electrochemical synthesis. PPy synthesized by the oxidation of the monomer with chemical oxidants such as aqueous or anhydrous $FeCl_3$, other salts of Fe^{+3} and Cu^{+2} have a form of black powder. There are several parameters that affect the yield and conductivity of the PPy which are the choice of solvent and oxidant, initial pyrrole/oxidant ratio, duration and temperature of the reaction.

The lattice distortion extends over four pyrrole rings in PPy structure. This combination of a charge site and a radical is called a polaron. This can be either a radical cation (oxidation) or a radical anion (reduction). The formation of polaron causes new localized electronic states in the gap, with the lower energy states being occupied by single unpaired electrons. When a polaron is removed from the polymer backbone due to further oxidation, two new positive charges are formed which is called bipolarons. As the dopping process increases, additional bipolaron states start to form and thus these states overlap to form bipolaron bands (Figure 2.19). Consequently, polarons and bipolarons formed in the two-step redox process:

$$PPy^0 \xrightarrow{E_1} PPy^{\bullet+} + e^-$$
$$PPy^{\bullet+} \xrightarrow{E_2} PPy^{2+} + e^-$$
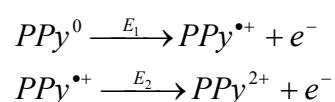
where E_1 and E_2 are the quasi-standard potentials of formation for polarons (PPy$^+$) and bipolarons (PPy^{2+}).
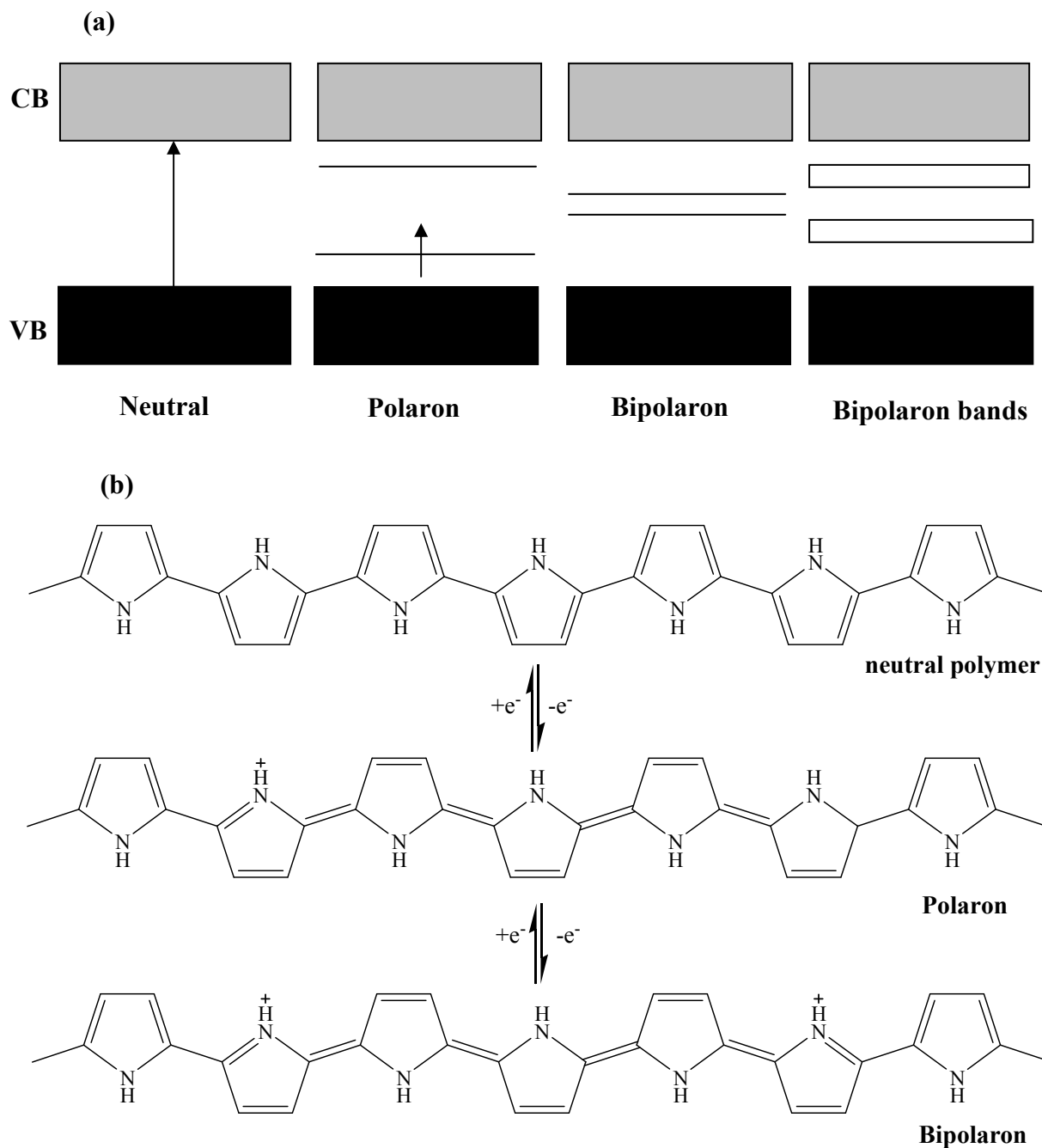
Figure 2.19. Schematic representations of **(a)** energy gaps and **(b)** chemical structures of polaron and bipolaron in PPy structure.

Conducting polymers represent an ideal fuel cell catalyst support in the oxidized state since they have both electronic and ionic conductivity and porous structure. PPy, poly(3,4-ethylenedioxythiophene) (PEDOT) or polyaniline based supports have reported previously [104-106]. Nanocomposites based on conducting polymers and carbon nanomaterials can be used as a potential catalyst support to improve the properties of supports and extend life cycle of fuel cells. There have been several attempts for the synthesis of these types of nanocomposites. Previously, Wang *et al.* [107] reported that the remarkable electrical conductivity and specific capacitance of graphene/polyaniline composites as a supercapacitor electrode material. Recently, a study was published on a graphene/polyaniline composite paper by in situ anodic electropolymerization of aniline monomer as a polyaniline film on graphene paper [108]. In addition, graphene sheets dispersed in the polymer matrix provide a stronger catalyst-support interaction and produce smaller catalyst particles which are more resistant to degradation [107, 109].

2.2.2.6. Catalyst Deposition Techniques

Deposition of Pt catalysts can be divided into two main groups: physical and chemical methods. Physical methods mostly involve in the atomization of metals in a vacuum by thermal evaporation or sputtering. On the other hand, chemical methods are more preferably due to the control of size, shape and compositions, as well as easy mass production. There are several chemical methods for the deposition of Pt catalysts on supports. Mostly used chemical deposition techniques are impregnation method, electrochemical method, colloidal method, ion-exchange method and sputtering method. The impregnation method is the most widely used wet-chemical technique. This method has the advantages of facile metal deposition on the carbon support and large scale production [110]. This method is applied by the impregnation of metal salt solution on the support materials and then the reduction of catalyst ions. The functionalization of carbon supports with reactive groups has a significant influence on the size and distribution of Pt particles during impregnation method. There are two types of functionalization: covalent and non-covalent functionalization. Covalent surface

modification causes a permanent change on the material surface and the functional groups form a covalent bond with metal catalysts [111].

Surface oxidation, one of the covalent modifications, provides the formation of functional groups like hydroxyl (-OH), carboxyl (-COOH) and carbonyl (-C=O) on the support surface. These functional groups can act as metal-anchoring sites to facilitate metal nuclei formation and electrocatalysts depositon [99]. For the surface oxidation, several oxidizing agents are used such as $KMnO_4$, $K_2Cr_2O_7$, H_2SO_4, HNO_3, H_2O_2, etc. Xu *et al.* [112] studied the effect of the treatment process on Pt catalyst deposition on CNTs. In their work, CNTs were oxidized by H_2SO_4 and HNO_3 and then immersed in H_2O_2 solution for Pt deposition. The size of Pt nanoparticles on the CNT's surface was estimated approximately 3 nm and the best catalytic properties were observed in PEMFCs. Matsumoto *et al.* [91] oxidized CNTs by HNO_3 through refluxing and then two different Pt compounds which are $H_2Pt^{+4}Cl_6 \cdot 6(H_2O)$ and $K_2Pt^{+2}Cl_4$ used for the deposition on functionalized CNTs. The deposition procedure is conducted by heating CNTs with these two catalysts in ethylene glycol at 313 K for 2 h. Two kinds of Pt deposited CNTs are characterized by Transmission Electron Microscope (TEM), Figure 2.20.
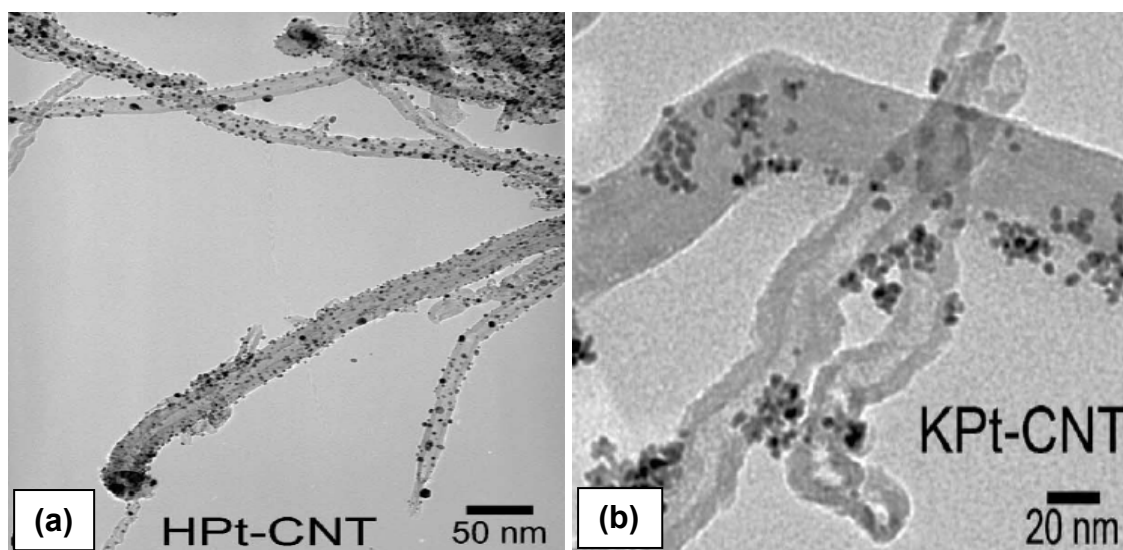
Figure 2.20. TEM images of Pt deposited CNT **(a)** HPt-CNT and **(b)** KPt-CNT [91].

After the discovery of graphene, researchers have started to utilize graphene sheets as catalyst supports and impregnated Pt nanoparticles on the surface of the sheets.

Yoo *et al.* [113] demonstrated that Pt catalyst deposited GNS shows a higher CO tolerance performance in the hydrogen oxidation reaction and enhances the catalytic activity. In their work, 20 wt% Pt catalysts were deposited onto GNS using a platinum precursor of $[Pt(NO_2)_2(NH_3)_2]$ in an ethanol solution. Before the deposition of Pt catalyst particles, graphene sheets have ripple structure, Figure 2.21 (a). After the Pt deposition, Pt particles disperse on the surface of sheets in the size range of 2-3 nm, Figure 2.21 (b).
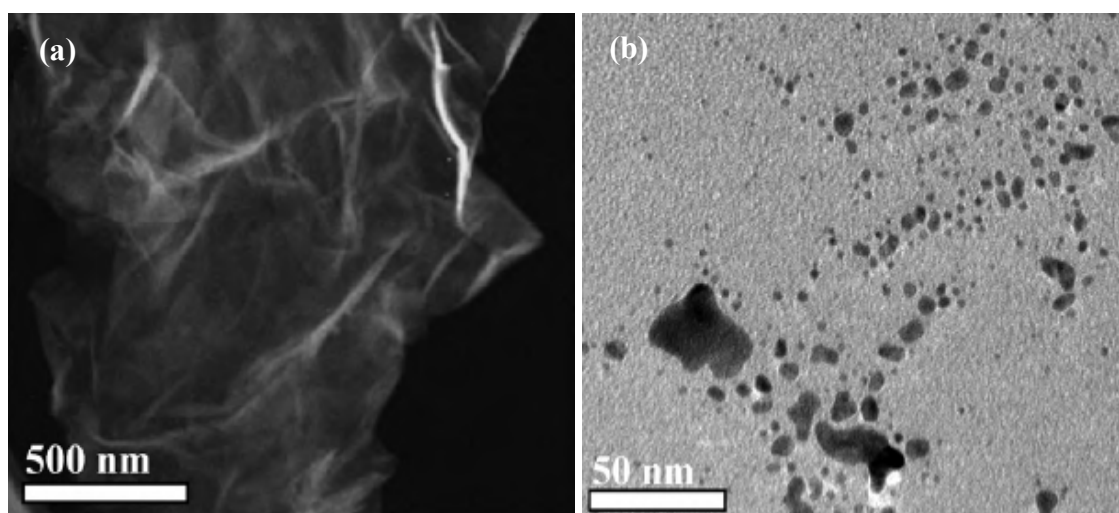
Figure 2.21. (a) TEM image of graphene sheets and **(b)** High-Angle Annular Dark-Field Scanning Transmission Electron Microscopy (HAADF-STEM) image of 20 wt% Pt/GNS [113].

Instead of impregnation method, electrochemical method, colloidal method, ion-exchange method, microwave heated polyol method and sputtering method are applied for the decoration of Pt nanoparticles on supports. For instance, electrochemical method provides selective deposition at the defined locations by controlling the nucleation and growth of Pt catalysts. In this method, pulse current, direct current and cyclic voltammetry are mostly used techniques to decorate catalyst particles on carbon supports and this technique provides low Pt loadings and enhances the Pt utilization at anode and cathode sides of PEMFCs [114]. In the colloidal method, the size of Pt catalysts is tailored by the protecting agents such as ligands, surfactants, or polymers [115]. This method includes the production of platinum metal colloid and then adsorption on carbon support or the fabrication of oxide colloidal Pt particles and then reduction and adsorption on support. In the ion-exchange method, protective colloiding

agents, reducing agents, precursor complexes, etc. are not used and only cation complex of Pt catalysts was ion-exchanged with hydrogen ions of the acid functional groups on carbon supports [58]. In the microwave heated polyol method, colloidal Pt and Pt alloys prepared by polyol process (mostly used ethylene glycol) are decorated on carbon supports by a microwave assisted process [116]. In the sputtering method, Pt deposition is conducted on a carbon gas diffusion media by sputtering to provide maximum Pt dispersion on support materials [117].

CHAPTER 3. AIM AND MOTIVATION

As mentioned previously in Chapter 2, there have been several reported oxidation-exfoliation methods for the oxidation of graphite, chemical reduction and thermal treatment. Each method has a number of advantages and disadvantages and especially hazardous and harsh chemicals such as hydrazine, nitric acid are used in these methods. Therefore, the synthesis of high-quality graphene sheets in commercial quantities is still the most significant step. In this study, we proposed a simple, safer and cheap method for the production of high-quality and high-yield graphene nanosheets (GNS).

The remarkable physical, chemical and mechanical properties of graphene sheets open up the extensive applications in energy storage devices. Especially polymer electrolyte membrane fuel cells (PEMFCs) deliver high-power density and offer the advantages of low weight and volume, compared with other fuel cells. They also operate at relatively low temperatures, around 80°C. However, there are several obstacles for both the production of GNS and the cost of fuel cells. A major obstacle to the commercialization of PEMFCs is the high cost and stability of Pt electrocatalysts. At this point, GNS as a catalyst support can provide maximum catalyst dispersion and thus enhance the catalyst activity in fuel cells due to their large surface area, good electrical conductivity, and exceptional chemical stability.

In addition, the incorporation of graphene sheets in conducting polymers can enhance thermal, electrical and chemical features of catalyst support. A critical step in polymer nanocomposites is the dispersion of the nanofillers. Herein, we proposed sonication combined with *in situ* polymerization technique for the formation of well-dispersed structures.

This thesis includes the topics of an extensive area from the synthesis of graphene sheets to the utilization of graphene-based electrodes in fuel cells. The main objectives of this study are summarized as follows:

i. Chemical exfoliation of graphite by an improved, safer and mild method for the large-scale synthesis of GNS.

ii. Tailoring characteristic properties of GO sheets and GNS at different oxidation times.

iii. Graphene based nanocomposite production.

iv. Pt deposition on graphene based nanocomposites and the effect of oxygen surface groups on Pt dispersion.

v. Fabrication of fuel cell electrodes.

vi. Fabrication of membrane electrode assembly (MEA) for fuel cells.

vii. Fuel cell testing.

i. In the literature, several techniques were described for the exfoliation of graphene sheets. In this study, we proposed an improved, safer and mild method for the exfoliation of graphene nanosheets from graphite at mild reaction conditions. Instead of strong oxidizing agents such as potassium chlorate, and potassium permanganate as used in the other papers, GO was prepared by the reaction of graphite with potassium dichromate and sulfuric acid as oxidizing agents. Since there are risks of explosions, when potassium chlorate, and potassium permanganate are used together with sulfuric acid. Therefore, the major aims in this step are to reduce the number of layers in the graphite material using a safer and mild technique, and to produce large quantities of graphene bundles to be used as catalyst support in PEMFCs.

ii. After oxidation process, GO still preserves a layered structure, yet is much lighter in colour than graphite owing to the loss of electronic conjugation. As the oxidation time is increased, the strong bonding between graphene layers in graphite can be reduced and graphene layers start to exfoliate forming clusters with a few number of graphene layers. In this step, there are three main objectives which are (i) to tailor the characteristic properties of GNS via various oxidation

times, (ii) to optimize reactant ratios during graphite oxidation, and (iii) to decrease the number of graphene layers in graphitic structure to be used as fuel cell electrodes.

iii. GNS can act as effective conductive fillers in polymer matrice due to the high aspect ratio, excellent electrical conductivity and cost efficiency as compared to CNTs. Therefore, in this step, GNS were fabricated in large quantities by adopting a safer and mild chemical route including oxidation, ultrasonic treatment and chemical reduction. Moreover, the products obtained after each step in the synthesis of GNS such as GO sheets and expanded GO were used as fillers in polymer matrix.

In this step, PPy was coated on GO sheets, expanded GO and GNS by *in situ* polymerization with different Py feed ratios. The influence of the feeding ratios on the morphologies, crystal structures, thermal properties, and electrical conductivities of PPy/GO, PPy/Expanded GO and PPy/GNS composites were investigated systematically by various characterization techniques.

iv. The material on which the catalyst is supported has a significant influence on the dispersion and size of the metal clusters. The capability of GNS to support metal particles provides new ways to improve electrocatalyst for fuel cells. For that reason, PPy/GO, PPy/Expanded GO and PPy/GNS composites were prepared to be employed as the catalyst supports. Then, Pt catalysts were impregnated on the surface of composites, and catalyst dispersion and size distribution were tailored by applying three different methods including sonication and direct deposition techniques. By applying different deposition techniques, we proposed a shorter and more effective deposition technique for maximum catalyst dispersion. In addition, we investigated the effect of oxygen surface groups on Pt dispersion by comparing XRD and EDX results of GO, expanded GO, GNS and their composites before and after the Pt deposition. To best of our knowledge, this is the first comprehensive and quantitative investigation in the literature about the relationship between the Pt dispersion and oxygen functional groups on the surface of graphene-based nanocomposites.

v.   New fuel cell electrodes composed of GO, GNS, and their composites can function as conventional electrodes and provide a significant reduction in weight of fuel cells. Since the weight and space of fuel cells are main requirements, the energy can be maximized by using a new and improved lightweight fuel cell electrode. Also, the large quatities of Pt catalysts in original PEMFCs is the main obstacle for the commercialization. In this step, thin-film composite electrodes were prepared using GO, GNS and their composites by drop-casting method. Then, Pt catalysts were decorated on these fuel cell electrodes.

vi.   The heart of PEMFCs is the MEAs. MEAs consists of PEM, catalyst layers, and GDLs. In this step, these components were sticked to each other by Nafion$^{®}$ solution as a binder, and pressed at adjusted pressure, and then cured at 70°C. Before MEA fabrication, commercial PEM was activated using concentrated HNO_3. Pt supported on GNS, GO sheets and their nanocomposites was used as electrocatalyst for PEMFC cathodes to achieve the highest catalytic activity of Pt metals for oxygen reduction reaction in fuel cell applications. In addition, Pt deposited electrodes were used in both cathode and anode sides in order to compare the performance of fuel cells.

vii.   Electrodes have a significant influence on the operation of PEMFC since they can correctly balance transport processes of protons, electrons and gases. In addition, catalyst loading is another key parameter for the effective operation of PEMFC.

Therefore, functionalized graphene sheets could potentially lead to a more stable, efficient, and lower-cost fuel cell. Especially graphene-based nanocomposites as fuel cell electrodes have a dramatic effect on fuel cell performance. We suggested that incorporation of few-layer graphene in composites as a catalyst support might enhance the surface area to volume ratio and increase the catalytic activity and reduce rare metal usage. At this stage, the prepared MEAs were tested in a single fuel cell and I-V polarization curves of Pt deposited GNS, GO sheets and their nanocomposite electrodes were investigated.

CHAPTER 4. EXPERIMENTAL

4.1. Materials

Graphite flake (Sigma–Aldrich); acetic anhydride (Merck, extra pure); sulfuric acid (H_2SO_4, MW: 98.08 g/mol, Fluka, purity 95–97%); potassium dichromate ($K_2Cr_2O_7$, MW: 294.185 g/mol, Chempur, purity 99.9%); hydroquinone ($C_6H_4(OH)_2$, MW: 110.1 g/mol, Acros, purity 99%); sodium hydroxide (NaOH, MW: 39.99711 g/mol, Merck, purity 97%), pyrrole (C_4H_5N, MW: 67.09 g/mol, Merck, purity 98%), iron (III) chloride hexahyrdate ($FeCl_3.6H_2O$, MW: 270.3 g/mol, Aldrich, purity 97%). Nitrogen (N_2, purity 99.99%) and Argon (Ar, purity 99.99%) were received from Linde Gaz. The Nafion®212 membrane was purchased from fuelcellstore.com. Kish graphite was purchased from Graphene Supermarket. Kish graphite is crystal precipitated from molten iron, nearly ideal graphite.

4.2. Reaction Set-up's

4.2.1. Chemical Vapor Deposition Set-up

Expansion process was conducted by using conventional CVD set-up, Figure 4.1. There are four control parameters investigated during CVD experiments: furnace temperature, catalyst type, flow rate of gases, and nature of the sample. The photograph of CVD set-up was shown in Figure 4.2.
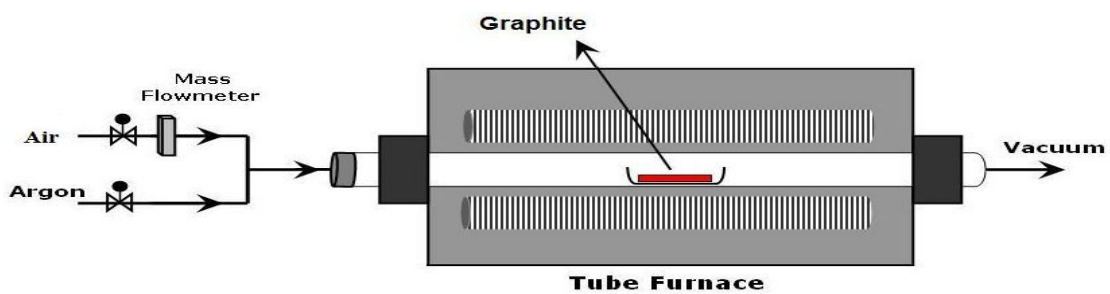
Figure 4.1. Schematic representation of CVD set-up.
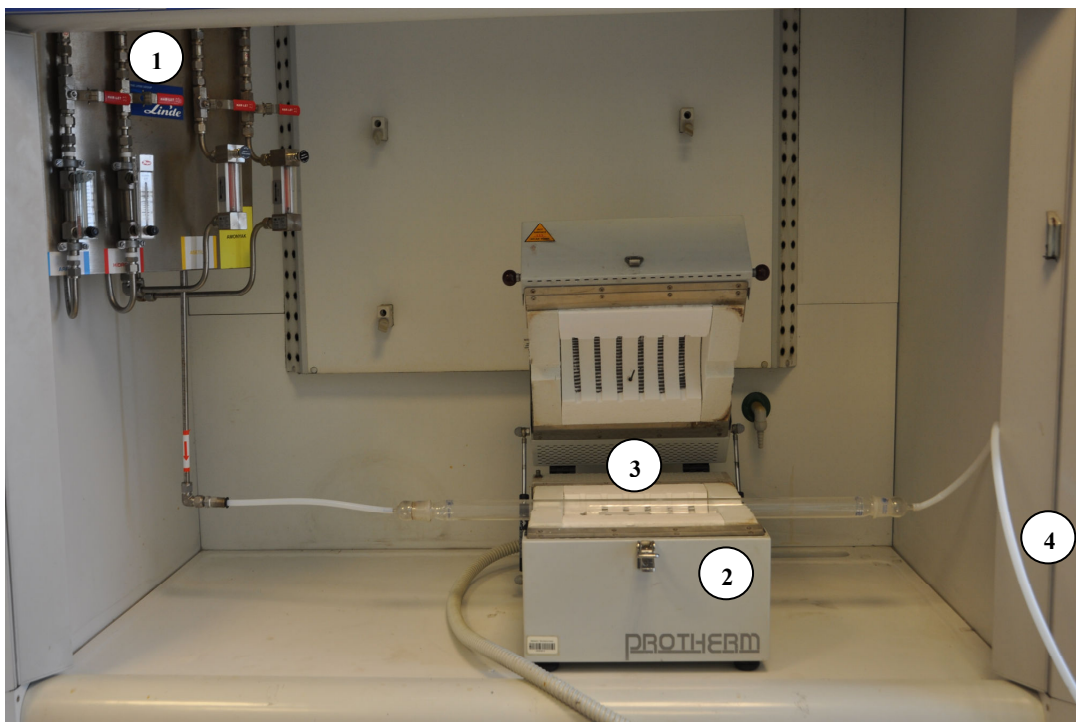
Figure 4.2. A photograph of CVD set-up (1: Flow rate control panel, 2: Tube furnace, 3: Quartz tube, 4: Teflon outlet pipe).

4.3. Material Synthesis

4.3.1. Chemical Exfoliation of Graphene Nanosheets from Graphite

4.3.1.1. Synthesis of Graphite Oxide

Graphite oxide (GO) was prepared according to the following method by using potassium dichromate as oxidant [118]. Using $KMnO_4$ as oxidizing agent as used in other papers was thought to be very severe and there were risks of explosions when it is used together with H_2SO_4. Therefore, we used a milder oxidant, $K_2Cr_2O_7$ to prevent such experimental dangers. $K_2Cr_2O_7$ and H_2SO_4 were stirred in a flask in two different weight ratios as 0.6:6.2, 2.0:9.3 and 2.1:55. For the second set, 1.5 mL distilled water was also added to prepare chromic acid. In both cases, flake graphite (1.0 g) was added to flask and the mixture was stirred gently. Then, acetic anhydride (1.0 g) used as an intercalating agent was slowly dropped into the solution. The solution was stirred at 45°C for 50 min. GO obtained was filtered and neutralized with 0.1 M NaOH and washed with distilled water until washings were neutral. After washing, GO was dried in a vacuum oven at 80°C overnight. Experimental conditions for graphite oxidation are summarized in Table 4.1.

Characteristic properties of GO sheets were tailored at different oxidation times as 50 min, 6 hrs, 12 hrs, 24 hrs, 48 hrs, 72 hrs, 96 hrs, 120 hrs and 10 days [119].

Table 4.1.

Experimental conditions for graphite oxidation

Experiment #	Graphite flake (g)	Acetic Anhydride (g)	Concentrated sulfuric acid (g)	Potassium dichromate (g)
1	1	1	6.2	0.6
2	1	1	9.3	2.0
3	1	1	55	2.1

4.3.1.2. Ultrasonic Treatment of GO Sheets

GO sheets were exfoliated into dispersed GO sheets in distilled water for 1 hr at room temperature via ultrasonic vibration. Alex table top ultrasonic cleaner (frequency: 40 Hz) was used for ultrasonic treatment.

4.3.1.3. Thermal Expansion of GO

GO was expanded by heating up to $900^{o}C$ rapidly in a tube furnace and kept for 15 min at this temperature under an argon atmosphere. GO samples were also expanded at $1000^{o}C$ and for 1 min and 5 min. Expanded GO was subjected to ultrasonic water bath for 1 hr for dispersion and then dried at $80^{o}C$ in a vacuum oven overnight.

4.3.1.4. Chemical Reduction

Both sonicated GO and expanded GO samples were exfoliated and reduced by refluxing in hydroquinone and distilled water under N_2 atmosphere for 1 day. The graphene-based sheets were separated by filtration and washed with methanol and water three times and, dried in a vacuum oven at $80^{o}C$ overnight. On the other hand,

unexpanded GO samples were also chemically reduced to graphene-based nanosheets by following the same reduction procedure.

General experimental procedures for the production of graphene nanosheets (GNS) were shown schematically in Figure 4.3 [3, 119].
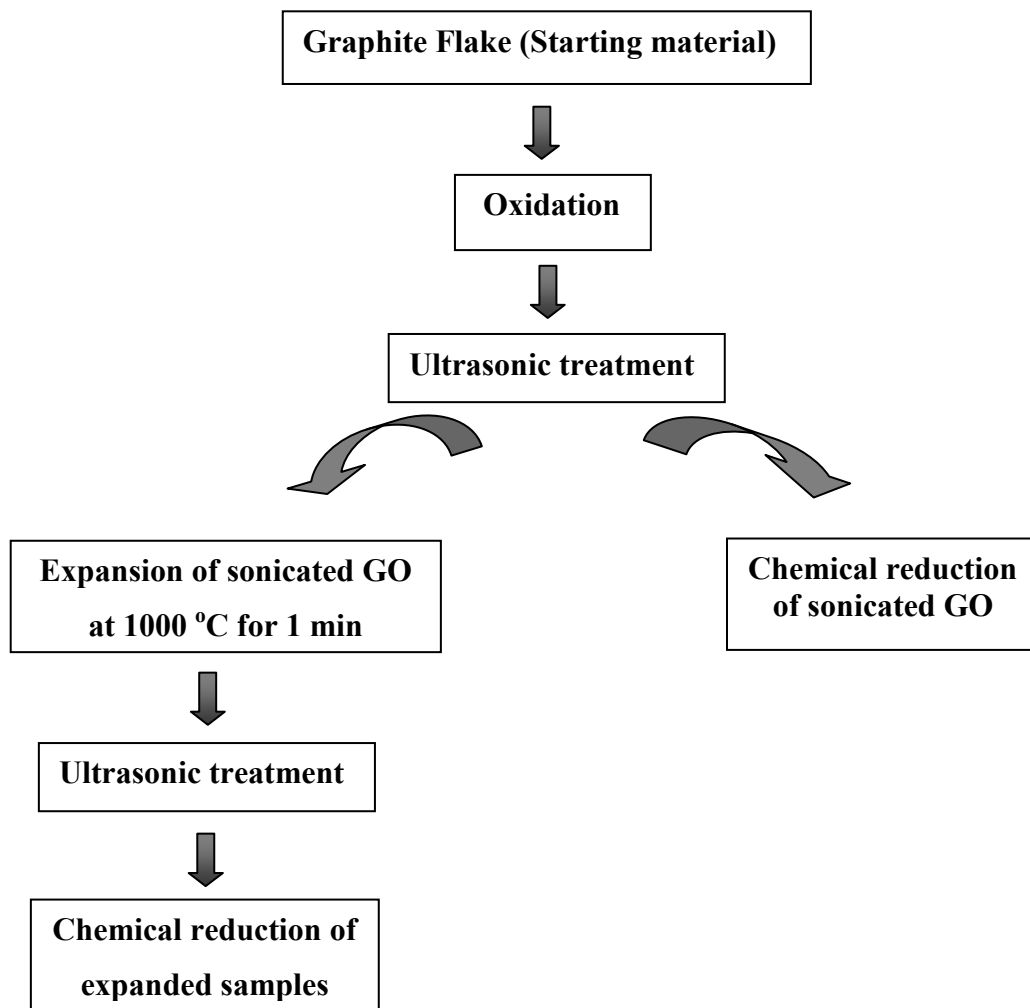
Figure 4.3. General experimental procedure for the production of GNS.

Each step in chemical exfoliation of GNS was shown in Table 4.2.

Table 4.2.

Summary of chemical process steps for the exfoliation of GNS

Treatment conditions	
Oxidation	Graphite flake, concentrated sulfuric acid, $K_2Cr_2O_7$, acetic anhydride
Sonication	1 hr at room temperature
Expansion	Performed in a tube furnace under Ar atmosphere
Reduction	- m(GO sheets): m(hydroquinone)= 0.036:1 - solvent=distilled water - Reflux for 24 hrs under N_2 atmosphere

Experimental conditions for the exfoliation of GNS were adjusted by changing oxidation time, the amount of intercalating agent, expansion time and expansion temperature in order to tailor the characteristic properties of GO sheets and GNS. All experiments were summarized in Table 4.3. In each experiment, the conditions for the sonication and reduction processes were kept same shown in Table 4.2.

Table 4.3.

Summary of experimental conditions for the exfoliation of GNS

Experiment	Oxidation & Reaction time	Sonication	Expansion time & Temperature	Reduction
I	1 g acetic anhydride, 30 mL H_2SO_4, 2.1 g $K_2Cr_2O_7$ 1 hr	SAME CONDITIONS	900°C, 15 min	SAME CONDITIONS
II	1 g acetic anhydride, 30 mL H_2SO_4, 2.1 g $K_2Cr_2O_7$ 1 hr	SAME CONDITIONS	1000°C, 5 min	SAME CONDITIONS
III	5 g acetic anhydride, 30 mL H_2SO_4, 2.1 g $K_2Cr_2O_7$ 1 hr	SAME CONDITIONS	1000°C, 5 min	SAME CONDITIONS
IV	1 g acetic anhydride, 30 mL H_2SO_4, 2.1 gr $K_2Cr_2O_7$ 6, 12, 24, 48, 72, 96, 120 hrs and 10 days	SAME CONDITIONS	1000°C, 1 min	SAME CONDITIONS

4.3.2. Synthesis of Graphene-based Nanocomposites

4.3.2.1. Synthesis of Polypyrrole

Pristine polypyrrole (PPy) was synthesized by using pyrrole (Py, 0.0447 mol) as the monomer and $FeCl_3$ (0.107 mol) as the oxidant in the mixture of H_2O and ethanol in 1:1 (v/v) under N_2 atmosphere [14]. The Fe^{3+}/Py molar ratio was adjusted as 2.4 [120]. At the beginning, the reaction mixture was placed in an ice bath about 1 hr to prevent a sudden heating. Then, the mixture was stirred at room temperature for 24 hrs. PPy was filtrated by washing with ethanol and distilled water three times. Polymer was dried in a vacuum oven at 80°C overnight.

4.3.2.2. Synthesis of PPy/GO Nanocomposites

PPy was coated on GO sheets by *in situ* polymerization of Py at room temperature under N_2 atmosphere for 24 hrs. The precipitated sample was filtered and rinsed several times by ethanol and distilled water to remove excess Py, catalyst and side products. The black powder was dried under vacuum at $60^{\circ}C$ for 24 hrs. During PPy synthesis, the Fe^{3+}/Py molar ratio was adjusted as 2.4 [120]. The feeding mass ratios of Py and GO sheets were 1:1, 2:1 and 1:3.

4.3.2.3. Synthesis of PPy/Expanded GO Composites

Firstly, GO sheets were expanded by heating up to $1000^{\circ}C$ rapidly in a tube furnace and kept for 1 min at this temperature under an argon atmosphere. Then, PPy was coated on expanded GO sheets by *in situ* polymerization of Py at room temperature under N_2 atmosphere for 24 hrs. Before polymerization, expanded GO and Py monomer in adjusted weight fractions were exposed to ultrasonic vibration for 2 hrs in order to diffuse Py monomer through GO layers. Ultrasonic treatment also provided to break expanded GO apart into thinner graphite nanoplatelets (GNPs) [41]. $FeCl_3$ was used as a catalyst and the Fe^{3+}/Py molar ratio was adjusted as 2.4 [120]. The feeding mass ratios of Py and expanded GO were 1:1, 2:1, 4:1, 1:2 and 1:3. The resulted powder was filtered and washed several times by ethanol and distilled water. All samples were dried in oven at $60^{\circ}C$ for 24 hrs.

4.3.2.4. Synthesis of PPy/Graphene Nanosheet Nanocomposites

After the sonication and reduction of GO sheets, GNS were received. PPy was coated layer-by-layer on the surface of GNS in the feeding mass ratios of Py and GNS as 1:1. Then, purification and filtration processes by ethanol and distilled water were conducted to obtain PPy/GNS nanocomposites.

4.3.3. Platinum Nanoparticle Deposition on Nanocomposites

Pt deposition on the surface of nanocomposites was conducted by applying three different deposition methods including direct and sonication techniques. The deposition conditions were summarized in Table 4.4. In the 1st method, samples were exposed to ultrasonic vibration about 1 hr for the homogeneous dispersion of sheets and 10 mM H$_2$PtCl$_6$ solution was added into mixture and sonication process was performed about 30 min for the diffusion of catalyst into layers. The mixture was put on the magnetic stirrer and 1 M NaBH$_4$ as a reducing agent was poured. In the 2nd method, samples were dispersed in distilled water by ultrasonic treatment about 10 min, then both H$_2$PtCl$_6$ solution and 1 M NaBH$_4$ were added into mixture simultaneously and sonicated about 1 hr. Then, mixture was placed onto the magnetic stirrer about 24 hrs. However, in the 3rd method, whole reaction was conducted in ultrasonic bath and the deposition time was adjusted to 2 hrs. In addition, 1st and 2nd methods were performed under vacuum filtration but for the 3rd method, filtration was conducted using syringe filters.

All deposition reactions were performed at room temperature. Moreover, the effect of sonication process on the dispersion of Pt particles on the surfaces was observed by comparing the methods.

Table 4.4.

Experimental conditions of Pt deposition techniques on the surface of samples

Run	Deposition time and technique	Samples	H$_2$PtCl$_6$	NaBH$_4$ (1M)	Distilled water
1	1.5 hr sonication and 24 hr direct synthesis	0.5 g	10 mM-5 mL	5 mL	5 mL
2	1 hr 10 min sonication and 24 hr direct synthesis	0.05 g	8% solution-0.5 mL	5 mL	10 mL
3	2 hr sonication	0.05 g	8% solution-0.5 mL	5 mL	10 mL

4.3.4. Fabrication of Electrodes

Powder samples, GO sheets, GNS, their composites, (0.05 g) were mixed with 10% Nafion$^®$ solution (1 mL) using as a binder in deionized water (5 mL) under ultrasonic treatment at room temperature for 30 min. Nafion$^®$212 membrane was employed as the base surface and the mixture was poured onto Nafion$^®$212 membrane in order to prepare homogeneously dispersed and thin film. Then, the electrodes were peeled off easily in the film form from Nafion$^®$ surface. Thin films were obtained after keeping in oven at 70°C overnight. Pt deposition on these films under sonication process about 2 hrs by using 10 mM H_2PtCl_6 as the Pt precursor and 1 M $NaBH_4$ was used as the reducing agent.

4.3.5. Fuel Cell Performance Test

4.3.5.1. Membrane Electrode Assembly Fabrication

Membrane Electrode Assembly (MEA) is a sandwiched structure of a Nafion$^®$ membrane between an anode and a cathode. MEAs were prepared either by Pt deposited graphene based electrode as a cathode and an anode or by Pt deposited graphene based electrode as a cathode and commercial carbon cloth electrode (0.6 Pt g/cm^3) as an anode. Nafion$^®$212 (DuPont) was treated for 1 hr in a 1:1 (vol/vol) solution of concentrated HNO_3 (65%) in distilled water at 90^{o}C to protonate all exchange sites and remove organic contaminants [72]. Then, nafion membranes were rinsed by deionized water several times and swelled in water at 90^{o}C for 1 hr. All swollen membranes were stored in deionized water until used. Swollen Nafion$^®$212 membranes were combined with Pt deposited electrodes by brushing 10% Nafion$^®$ solution on the surface of electrodes to form MEAs. These MEAs were cured at 70°C in oven. The MEAs were assembled into graphite single cells with an active area of 5 cm^2.

4.3.5.2. Fuel Cell Testing

The cells were operated in counter flow mode at a temperature of $60^{o}C$, using H_2 humidified to $60^{o}C$ in a bubbler and dry O_2 as reactants. In situ characterization of the MEAs was performed by means of polarization experiments [72]. Figure 4.4 and Figure 4.5 showed photographs of fuel cell test machine and single fuel cell. Fuel cell tests have been carried out at both UNIDO-ICHET and Sabancı University (Green Light G50 Test Station).
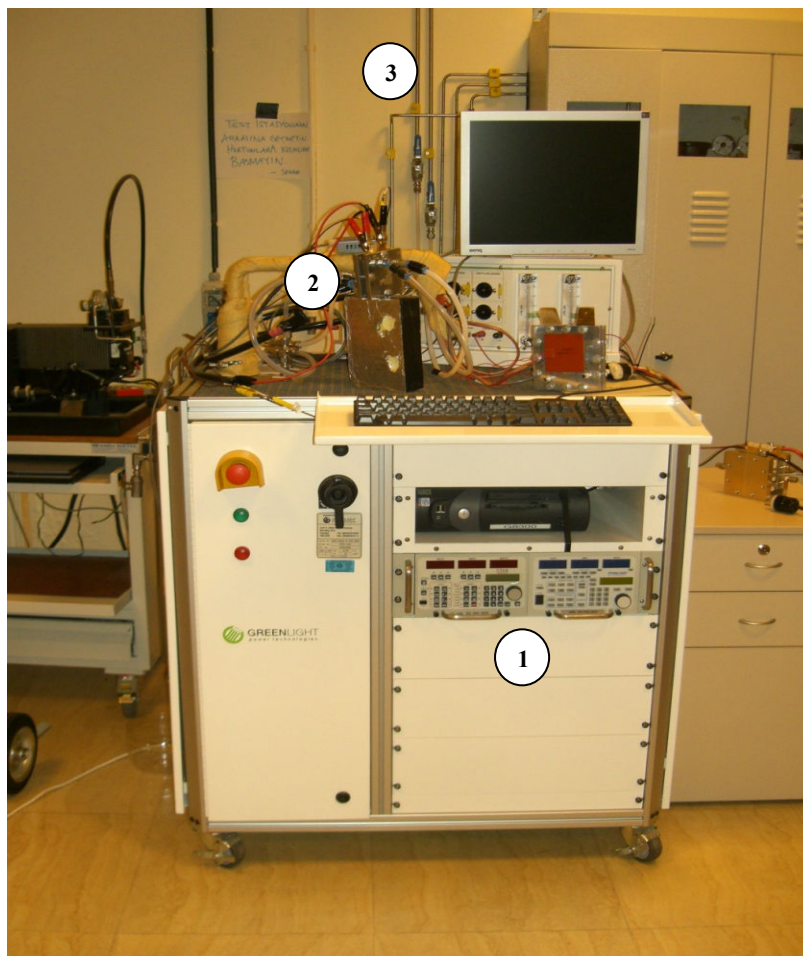
Figure 4.4. A photograph of fuel cell test station
(Sabancı University, Green Light G50 Test Station)
(1: power source, 2: single fuel cell, 3: gas flow system).
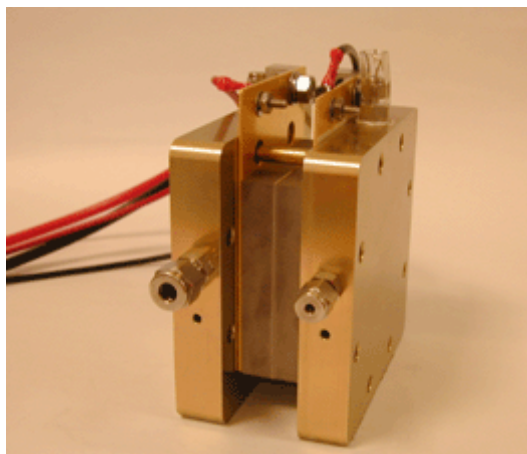
Figure 4.5. A photograph of single fuel cell.

4.4. Characterization Techniques

4.4.1. Scanning Electron Microscopy

The morphologies of nanocomposites were examined by a Leo Supra 35VP Field Emission Scanning Electron Microscope (SEM). Elemental analysis was conducted by using Energy-Dispersive X-Ray (EDX) analyzing system.

4.4.2. Atomic Force Microscopy

The surface morphologies of nanocomposites were analyzed by Ambiant Atomic Force Microscope (AFM) LAMF02-007, NanoMagnetics Instruments by using tapping mode.

4.4.3. X-Ray Diffraction Analysis

Powder X-ray diffraction (XRD) measurements of samples were performed with a Bruker AXS Advance Powder Diffractometer fitted with a Siemens X-ray gun, using Cu Kα radiation ($\lambda = 1.5406$ Å). The samples were swept from $2\theta = 10°$ through to $90°$

using default parameters of the program of the diffractometer that was equipped with Bruker AXS Diffrac PLUS software. The X-ray generator was set to 40 kV at 40 mA.

The numbers of the layers of the samples were calculated by using the classical Debye-Scherer equations:

$$L_a = 0.89\lambda / \beta_{002} \cos\theta_{002}$$

$$n = L_a / d_{002}$$

where L_a is the stacking height; β is the full width half maxima (FWHM); n is the number of graphene layers; d_{002} interlayer spacing.

4.4.4. Raman Spectroscopy

Structural changes of samples were analyzed by Renishaw InVia Reflex Raman Microscopy System using (Renishaw Plc., New Mills, Wotton-under-Edge Gloucestershire, UK) using a 514 nm argon ion laser in the range of 100 to 3200 cm^{-1}.

4.4.5. Fourier Transform Infrared Spectroscopy

Functional groups on the surface of samples were determined by a Nicolet iS10 Fourier Transform Infrared Spectroscopy (FT-IR).

4.4.6. Thermal Gravimetric Analyzer

Thermal behaviors of the samples were investigated by NETZSCH Thermal Gravimetric Analyzer (TGA). TGA was used to measure the weight loss of the sample as a function of temperature under air atmosphere. The heating rate was 10 K/min to a final temperature of 1000$^{\rm o}$C.

4.4.7. Surface Area Measurement

The surface areas of samples were measured by Quantachrome NOVA 2200e series Surface Analyzer. The determination was based on the measurements of the adsorption isotherms of nitrogen at 77 K. The specific surface areas were evaluated with the Brunauer–Emmett–Teller (BET) method in the P/P_0 range of 0.05–0.35. All samples were outgassed for 24 hrs at 150°C.

4.4.8. Four-probe Electrical Conductivity

The electrical conductivities of nanocomposites in pellet forms were measured by a standard four-probe technique at room temperature.

4.4.9. X-ray Photoelectron Spectroscopy

X-ray photoelectron spectroscopy (XPS) measurements were performed using a Physical Electronics Quantum 2000 Scanning ESCA Microprobe. This system uses a focused monochromatic Al Kα X-rays (1486.7 eV) source and a spherical sector analyzer.

CHAPTER 5. RESULTS AND DISCUSSION

5.1. Exfoliation of Graphene Nanosheets from Graphite

Graphene nanosheets (GNS) were exfoliated by following two ways. 1st way, the shortest exfoliation technique, included graphite oxidation, ultrasonic treatment and chemical reduction. 2nd way, the longest exfoliation technique, contained these steps: graphite oxidation, ultrasonic treatment, thermal exfoliation, ultrasonic treatment and chemical reduction. Both the reaction procedures with thermal expansion and without thermal expansion led to the formation of GNS. Experimental procedures for the exfoliation of GNS were shown schematically in Chapter 4 "Experimental" in Figure 4.3.

5.1.1. Graphite Oxide

Graphite oxided (GO) sheets were obtained in the adjusted synthesis conditions using concentrated sulfuric acid and potassium dichromate as oxidizing agents, and acetic anhydride as an intercalating agent [3].

5.1.1.1. Scanning Electron Microscopy

SEM image of the raw natural graphite contained sharp, rigid and compacted layers, Figure 5.1. Effect of amount of acid used in the oxidation reactions on the morphology of GO prepared was investigated also by SEM. GO sheets became swollen after the treatment of graphite flakes according to the 1st experimental conditions (Table 4.1), Figure 5.2. The oxidation process seemed to create expanded and leafy structures of GO layers.
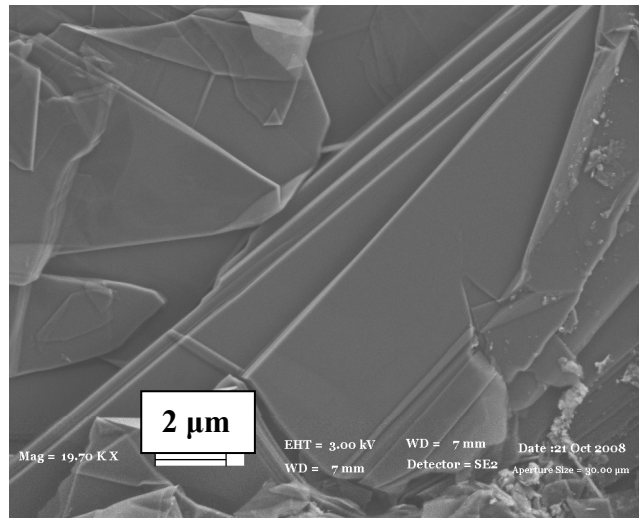
Figure 5.1. SEM image of raw graphite flake.
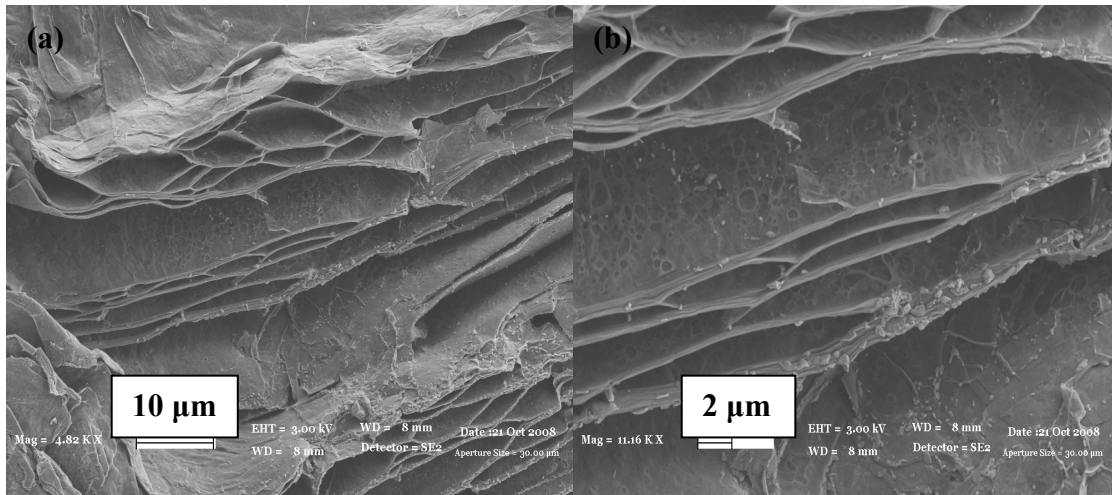
Figure 5.2. SEM images **(a)** and **(b)** of GO at different sites. Graphite oxidation was conducted according to 1st experimental conditions in Table 4.1.

SEM images of graphite samples treated according to the 3rd experimental conditions (Table 4.1) indicated that the layers were further swollen when using higher amount of sulfuric acid in the oxidation experiment, Figure 5.3. It appeared that higher sulfuric acid amount increased the effect of oxidation caused by the dichromate ions. With this amplified effect of oxidation, it was possible that more oxygen atoms were force to attach to graphite layers which resulted in a more loose structure compared to that of the rigid structure of raw graphite.
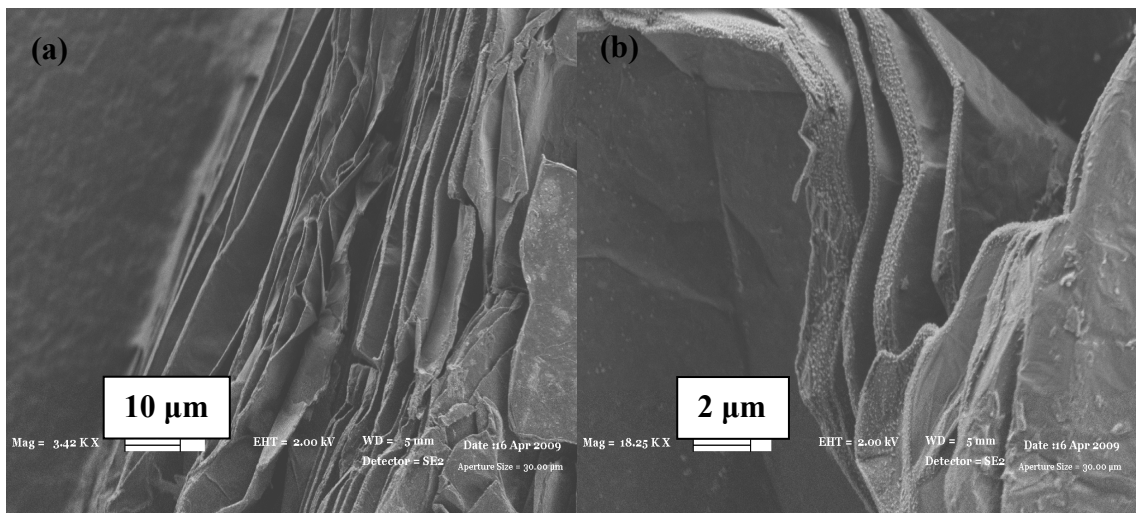
Figure 5.3. SEM images **(a)** and **(b)** of GO at different sites. Graphite oxidation was conducted according to 3rd experimental conditions in Table 4.1.

The influence of sulfuric acid concentration on graphite oxidation was examined by SEM characterization. During oxidation process, sulfuric acid was used as an inserting agent which caused swelling of the graphite oxide layers. When the acid amount was insufficient, complete oxidation could not be achieved. Three different experiments were performed in order to understand the acid effect on oxidation, Table 4.1. Figure 5.4 (a) shows the graphite layers after the oxidation process conducted using low amount of sulfuric acid (9.3 g sulfuric acid/g of graphite) and the expansion of layers was not enough due to the low oxidation. However, when the acid concentration was increased (55 g sulfuric acid/g of graphite), a more loose structure formation and much more enlargement between the layers were observed, Figure 5.4 (b).
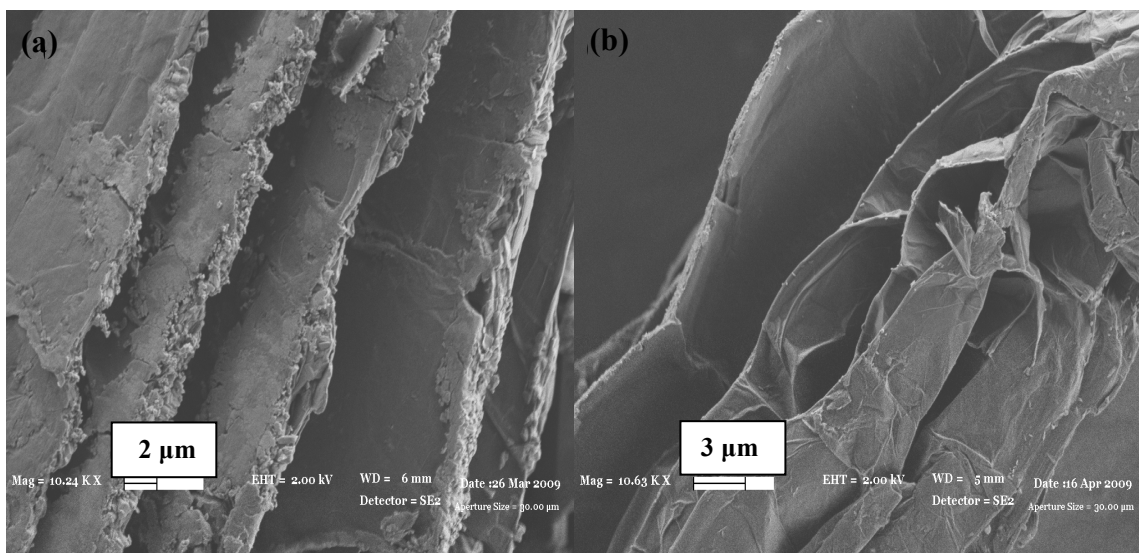
Figure 5.4. SEM images of GO **(a)** in low acid amount (oxidation process about 50 min using 2nd experimental conditions in Table 4.1) **(b)** in higher acid amount (oxidation process about 50 min using 3rd experimental conditions in Table 4.1) via secondary electron detector.

Sonication of GO samples created more separated structures. Morphology of the sonicated GO samples exhibited expanded the layer structures and formed some tulle-like translucent and crumpled GO sheets as presented by the SEM image in Figure 5.5.
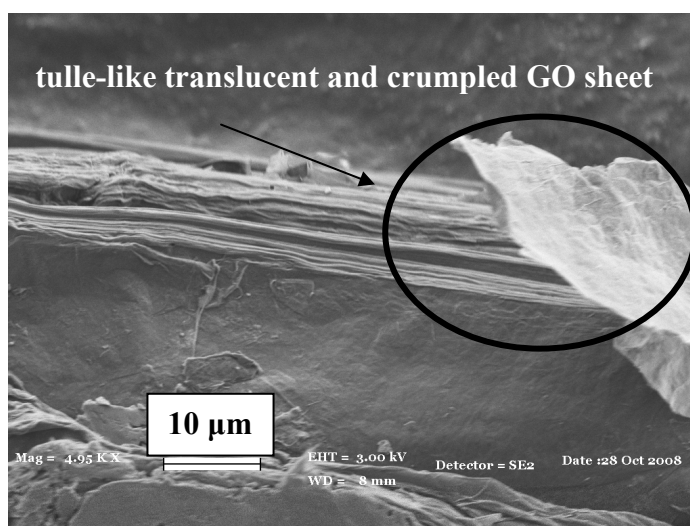
Figure 5.5. SEM image of GO (oxidation process using 1st experimental conditions in Table 4.1) after sonication for 1 hr at room temperature.

5.1.1.2. Oxidation of Different Graphite Samples

Instead of natural graphite flake, kish graphite powder and kish graphite flakes were also oxidized by using concentrated sulfuric acid and $K_2Cr_2O_7$. Kish graphite is formed by the precipitation of supersaturated carbon from molten iron. Kish graphite is also called synthetic single-crystal graphite.

Kish graphite powder is a low-cost carbon material produced through the steelmaking process. SEM image of kish graphite powder showed in Figure 5.6. After 120 hr oxidation process, the surface of graphite became porous and graphene sheets started to separate, Figure 5.7.

Kish graphite flakes, mostly larger than natural graphite flakes, exhibit single crystal structure. Kish graphite flake has a rigid and condensed structure, Figure 5.8. After 120 hr oxidation process, thinner sheets started to separate from the graphite structure and tulle-like formation was observed, Figure 5.9.
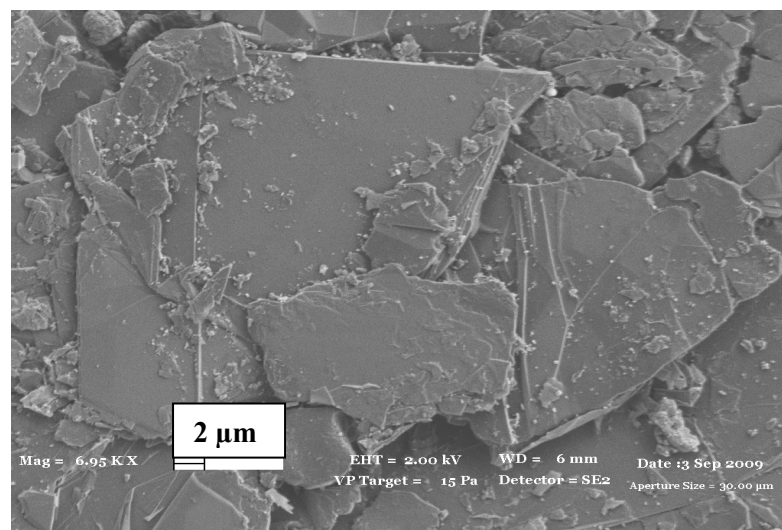
Figure 5.6. SEM image of kish graphite powder.
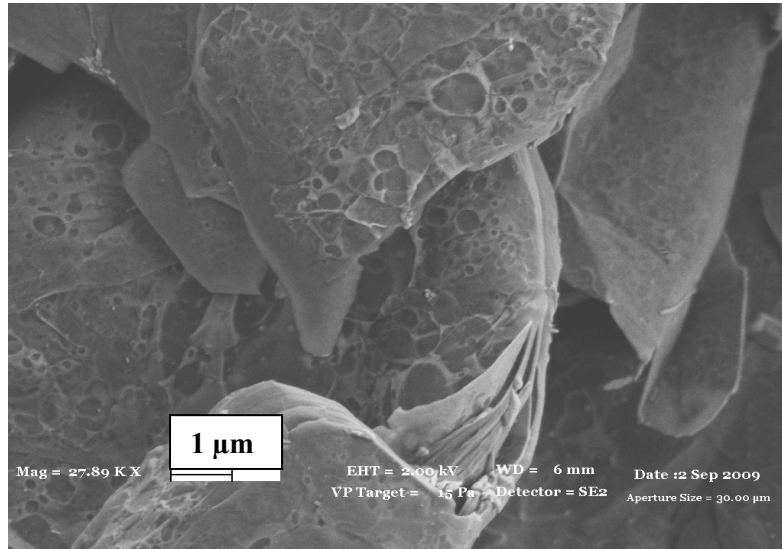
Figure 5.7. SEM image of oxidized kish graphite powder after 120 hr oxidation process
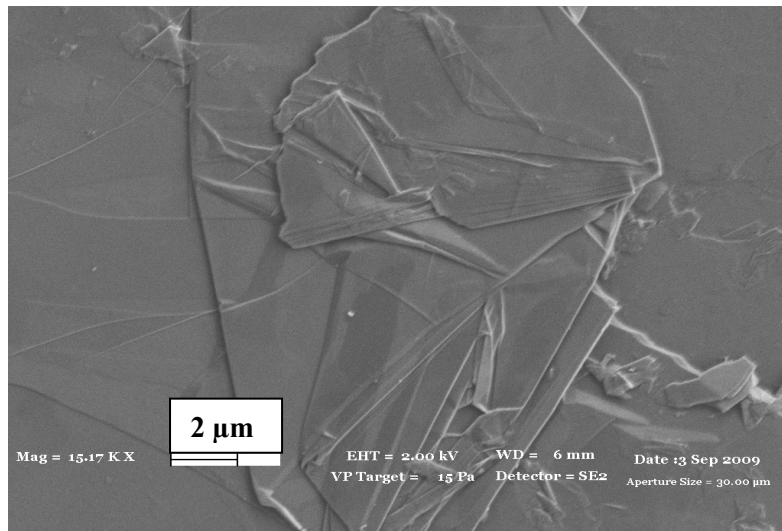
Figure 5.8. SEM image of kish graphite flake.
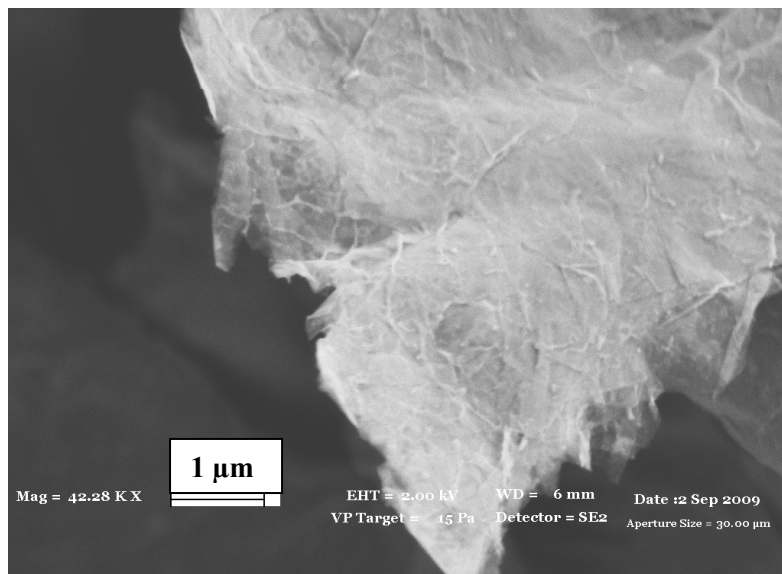
Figure 5.9. SEM image of oxidized kish graphite flake after 120 hr oxidation process.

5.1.1.3. Oxidation by Available Chemical Techniques

In order to compare our mild oxidation technique, graphite flakes were oxidized by applying available procedures. Graphite flakes (1 g) were immersed in HNO_3-H_2SO_4 mixture (v:v=1:3) and stirred at room temperature for 24 hrs [121]. SEM images of GO sheets exhibited the formation of cracks through layers due to highly oxidizing agents, Figure 5.10 (a) and (b). This oxidation procedure did not cause enough swelling through graphene layers, Figure 5.10 (c).
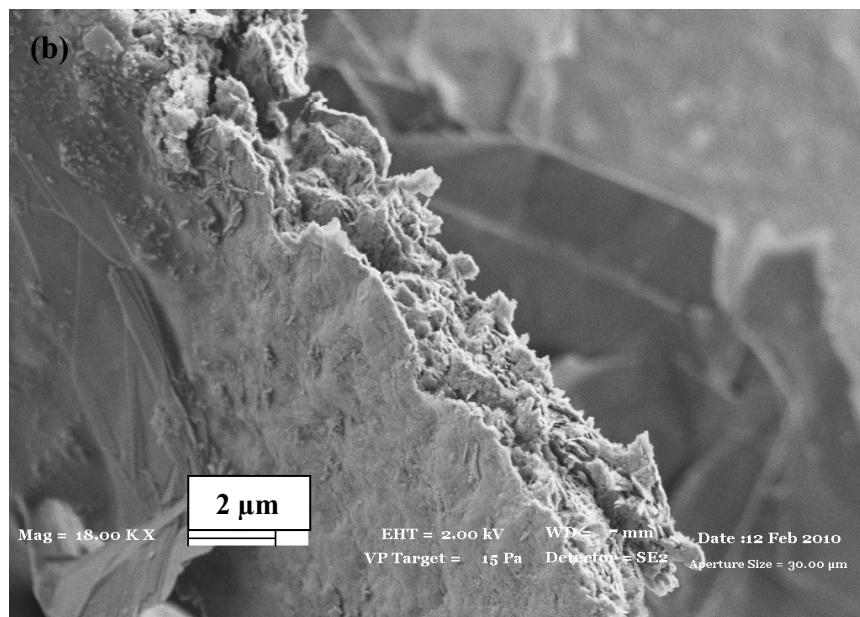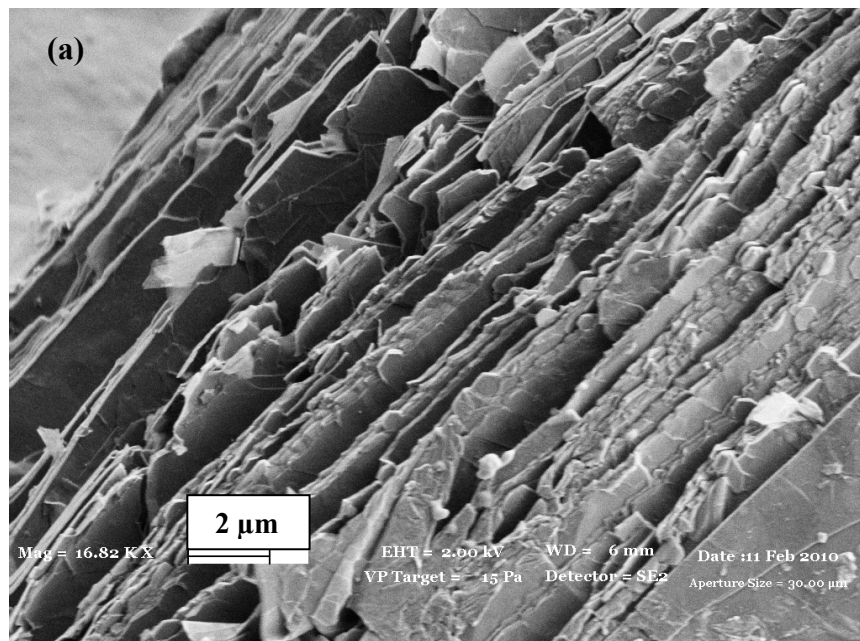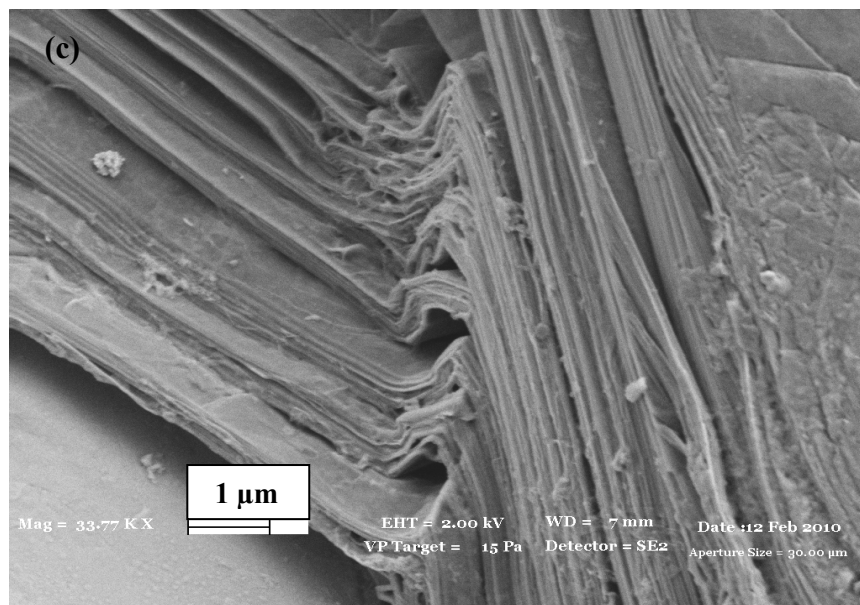
Figure 5.10. SEM images **(a)**, **(b)** and **(c)** of GO sheets obtained by using both HNO_3 and H_2SO_4 as oxidizing agents.

5.1.2. Expanded GO

Potassium dichromate oxidation of raw graphite created oxygenated polar structures on the surface of graphite layers after the cleavage of C-C bonds which facilitated the diffusion of acetic anhydride and oxygen into the layers. The oxidation step depends on the amount of sulfuric acid used in this reaction [118]. Heat treatment of such treated samples led to the thermal decomposition of acetic anhydride into CO_2 and H_2O vapor which further swelled the layered graphitic structure. SEM images of the GO samples (prepared regarding to 1st experiment in Table 4.1) that expanded during heating under an argon atmosphere at 900°C for 15 min in a tube furnace are presented in Figure 5.11 (a) and (b).
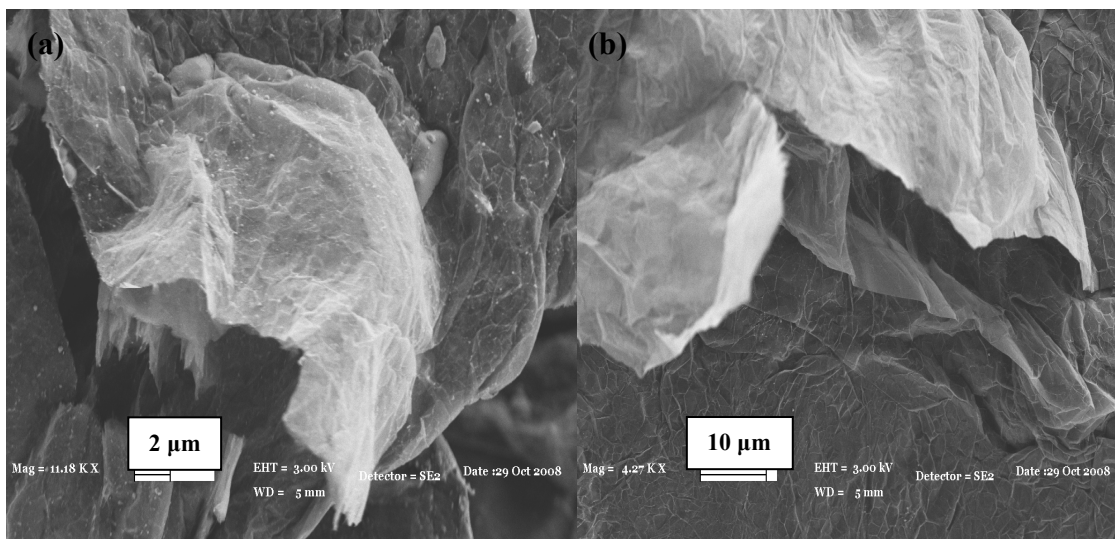
Figure 5.11. SEM images **(a)** and **(b)** of expanded GO obtained at 900°C for 15 min expansion.

The heat treatment process caused the expansion of graphitic crystal lattice, and further separated the tulle-like GO sheets as it was the case after the sonication step. The tulle-like GO sheets were even more easily observable after the 15 min-heat treatment. GO samples obtained after 2nd experiment (Table 4.1) were also expanded at 1000°C for 5 min and the layers became wavy but the tulle-like layers of this sample could not be easily observed, Figure 5.12 (a) and (b). This might have stemmed from the short of heat treatment period that could not initiate the separation of the tulle-like GO sheets.
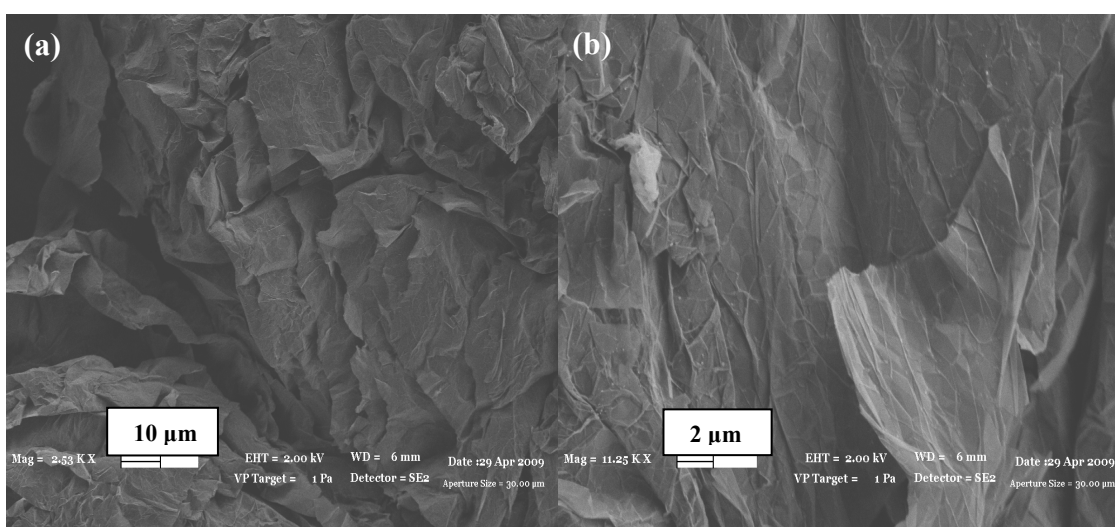
Figure 5.12. SEM images of **(a)** and **(b)** of expanded GO obtained at 1000°C for 5 min expansion.

Sonications of thermally expanded GO samples produced smoother and wider tulle-like GO sheets, Figure 5.13 (a) and (b). Some unexfoliated graphitic layers were observable through semi-transparent GO sheets separated in this work, Figure 5.13 (a).
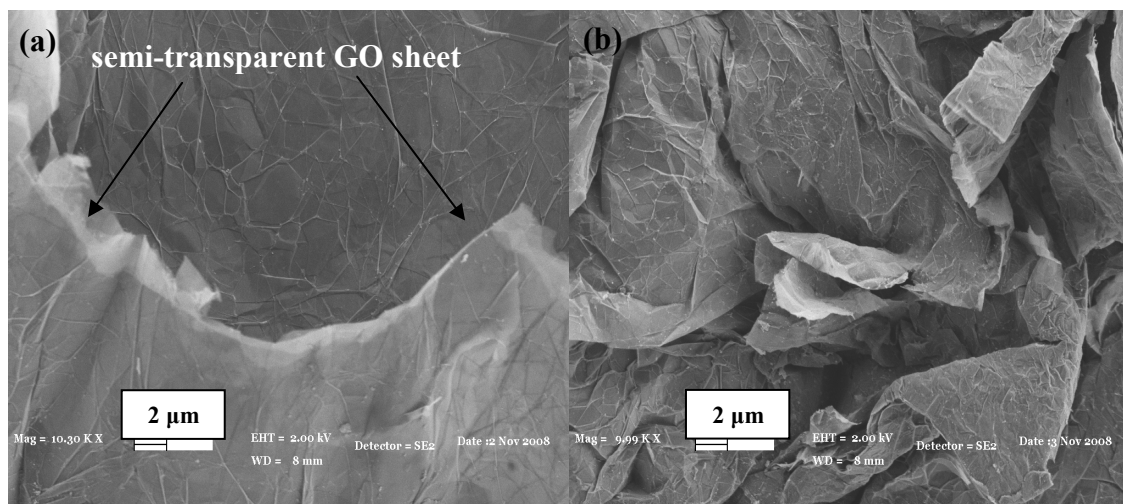
Figure 5.13. SEM images **(a)** and **(b)** of expanded GO (prepared using 1st experimental conditions in Table 4.1) obtained at 900°C for 15 min expansion after sonication for 1 hr at room temperature.

The effect of intercalating agent on the formation of GNS was analyzed by Raman characterization. In oxidation process, two different amounts of acetic anhydride were added as 1 g and 5 g, respectively. In Figure 5.14, the characteristic D and G peaks of samples can be seen clearly. I_D/I_G ratio change indicated that as the amount of intercalating agent increased, structure of expanded GO sheets became similar to graphite (Table 5.1).
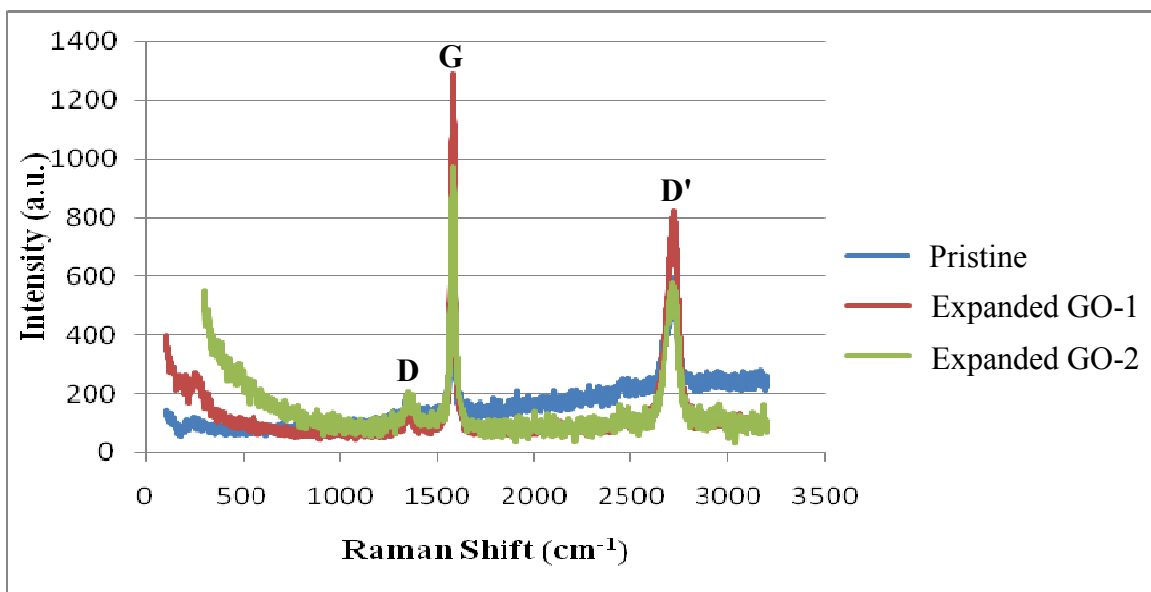
Figure 5.14. Raman spectra of pristine graphite, expanded GO-1 (1 g acetic anhydride) and expanded GO-2 (5 g acetic anhydride).

Table 5.1.

I_D/I_G comparison of pristine graphite, expanded GO-1 (1 g acetic anhydride) and expanded GO-2 (5 g acetic anhydride)

Samples	I_D/I_G
Pristine graphite	0.22
Expanded GO-1 (1 g acetic anhydride)	0.11
Expanded GO-2 (5 g acetic anhydride)	0.21

5.1.3. Reduction of GO and Expanded GO Samples into Graphene-based Nanosheets

Both GO and expanded GO samples were chemically reduced through refluxing with hydroquinone in water to produce GNS. During this reaction, it is known that hydroquinone loses either one H^+ ion from one of its hydroxyls to form a monophenolate ion or two H^+ ions from both hydroxyls to form a diphenolate ion called as quinine [122]. Reflux solution became yellowish during reduction by hydroquinone. The solid product was separated by filtration at the end of the experiment, washed with water, methanol and dried.

SEM images of graphene-based nanosheets obtained after the 50 min oxidation and chemical reduction processes are presented in Figure 5.15. Ruffled appearance of tulle-like graphene-based sheets was very easily observable in these images. Investigation of all regions of the reduced samples by SEM revealed that the experimental procedure was successful and yielded exfoliated graphene-based sheets.
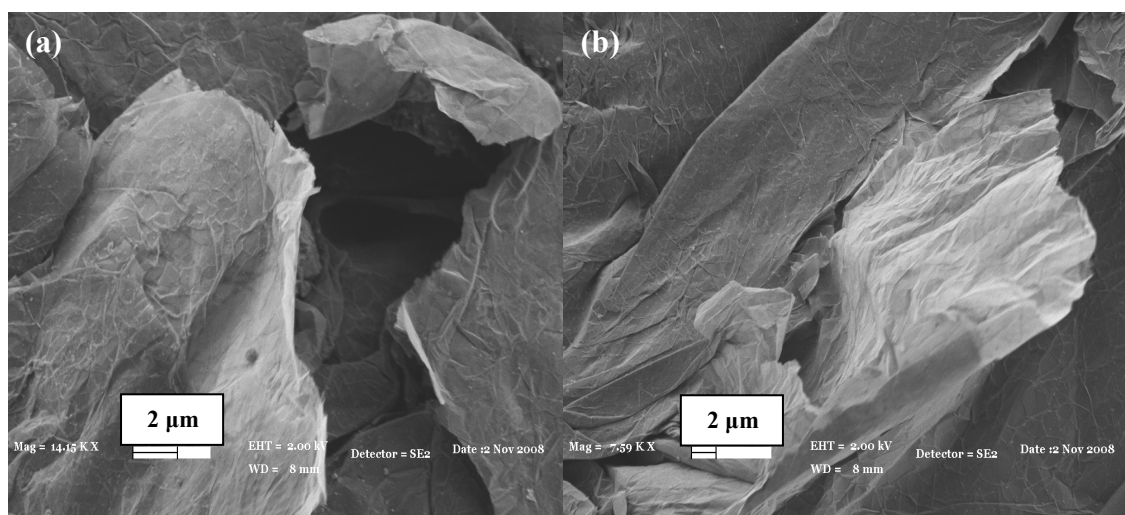
Figure 5.15. SEM images **(a)** and **(b)** of GNS obtained after the 50 min oxidation and chemical reduction processes at different regions of samples.

SEM images of the samples obtained using either of the two routes in the scheme in Figure 4.3, indicated that GNS could be obtained after the reduction process, Figure 5.16 (a) and (b). The wrinkled appearance of sheets was due to the rapid heating of GO because its expansion and delamination brought about rapid evaporation of intercalants (acetic anhydride and sulfuric acid) into CO_2 and H_2O vapor produced by thermal pyrolysis of the oxygen-containing functional groups [123]. GNS could also be separated using a method without the thermal expansion step in the chemical reduction of GO samples which were obtained after 120 hr oxidation in Figure 5.17. Graphene sheets made of a few graphene layers could be clearly seen in Figure 5.17 (b). Consequently, both the reaction procedures with thermal expansion and without thermal expansion led to the formation of GNS. Therefore, the process time could be reduced by using the steps of graphite oxidation, ultrasonic treatment and chemical reduction of GO samples.
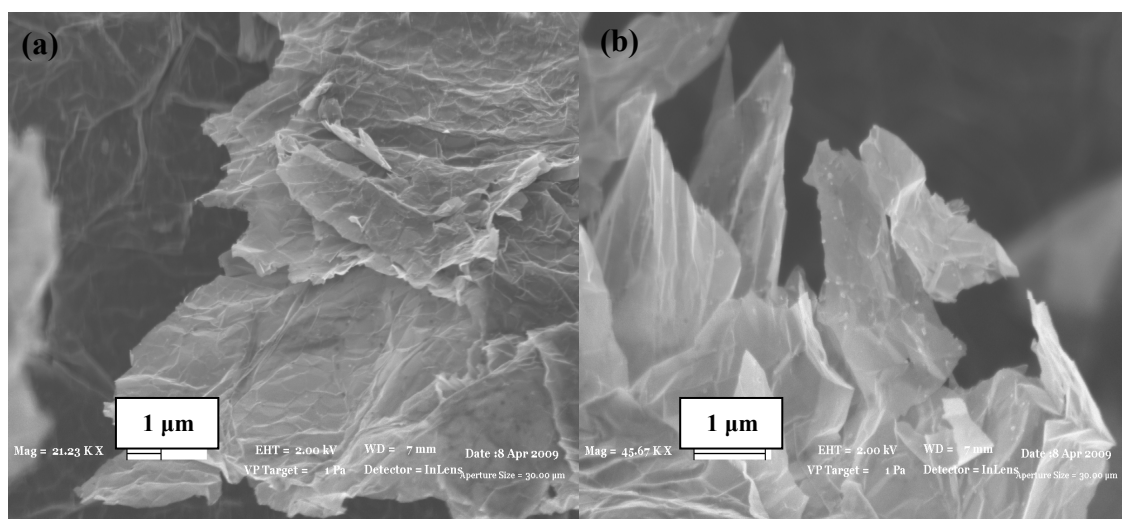
Figure 5.16. SEM images via inlens detector **(a)** and **(b)** of GNS obtained after thermal expansion and reduction process at different magnifications.
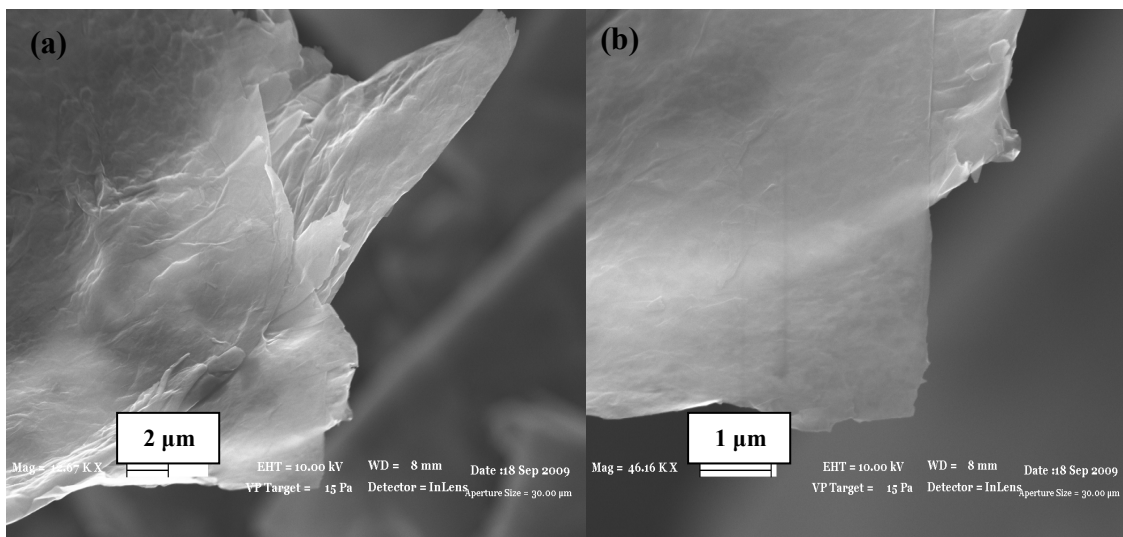
Figure 5.17. SEM images via inlens detector **(a)** and **(b)** of GNS received by direct reduction after 120 hr oxidation period.

5.1.4. Structural Analysis of Each Step of Exfoliation Process by XRD

XRD patterns of raw graphite, GO, expanded GO and graphene-based nanosheets are presented in Figures 5.18-21. The XRD pattern of raw graphite sample contained a very sharp and high intensity 002 peak near $2\theta=26.5°$ and 004 peak near $2\theta=54.5°$ (Figure 5.18). XRD pattern of GO which was obtained by using 1st oxidation conditions in Table 4.1 contained a wide peak at $2\theta=25.7°$ and a shoulder at near $2\theta = 28.8^{o}$, Figure 5.19 (a). Jihui-Li *et al.* [124] also observed a similar diffraction pattern and a shoulder at 28 degrees in the XRD pattern for graphite intercalated compound (GIC). The reason that this shoulder was observed at 28 degrees was due to the intercalating agent used in the present work as it was also in the work of Jihui-Li *et al.* [124]. Also, XRD pattern of GO which was obtained by using 3rd oxidation conditions in Table 4.1 contained a sharper and shifted shoulder at around $2\theta=30^{o}$ likely due to increase in the amount of oxidant between the layers, Figure 5.19 (b).

Due to oxidation, the crystal nature of the raw graphite was changed and occurrence of a broad 001 peak near $2\theta=14°$, and a relatively wider and very low intensity 002 peak near $2\theta=27.5°$ were observed in the XRD pattern of expanded GO, Figure 5.20. Chemical reduction restored the crystal structure again in graphene-based

75

nanosheets by removing the effect of oxidation observed in the expanded GO sample; a sharp and high intensity 002 peak near $2\theta=26.5°$ was observed in the XRD pattern of the graphene-based nanosheets and the 001 peak near $2\theta=13-14°$ owing to oxidation of graphite was barely detected in the diffractrogram, Figure 5.21.

Average number of graphene layers calculated using Debye-Scherrer equation is presented in Table 5.2 and 5.3. Debye-Scherrer equation was also used previously by Sakintuna and Yürüm [125] in the x-ray diffraction analysis of crystallites produced during the carbonization of Turkish lignite. Gurudatt and Tripathi [126] claimed that stacking height and lateral size of the crystallites calculated by Debye-Scherrer equation were not actually equal to the exact height and the size but in fact gave convenient relative estimates of actual stacking height and lateral size of the crystallites produced in the carbonization and this can also be assumed correct for the graphene structures. The graphene structures produced in the present work were not flat and therefore the values obtained by Debye-Scherrer equation were reasonable estimates that described the situation.

Average number of layers calculated for raw graphite, GO, expanded GO and graphene-based nanosheet samples were 86, 14, 56, and 44, respectively (Table 5.2). The increase of layer numbers from 14 to 56 after the expansion process was the result of stacking of the layers due to the removal of acetic anhydride group that intercalated the graphene planes and the decrease in interplanar spacing (near to pristine graphite value). Sonication process was not applied to these samples to discriminate the effect of dispersion on the layer numbers. On the other hand, the average number of layers for raw graphite, sonicated graphite, GO, sonicated GO and graphene-based nanosheets were calculated as 86, 79, 17, 12 and 9 (Table 5.3). The stepwise chemical procedure used in the present report indicated that the average number of graphene layers reduced steadily from raw graphite to graphene-nanosheet samples. Change of interplanar spacings also explained how each step in the proposed procedure affected the morphology of graphite. In the oxidation step, the interplanar spacing increased by the introduction of oxygen groups between the graphene layers in raw graphite. Sonication process after each step decreased the number of layers. The mild procedure applied was capable of reducing the average number of graphene sheets from 86 in the raw graphite to 9 in graphene-based nanosheets. When comparing the values in Table 5.2 and

Table 5.3, results indicated that the expansion step in the procedure has potential drawback due to the increase of the layer number in graphitic structure. Application of more severe chemical methods might reduce the number of graphene layers further.

Table 5.2.

Number of layers and interplanar spacing (d) of samples from XRD characterization results (oxidation process using 1st experimental conditions in Table 4.1).

Samples	Average number of layers	d (Å)
Graphite flake	86	3.37
GO	14	3.46
Expanded GO	56	3.36
Graphene-based nanosheets	44	3.39

Table 5.3.

Effect of sonication on the number of layers and interplanar spacings (d) of samples from XRD characterization results (oxidation process using 3rd experimental conditions in Table 4.1).

Samples	Average number of layers	d (Å)
Graphite flake	86	3.37
Sonicated graphite flake	79	3.35
GO	17	3.61
Sonicated GO	12	3.64
Graphene-based nanosheets	9	3.62
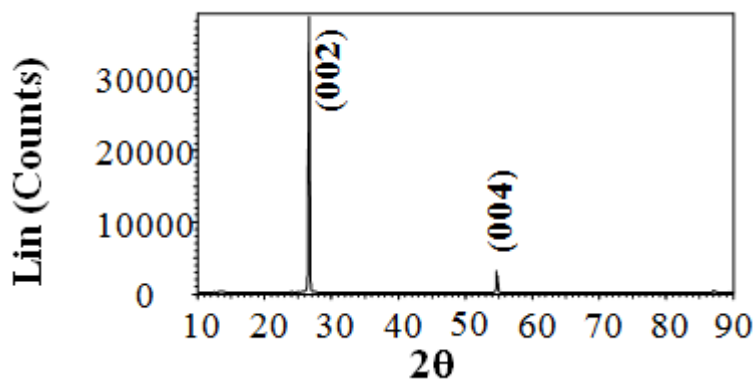
Figure 5.18. XRD pattern of raw graphite.
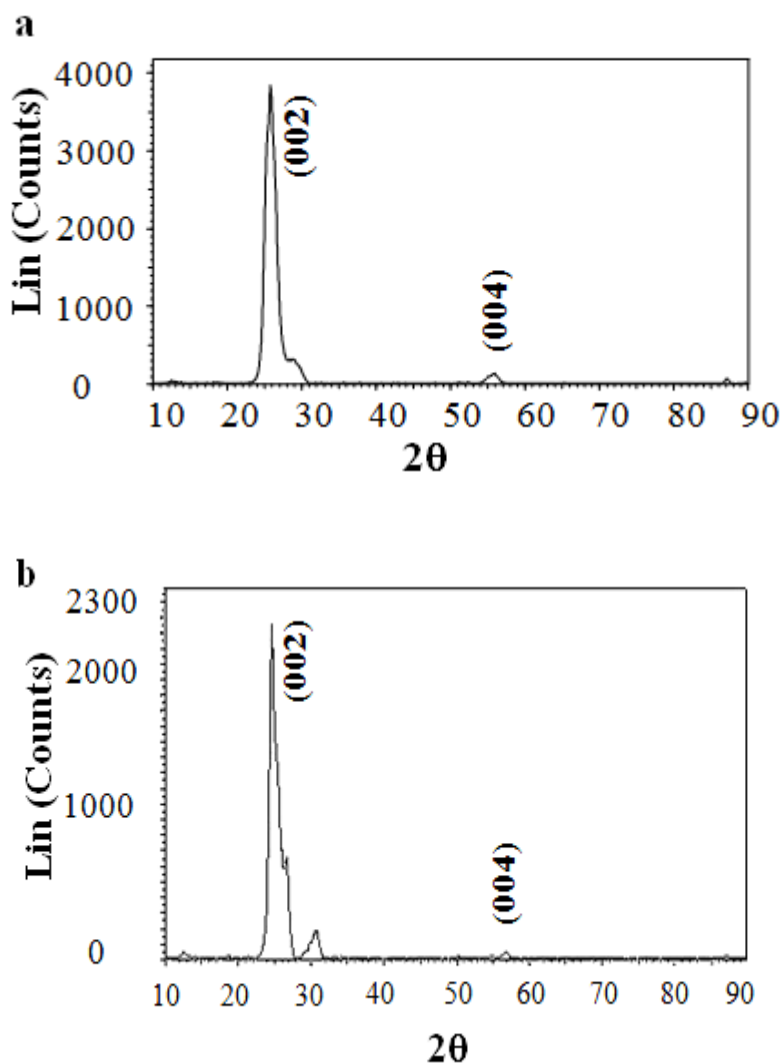
Figure 5.19. XRD patterns of **(a)** GO (Oxidation process was conducted by using 1st experimental condition in Table 4.1) and **(b)** GO (Oxidation process was conducted by using 3rd experimental condition in Table 4.1).
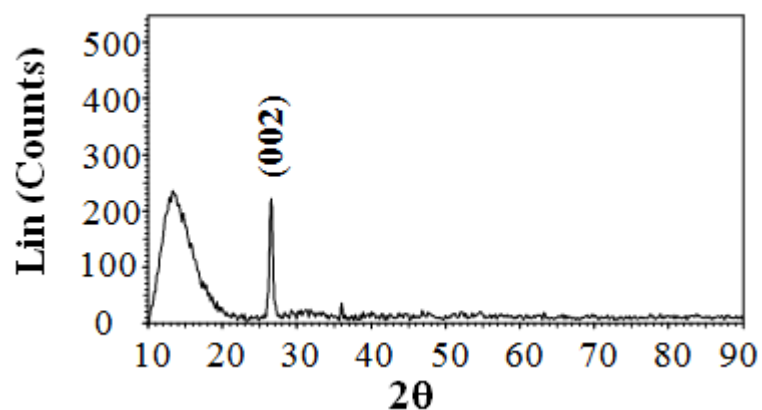
Figure 5.20. XRD pattern of expanded GO obtained at 900°C for 15 min expansion.
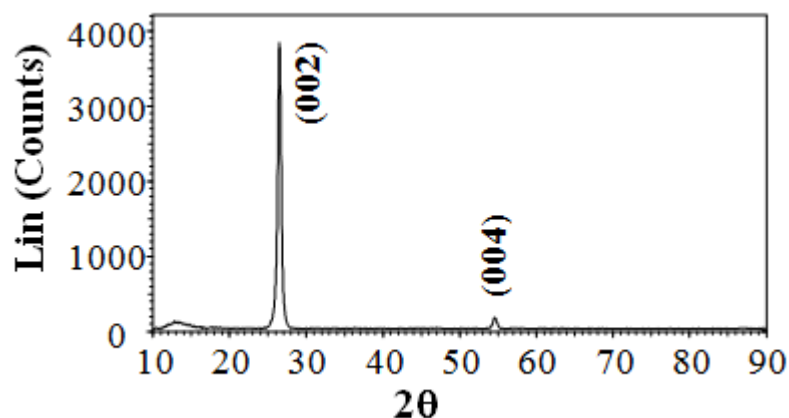
Figure 5.21. XRD pattern of the graphene-based nanosheets after chemical reduction of expanded GO.

5.1.5. Raman Spectroscopy Characterization of Each Step of Exfoliation Process

Raman spectroscopy is a quick and accurate technique to determine the number of graphene layers and the change of crystal structure of the materials after chemical treatments [54]. There are four remarkable peaks in the Raman spectrum of graphite which are the G line around 1580 cm^{-1}, the G' line (the overtone of the G line) around 3248 cm^{-1}, the D line around 1360 cm^{-1} and the D' line (the overtone of the D line) around 2700 cm^{-1}. The intensity of the D line depends on the amount of the disorderness

of the graphitic materials and its position shifts regarding to incident laser excitation energies [54].

A strong G line at 1580 cm^{-1}, a weak D line at 1360 cm^{-1} and a broad D' line at 2724 cm^{-1} were seen in the Raman spectrum of raw graphite, Figure 5.22. After oxidation process, G line of GO sample was broadened and the intensity of D line was increased due to the reduction in the thickness of the graphitic structure, Figure 5.23. In the Raman spectrum of reduced GO, the G line was broadened and shifted to 1600 cm^{-1}, Figure 5.24. In addition, an increased intensity of the D line around 1355 cm^{-1} indicated the considerable reduction in size of the in-plane sp^2 domains owing to oxidation and sonication processes, and the formation of GNS having highly oriented crystal structure. In the Raman spectrum of graphene-based nanosheets obtained after chemical reduction of expanded GO, the intensity of the D line around 1356 cm^{-1} decreased considerably as a result of an increase of the graphitic domain sizes and an increase of the thickness of graphitic structure after thermal treatment, Figure 5.25. This increase could also be seen by the increase in the number of average graphene layers after thermal treatment that was calculated from XRD patterns by using Debye-Scherrer equation as observed in Table 5.2.

For the comparison of the structural changes after the chemical treatments, another critical factor was the disorder amount. As the structure changes from graphite to nanocrystalline graphite, the ratio between the intensity of D and G line, I_D/I_G, changes inversely with the size of the crystalline grains or interdefect distance [57]. I_D/I_G values for graphite, GO, reduced GO and reduced expanded GO were calculated as 0.2, 0.3, 1.0 and 0.6, respectively. The highest I_D/I_G ratio of reduced GO sample was evidence for the structure with highest order.

When the layer number is smaller than 5, the D' peak becomes more intense than G peak [127]. The increase in the ratio between the intensity of G and D' peak, $I_G/I_{D'}$, indicated an increase in the number of graphene layers. $I_G/I_{D'}$ values for graphite, GO, reduced GO and reduced expanded GO were estimated as 1.5, 1.6, 2.1 and 1.8, respectively. The highest $I_G/I_{D'}$ ratio of reduced GO sample demonstrated the largest number of graphene layers.
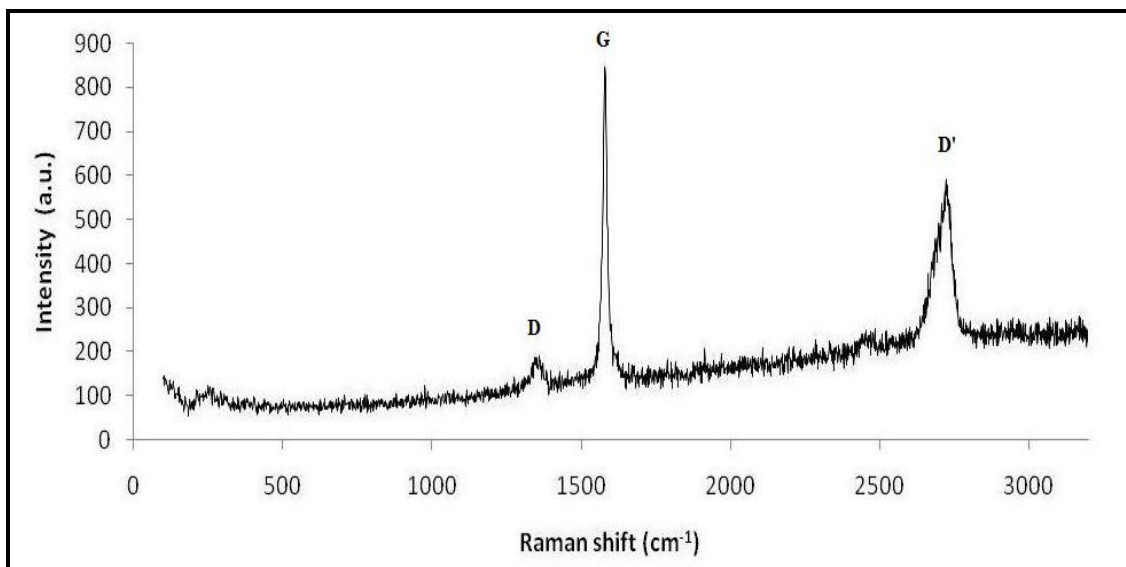
Figure 5.22. Raman spectrum of raw graphite.
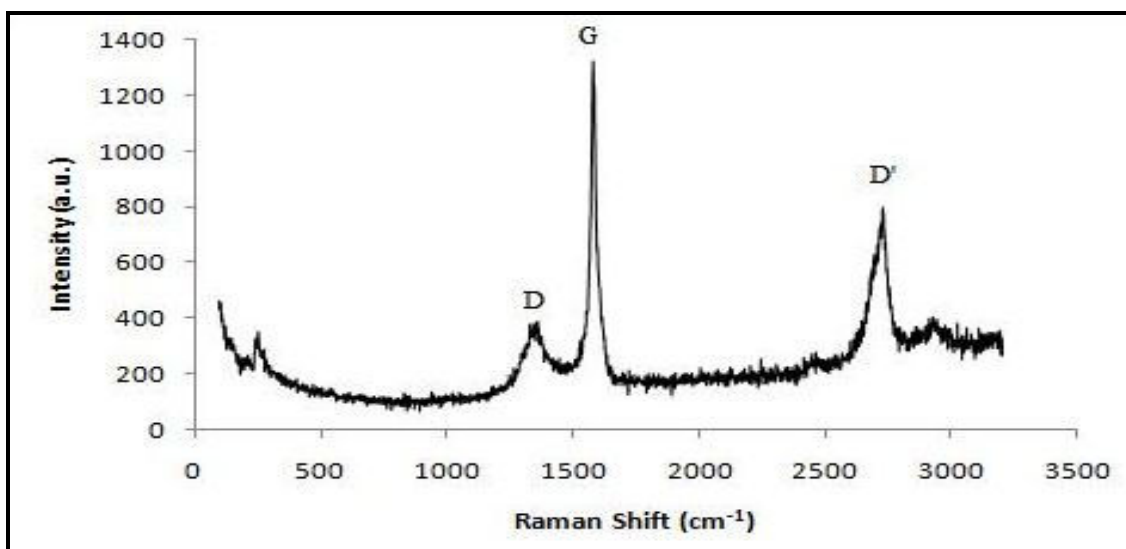
Figure 5.23. Raman spectrum of GO.
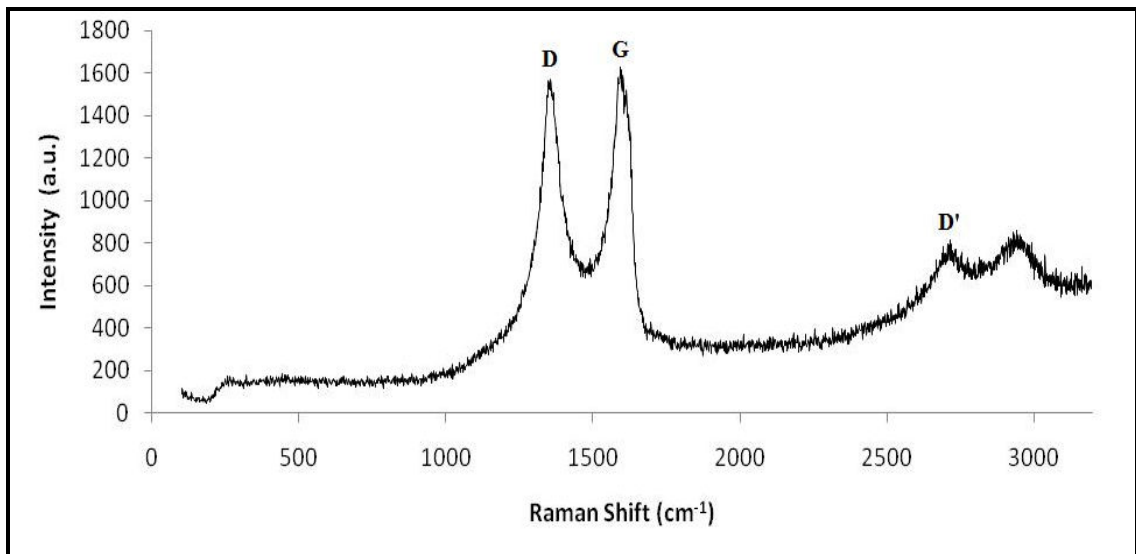
Figure 5.24. Raman spectrum of graphene-based nanosheets after chemical reduction of GO.
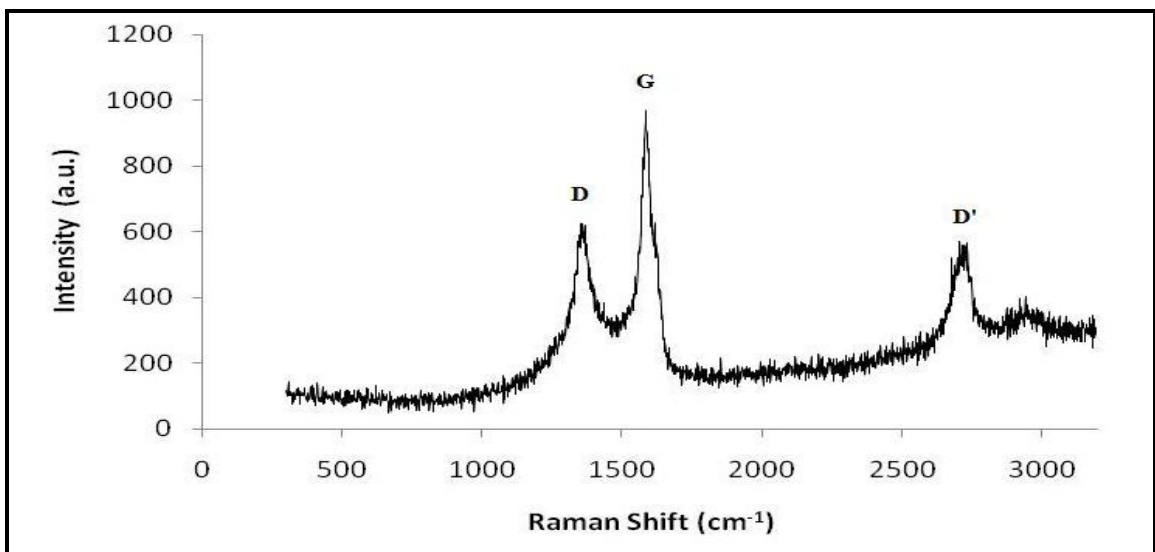
Figure 5.25. Raman spectrum of graphene-based nanosheets after chemical reduction of expanded GO.

5.2. The Effect of Oxidation Process on the Characteristics of Graphene Nanosheets and GO sheets

With the appropriate surface treatments, single graphene sheets can be separated from the graphite material and the layer-to-layer distance can be extended. There are numerous old methods for the graphite modifications to reduce the number of graphene layers in graphitic structure. One of the applicable methods is the graphite oxidation in order to reduce the strong bonding between sheets in graphite and to receive monolayer graphene sheet.

As the oxidation time was increased, the strong bonding between graphene layers in graphite was reduced and graphene layers started to exfoliate forming clusters with a few number of graphene layers. The variations in interplanar spacings, layer number and percent crystallinity indicated how stepwise chemical procedure influenced the morphology of graphite. It was possible to produce relatively flat graphene clusters with definite number of layers by controlling the oxidation time.

5.2.1. SEM Characterization

GO sheets started to exfoliate at longer reaction times. After 6 hrs of oxidation process, graphite started to crumble forming randomly stacked irregular structures, Figure 5.26 (a). As the oxidation time increased from 6 hrs to 96 hrs, graphite layers were damaged much more and layers in the graphitic structure were further swelled, Figure 5.26 (b). 120 hrs of oxidation caused GO sheets to separate from graphitic layers that were separated in the early steps of the process, Figure 5.26 (c).
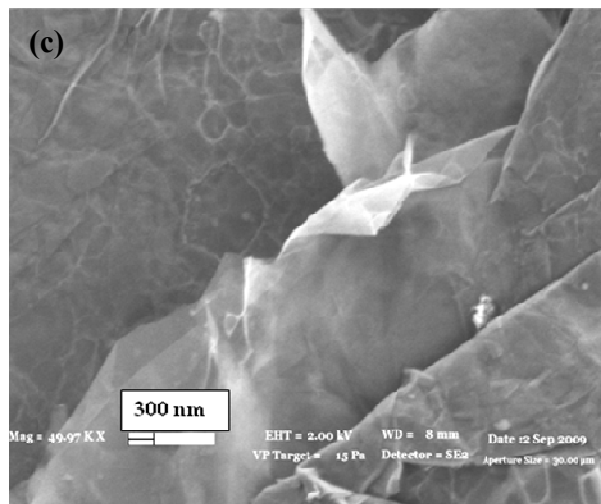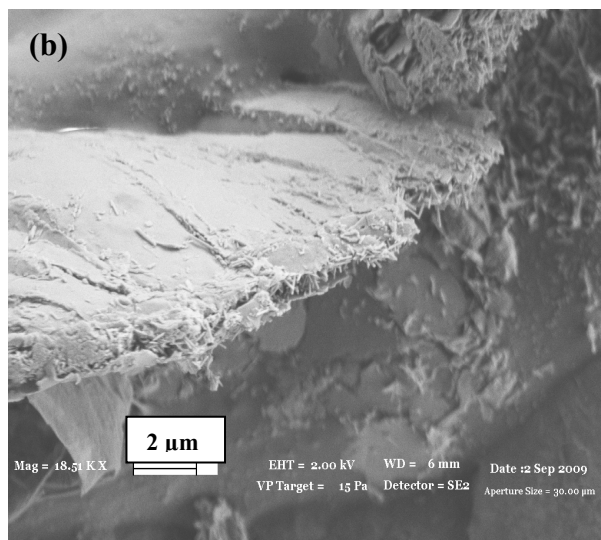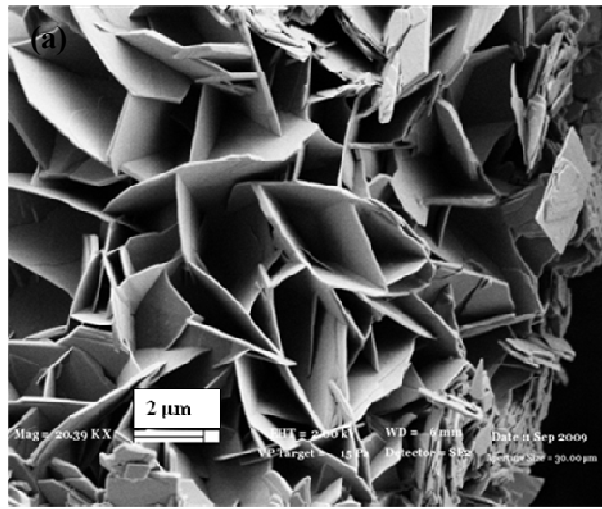
Figure 5.26. SEM images via secondary electron detector of GO after **(a)** 6 hr, **(b)** 96 hr**,** and **(c)** 120 hr oxidation processes.

5.2.2. AFM Characterization

AFM was used for the measurement of sheet thickness and the surface morphology. All AFM experiments were performed in tapping mode using a silicon cantilever probe. 3D views of samples produced evidence for the reactions that occurred in each step of the process (Figure 5.27). 3D surface topography of pristine graphite flakes indicated smooth and flat morphology, Figure 5.27 (a). However, after oxidation process, intercalating compounds diffused between the graphene layers caused wavy and swelled structure as it was observed in Figure 5.27 (b). Also, the functional groups (epoxide, carbonyl, quinone, ketone, and hydroxyl) on the basal plane of GO caused corrugation or local "puckering" of the carbon skeleton [128]. After direct reduction of GO sheets, surface topography of the sheet became rigid and flat in Figure 5.27 (c).

On the other hand, after heat treatment the layers appeared as a loose worm-like material, Figure 5.27 (d). The formation of this appearance stemmed from the gas evolution between layers during thermal shock. Reduction of expanded GO induced the flattening of the sheets, Figure 5.27 (e) but still the thickness was not identical because oxidation process was not uniform throughout the sample.

AFM measurements showed that layers were flattened and the height difference on the surface decreased after chemical reduction. AFM measurements supported the SEM results of the samples obtained after ultrasonic vibration and chemical reduction, bulk GO could be exfoliated into GNS without thermal shock.
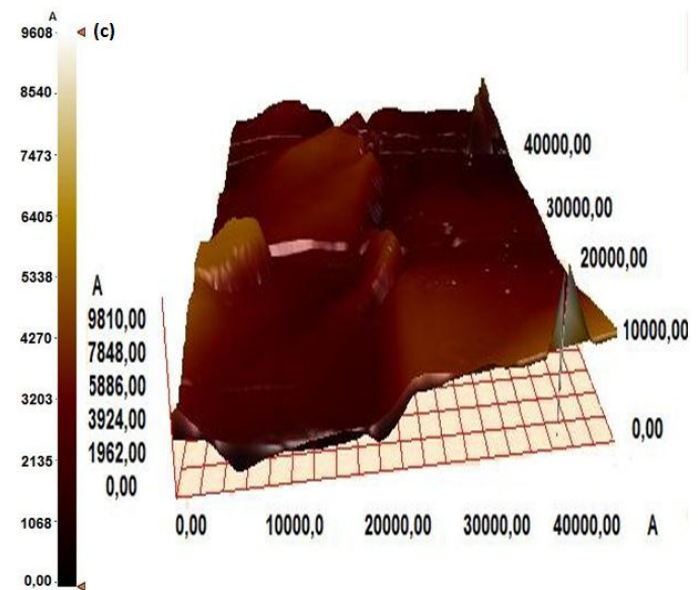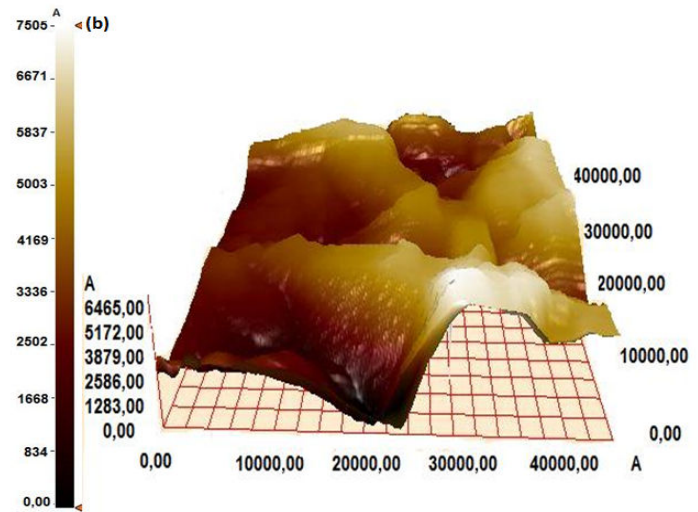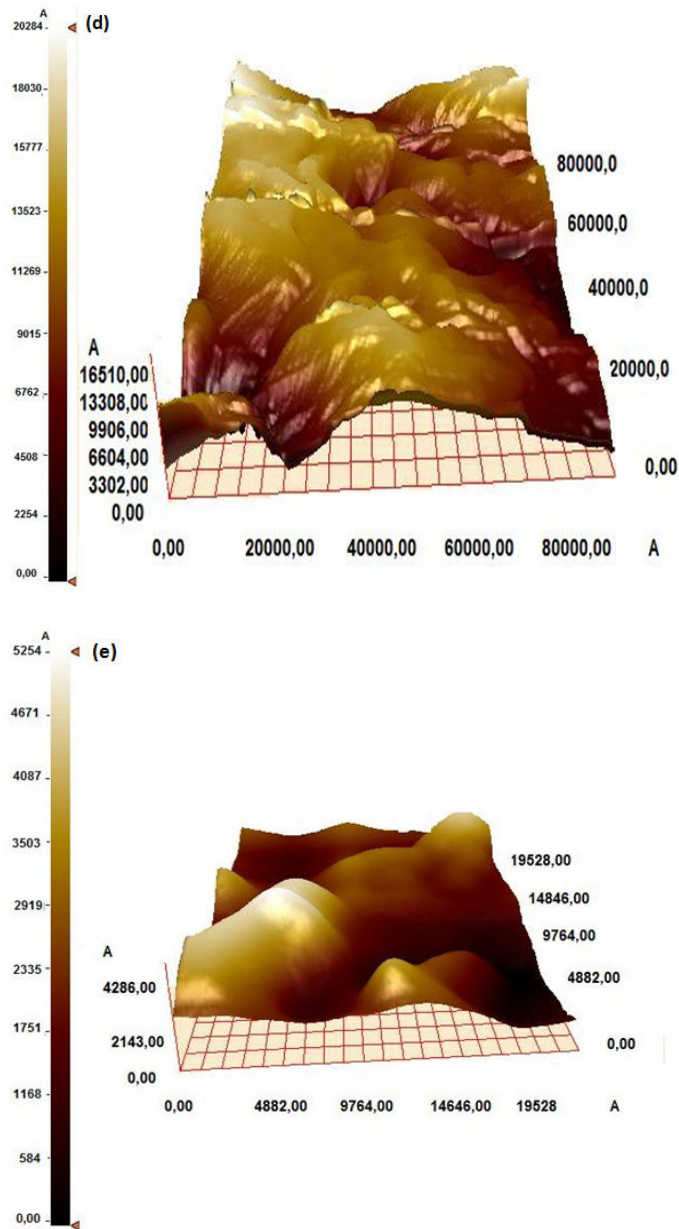
Figure 5.27. 3D AFM images by tapping mode of **(a)** pristine graphite flake, **(b)** GO sheet obtained after 72 hr oxidation, **(c)** GNS after direct reduction of GO, **(d)** expanded GO, and **(e)** GNS after heat treatment and reduction.

5.2.3. Raman Spectroscopy Characterization

Raman spectroscopy is an efficient technique to establish the number of graphene layers and the change of crystal structure of carbon materials. Raman spectrum of graphite has four principal peaks: the G band around 1580 cm^{-1}, the G' band around 3248 cm^{-1}, the D band around 1360 cm^{-1} and the D' band around 2700 cm^{-1}. The intensity of D band relies on any kind of disorder of defects in sample, and G band intensity increases almost linearly as the flake thickness increases [129]. In Figure 5.28 (a), a strong G band at 1580 cm^{-1}, a weak D band at 1360 cm^{-1} and a broad D' band at 2724 cm^{-1} were observed in the Raman spectrum of raw graphite. After 6 hr oxidation process, G band of GO sample was broadened and the intensity of D band was increased due to the significant reduction in size of the in-plane sp^2 domains, Figure 5.28 (b). During oxidation reactions, diffusing oxygen species randomly attached through the layers and thus graphite lattice was destroyed. After thermal shock, the strong G band with a weak D band and broad D' band was detected in Figure 5.28 (c). The broad D' multi-band peaks observed at ~2700 cm^{-1} are compatible with multi-layer aspect of bulk graphite [55]. Then, thermally exfoliated GO was subjected to a chemical reduction, D band around 1350 cm^{-1} disappeared due to the defect-free graphene nanosheet formation, Figure 5.28 (d). Additionally, direct reduction of GO sheets led to a decrease in the G band intensity (lowering from 2002 a.u. to 815 a.u.) which indicated a reduction in the number of layers when compared to GO, Figure 5.28 (e).

The structural change from graphite to GNS could be observed by the intensity ratio of the D and G bands, I_D/I_G. This ratio varied inversely with the size of the crystalline grains or interdefect distance and this was also used to estimate the amount of defects [57]. In Figure 5.29 (a), I_D/I_G values decreased via an increase of oxidation time and this indicated an increase of order in structure. D band intensity decreased with increasing layer numbers. D' band became more prominent than G band if only the number of graphene layers were smaller than 5 [127]. Subsequently, layer number could be determined regarding to the intensity of G band. Figure 5.29 (b) exhibited that the ratio between the intensity of G and D' peak, $I_G/I_{D'}$, raised with increasing oxidation time. The gradual increase in the values of $I_G/I_{D'}$ ratio indicated an increase of layer number in the structure.

Raman spectroscopy characterization was also used for the reduced GO and reduced expanded GO samples. After the chemical reduction of both GO and expanded GO sheets, $I_G/I_{D'}$ decreased by increasing oxidation time which denoted reduction in the number of graphene layers as shown in Figure 5.30 (a) and (b). Therefore, stacking height of graphene sheets decreased as oxidation degree increased.
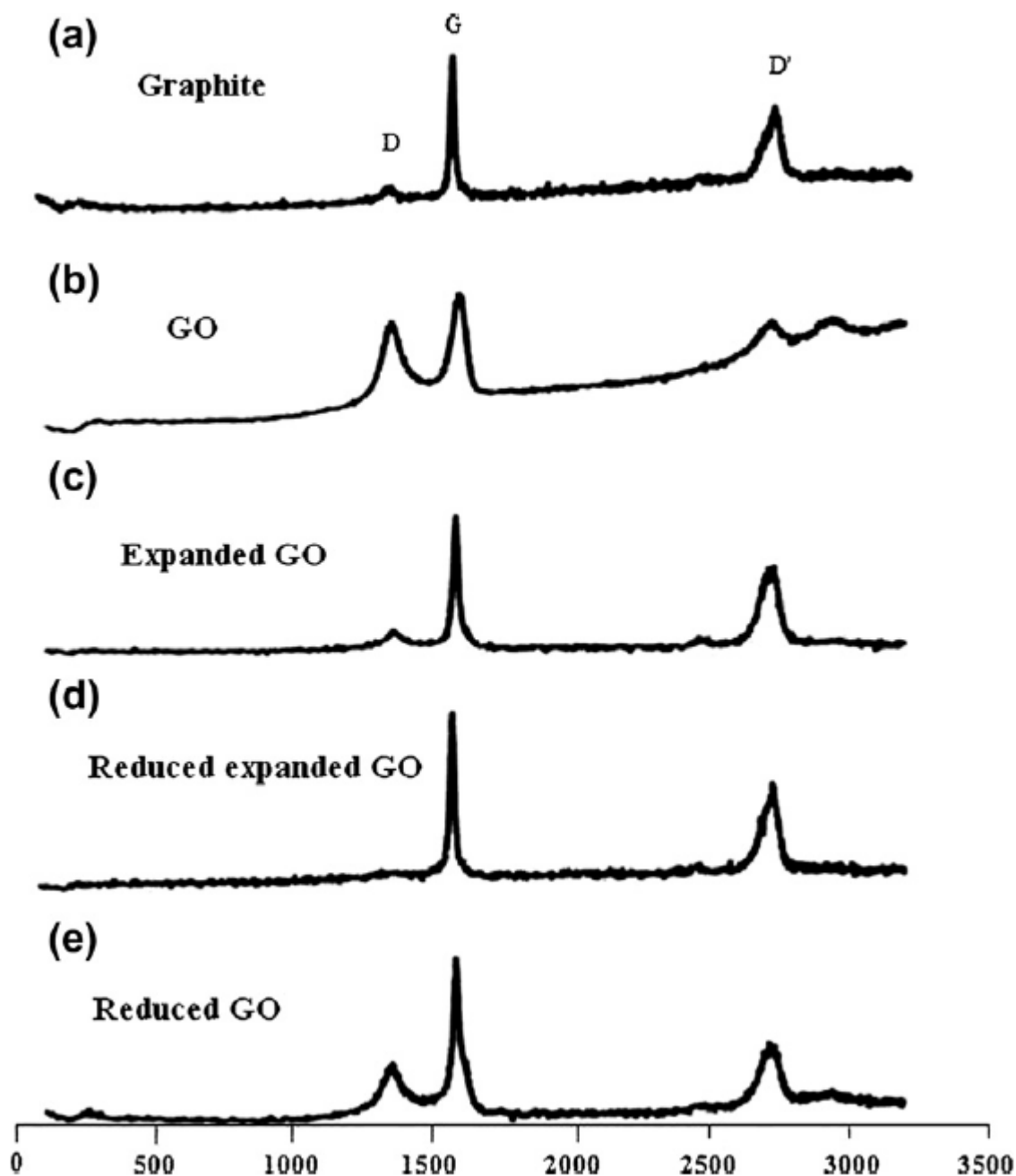
Figure 5.28. Raman spectra of **(a)** graphite, **(b)** GO, **(c)** expanded GO, **(d)** reduced expanded GO (GNS), and **(e)** reduced GO (GNS) samples belonging to the experimental results obtained after 6 hr oxidation.
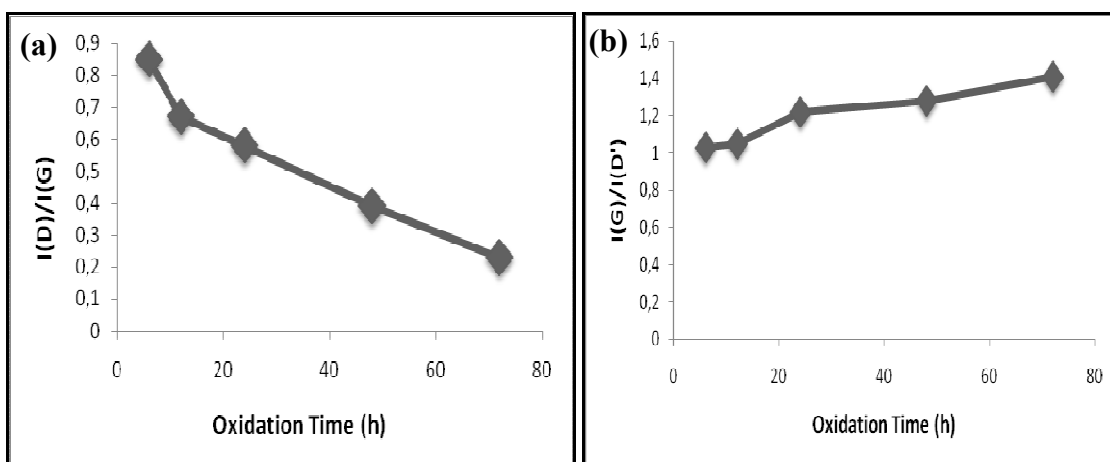
Figure 5.29. According to Raman Spectroscopy results of GO sheets, graphs **(a)** I_D/I_G and **(b)** $I_G/I_{D'}$ as a function of oxidation time.
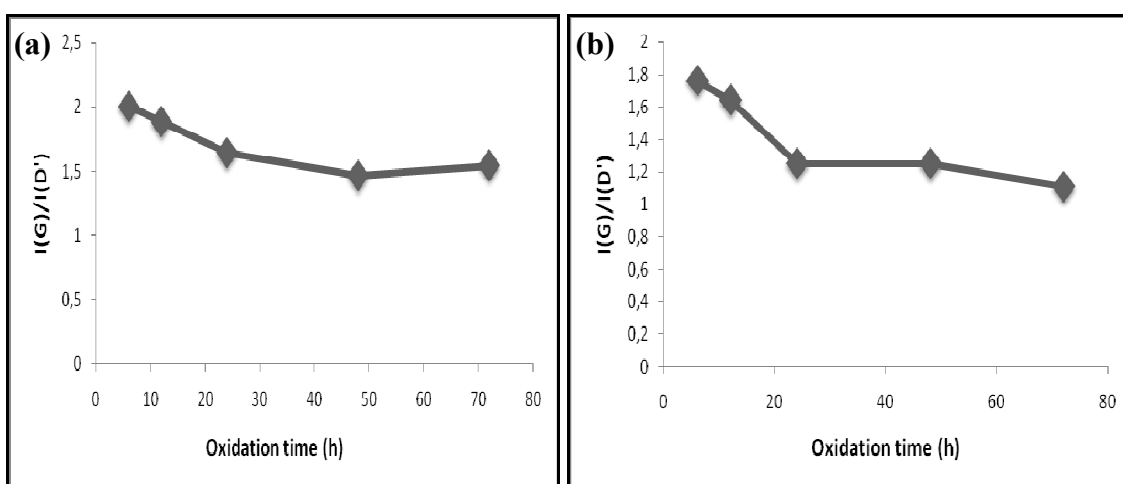
Figure 5.30. $I_G/I_{D'}$ as a function of oxidation time of **(a)** reduced GO (GNS) and **(b)** reduced expanded GO (GNS).

5.2.4. Thermal Analysis by TGA

The thermal behaviour of pristine graphite flakes, GO obtained after 6 hrs of oxidation, and GNS obtained after direct reduction were analyzed by TGA in both dry air and N_2 atmospheres. Pristine graphite flake started to lose weight around 750^oC due to the carbon dioxide evolution, Figure 5.31 (a). The thermal decomposition of GO sheets under dry air occurred in two steps around 300^oC and 550^oC due to the removal of oxygen functional groups and carbon oxidation [130]. GNS exhibited a weight loss at about 240^oC. Thermal analysis under dry air indicated that GNS decomposed thermally at lower temperatures when compared to pristine graphite flakes.

Figure 5.31 (b) also supported thermally unstable behaviour of GO samples under a nitrogen atmosphere. Graphene nanosheet samples seemed to decompose considerably at higher temperatures when compared with GO samples. Furthermore, the percentage of weight loss of GO sample was about 40% after thermal treatment under a nitrogen atmosphere, while no weight loss was observed in graphite and GNS samples.
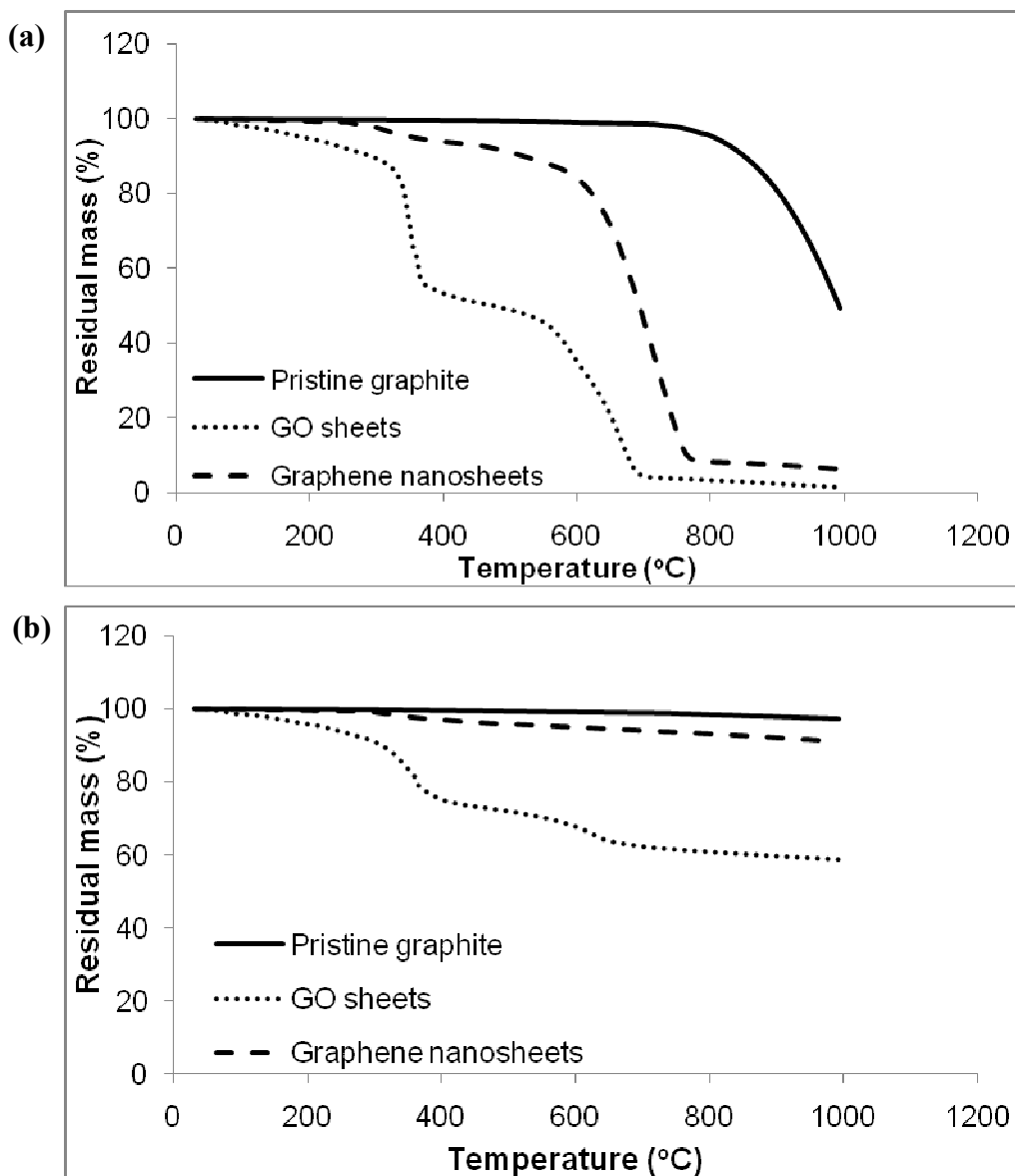
Figure 5.31. TGA curves for pristine graphite flake, GNS and GO-6 hr **(a)** under a dry air atmosphere and **(b)** under a nitrogen atmosphere.

92

5.2.5. Calculation of the Average Number of Graphene Layers

For the calculation of the average number of graphene layers in treated graphite samples two methods were proposed. The first way is the application of Debye-Scherrer equations [125]:

$$L_a = 0.89\lambda / \beta_{002} \cos\theta_{002}$$

$$n = L_a / d_{002}$$

where L_a (stacking height), β (FWHM), n (number of graphene layers), d_{002} (interlayer spacing) were obtained by using the data from XRD patterns.

In the second method, for the determination of the stacking height AFM micropgraphs of the samples were used. The average stacking height, L_a, determined from AFM measurements obtained from different zones of the surface of the sample was divided into interplanar spacing, d_{002}, obtained from XRD patterns and thus the number of the graphene layers was calculated. Stacking height and lateral size of the crystallites computed by Debye–Scherrer equation were approximate values due to wavy structure of graphene sheets.

Comparison of these two methods was exhibited in Table 5.4. The average number of layers for pristine graphite flake, GO, expanded GO, reduced expanded GO (GNS) and reduced GO (GNS) were calculated as 86, 79, 30, 37 and 9 via XRD characterization [3], and 89, 17, 25, 17 and 11 via AFM characterization, respectively. When looking the layer number results obtained either by XRD or by AFM characterization techniques, there were small deviations. This proved that both two techniques supported each other to calculate average number of layers and the average number of graphene layers decreased steadily from pristine graphite flake to GNS samples by applying proposed chemical routes. The variations of interplanar spacings also clarified how stepwise chemical procedure influenced the morphology of graphite. Intercalation of acetic anhydride into the crystal structure of graphite during oxidation increased the interplanar spacing of graphite from 3.37 Å to 3.61 Å. Expansion process initiated the formation of "worm-like" or accordion structure. However, this structure is flexible and can be cut into different shapes and compressed [131]. Therefore, the

interplanar spacing of expanded GO is lower than that of GO because graphite layers can also be easily restacked during characterization. Increase in the average number of graphene layers after thermal expansion was thus also explained by Raman Spectroscopy characterization results which revealed a return to the graphitic structure with the thermal treatment.

Table 5.4.

Comparison of layer number with XRD and AFM techniques

Samples	d (Å)	Average Number of layers (XRD)	Average Number of layers (AFM)
Graphite flake	3.37	86	89
GO-50 min	3.61	17	17
Expanded GO	3.36	30	25
Reduced Expanded GO (GNS)	3.38	37	17
Reduced GO (GNS)	3.62	9	11

5.2.6. Crystallinity Analysis via XRD

XRD data was employed to characterize the percent crystallinities of modified graphitic structures at different oxidation times. The area of (002) peak of 1 g pristine graphite was accepted as reference data. The area of the same peak in diffractograms of the samples will give the amount of the graphite (g) present in the samples. The ratio of the area of (002) peak in the treated samples to the area of the (002) peak of 1 g pristine graphite gave the ratio of the graphite (crystallinity) present in the sample.

Table 5.5 shows the XRD data analysis for the calculation of percent crystallinity. As seen in Table 5.5, FWHM values of the (002) XRD peak are considerably larger for GO samples than that for pristine graphite [128].

Table 5.5.

XRD data analysis for the calculation of percent crystallinity of GO samples

Sample	Intensity of (002) peak (counts)	FWHM (degree)	Area (Experimental)	Area (Theoretical)	Crystallinity (%)
Graphite	169814	0.327	50944	-	100
GO-50 min	761	1.294	647	26415	2.5
GO-6 hr	574	1.151	603	18803	3.2
GO-12 hr	378	1.501	397	20688	1.9
GO-24 hr	780	1.631	1092	11811	9.3
GO-48 hr	556	1.876	584	9831	5.9
GO-72 hr	431	1.664	410	9831	4.2

Assume that the graphite flake is nearly 100% crystalline, chemical process induced the change in the structure from crystalline to amorphous. GO samples became amorphous and the percent crystallinity decreased down to nearly 2%. However, there was no gradual decrease in percent crystallinity regarding to oxidation times, Figure 5.32. This disorder in percent crystallinity values stemmed from the change of stacking order between graphene layers and the random destruction of graphitic structure after oxidation process. Furthermore, turbostratic random ordering of GO structure obtained after the acid exposure at different hours may affect the crystallinity [128].
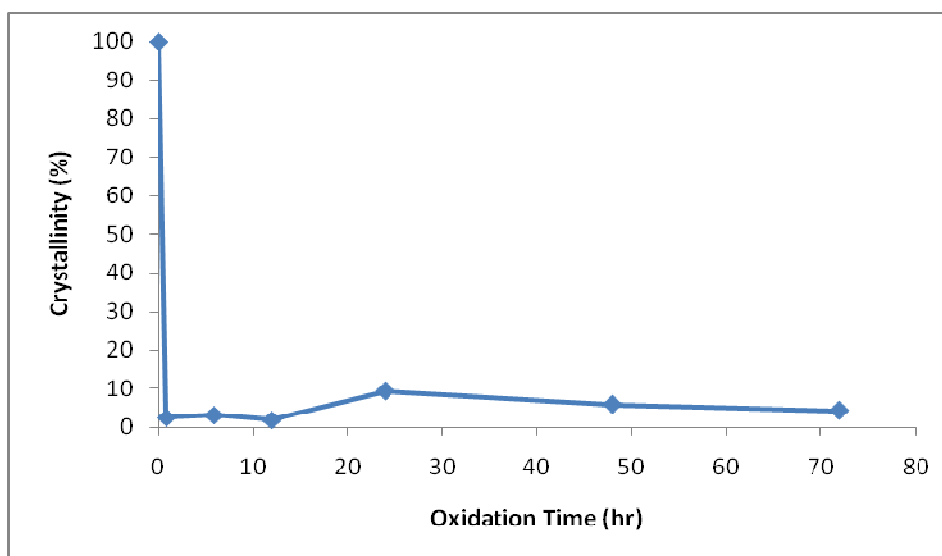
Figure 5.32. Crystallinity behaviour of GO samples at different oxidation times.

5.3. Layer-by-Layer Polypyrrole Coated GO and Graphene Nanosheets

5.3.1. SEM Characterization

Polypyrrole (PPy) synthesized by oxidation of the monomer with $FeCl_3$ had a form of fine black powder. SEM image of pristine PPy contained irregular sphere-like particles of PPy, Figure 5.33. Oxidizing agents and monomer concentration have a considerable influence on the formation of the PPy morphology (the sphere-like, the ribbon-like, the wire-like) during polymerization [132]. Also, pure PPy is brittle, insoluble and infusible, and hence not processable.
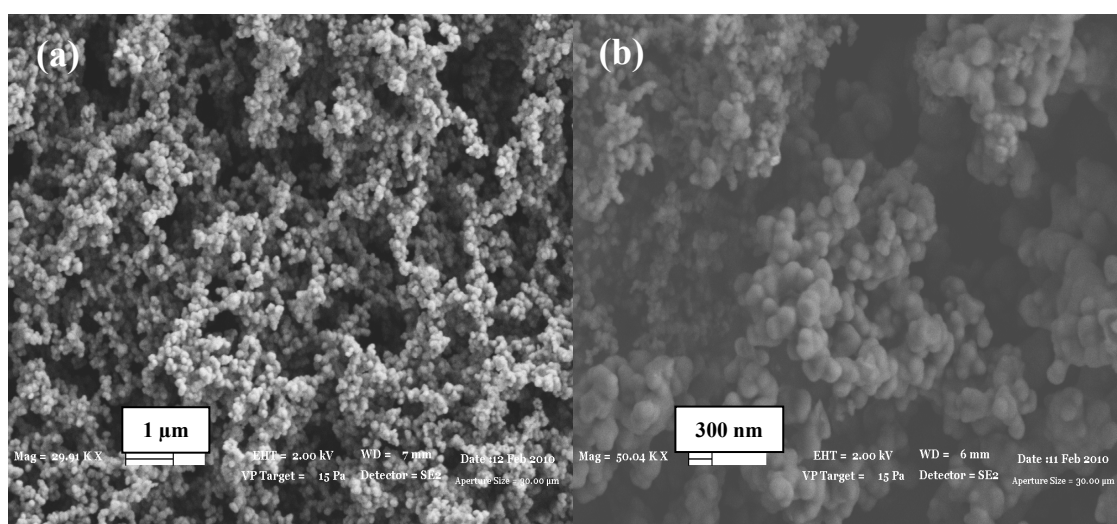
Figure 5.33. SEM images **(a)** and **(b)** of pristine PPy at different magnifications.

Smooth and rigid GO layers were seen in Figure 5.34 (a). After PPy coating, laminated structure of GO sheets was observed clearly in SEM image, Figure 5.34 (b). Py monomer dispersed into the layers of GO and all layers were covered by PPy after oxidative polymerization. Also, acetic anhydride used as an intercalating agent during oxidation extended the layer distance in graphite and thus provided good dispersion of PPy through GO layers during polymerization.
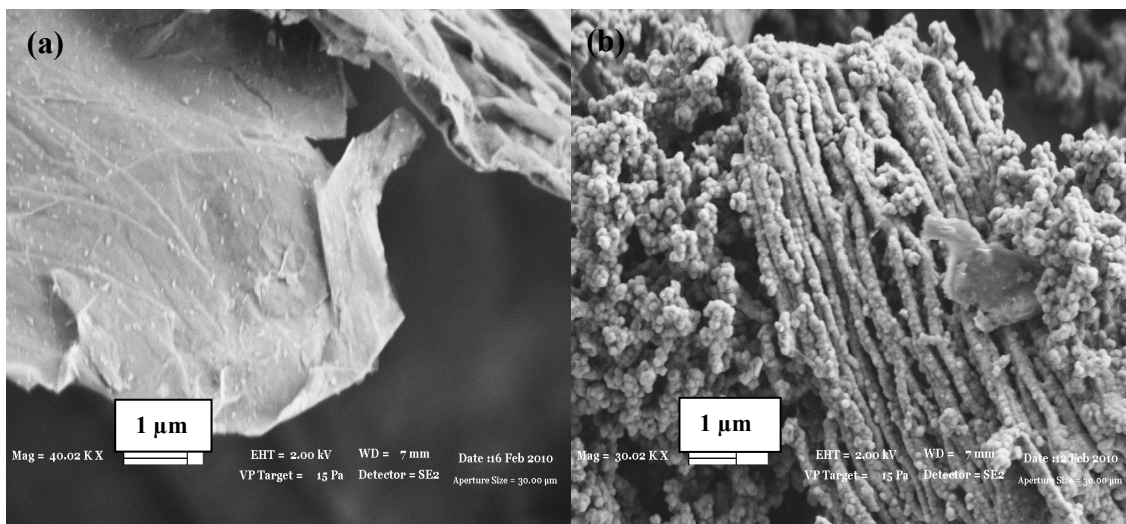
Figure 5.34. SEM images of **(a)** GO sheets and **(b)** PPy coated GO sheets (the ratio by weight between Py and GO sheets as 1:1).

GO sheets were dispersed via ultrasonic treatment and then dispersed sheets were reduced by hydroquinone [3]. Separated GNS obtained by chemical reduction are presented in Figure 5.35 (a). Py intercalated into GNS during *in situ* polymerization and polymerized on GNS layer-by-layer. Uniformly layer coating of PPy/graphene nanosheet composites and spherical morphology of PPy nanoparticles on sheets were seen clearly in Figure 5.35 (b).
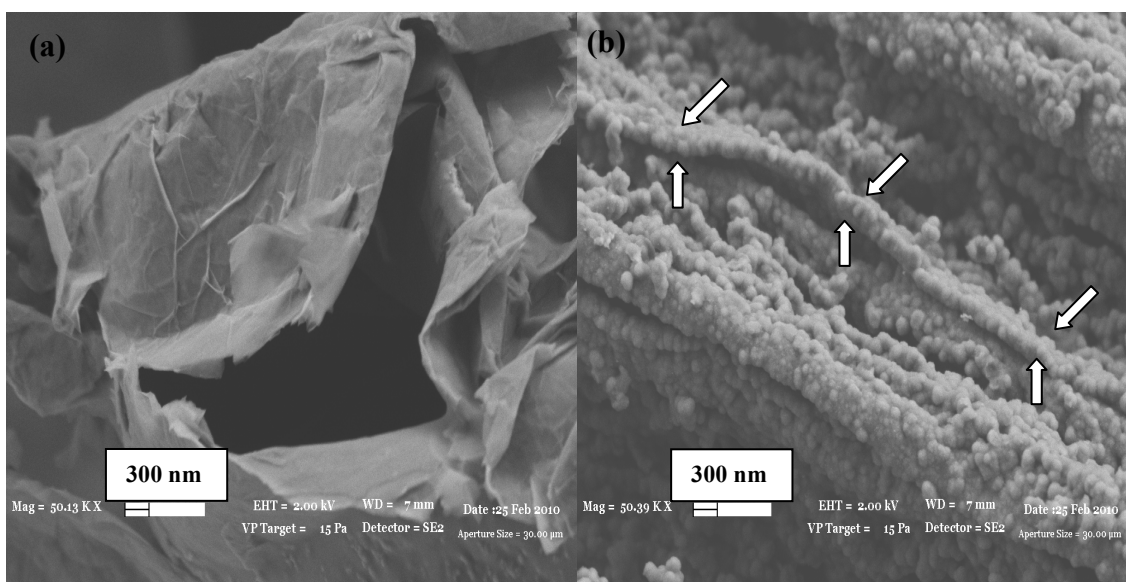
Figure 5.35. SEM images of **(a)** GNS obtained after chemical reduction of GO sheets and **(b)** PPy/graphene nanosheet composites (the ratio by weight between Py and GNS as 1:1).

5.3.2. XRD Characterization

XRD patterns of pristine PPy, GO sheets, Py:GO sheets=1:1 and Py:GO sheets=2:1 were presented in Figure 5.36. The results indicated that PPy had an amorphous structure. Graphite flakes were partially oxidized in the adjusted synthesis conditions using concentrated sulfuric acid, potassium dichromate, and acetic anhydride [3]. XRD pattern of GO sheets showed low intensity of 002 diffraction peak at $2\theta=26.5^{o}$. Longer oxidation time led to decrease in the intensity of 002 peak, enhanced the interlayer spacing between graphene sheets and switched the carbon backbone from sp^2 to sp^3 structure [133]. After covering of GO sheets by PPy with different feeding ratios, 002 peak intensity decreased and the peak was broadened. The intensity of 002 peak of Py:GO sheets=1:1 decreased down to 53 cps. The intensity of 002 peak of Py:GO sheets=2:1 was down to 40 cps. The structure of nanocomposites became more amorphous by increasing PPy content.
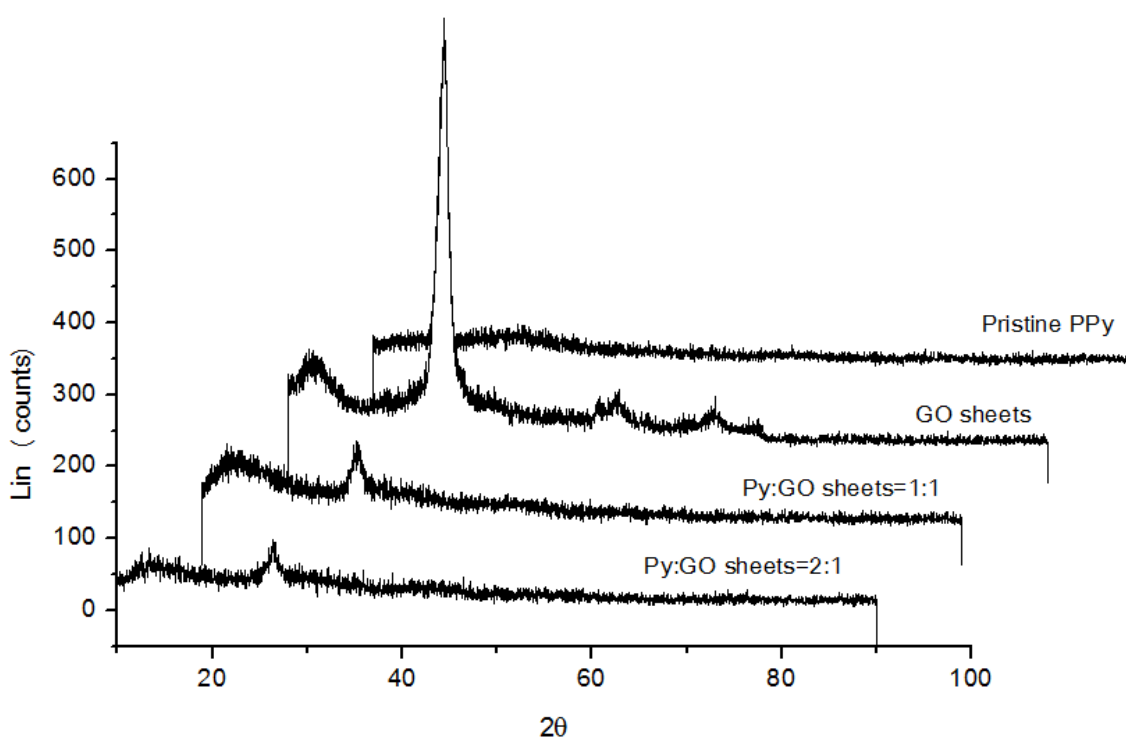
Figure 5.36. XRD patterns of pristine PPy, GO sheets, Py:GO sheets=1:1 and Py:GO sheets=2:1.

XRD data were also used to measure the percent crystallinities of GO sheets, PPy/GO nanocomposites, Figure 5.37. The area of (002) peak of 1 g pristine graphite was accepted as reference data and graphite flake was assumed as 100% crystalline. Also, PPy had an amorphous structure. After 10 days of oxidation, the percent crystallinity of GO sheets decreased down to nearly 1.8%. After coating on GO surface by PPy (Py/GO sheet weight ratio: 1/1), the percent crystallinity of new materials decreased down to ~0.6%. Increasing the weight of Py in nanocomposites, the percent crystallinity became much lower. Accordingly, highly ordered substrates provide strong metal-support interaction and reduce self-poisoning [95]. As the amount of GO sheets in nanocomposites increases, crystallinity increases and thus Pt particles can be easily deposited on well-ordered graphene oxide sheets.
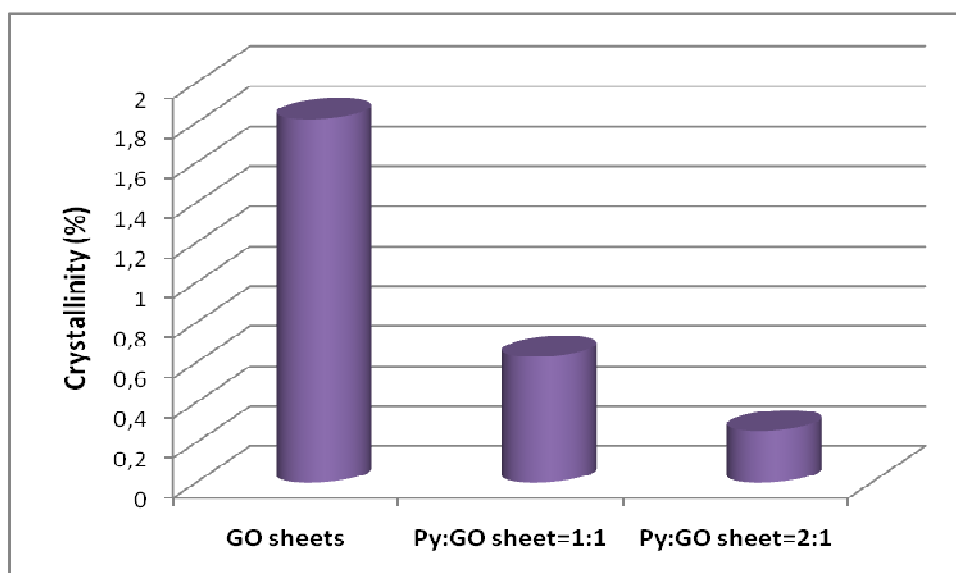
Figure 5.37. Percent crystallinity changes of GO sheets and PPy/GO nanocomposites.

5.3.3. Raman Spectroscopy Characterization

In Raman spectrum, D band intensity changes with defects and disorder in sample, and G band intensity increases linearly by increasing flake thickness [129]. The Raman spectrum of pristine PPy demonstrated the two bands at around 1380 cm^{-1} (D band) and 1561 cm^{-1} (G Band), Figure 5.38. In this spectrum, the characteristic D and G bands were due to the ring-stretching mode of PPy [134] and the C=C backbone stretching of PPy [135], respectively.
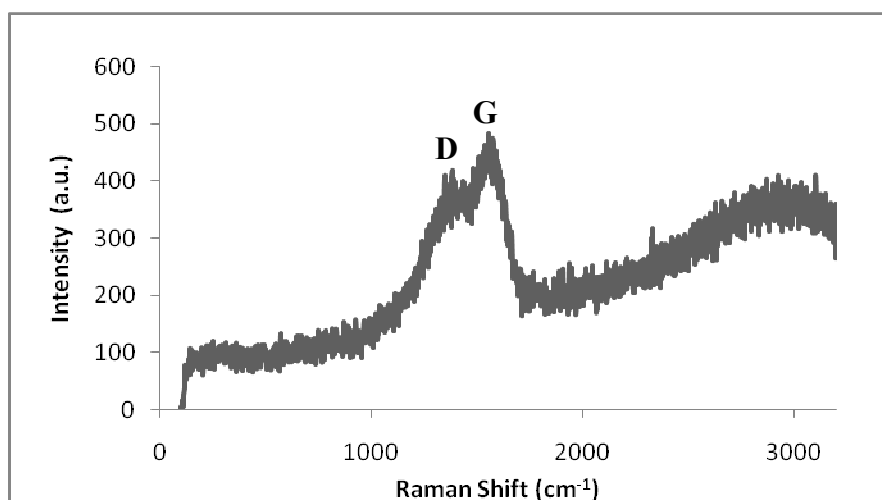
Figure 5.38. Raman spectrum of pristine PPy.

During oxidation of graphite flakes, oxygen species diffused into the layers randomly and graphitic structure was distorted. There were three characteristic Raman bands of partially oxidized GO sheets which were the D band around 1354 cm^{-1}, the G band around 1580 cm^{-1} and the D' band around 2708 cm^{-1}, Figure 5.39.
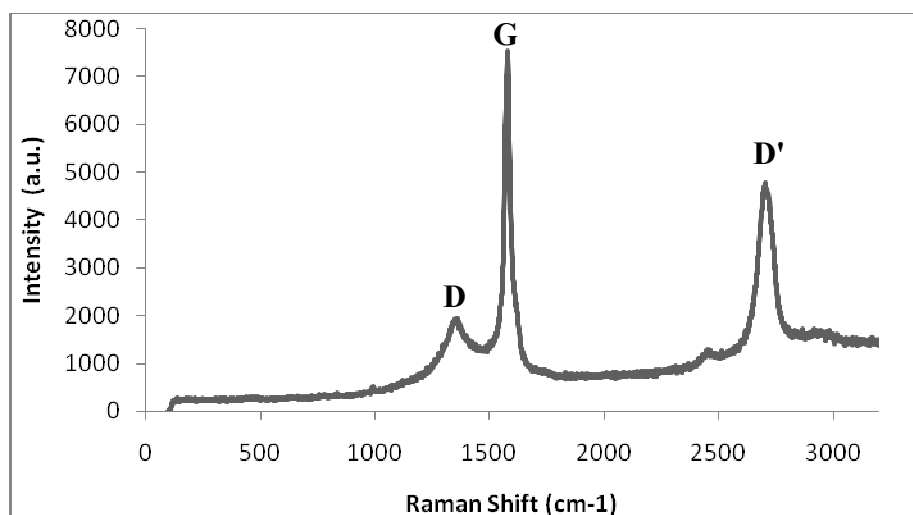
Figure 5.39. Raman spectrum of GO sheets after 10 days of oxidation.

The structural change could be observed by the intensity ratio of the D and G bands, I_D/I_G. This ratio directly correlated with the size of the crystalline grains or interdefect distance and this was also used to estimate the amount of defects [57]. In Raman spectra of PPy/GO sheet nanocomposites, Figure 5.40, I_D/I_G ratio decreased with

the increase of the feeding mass ratio of Py to GO sheets. I_D/I_G ratios of Py:GO sheets=1:1 and Py:GO sheets=2:1 were calculated as 0.66 and 0.63, respectively. Therefore, the graphitic in-plane crystallite size, L_a, increased with the enhanced covering onto the surface of GO layers by PPy.
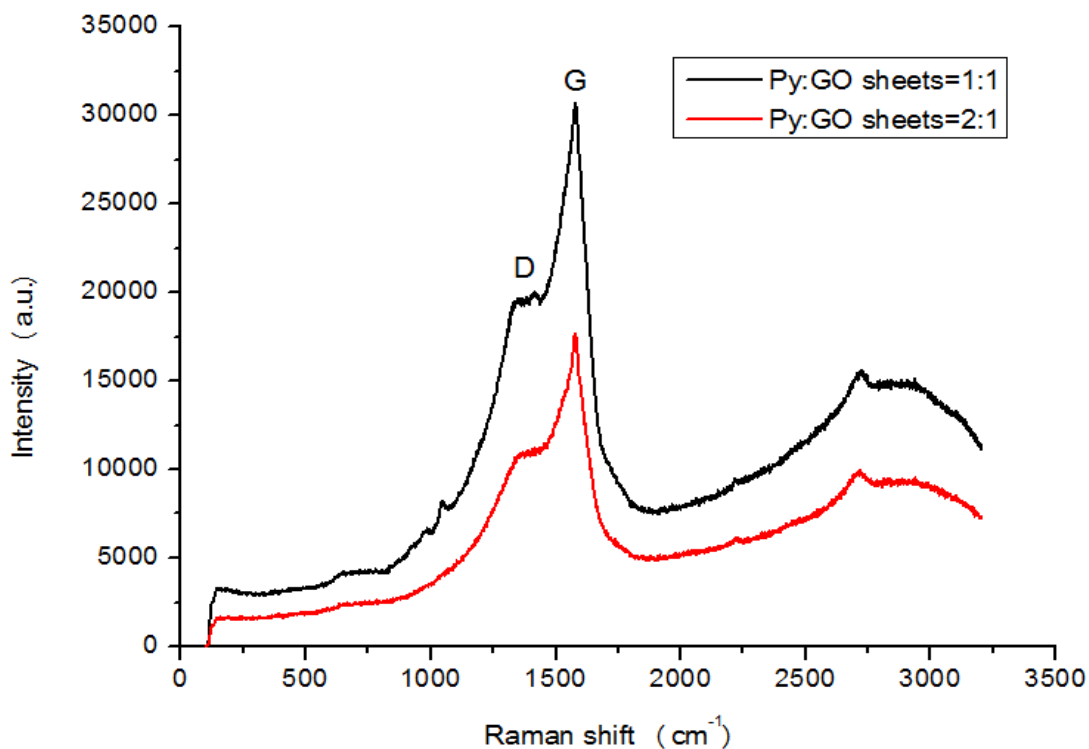
Figure 5.40. Raman spectra of Py:GO sheets=1:1 and Py:GO sheets=2:1.

In the Raman spectrum of GNS, the D band around 1364 cm^{-1}, the G band around 1582 cm^{-1} and the D' band around 2709 cm^{-1} appeared, Figure 5.41. I_D/I_G ratios of GO sheets and GNS were calculated as 0.25 and 0.31, respectively. This increase in I_D/I_G ratio indicated the stacking height of graphene sheets decreased by ultrasonic vibration and chemical reduction of GO sheets. After coating of PPy on GNS, D and G bands broadened and their intensities increased, Figure 5.41. G band intensity is directly proportional to the graphitic in-plane crystallite size, L_a [136]. Therefore, increasing G band intensity revealed that flake thickness increased after the covering of GNS by PPy.
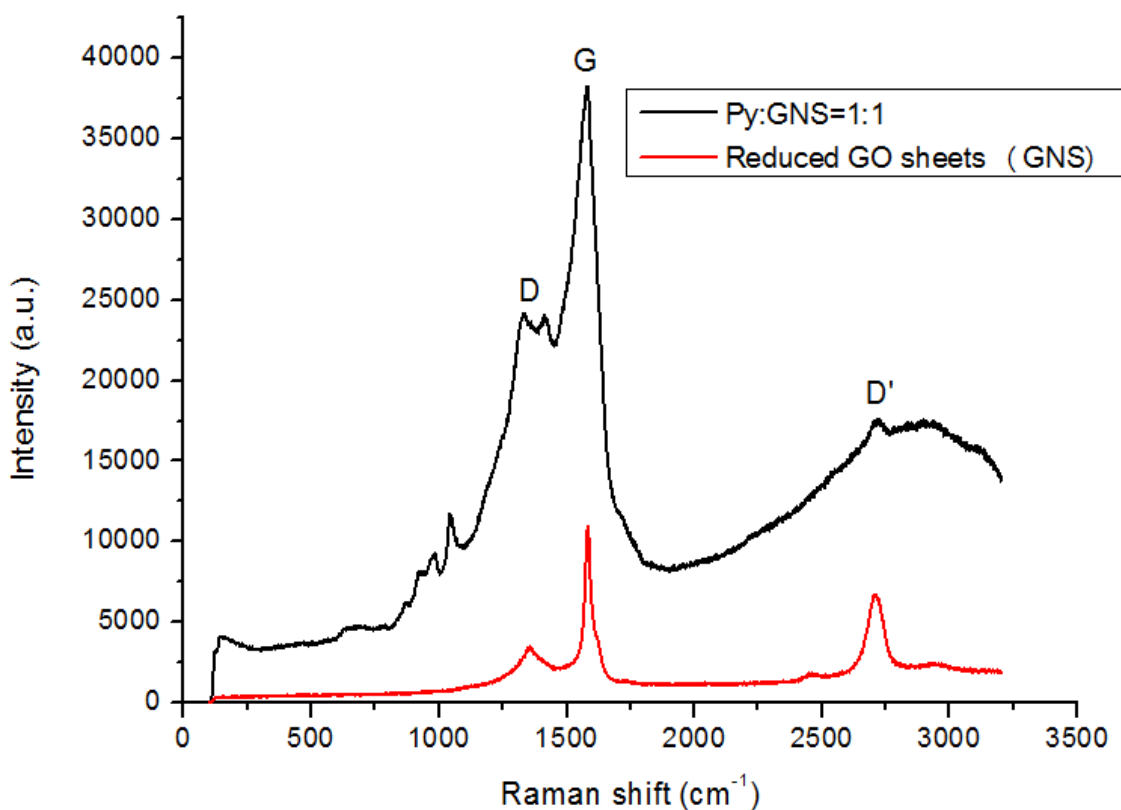
Figrue 5.41. Raman spectra of reduced GO sheets (GNS) and Py:GNS=1:1.

In addition, the thickness of graphite flake, GO sheets and reduced GO sheets were compared regarding to the change of I_D/I_G ratio. Figure 5.42 showed I_D/I_G ratio change of graphite flake, partially oxidized GO sheets and reduced GO sheets. After each chemical reaction, I_D/I_G ratio increased, and thus flake thickness decreased [129]. This decrease was also supported by the results obtained from XRD characterization by using Debye-Scherer equations. Average number of graphene layers for graphite flakes, GO-10 day oxidation and reduced GO (GNS) were calculated as 86, 21 and 19, respectively (Table 5.6). This indicated that how stepwise chemical procedure influenced the morphology of graphite.
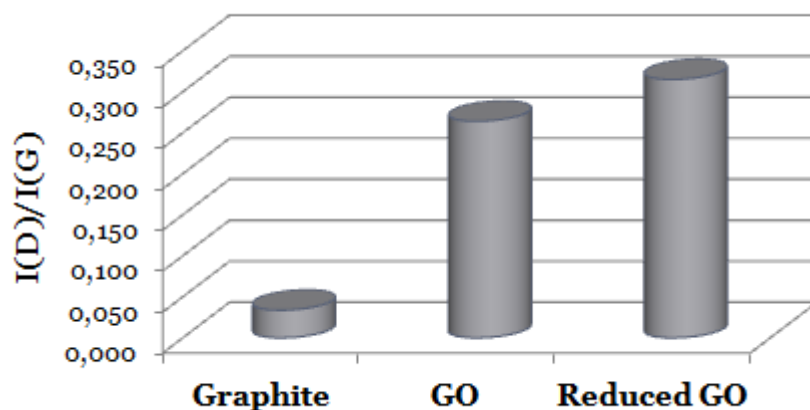
Figure 5.42. I_D/I_G ratio change of graphite flake, GO sheets, and reduced GO (GNS)

Table 5.6.

Average number of graphene layers of graphite, GO sheets and reduced GO sheets (GNS) calculated by using Debye-Scherer equations

Samples	Average number of graphene layers	d(nm)
Graphite flakes	86	0.337
GO sheets (10 day oxidation)	21	0.339
Reduced GO (GNS)	19	0.342

5.3.4. Thermogravimetric Analysis

Figure 5.43 indicated the thermogravimetric curves of GO sheets, pristine PPy, PPy/GO nanocomposites synthesized with different feeding mass ratios. The weight loss curve of nanocomposites appeared between pristine PPy and GO sheets. When comparing to thermal behavior of PPy, PPy/GO sheet nanocomposites had an improved thermal stability. In addition, thermal stability decreased by increasing PPy content in GO layers. The percent weight changes of materials as a function of increasing temperature were also analyzed by TGA. GO sheets started to lose weight at about $350^{\circ}C$ due to the thermal decomposition of acetic anhydride into CO_2 and H_2O vapor which swelled the layered graphitic structure. Pristine PPy was quite stable up to $150^{\circ}C$ and began to degrade at temperatures higher than $150^{\circ}C$. As the amount of PPy was increased in PPy/GO nanocomposites, the decomposition temperature decreased. The

thermal stabilities of these composites were much higher than pristine PPy. The amount of weight losses of pristine PPy, GO sheets, Py:GO sheets=1:1 and Py:GO sheets=2:1 at 700 ^{o}C were about 88%, 25%, 51% and 53%, respectively. These differences also supported the stability of synthesized PPy/GO nanocomposites between pristine PPy and GO sheets.
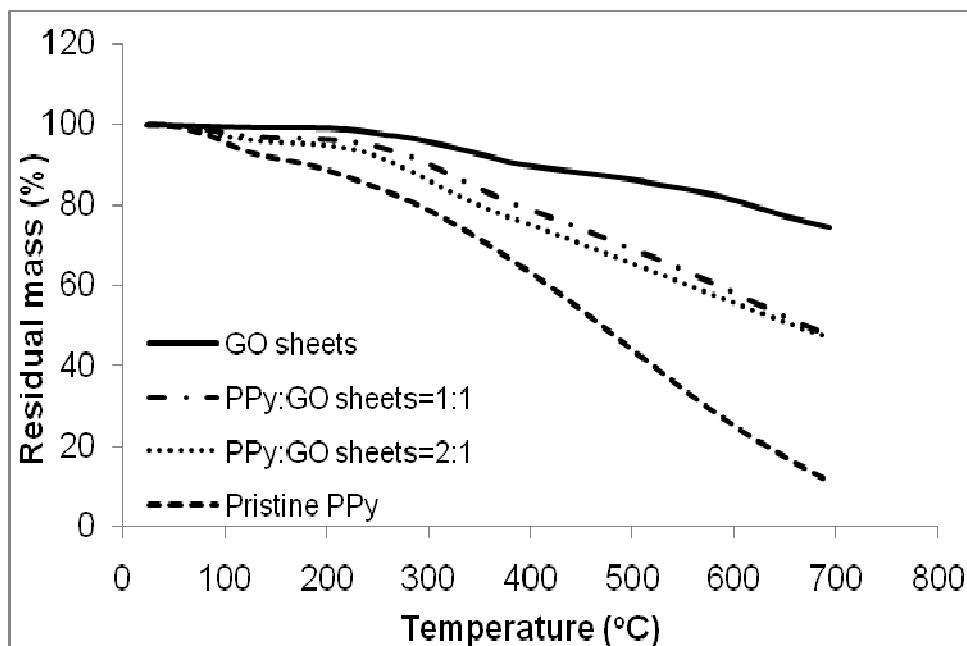
Figure 5.43. TGA curves of GO sheets, Py:GO sheets=1:1, Py:GO sheets=2:1, and pristine PPy in air atmosphere.

In Figure 5.44, thermal stabilities of GNS, pristine PPy and Py:GNS=1:1 composite were compared between 25-700°C under air atmosphere. GNS exhibited 5% weight loss at about 310°C. GNS effectively reinforced the PPy matrix in nanocomposite. Therefore, the mass loss of PPy/graphene nanosheet composite during the thermal decomposition was approximately 5% of the initial mass at 300°C. However, the mass loss of PPy was about 5% at 150°C and then rapid mass loss took place between 150°C and 700°C. Consequently, mass loss percentage of nanocomposite was significantly less than pristine PPy. The amount of weight losses of pristine PPy, GNS and Py:GNS=1:1 at 700°C were about 88%, 56%, and 70%, respectively.
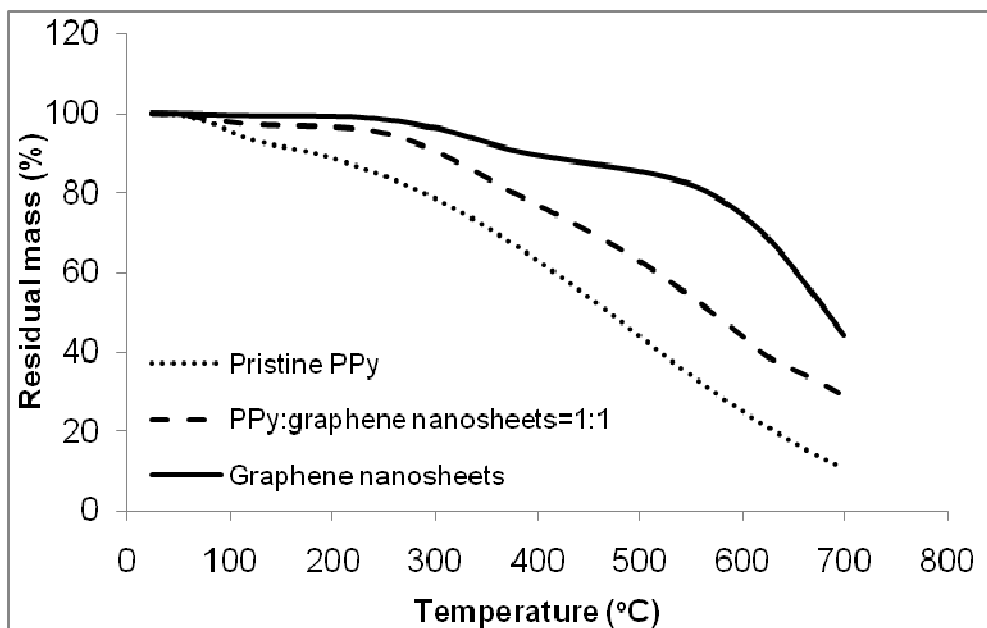
Figure 5.44. TGA curves of GNS, Py:GNS=1:1-nanocomposite, and pristine PPy in air atmosphere.

5.3.5. AFM Analysis of Composites

All AFM experiments were performed in tapping mode using a silicon cantilever probe. As Py concentration increased, the composite surface became smoother. 3D surface topography of PPy composites displayed smooth morphology, Figure 5.45 (a). As the amount of GO sheet increased, the height difference of surface increased due to ripples in GO sheets, Figure 5.45 (b). In addition, the functional groups such as epoxide, carbonyl, quinone, ketone, and hydroxyl on the basal plane of GO triggered corrugation or local puckering of the carbon skeleton [128]. However, increasing the amount of PPy in the nanocomposite caused to reduce the topography variations which were observed in 3D AFM image, Figure 5.45 (c).
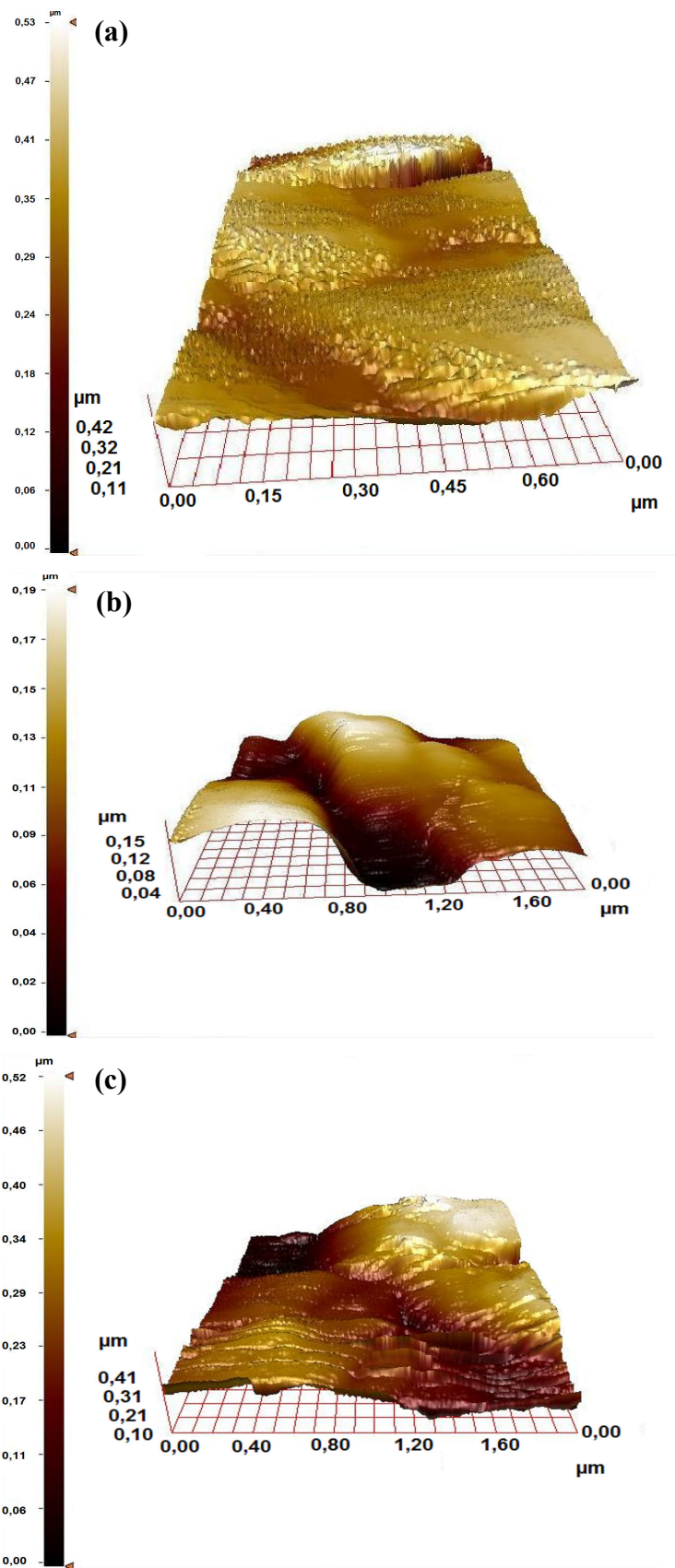
Figure 5.45. 3D AFM images by tapping mode of **(a)** pristine PPy, **(b)** Py:GO sheets=1:1, and **(c)** Py:GO sheets=2:1.

5.3.6. Electrical Conductivity and Surface Area Measurements

The electrical conductivity of samples in the pellet form was measured by the conventional four-probe method. The electrical conductivity results of samples (pristine PPy, GO sheets, Py:GO sheet=1:1, and Py:GO sheet=2:1) were given in Table 5.7. Conductivity of pristine PPy was relatively poor due to weak compactness and randomly orientation of PPy nanostructures and weak bonding between the polymer particles through the boundaries [137]. Although GO is electrically insulating material, partially oxidized GO sheets can be utilized as a conductive filler to enhance the conductivity of PPy. The electrical conductivity of fully oxidized GO sheets prepared by the Hummers-Offeman method [6] was measured as 10^{-4} S/cm by using the four-probe method [138]. The conductivity of partially oxidized GO sheets synthesized by a mild and safer oxidation method [3] was measured as 0.69 S/cm. The conductivity value of GO sheets can also be controlled by changing the degree of oxidation [3]. The conductivity values of nanocomposites were between the values of pristine PPy and GO sheets and the increasing PPy content decreased the conductivity of nanocomposites. According to recently published works, in the production of GO-based nanocomposites, oxidation degree of GO sheets, oxidizing agents, intercalating agents, monomer type and concentration, and reaction media considerably affects the conductivities of composites [138, 139].

Table 5.7.

Electrical conductivity results of pristine PPy, GO sheets and PPy/GO nanocomposites

Samples	Conductivity (S/cm)
Pristine PPy	7.6×10^{-4}
GO sheets	0.69
Nanocomposite-1 (Py:GO sheets=1:1)	0.08
Nanocomposite-2 (Py:GO sheets=2:1)	0.05

Pan *et al.* [140] reported the electrical conductivity of graphene sheets obtained by hydrazine reduction as 4.6 S/cm. The conductivity of reduced GO sheets (GNS) obtained by hydroquinone reduction [3] was measured as 3.96 S/cm. After PPy was coated onto the surface of reduced GO sheets, the conductivity of the composite improved due to the better compactness and structure of PPy in the composite than in pristine PPy (Table 5.8). Therefore, nanocomposites including GNS showed better conductivity when comparing nanocomposites including the partially oxidized GO sheets.

Table 5.8.

Electrical conductivity results of pristine PPy, reduced GO sheets (GNS), PPy/GNS nanocomposite

Samples	Conductivity (S/cm)
Pristine PPy	7.6×10^{-4}
Reduced GO sheets (GNS)	3.96
Nanocomposite (Py:GNS=1:1)	0.13

High specific surface area is one of the main requirements for the enhancement of the dispersion and narrow distribution of catalytic metals on catalyst support materials. Nitrogen adsorption isotherms showed that BET surface area of reduced GO sheets was 507 $m^2\,g^{-1}$. Ruoff *et al.* [141] demonstrated that BET surface area of reduced GO sheets was measured as 466 $m^2\,g^{-1}$ via nitrogen gas absorption. This BET value was similar to one calculated by using our reduced GO sheets. After coating on reduced GO sheets by PPy, BET surface area of this nanocomposite was measured as 270 $m^2\,g^{-1}$. BET surface area results of reduced GO (GNS) and Py:GNS=1:1 composite were given in Table 5.9. In PPy/GNS composites, GNS provided higher surface area and better electronic conductivity while PPy facilitated the electron transfer through the conducting matrix. Because of large aspect ratio and surface area of reduced GO sheets, they serve as effective percolative conducting bridges that increase the conductivity of nanocomposites [142].

Table 5.9.

Surface area results of reduced GO (GNS) and Py:GNS=1:1 nanocomposite calculated according to BET method

Samples	Surface Area (m^2/g) According to BET method
Reduced GO (GNS)	507
Py:GNS=1:1	290

5.4. Pt Deposition on Polypyrrole/Graphene Nanosheets and Polypyrrole/GO Nanocomposites

5.4.1. Pt deposited PPy/Graphene Nanosheets nanocomposites

Graphene nanosheets (GNS) were received in large quantities by chemical exfoliation of graphite [3] and separate sheets were shown in Figure 5.46 (a). Three different impregnation techniques shown in Table 4.4 showed that some Pt catalysts formed clusters and aggregated on the surface of GNS, Figure 5.46 (b), (c) and (d). However, with the sonication technique, the aggregation of Pt catalysts was reduced in comparison to sonication combined with direct synthesis technique, Figure 5.46 (c) and (d). Coloma *et al.* [143] demonstrated that oxygen surface groups make the carbon surface more hydrophilic and thus a better dispersion of Pt catalysts is provided. Herein, the oxygen content in GNS decreased after chemical reduction. This led to the decrease the centers for the strong adsorption of $PtCl_6^{-2}$.
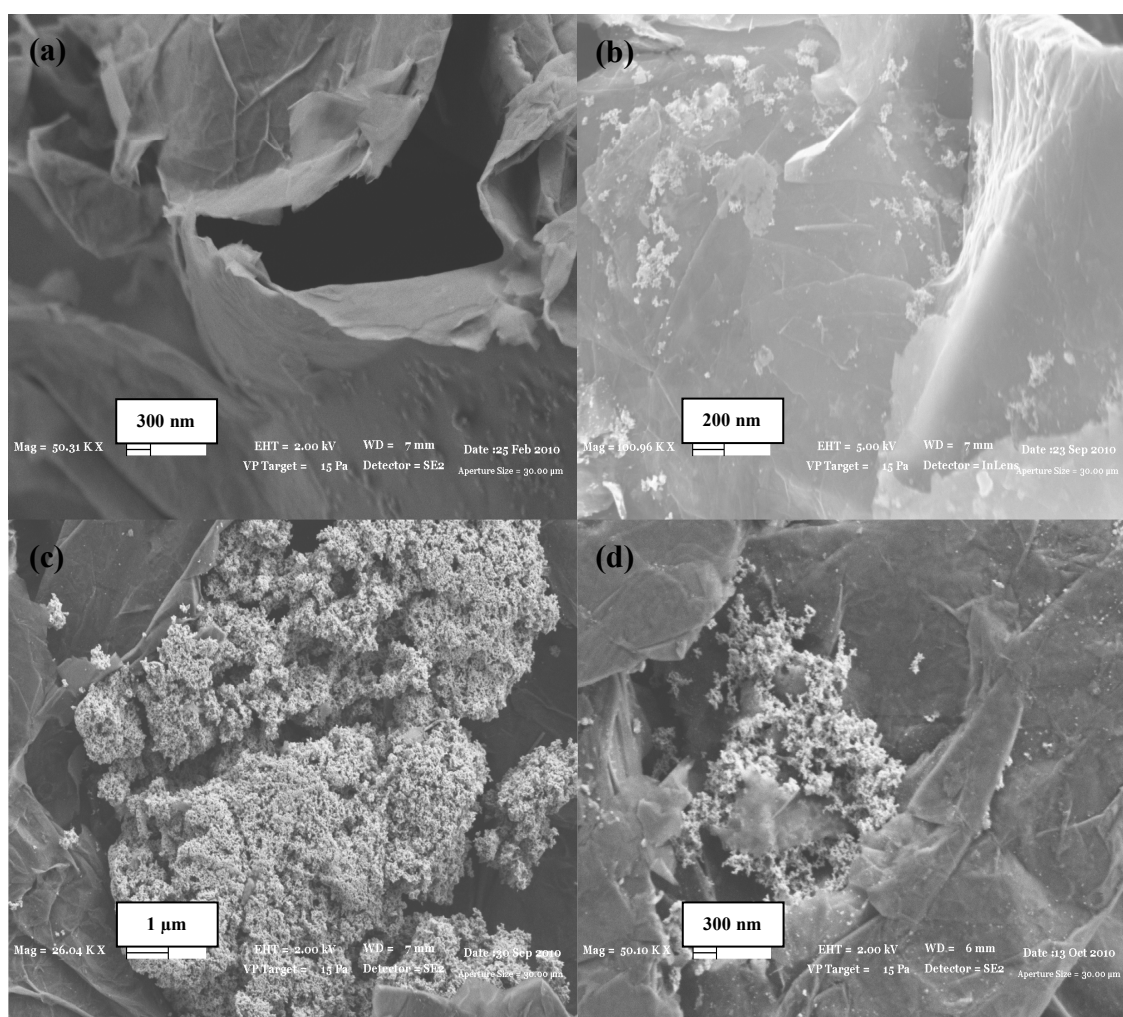
Figure 5.46. SEM images of **(a)** GNS, **(b)** Pt/GNS according to 1st method, **(c)** Pt/GNS according to 2nd method, and **(d)** Pt/GNS according to 3rd method (Pt deposition methods were shown in Table 4.4).

Table 5.10 shows EDX results for GNS and Pt deposited GNS by three different deposition techniques. The measured results clearly demonstrated that GNS contained 70.3 wt% C, 27.9 wt% O and other elements (Na, Al, Si, S) 1.8 wt%. After each impregnation technique, the amount of Pt was changed on the surface of GNS due to the aggregation of Pt catalysts on different sites of GNS. EDX analyses performed on different sites of samples showed that Pt catalysts were absent or available as clusters in some areas.

Table 5.10.

EDX results of GNS, Pt/GNS according to 1st, 2nd and 3rd methods

Samples	Carbon (wt%)	Oxygen (wt%)	Platinum (wt%)	Other elements (wt%)
GNS	70.3	27.9	-	1.8
Pt/GNS (1st method)	61.6	29.0	9.4	-
Pt/GNS (2nd method)	61.3	33.1	-	5.6
Pt/GNS (3rd method)	57.0	31.8	1.4	9.8

PPy was coated on the surface of GNS by *in situ* chemical oxidative polymerization of Py. A layer-by-layer polymer coating observed clearly in SEM image, Figure 5.47 (a). In the PPy/GNS composites, GNS are electron acceptors while PPy serves as an electron donor [144]. In the presence of PPy, Pt particles adhered well to the composite surface. Therefore, coating by PPy on GNS induced electronic conduction, and the adhesion of Pt on the membrane surface was significantly enhanced [145]. In Figure 5.47 (b), catalyst particles were dispersed partly and a uniform distribution was not observed on the surface of composite because of Pt deposition in low amounts and shorter sonication time. In Figure 5.47 (c), Pt particles decorated closely each other on the surface. Size distribution of Pt particles changed between 20-40 nm. SEM image of this sample at higher magnification exhibited that Pt catalysts started to grow on each other during deposition process and their size were approximately 5 nm, Figure 5.48. When comparing direct deposition techniques 1 and 2 shown in Table 4.4, longer sonication process provided much dispersed catalysts by creating dispersed GNS, Figure 5.47 (d). Pt catalyst size was in the range of 20-30 nm. SEM image of this composite at higher magnification showed that Pt catalyst started to grow on its surface and the particle size was about 4 nm, Figure 5.49.
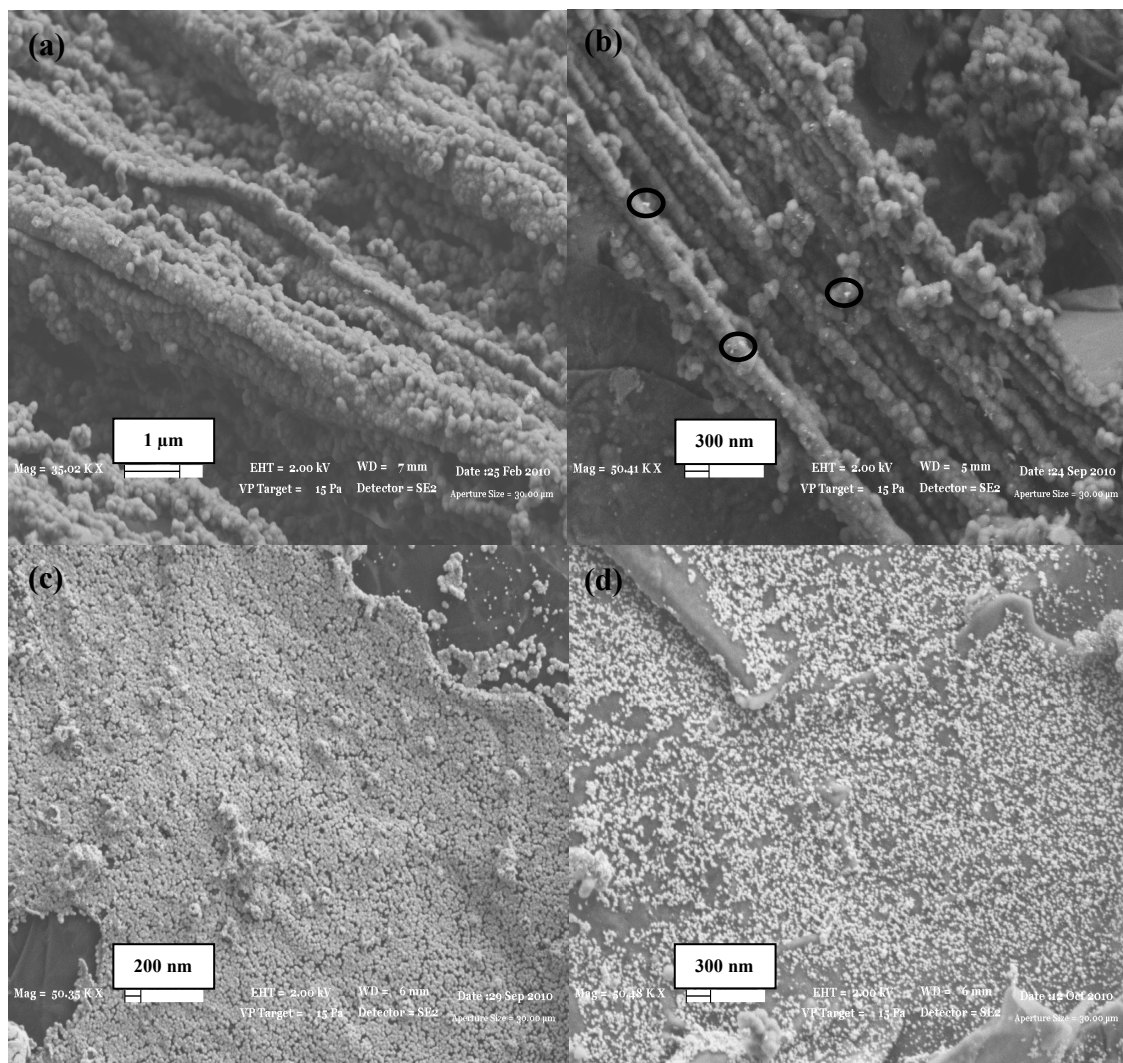
Figure 5.47. SEM images of **(a)** Py:GNS=1:1 nanocomposites, **(b)** Pt/Py:GNS=1:1 according to 1st method, **(c)** Pt/Py:GNS=1:1 according to 2nd method, and **(d)** Pt/Py:GNS=1:1 according to 3rd method (Pt deposition methods were shown in Table 4.4).
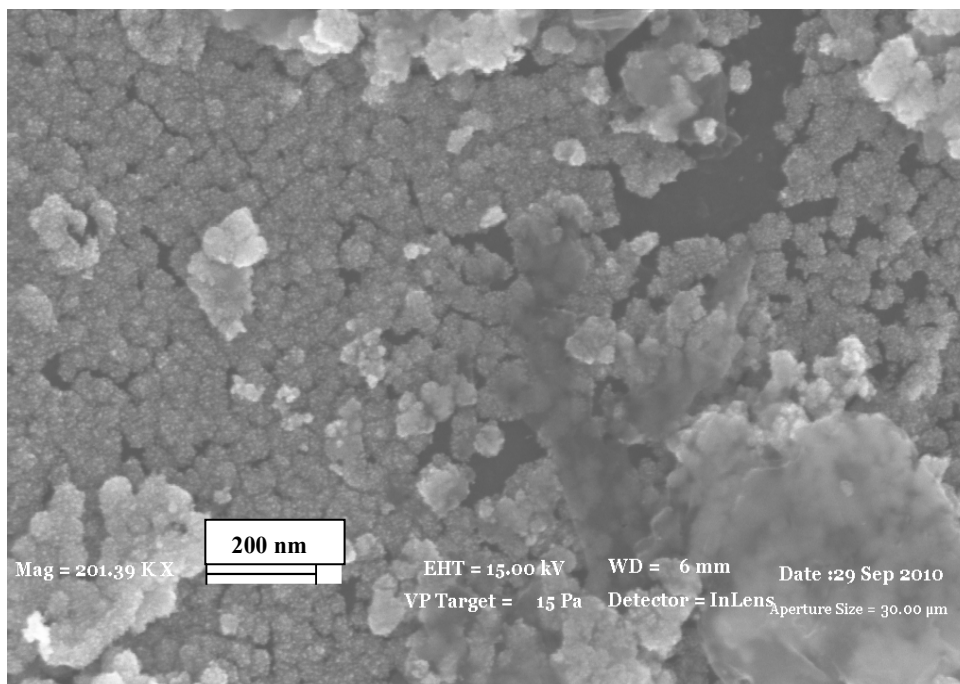
Figure 5.48. SEM image of Pt/Py:GNS=1:1 according to 2nd method at higher magnification via inlens detector.
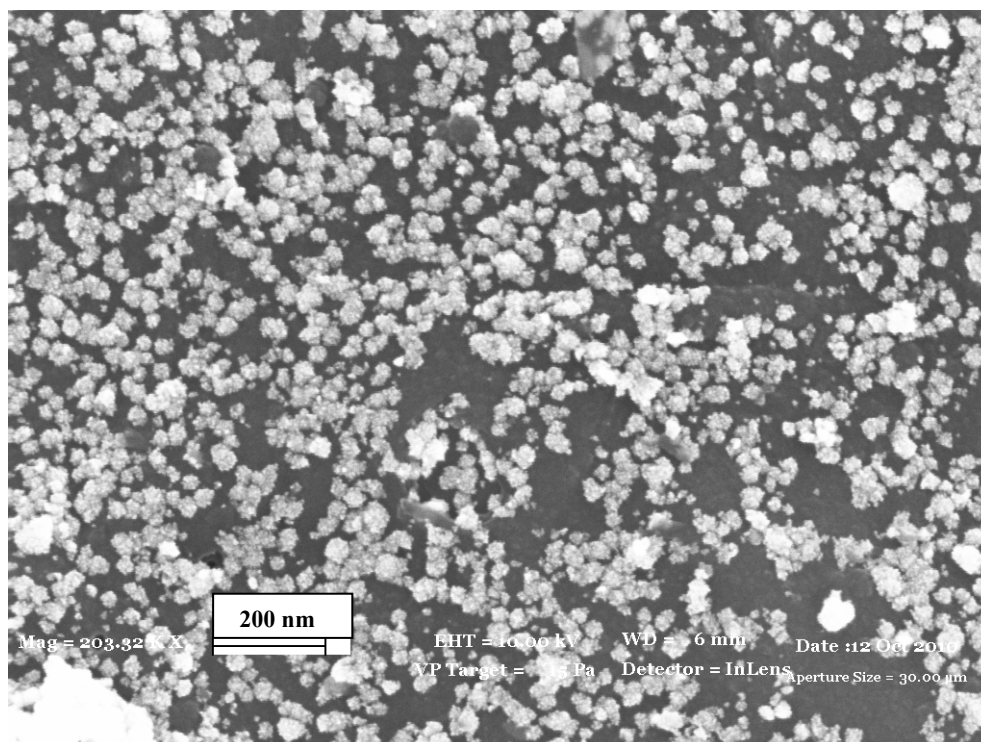
Figure 5.49. SEM image of Pt/Py:GNS=1:1 according to 3rd method at higher magnification via inlens detector.

EDX results of GNS-based nanocomposites were shown in Table 5.11. PPy/GNS composites included 42.3 % C, 7.9 % N, 44.3% O and 5.5 % other elements. The amount of nitrogen indicated the presence of PPy. After each impregnation method, the amount of Pt was measured on the surface of composites. The results showed that both PPy and oxygen surface groups affected the dispersion and amount of Pt catalysts. The difference of deposition can be explained by considering Pt deposition technique and catalyst support.

Table 5.11.

EDX results of Py:GNS=1:1 nanocomposite, Pt/Py:GNS=1:1 according to 1st, 2nd and 3rd methods

Samples	Carbon (wt%)	Nitrogen (wt%)	Oxygen (wt%)	Platinum (wt%)	Other elements (wt%)
Py:GNS=1:1	42.3	7.9	44.3	-	5.5
Pt/Py:GNS=1:1 (1st method)	49.2	17.1	24.1	6.8	2.8
Pt/Py:GNS=1:1 (2nd method)	51.8	7.6	24.4	8.1	8.1
Pt/Py:GNS=1:1 (3rd method)	39.1	3.6	40.9	7.9	8.5

5.4.2. Pt Deposited PPy/GO Sheet Nanocomposites

The oxidation process weakened van der Waals cohesive forces between graphene layers in graphite by the intercalation of oxidizing agents. In our proposed method, graphite was oxidized by using potassium dichromate and sulfuric acid as oxidants [3]. The oxidation process led to the expanded and leafy structure formation, Figure 5.50 (a). Oxidation of graphite rendered the carbon surface more acidic and thus negatively charged over a wide range of pH. This caused electrostatic repulsion of $PtCl_6^{2-}$ anions and promoted electrostatic attraction of Pt-based cations. Therefore, catalyst dispersion could be maximized by increasing metal-support interaction [146]. After the impregnation of Pt catalysts on GO sheets, the higher oxygen amount hindered agglomeration and favored the Pt dispersion in some regions due to the partial oxidation

of graphite. If the surface of graphite was fully oxidized, catalyst dispersion could be maximized [146]. According to deposition techniques, as sonication time increased, a better Pt dispersion was achieved on the surface of support. In Figure 5.50 (d), size distribution of Pt particles on the surface of Pt/GO sheets according to 3rd method changed from 13 nm to 22 nm. Also, SEM image of this sample at higher magnification exhibited catalyst growth on its surface, Figure 5.51.
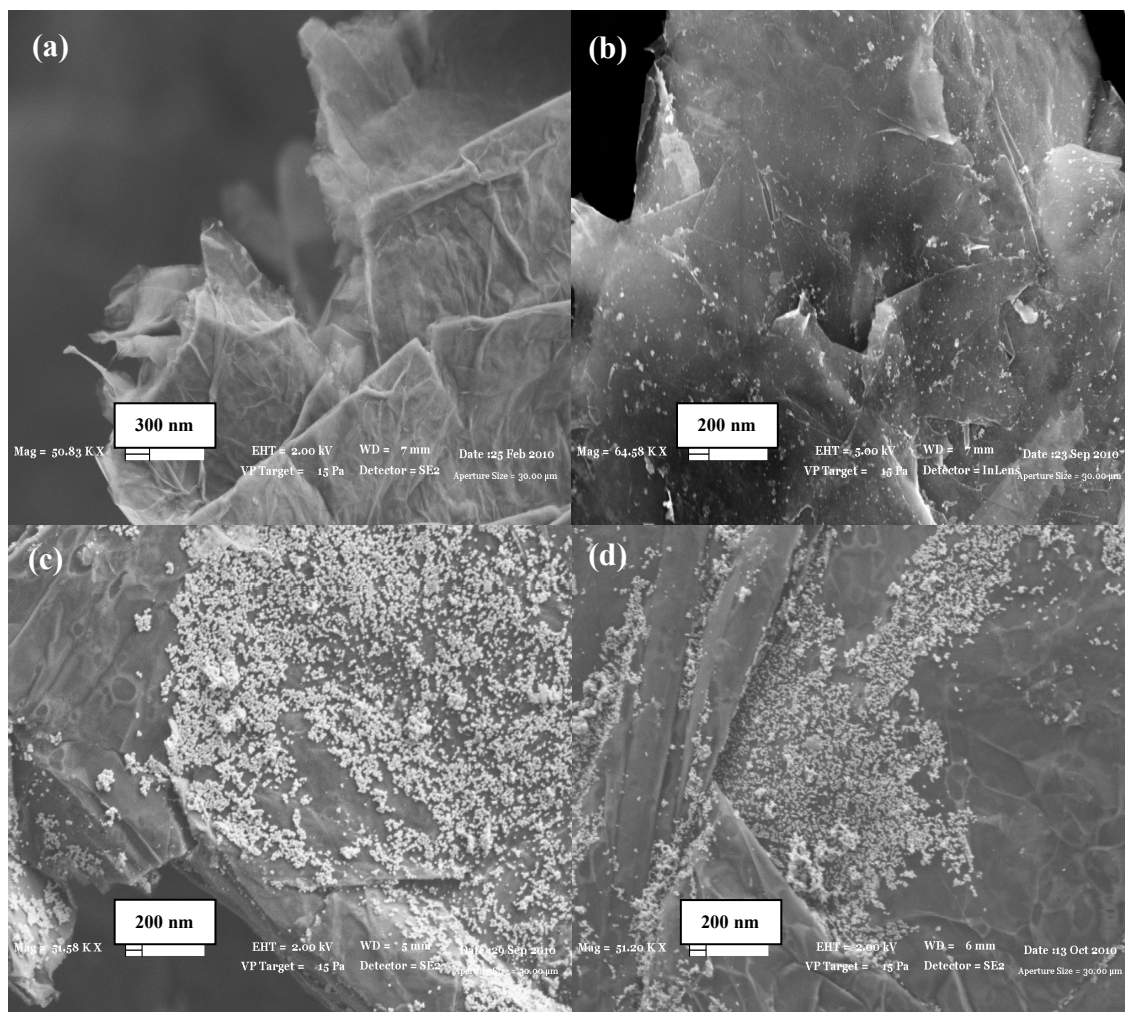
Figure 5.50. SEM images of **(a)** partially oxidized GO sheets, **(b)** Pt/GO sheets according to 1st method, **(c)** Pt/GO sheets according to 2nd method, and **(d)** Pt/GO sheets according to 3rd method (Pt deposition methods were shown in Table 4.4).
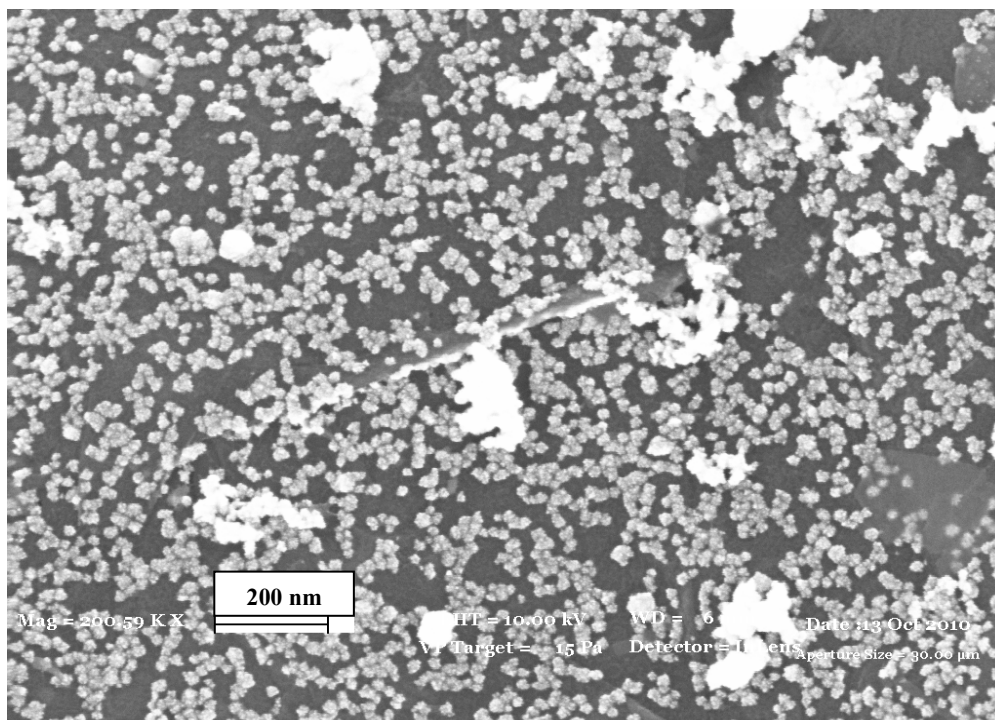
Figure 5.51. SEM image of Pt/GO sheets according to 3rd method at higher magnification via inlens detector.

EDX results of Pt deposited GO sheets were shown in Table 5.12. GO sheets contained 46.5 % C and 42.8 % O in its structure. EDX results supported the presence of Pt catalyst after the impregnation. Both EDX data and SEM images proved that higher amount of oxygen surface groups of the support plays a significant role in metal dispersion when comparing Pt decoration on the surface of GNS.

Table 5.12.

EDX results of GO sheets, Pt/GO sheets according to 1st, 2nd and 3rd methods

Samples	Carbon (wt%)	Oxygen (wt%)	Platinum (wt%)	Other elements (wt%)
GO sheets	46.5	42.8	-	10.7
Pt/GO sheets (1st method)	49.3	48.7	2.0	-
Pt/GO sheets (2nd method)	48.6	37.9	1.2	12.3
Pt/GO sheets (3rd method)	41.8	44.8	3.5	9.9

PPy/GO composites were prepared by *in situ* polymerization of Py on the surface of GO sheets with different feed ratios of Py to GO sheets. A layer coating of PPy/GO composites (feed ratio of Py to GO sheets 1:1) and spherical morphology of PPy nanoparticles on sheets were observed clearly in Figure 5.52 (a). Regarding to 1st impregnation technique, shorter sonication time and low loading of Pt catalysts did not provide fine and dense distribution on the surface of GO sheets, Figure 5.52 (b). On the other hand, Figure 5.52 (c) and Figure 5.52 (d) revealed that longer sonication time and high loading of Pt catalysts caused to enlarge catalyst dispersion. In Figure 5.52 (c) and Figure 5.53, size of Pt catalysts was measured about 16 nm. In Figure 5.52 (d), size distribution of Pt particles on the surface of Pt/GO sheets according to 3rd method changed from 19 nm to 32 nm. SEM image of this sample at higher magnification displayed the formation of Pt nanoparticles on its surface instead of support surface and the size of Pt nanoparticles was around 4 nm, Figure 5.54. Furthermore, the electrocatalyst of Pt was more easily fabricated on GO sheets covered by PPy compared with on bare GO sheets. Herein, PPy combines with the functional groups of GO sheets and these PPy/GO composites offer the electronic conduction pathway which is required to sink the electrons generated from the chemical reduction of H_2PtCl_6 solution [147].
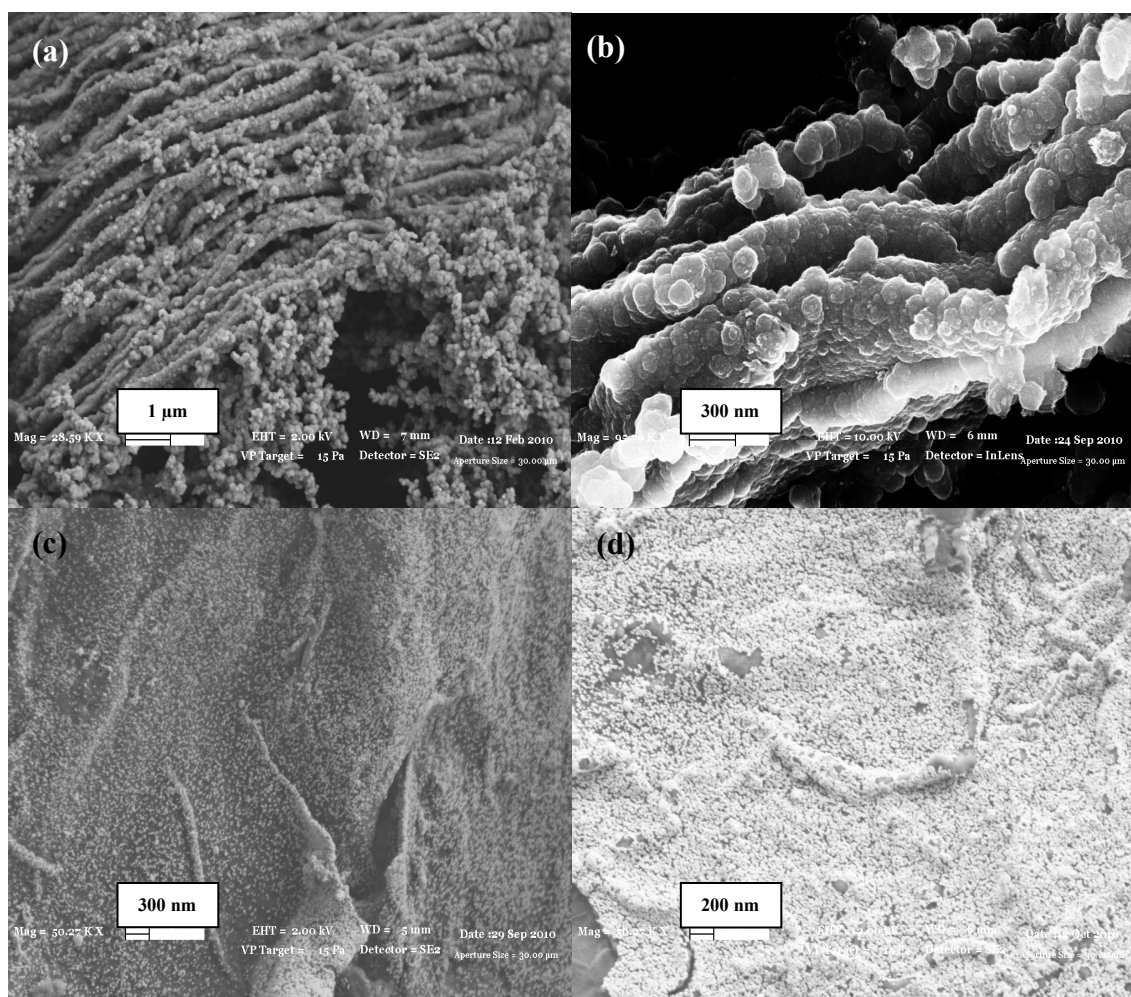
Figure 5.52. SEM images of **(a)** Py:GO=1:1, **(b)** Pt/Py:GO=1:1 according to 1st method, **(c)** Pt/Py:GO=1:1 sheets according to 2nd method, and **(d)** Pt/Py:GO=1:1 sheets according to 3rd method (Pt deposition methods were shown in Table 4.4).

Figure 5.52. SEM images of **(a)** Py:GO=1:1, **(b)** Pt/Py:GO=1:1 according to 1st method, **(c)** Pt/Py:GO=1:1 sheets according to 2nd method, and **(d)** Pt/Py:GO=1:1 sheets according to 3rd method (Pt deposition methods were shown in Table 4.4).
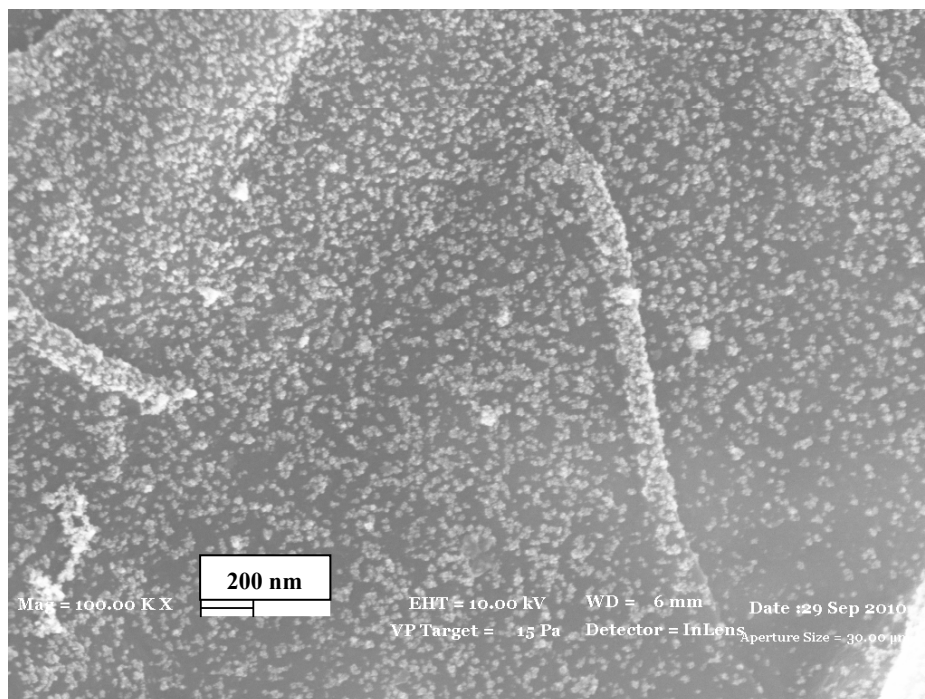
Figure 5.53. SEM image of Pt/Py:GO=1:1 sheets according to 2nd method at higher magnification via inlens detector.
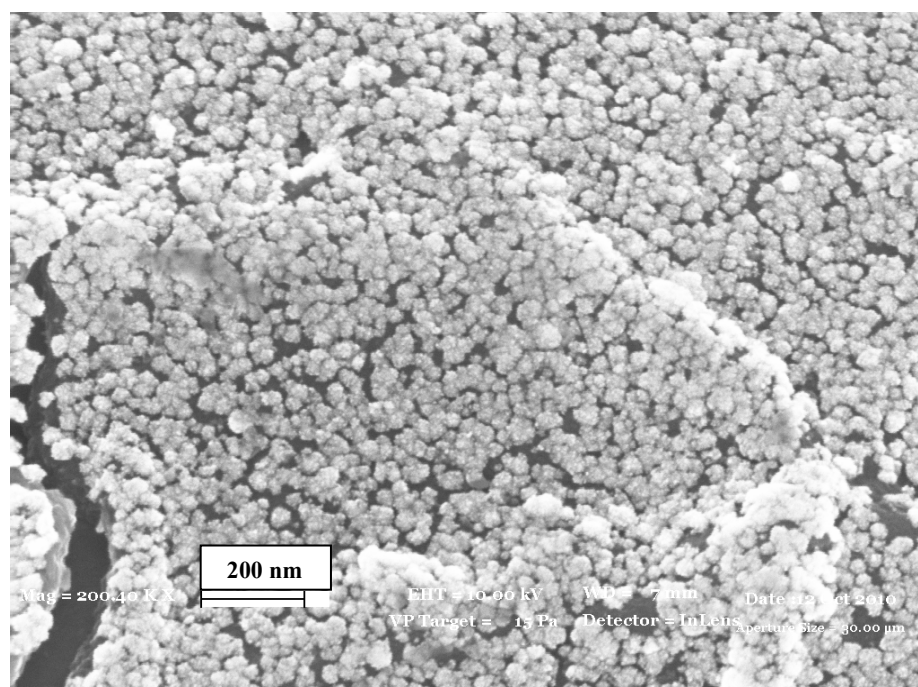
Figure 5.54. SEM image of Pt/Py:GO=1:1 sheets according to 3rd method at higher magnification via inlens detector.

The EDX compositional analysis of several Pt nanoparticles confirmed the presence of Pt catalyst on the composite surface, Table 5.13. PPy/GO composites consisted of 40.2% C, 32.9% O, and 16.7% N (resulting from PPy). Also, EDX results showed that when oxygen and nitrogen contents in an investigated region increased, the amount of Pt loading increased.

Table 5.13.

EDX results of Py:GO=1:1, Pt/Py:GO=1:1 according to 1st, 2nd and 3rd methods

Samples	Carbon (wt%)	Nitrogen (wt%)	Oxygen (wt%)	Platinum (wt%)	Other elements (wt%)
Py:GO=1:1	40.2	16.7	32.9	-	10.2
Pt/Py:GO=1:1 (1st method)	62.1	12.1	17.2	3.3	5.3
Pt/Py:GO=1:1 (2nd method)	34.3	18.3	31.5	11.9	4.0
Pt/Py:GO=1:1 (3rd method)	37.4	20.2	34.2	6.1	2.1

SEM image of Py:GO=2:1 composite was shown in Figure 5.55 (a). After 1st impregnation technique, some Pt particles were peeled off and some Pt particles linked to each other on the surface of nanocomposite, Figure 5.55 (b). Increasing both sonication time and Pt loading provided more and denser Pt distribution. Some Pt particles formed a porous structure on the surface of composite, Figure 5.55 (c). Longer impregnation time and nonuniform polymerization might lead to the formation of different Pt clusters. Size distribution of Pt particles on the surface of Pt/ Py:GO=2:1 sheets according to 2nd method changed from 5 nm to 17 nm. When Pt dispersion was performed according to 3rd method, some Pt particles aggregated into clusters in the 23-43 nm range and other Pt particles with average diameter of 3 nm started to grow on these clusters, Figure 5.55 (d) and Figure 5.56. Liu et al. [145] reported that after the addition of reducing agent in H_2PtCl_6 solution, size of the particles increases because the growth mechanism of the particles and their aggregation to clusters is turned into a predominantly electroless reaction. This means that electron can not transfer inside the composite and thus Pt does not adhere to the surface.
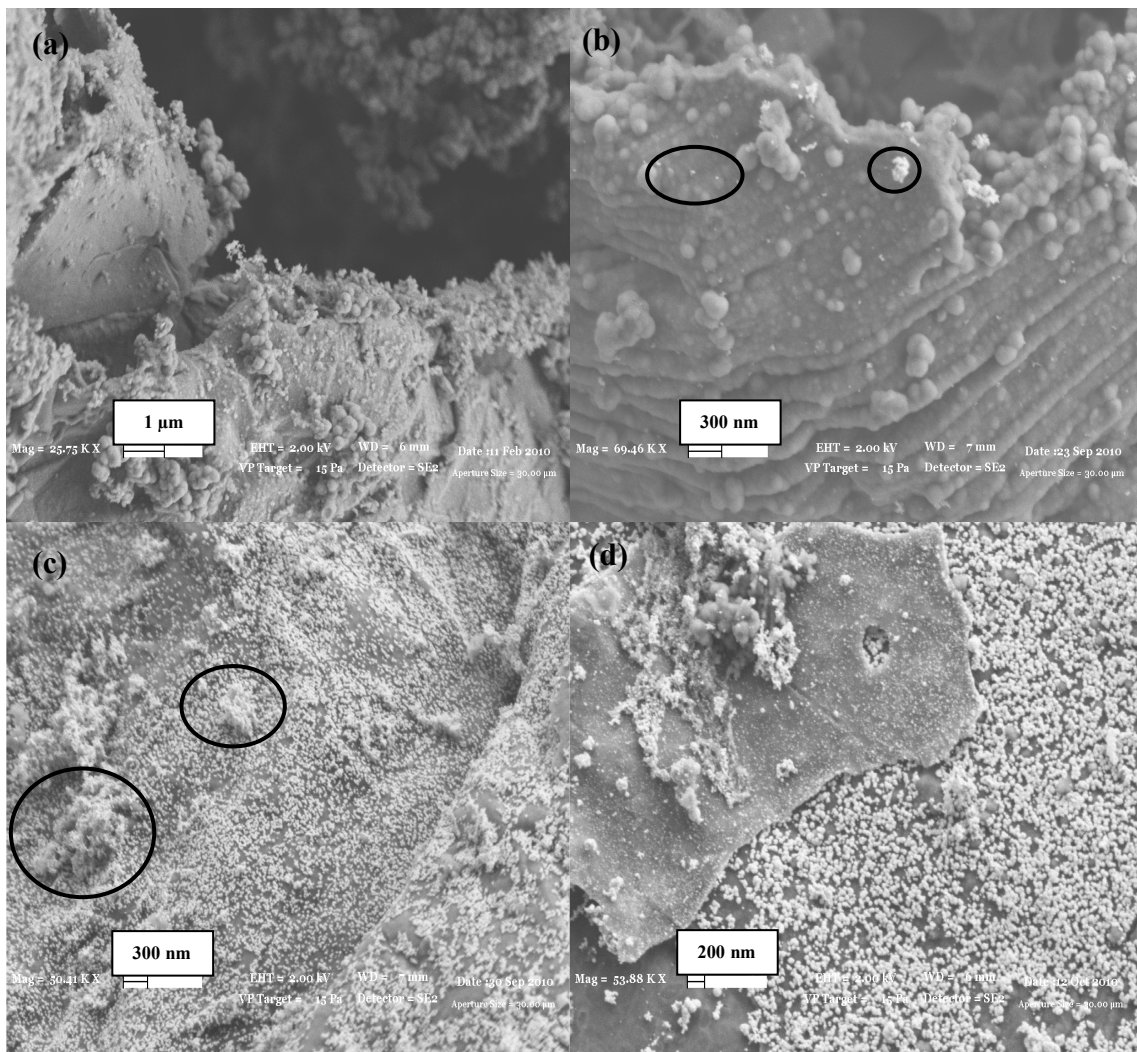
Figure 5.55. SEM images of **(a)** Py:GO=2:1, **(b)** Pt/Py:GO=2:1 according to 1st method, **(c)** Pt/Py:GO=2:1 sheets according to 2nd method, and **(d)** Pt/Py:GO=2:1 sheets according to 3rd method (Pt deposition methods were shown in Table 4.4).
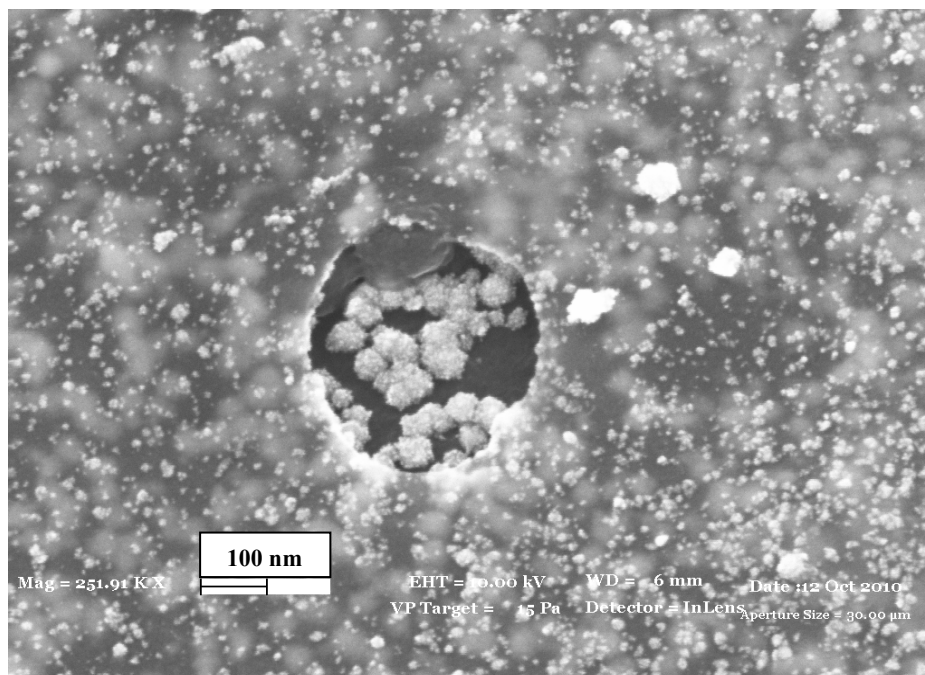
**Figure 5.56.** SEM image of Pt/Py:GO=2:1 sheets according to 3rd method at higher magnification via inlens detector.

The EDX analyses of Pt deposited Py:GO=2:1 composites were exhibited in Table 5.14. Py:GO=2:1 composite included 41.9% C, 21.8% N and 24.4% O. When Py content increased, nitrogen content increased in the structure and thus the electrons generated from the chemical reduction of H_2PtCl_6 solution could sink on the composite surface and highly dispersed Pt catalysts were observed. Also, shorter impregnation time in 3rd method provided high Pt dispersion. 17.9% Pt catalysts were deposited on Py:GO=2:1 composite.

Table 5.14.

EDX results of Py:GO=2:1, Pt/Py:GO=2:1 according to 1st, 2nd and 3rd methods

Samples	Carbon (wt%)	Nitrogen (wt%)	Oxygen (wt%)	Platinum (wt%)	Other elements (wt%)
Py:GO=2:1	41.9	21.8	24.4	-	11.9
Pt/Py:GO=2:1 (1st method)	41.5	19.7	23.8	4.7	10.3
Pt/Py:GO=2:1 (2nd method)	38.6	12.7	35.5	9.8	3.4
Pt/Py:GO=2:1 (3rd method)	35.3	15.0	26.8	17.9	5.0

The EDX analysis of Pt deposited on Py:GO=1:3 composites confirmed the presence of Pt catalyst as 6.3%. Pt/ Py:GO=1:3 composite contained 37.0% C, 41.1% O and 5.95% N. When GO sheet content increased in the composite, surface oxygen groups increased and thus high Pt dispersion was achieved. SEM images supported well-dispersed Pt catalysts, Figure 5.57. Size distribution of Pt particles on the surface of Pt/ Py:GO=3:1 sheets according to 3rd method changed from 9 nm to 16 nm. Also, Pt catalysts grew on their surfaces and the diameter of the grown catalysts was approximately 6 nm.
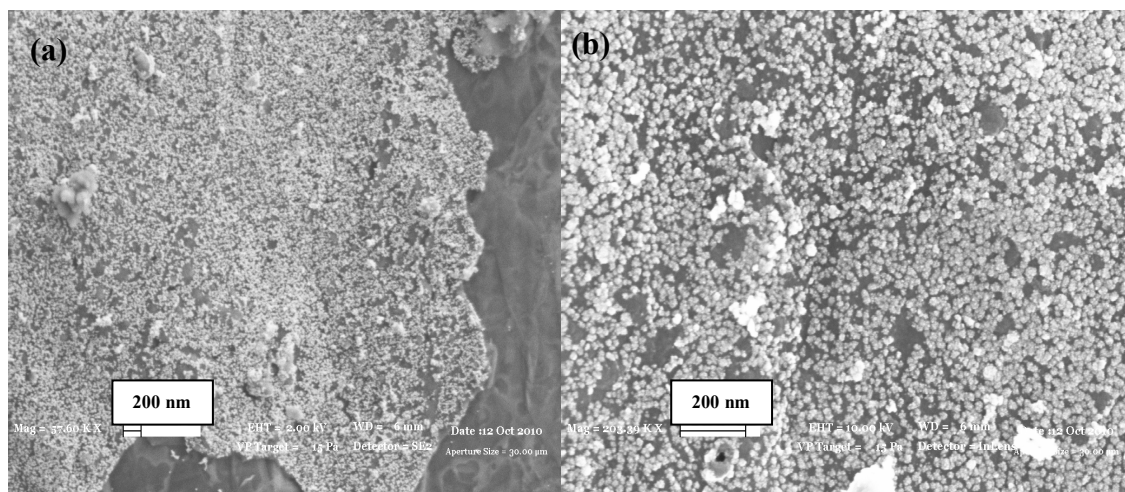
Figure 5.57. SEM images of Pt/Py:GO=1:3 according to 3rd method **(a)** via secondary electron detector **(b)** via inlens detector.

Consequently, SEM results showed that as PPy content increased in the composition of composite, catalyst-particle size range increased because the electronic properties of PPy caused to induce electronic conduction. With the help of sonication technique, the impregnation time was shortened to 2 hrs. Furthermore, as the amount of GO sheets increased in composite, smaller size catalyst particles could be dispersed on the surface due to the amount of oxygen surface groups. On the other hand, higher amount PPy maximized catalyst dispersion on the surface because the adhesion of Pt catalysts is considerably improved and thus catalytic activity is enhanced [148]. At this point, Py:GO=1:1 composite became a promising candidate material as catalyst support.

5.4.3. Structural Analysis of Pt Deposited Nanocomposites by Raman Spectroscopy

Structural changes of nanocomposites with different feed ratios were investigated by Raman spectroscopy. The characteristic features of graphite in Raman spectrum are the G band around 1580 cm^{-1}, the G' band (the overtone of the G band) around 3248 cm^{-1}, the D band around 1360 cm^{-1}, and the D' band (the overtone of the D band) around 2700 cm^{-1}. The intensity ratio of the D and G bands, I_D/I_G varies inversely with the size of the crystalline grains or interdefect distance [57]. The structural change and the thickness of PPy coverage could be examined by the I_D/I_G change. In Figure 5.58 (a), I_D/I_G decreased considerably after the polymerization of Py on GNS and this indicated the thickness of crystallite size increased [57]. Therefore, PPy coating provided a better metal dispersion on GNS-based composites as seen in SEM images, Figure 5.47.

In the Raman spectra of PPy/GO composites, Figure 5.58 (b), I_D/I_G values of GO sheets and Py:GO=1:3 were calculated as 0.28 and 0.19, respectively. This decrease in I_D/I_G values showed an increase of thickness after the coating on the surface of GO sheets by PPy. Moreover, I_D/I_G values of Py:GO=1:1 and Py:GO=2:1 were 0.50 and 0.47, respectively. This decrease revealed that when Py content increased in composite composition, the coverage of surface increased.

The effective surface area of these composites relies on the number of graphene sheets since few layer graphene sheets with less aggregated Pt clusters have higher surface area and thus better fuel cell performance [93]. As the number of graphene layers is smaller than five, the D' band becomes more intense than G peak [127]. The decrease in the intensity ratios of G and D' bands, $I_G/I_{D'}$, designated a decrease in layer number. $I_G/I_{D'}$ values of GO sheets, Py:GO=1:1, Py:GO=2:1 and Py:GO=1:3 were evaluated as 1.69, 0.96, 1.12 and 1.28, respectively (Figure 5.58 (b)). Especially, the layer number of GO sheets in Py:GO=1:1 composite was less than five. Even though the starting material, GO sheets, was the same in the produced composites, there was a difference in layer number because of the partial oxidation of graphite. These results supported an increase of Pt dispersion on the surface of PPy/GO composites when

comparing bare GO sheets. This also explained higher catalyst dispersion on the surface of Py:GO=1:1 without the aggregation of Pt catalysts due to few layer number in its composite.
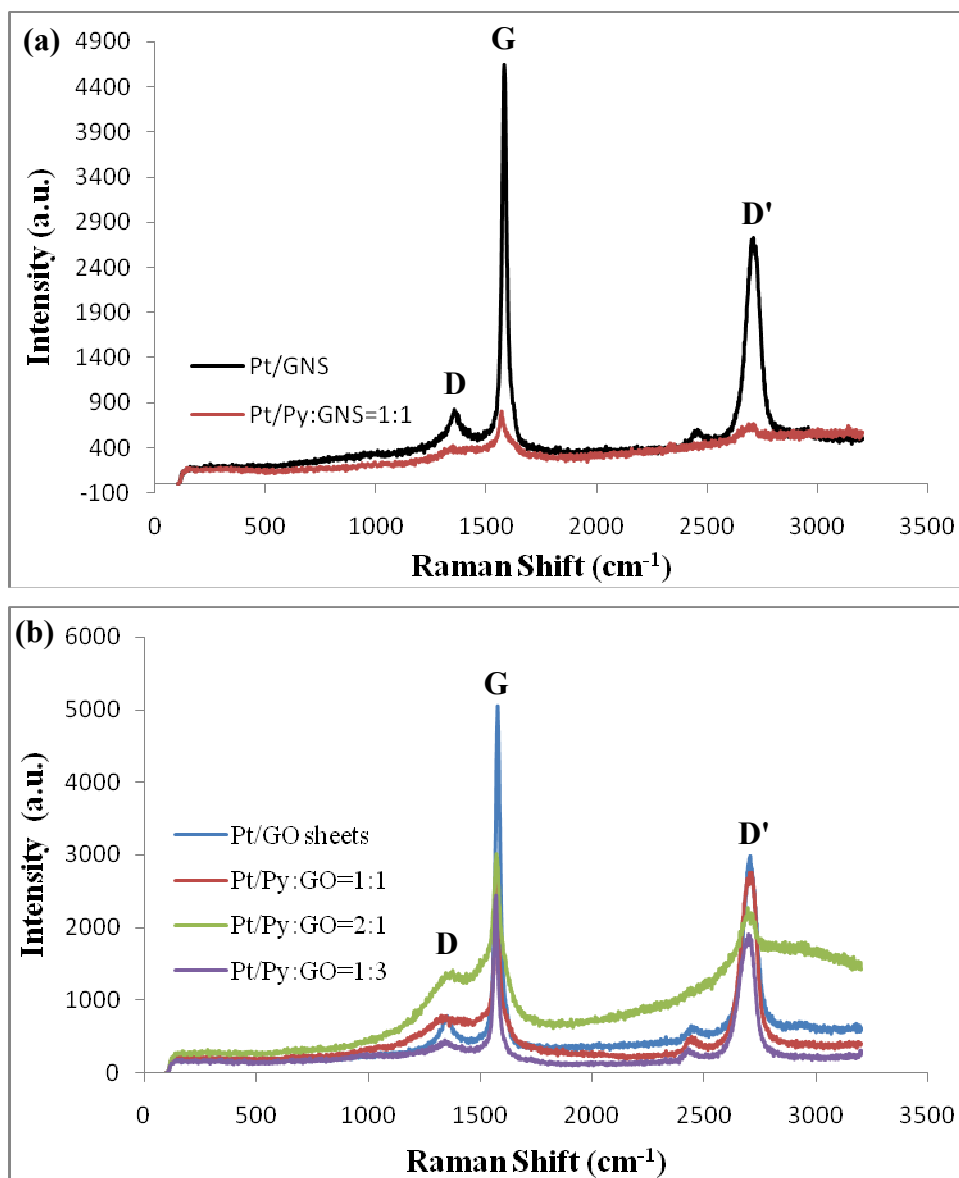
Figure 5.58. Raman spectra of **(a)** Pt/GNS and Pt/Py:GNS=1:1 obtained according 3rd method and **(b)** Pt/GO sheets, Pt/Py:GO=1:1, Pt/Py:GO=2:1 and Pt/Py:GO=1:3 obtained according to 3rd method.

5.5. Polypyrrole Coated Thermally Exfoliated GO Sheets and Pt Deposition on Expanded GO Composites

GO sheets was expanded by heating up to 1000ºC rapidly in a tube furnace and kept for 1 min at this temperature under an argon atmosphere. An increase of pressure due to CO_2 release during rapid heating leads to the separation of stacked GO sheets and the production of functionalized graphene sheets. While the C/O ratio of GO is 2, the functionalized graphene sheets separated by thermal expansion have a C/O ratio of 10-20 because some of the epoxide and hydroxyl sites are removed [2].

5.5.1. SEM and EDX Characterization

Intercalated graphite with sulfuric acid, potassium dichromate and acetic anhydride heated to yield an increase of c-axis direction and form an accordion or "worm-like" structure. The volume of expanded graphite can increase with the enhancement of ultrasonic vibration [149]. Therefore, expanded GO samples were exposed to ultrasonic treatment before polymerization. During ultrasonic vibration, Py as the monomer was also added into the solution including expanded GO in order to increase the diffusion of Py monomer through layers. SEM image of expanded GO exhibited that these layers were crumbled due to the thermal expansion as depicted in Figure 5.59 (a). Then, Pt nanoparticles were successfully deposited on the surface of expanded GO and the size distribution of Pt particles were in the range of 10 nm and 20 nm, Figure 5.59 (b). EDX results showed that expanded GO included 87.6% C and 3.5% O in its structure, Table 5.15. The higher C content indicated that most of oxygen functional groups were eliminated from GO surface during thermal shock. After Pt deposition, 1.2% Pt was deposited on the surface of GO samples, Table 5.16.
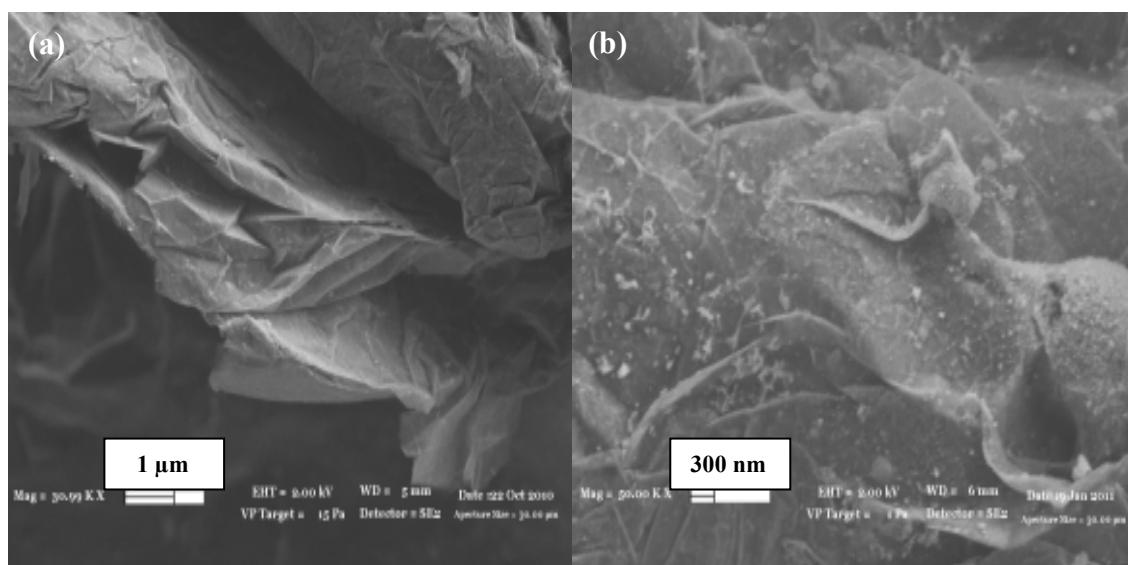
Figure 5.59. SEM images of **(a)** expanded GO and **(b)** Pt deposited expanded GO.

PPy was coated on the surface of expanded GO by *in situ* chemical oxidative polymerization of Py. Polymer coating and irregular sphere-like PPy formation observed clearly in SEM image, Figure 5.60 (a). Pt dispersion on the laminated structure of expanded GO sheets was not seen clearly in the SEM image of Py:Expanded GO=1:1 composite, Figure 5.60 (b). EDX results of Py:Expanded GO=1:1 composite were shown in Table 5.15. PPy/Expanded GO composites consisted of 54.6% C, 23.0% N, and 15.4% O. Nitrogen content proved the PPy polymerization. After the Pt deposition, the Pt content on the composite surface was much lower as about 0.7%, Table 5.16. During the thermal shock of GO sheets, most of the functional groups degraded and small amounts of functional groups in the structure of expanded GO combined with PPy, and some PPy chains agglomerated with each other as seen in Figure 5.60 (a). Therefore, some parts of PPy/expanded GO composites do not provide the electronic conduction pathway which is required to sink the electrons generated from the chemical reduction of H_2PtCl_6 solution, and thus Pt dispersion decreases [147].
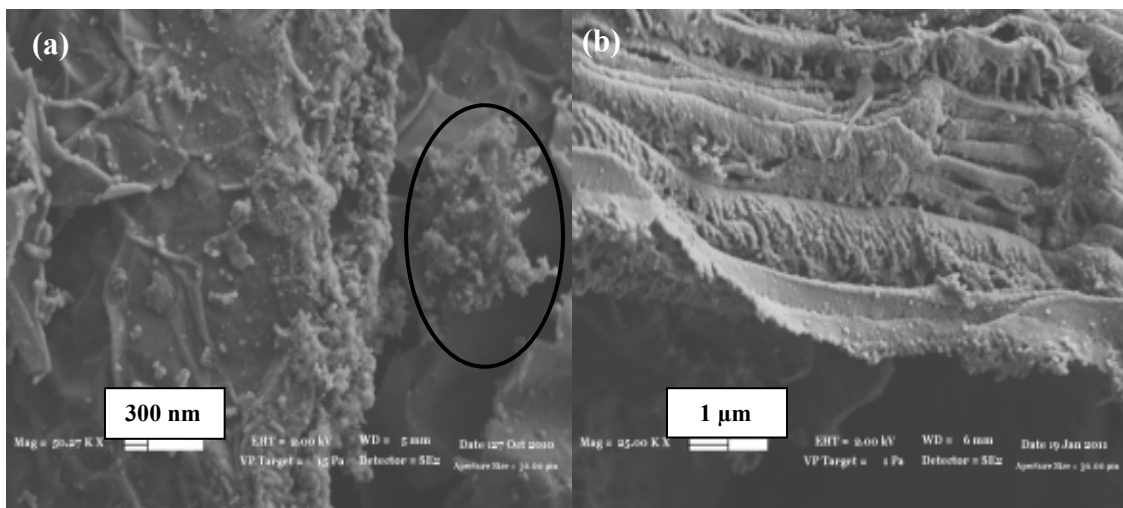
Figure 5.60. SEM images of **(a)** Py:Expanded GO=1:1 and **(b)** Pt deposited Py:Expanded GO=1:1.

The amount of PPy in the composites increased in order to observe the polymer thickness and the Pt dispersion. PPy coated GO layers were seen in SEM image of Py:Expanded GO=1:2 composite, Figure 5.61 (a). In Figure 5.61 (b), Pt particles did not adhere to the surface. This stemmed from the agglomeration of some PPy particles instead of layer coating, and thus the reduction of the Pt precursor was hindered [146]. EDX results showed that Py:Expanded GO=1:2 composite contained 53.7% C, 18.0% N and 16.6% O, Table 5.15. As the Py content increased in the composite, the amount of anchored Pt on the surface decreased. The EDX analysis of Pt deposited Py:Expanded GO=1:2 composite included 0.3% Pt, Table 5.16.
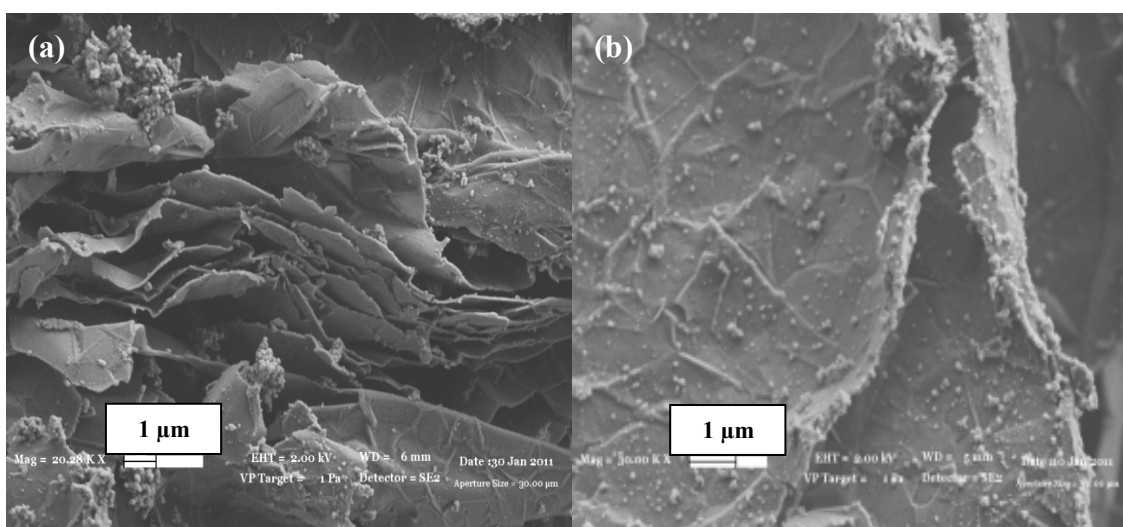
Figure 5.61. SEM images of **(a)** Py:Expanded GO=1:2 and **(b)** Pt deposited Py:Expanded GO=1:2.

Table 5.15 and Table 5.16 showed the EDX analyses of all composites at different feeding ratios of expanded GO and Py before and after Pt deposition. The amount of oxygen surface groups plays an important role in the carbon-Pt interaction [143]. Oxygen groups make the carbon surface more hydrophilic, and thus maximum catalyst dispersion is achieved [143]. On the other hand, thermal treatment leads to an increase in the basicity of the carbon and eliminate oxygen functional groups. The basicity of the carbon surface can be estimated by the number of the π sites of the carbon basal plane acting as anchoring centers for Pt catalysts [84]. Loen *et al.* [150] demonstrated the interaction of oxygen-free basic carbon sites leads to an electron-donor-acceptor complex described in the following equations (1) and (2):

$$C\pi + H_3O^+ \leftrightarrow \left[C\pi - H_3O\right]^+ \qquad (1)$$
$$C\pi + 2H_2O \leftrightarrow \left[C\pi - H_3O\right]^+ + OH^- \qquad (2)$$
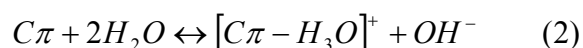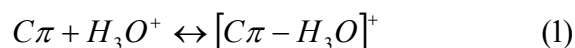
Therefore, the metal-support interaction depends on the amount of surface oxygen functional groups and the strength of the π sites on carbon support. However, in PPy/expanded GO composites, the relationship between Pt catalyst and the oxygen amount was not observed due to non-uniform layer coating and the random destruction of graphene layers after thermal treatment, Table 5.15. On the other hand, there was a correlation between PPy amount and Pt dispersion. As the amount of PPy increased in the composite, Pt dispersion minimized, Table 5.16. Pt deposited Expanded GO:Py=1:4 contained 0.2% Pt whereas Pt deposited expanded GO:Py=2:1 consisted of 1.0% Pt.

Table 5.15.

EDX results of expanded GO and PPy/expanded GO composites at different feed ratios of expanded GO and Py

Samples	Carbon (wt%)	Nitrogen (wt%)	Oxygen (wt%)	Other elements (wt%)
Expanded GO	88.9	-	4.9	6.2
Expanded GO:Py=1:1	54.6	23.0	15.4	7.0
Expanded GO:Py=1:2	53.7	18.0	16.6	11.7
Expanded GO:Py=2:1	56.2	14.1	20.4	9.3
Expanded GO:Py=3:1	63.6	7.8	24.3	4.3
Expanded GO:Py=1:4	47.7	17.5	13.4	21.4

Table 5.16.

EDX results of Pt deposited expanded GO and PPy/expanded GO composites at different feed ratios of expanded GO and Py

Samples	Carbon (wt%)	Nitrogen (wt%)	Oxygen (wt%)	Platinum (wt%)	Other elements (wt%)
Pt/Expanded GO	82.6	-	10.3	1.2	5.6
Pt/Expanded GO:Py=1:1	46.1	22.8	28.0	0.7	2.4
Pt/Expanded GO:Py=1:2	54.7	17.6	25.7	0.3	1.7
Pt/Expanded GO:Py=2:1	57.5	12.5	23.0	1.0	6.0
Pt/Expanded GO:Py=3:1	70.5	10.3	14.7	0.5	4.0
Pt/Expanded GO:Py=1:4	23.1	9.6	44.2	0.2	22.9

5.5.2. XRD Characterization

PPy had an amorphous structure, Figure 5.36. Due to the thermal treatment, the crystal structure of expanded GO had a broad and intense 001 peak near $2\theta=13^{o}$ and a sharp and lower intense 002 peak near $2\theta=26^{o}$ in the XRD pattern, Figure 5.62.

As the content of PPy increased in composite, 002 peak intensity decreased, and as the amount of expanded GO increased in composite, the intensity of 002 peak became more intense, Figure 5.63 and Figure 5.64. The maximum intensity of 002 peak of expanded GO:Py=3:1 was about 453 a.u. at 2θ=26.5. This indicated that the structure of composite became more crystalline by increasing the amount of expanded GO. In addition, ultrasonic treatment before the polymerization provided easy diffusion of Py monomers through layers and after the polymerization, all layers were stacked and formed crystalline structure. For instance, the intensity of 002 peak of expanded GO was about 98 a.u., Figure 5.62. On the other hand, the coverage of expanded GO by PPy in the feeding mass ratio of expanded GO and Py as 3:1 led to an increase in 002 peak intensity and provided well-ordered structure, Figure 5.63.
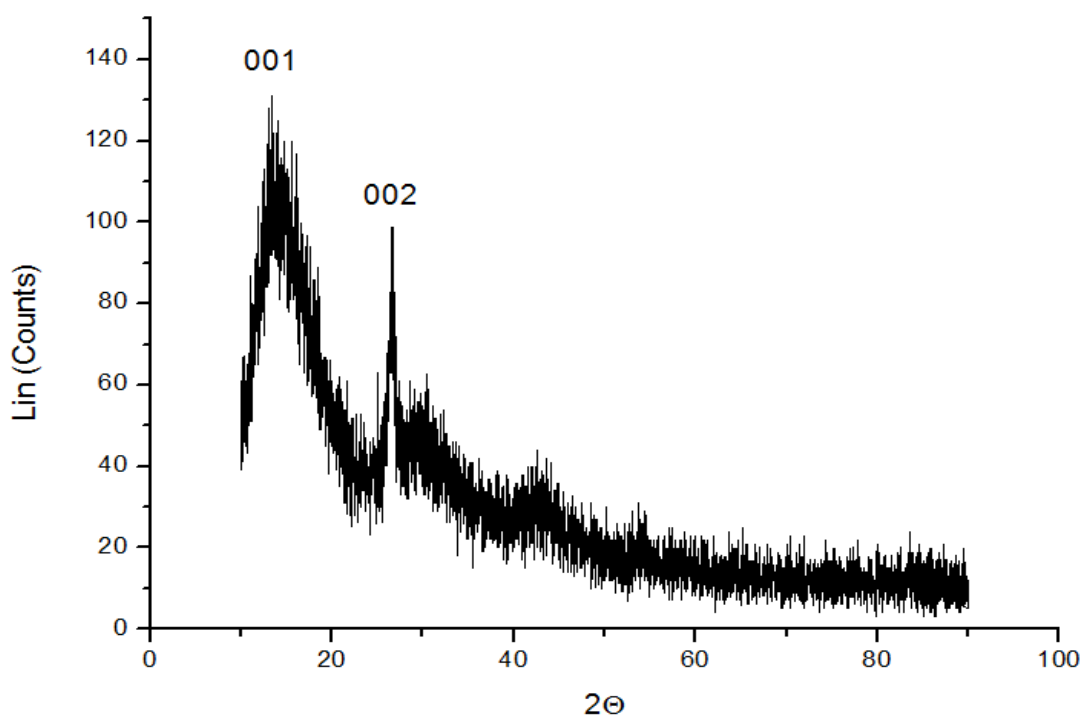
Figure 5.62. XRD pattern of expanded GO obtained after 10 days of oxidation.
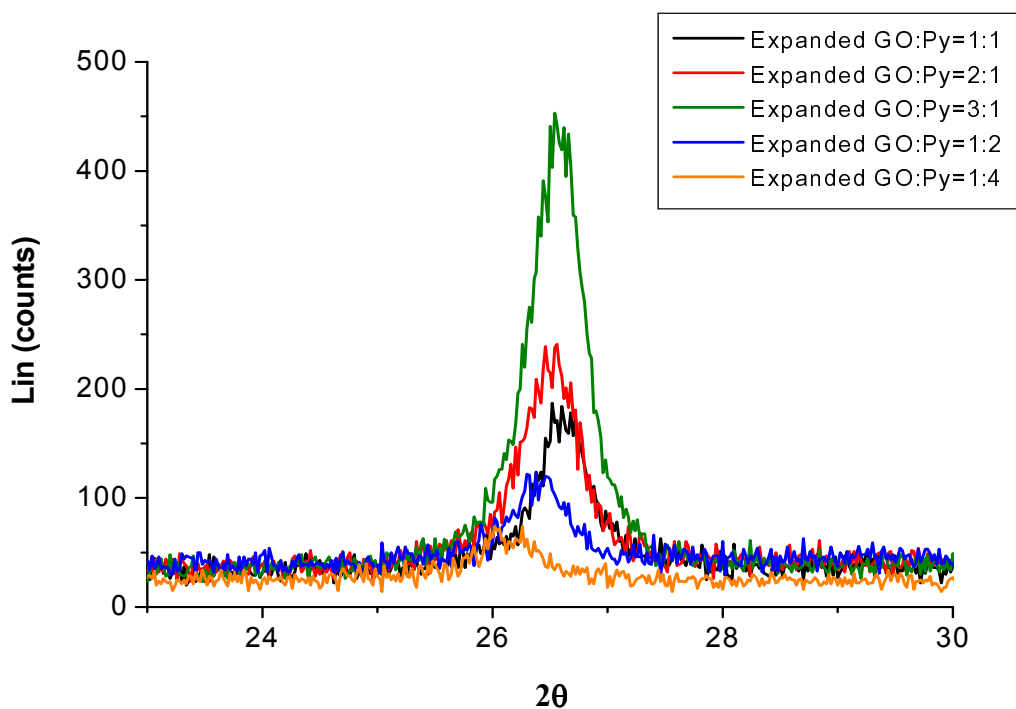
Figure 5.63. XRD patterns of PPy/expanded GO composites at different feed ratios of expanded GO and Py.
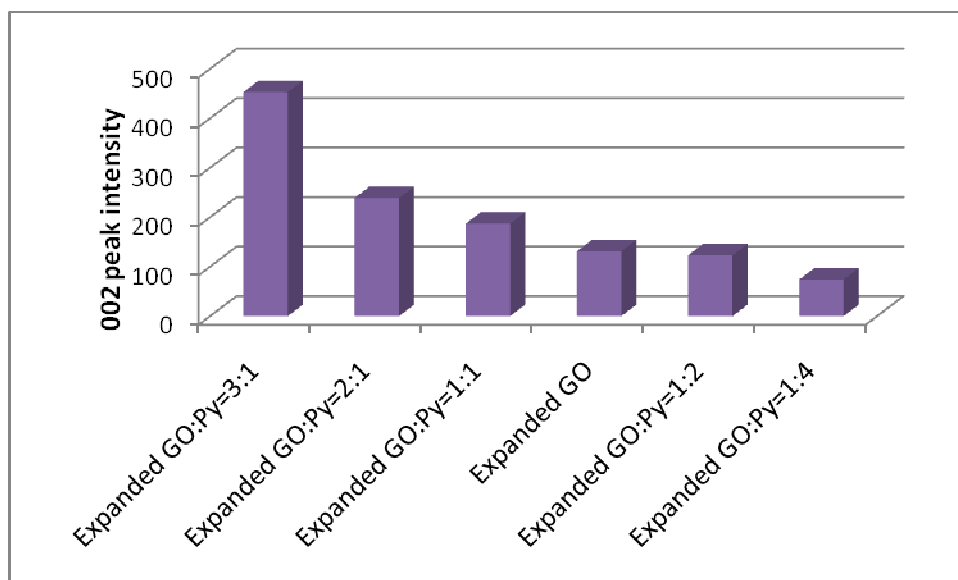
Figure 5.64. The change of 002 peak intensity as a function of the feeding mass ratios of expanded GO and Py.

5.5.3. Raman Spectroscopy Characterization

Raman spectroscopy is one of the sensitive techniques for the characterization of crystalline perfection. There are three prominent peaks at about 1404 cm^{-1}, 1582 cm^{-1}, and 2729 cm^{-1} which correspond to the D, G and D' bands of graphene, Figure 5.65.

The structural change of expanded GO-based composites could be investigated by the intensity ratio of the D and G bands, I_D/I_G. This ratio inversely changed with the size of the crystalline grains or interdefect distance [57]. As the amount of Py content increased, the I_D/I_G ratio increased due to the relative increase of defects (chemical and structural changes, the agglomeration of PPy chains). Raman spectra of expanded GO/PPy composites as a function of increasing Py amount depicted in Figure 5.66. As shown in Table 5.17, I_D/I_G ratios of expanded GO:Py=1:1, expanded GO:Py=1:2 and expanded GO:Py=1:4 were estimated as 0.37, 0.51 and 0.52, respectively. D' band can be used to determine the number of graphene layers and D' band became more dominant than G band if the number of graphene layers were smaller than 5 [127]. This proved that when the I_D/I_G ratio of the composites increased, the coverage of expanded GO layers by PPy increased. However, in contrast to layer-by-layer coated GO and GNS nanocomposites, non-uniform polymer dispersion on the surface of expanded GO occurred due to the lack of most of the oxygen functionalities. I_D/I_G ratios of expanded GO:Py=1:1, expanded GO:Py=2:1 and expanded GO:Py=3:1 were also estimated as 0.37, 0.35 and 0.31, respectively. As the amount of expanded GO in the composite increased, the I_D/I_G ratio decreased due to the decrease in polymer coating and thus the decrease in thickness. Also, Raman spectra of expanded GO/PPy composites as a function of increasing expanded GO amount exhibited in Figure 5.67.
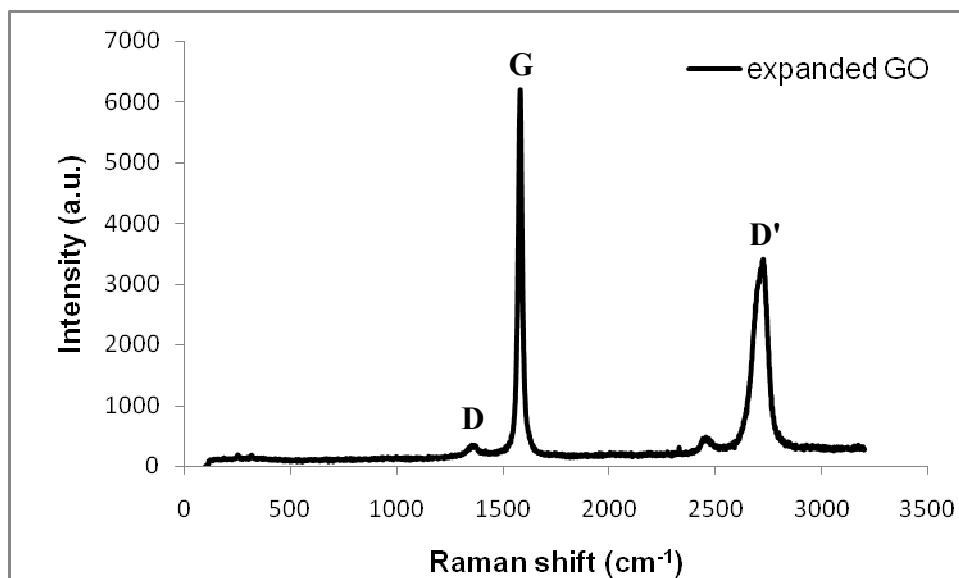
Figure 5.65. Raman spectrum of expanded GO after 10 days of oxidation.
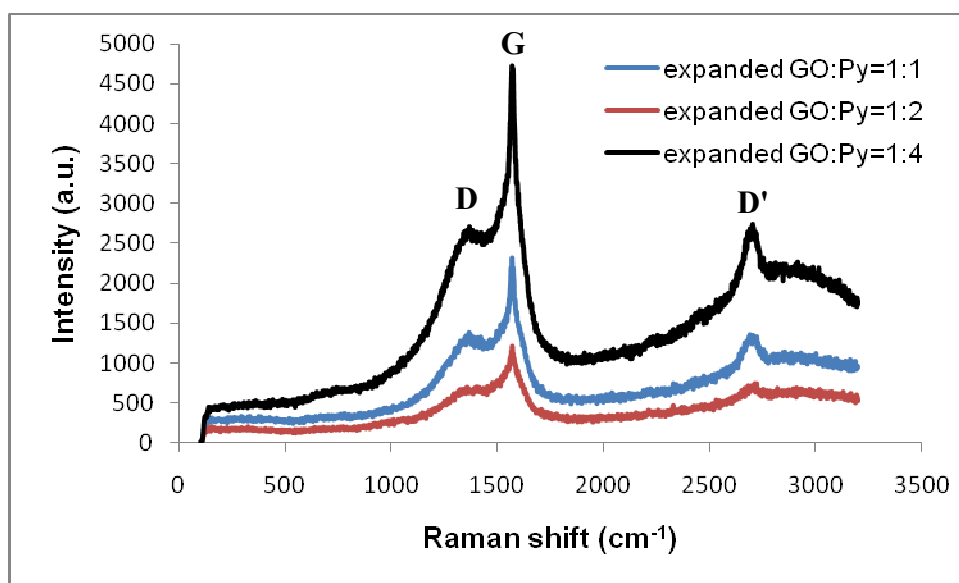
Figure 5.66. Raman spectra of expanded GO/PPy composites as a function of increasing Py amount.
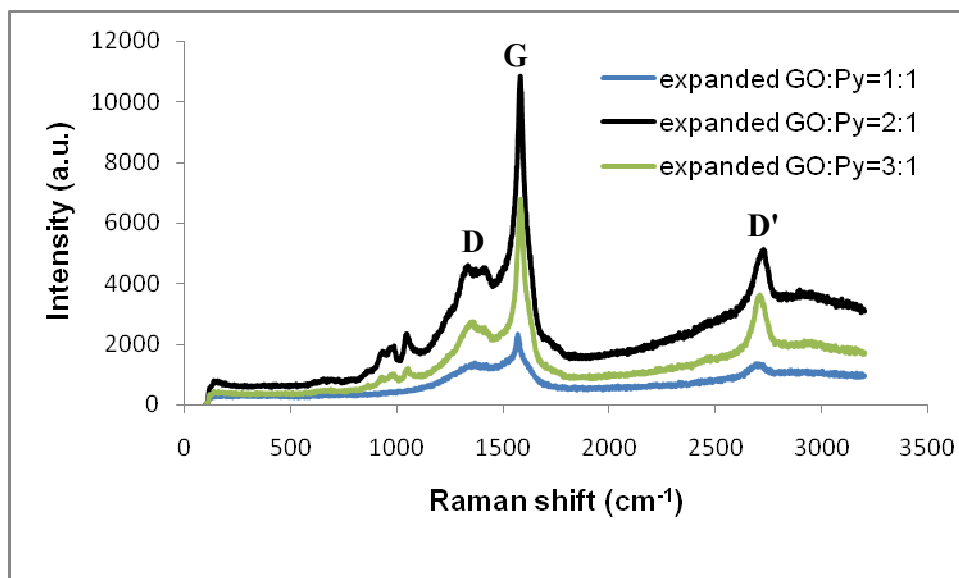
Figure 5.67. Raman spectra of expanded GO/PPy composites as a function of increasing expanded GO amount.

Table 5.17.

Relative raman intensities of the peaks as a function of I_D/I_G and $I_G/I_{D'}$

Intensity Ratio	I_D/I_G	$I_G/I_{D'}$
Expanded GO	0.03	1.86
Expanded GO:Py=1:1	0.37	2.96
Expanded GO:Py=1:2	0.51	1.78
Expanded GO:Py=1:4	0.52	1.72
Expanded GO:Py=2:1	0.35	2.36
Expanded GO:Py=3:1	0.31	1.95

5.5.4. Electrical Conductivity Measurements

Expanded GO can provide percolated pathways for electron transfer, making the composites electrically conductive [151]. The electrical conductivity of samples in the pellet form was measured by the conventional four-probe method. The electrical conductivity results of samples (pristine PPy, expanded GO, and expanded GO/PPy composites) were given in Table 5.18. Pristine PPy has relatively poor conductivity

because of weak compactness and randomly orientation of PPy nanostructures and weak bonding between the polymer particles through the boundaries [137]. The conductivity of expanded GO was measured as 0.75 S/cm. After the addition of expanded GO into polymer matrice in adjusted feeding ratios, the conductivity of composites were enhanced. The conductivity of composite synthesized with the feeding mass ratios of expanded GO and Py as 3:1 was measured as 4 S/cm. Therefore, the composites exhibited a comparably higher electrical conductivity than pure PPy because the layered and network structure of expanded GO formed large fractions of electron conducting paths in the composite. However, as the amount of PPy in composite increased, the conductivity values decreased.

Table 5.18.

Four-probe electrical conductivity results of expanded GO and its composites

Samples	Conductivity (S/cm)
Pristine PPy	7.6×10^{-4}
Expanded GO	0.75
Expanded GO:Py=1:1	0.15
Expanded GO:Py=1:2	0.04
Expanded GO:Py=2:1	1.00
Expanded GO:Py=3:1	4.00

5.5.5. The Effect of Oxygen Surface Groups on Pt Deposition

FTIR, XPS and EDX analyses were used in order to estimate the amount of surface oxygen functional groups in samples and investigate the effect of surface oxygen groups and thermal treatment on the Pt dispersion.

The characteristic peaks in the FTIR spectrum of GO sheets were two sharp C-H stretching bands at 2850 cm^{-1} and 2916 cm^{-1} and a sharp CH$_2$ bending band near 1480 cm^{-1}, Figure 5.68. Also, there were a broad band at around 1100 cm^{-1} due to the aromatic C-O stretching and two small peaks due to the C=O stretching. Expanded GO

had high carbon content as seen in Figure 5.68. This indicated that thermal expansion eliminated oxygen functional groups. After the chemical reduction of GO, the intensity of C=O stretching peaks at $1500\,cm^{-1}$ decreased comparably, Figure 5.68.
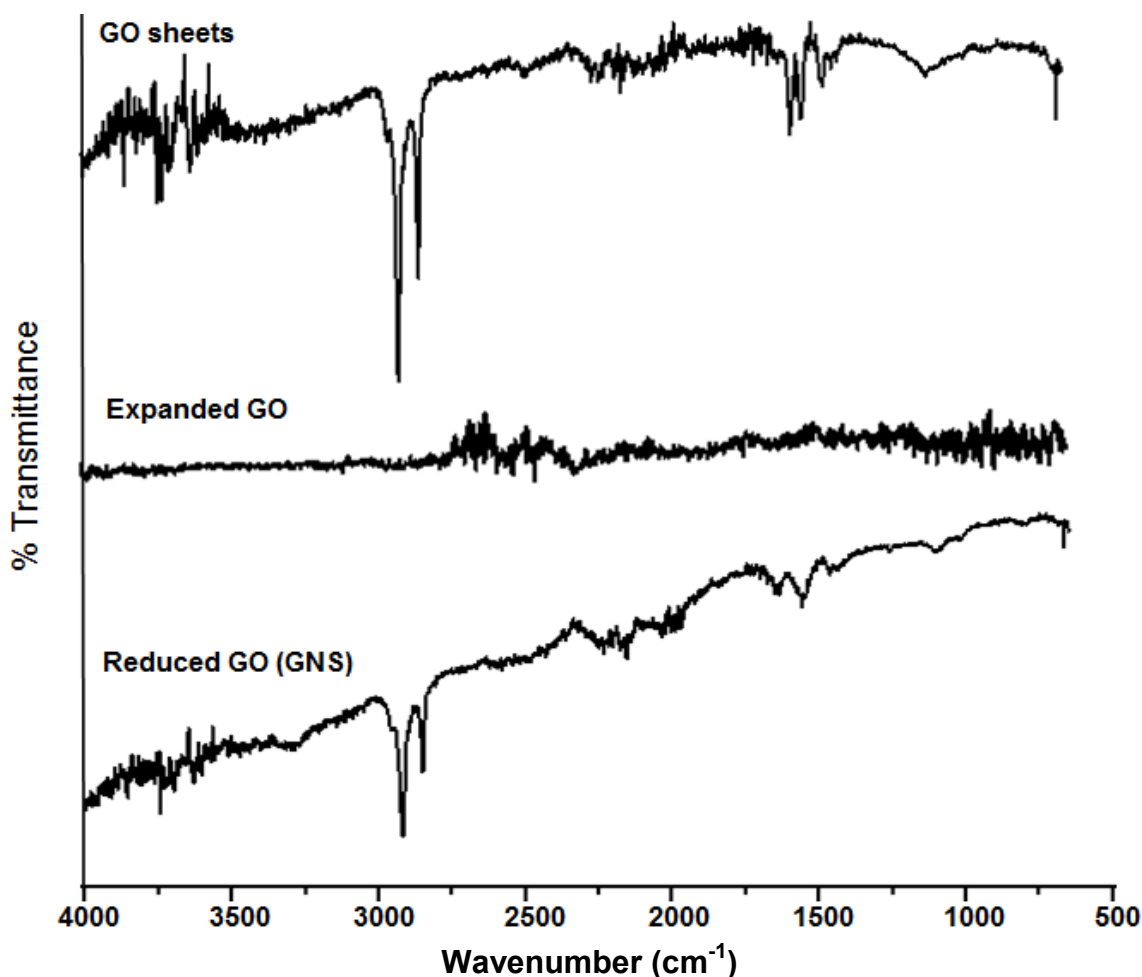
Figure 5.68. FT-IR spectra of GO sheets, expanded GO and reduced GO (GNS).

XPS is a quantitative surface analysis technique that evaluates the elemental composition, empirical formula, chemical state and electronic state of the elements. For the identification of oxygen-containing functional groups, the C1s, O1s and N1s signals were measured and groups were assigned based on the differences in their binding energy of carbon atoms [152].

The atomic ratios and surface functional groups of GO sheets, expanded GO, GNS, and their composites were determined by using the XPS elemental analysis. The intensities of O1s and C1s peaks for GO, expanded GO and GNS were compared in the XPS survey scan spectra, Figure 5.69. The C/O ratios of GO, expanded GO and GNS were measured as 2.3, 6.0, and 3.2, respectively. These results indicated that thermal expansion led to the removal of oxygen functional groups on the surface and thus carbon content increased in the structure of expanded GO.

The deconvolution of the XPS C1s peaks of GO sheets was shown in Figure 5.70 (a). The C1s envelope contained two peaks at 284.3 and 285.2 eV which assigned to the nonoxygenated ring C and the C in C-O [153]. The O1s XPS spectrum of the GO sheets included two deconvoluted peaks at 531.7 and 533.1 eV which attributed to C=O and HO-C=O groups, respectively, Figure 5.70 (b) [152]. Although the C1s XPS spectrum of expanded GO had the same oxygen functional groups like GO sheets, Figure 5.71 (a), its C-C peak intensity was much higher than that in the C1s XPS spectrum of GO. This proved the removal of oxygen functional groups from the surface during thermal treatment. In addition, the O1s peak intensity of expanded GO in Figure 5.71 (b) was quite lower than that of GO sheets. The C1s XPS spectrum of the GNS also displayed the same carbon-oxygen containing functional groups, Figure 5.72 (a), and their peak intensities were much smaller than those in GO. Furthermore, the deconvoluted O1s XPS spectrum of GNS exhibited that C-O peak near 532.4 eV was observed, Figure 5.72 (b), and the O1s peak intensity was considerably lower than that in GO spectrum. Also, C=O bonds in the structure of GO sheets were converted to C-O bonds due to the chemical reduction of GO sheets by hydroquinone. In this reaction, hydroquinone loses either one H^+ ion from one of its hydroxyls to form a monophenolate ion or two H^+ ions from both hydroxyls to form a diphenolate ion and thus GO sheets gain H^+ ions [122].
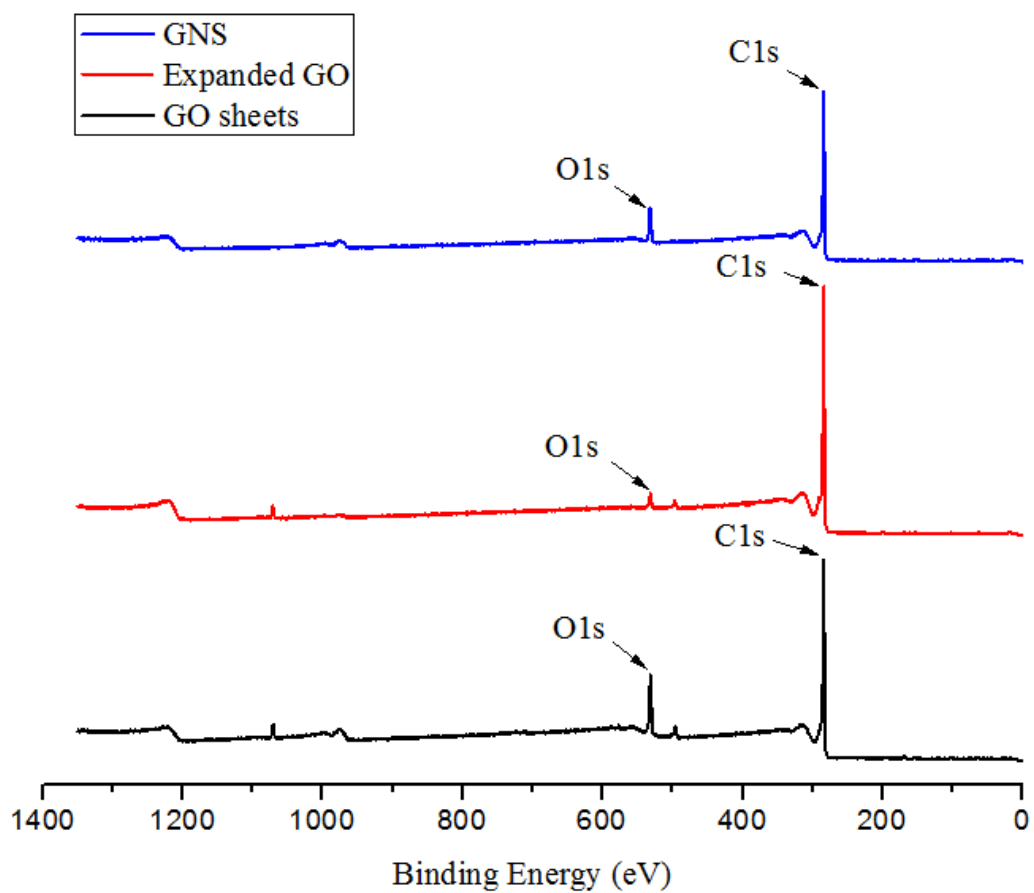
Figure 5.69. XPS survey scan spectra of GO sheets, expanded GO and GNS.
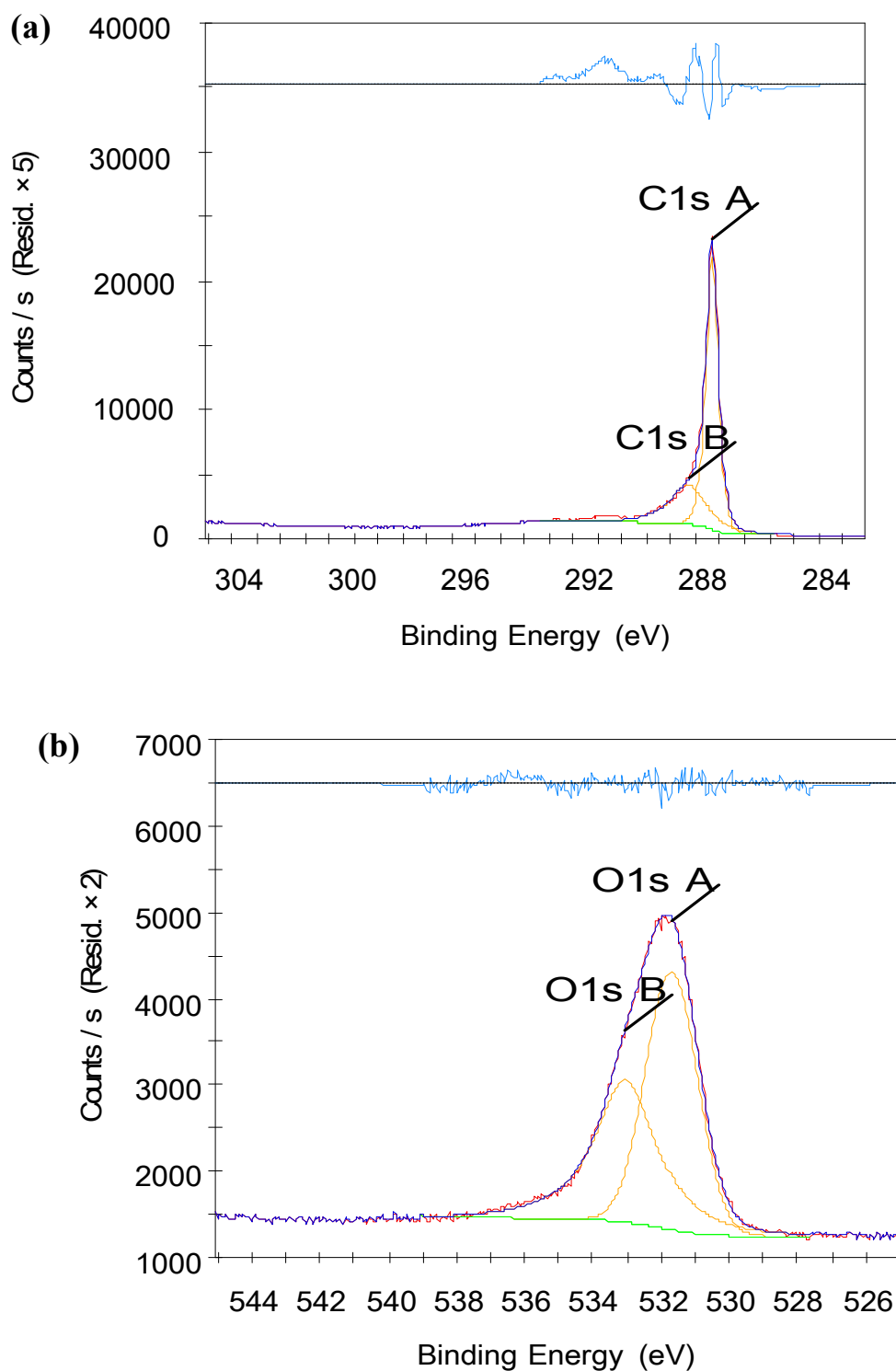
Figure 5.70. Deconvoluted XPS **(a)** C1s spectrum(C1s A= C-C, C1s B=C-O) and **(b)** O1s spectrum (O1s A: C=O, O1s B: HO-C=O) of GO sheets.
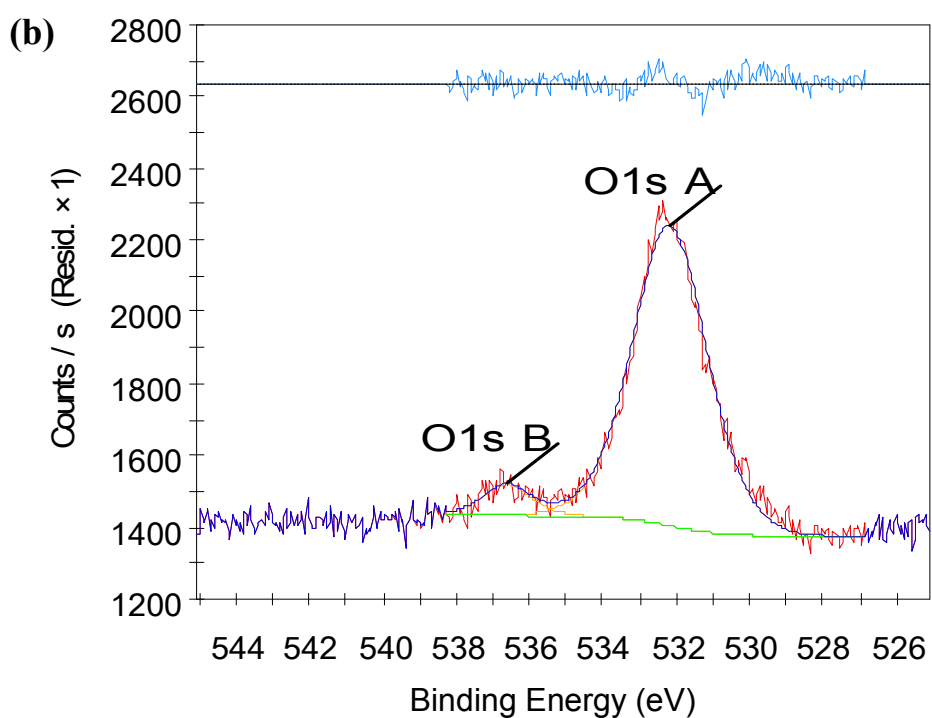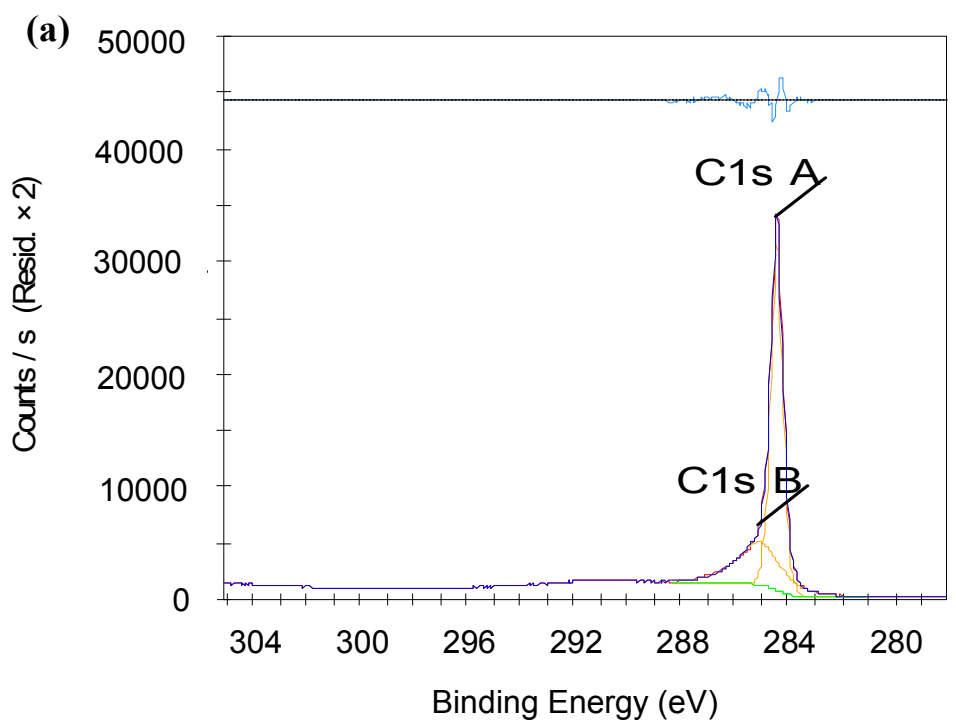
Figure 5.71. Deconvoluted XPS **(a)** C1s spectrum (C1s A= C-C, C1s B=C-O) and **(b)** O1s spectrum (O1s A: C=O, O1s B: -OH) of expanded GO.
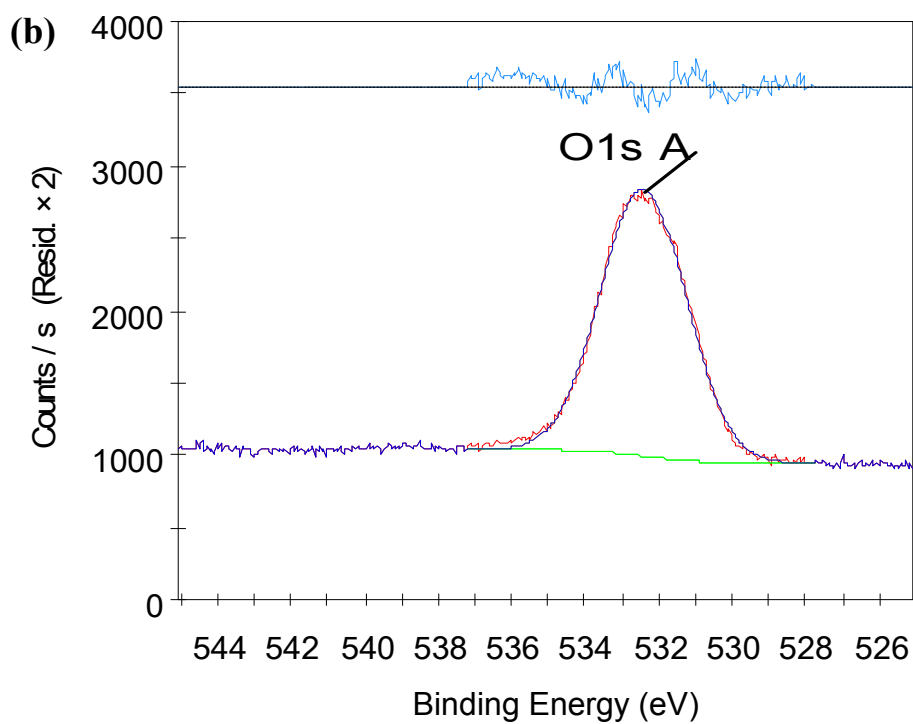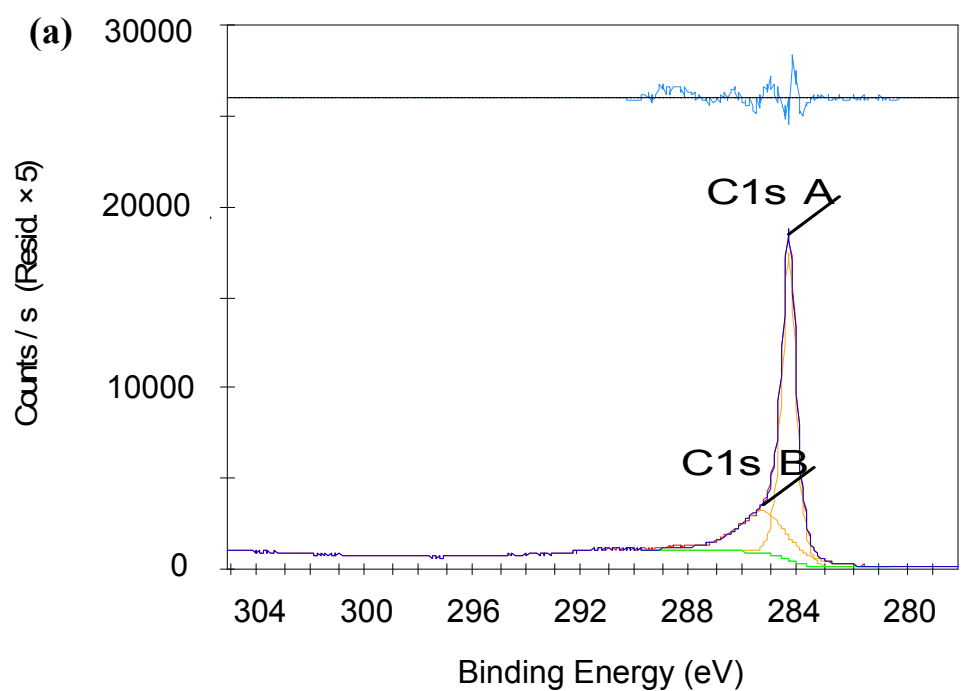
Figure 5.72. Deconvoluted XPS **(a)** C1s spectrum (C1s A= C-C, C1s B=C-O and C-OH) and **(b)** O1s spectrum (O1s A: C-O) of GNS.

Table 5.19 summarized functional groups, binding energies, FWHM values and atomic percentages which were estimated from the C1s and O1s XPS spectra of GO sheets, expanded GO and GNS. The FWHM of the peak assigned to C–O in the XPS O1s spectrum of GNS with a value of 2.7 appeared quite larger than all other carbon-oxygen containing bonds. Herein, the large FWHM and the broad tail towards higher binding energy stated that different types of carbon-oxygen containing bonds were overlapped each other [154].

Table 5.19.

XPS spectra results for C1s and O1s in the samples of GO sheets, expanded GO and GNS

Samples	*C1s*				*O1s*			
	Group	**Binding Energy (eV)**	**FWHM**	**At. (%)**	**Group**	**Binding Energy (eV)**	**FWHM**	**At. (%)**
GO sheets	C-C	284.3	0.6	56.0	C=O	531.7	1.8	9.4
	C-O	285.2	1.7	27.3	HO-C=O	533.1	2.2	7.3
Expanded GO	C-C	284.4	0.5	64.9	C=O	532.2	2.4	3.3
	C-O	285.1	1.9	31.6	-OH	536.6	1.6	0.2
GNS	C-C	284.3	0.6	59.2	C-O	532.4	2.7	11.0
	C-O, C-OH	285.3	2.1	29.8				

The XPS peaks of C1s, O1s and N1s for Py:GO=1:1, Py:Expanded GO=1:1 and Py:GNS=1:1 composites were shown in the the XPS survey scan spectra, Figure 5.73. The C/O ratios of Py:GO=1:1, Py:Expanded GO=1:1 and Py:GNS=1:1 were 1.4, 1.6, and 1.2, respectively. Py:Expanded GO=1:1 composite with the highest C/O ratio had less hydrophilic carbon surface and this decreased the interaction of the catalyst particles with the support [155].
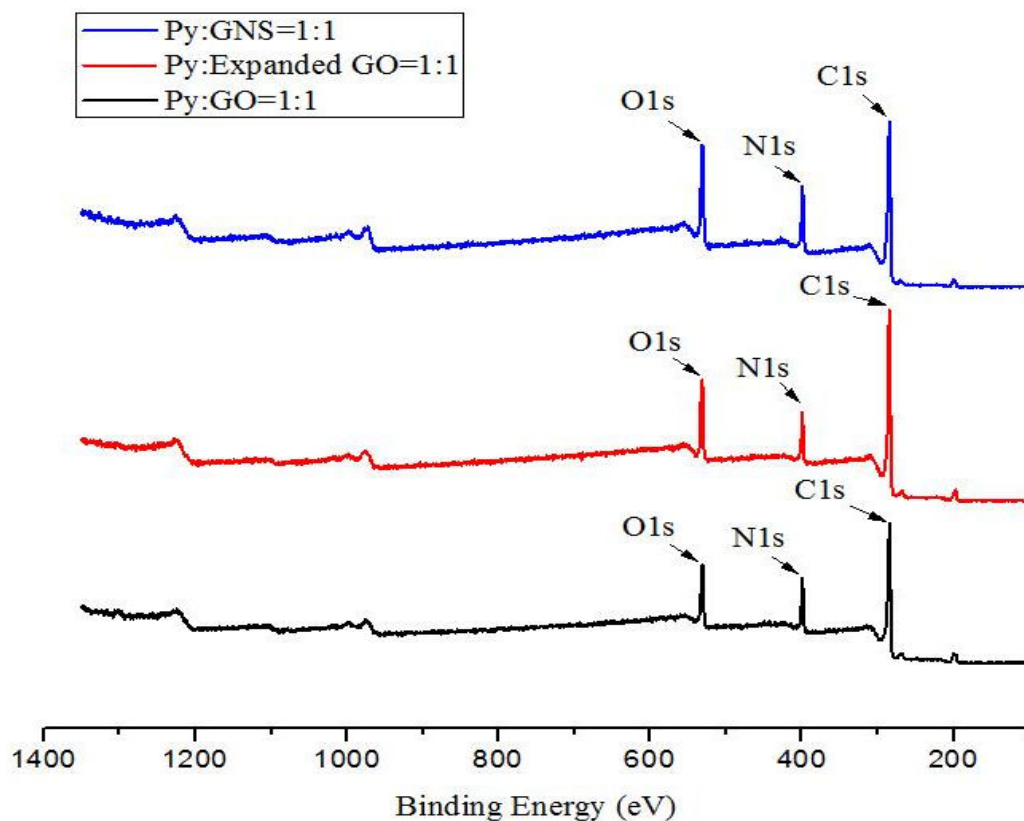
Figure 5.73. XPS survey scan spectra of composites: Py:GO=1:1, Py:Expanded GO=1:1 and Py:GNS=1:1.

The deconvoluted C1s spectrum of Py:GO=1:1 nanocomposite in Figure 5.74 (a) had two main peaks near 284.8 eV and 287.3 eV which assigned to the nonoxygenated ring C and the overlapped C=O and C-N peaks, respectively [156]. In Figure 5.74 (b), the XPS O1s peaks at 531.2 eV and 532.7 eV belonged to C-O and C=O bonds, respectively. Also, the N1s spectrum of Py:GO=1:1 nanocomposite supported a considerable PPy coating, Figure 5.74 (c). The peak around 399.9 eV were assigned to the overlap of the N–H and C–N components [157].

The C1s chemical shifts of Py:Expanded GO=1:1 composite at 284.7 eV, 286.2 eV and 288.4 eV in Figure 5.75 (a) were attributed to C-C, C-O-C, and the overlap of C=O, C=N, and N=C-O bonds, respectively. The higher amount of carbon groups in the structure of Py:expanded GO=1:1 composite was also supported by its deconvoluted C1s peaks. Moreover, the XPS O1s spectrum of Py:Expanded GO =1:1 composite shown in Figure 5.75 (b) had two main peaks at 531.6 eV and 533.1 eV which were assigned to the overlapped C-O and C=O bonds, and OH-C=O bond, respectively. The

144

XPS N1s peak near 399.9 eV corresponded to the overlapping peaks of N–H and C–N bonds, Figure 5.75 (c), [157].

The deconvoluted XPS C1s spectrum of Py:GNS=1:1 was exhibited in 5.76 (a). Although Py:GNS=1:1 nanocomposite included the same carbon-containing functional groups as Py:GO=1:1 nanocomposite, the intensity of C1s peak was higher than that in Py:GO=1:1 composite because chemical reduction decreased the amount of oxygen groups in the structure. Also, the deconvoluted O1s peaks at 530.9 eV and 532.3 eV were assigned to C-O and C=O bonds, respectively, (Figure 5.76 (b)). This indicated that most of C=O bonds in the structure of GO were converted to C-O bonds using hydroquinone as a reducing agent. The XPS N1s spectrum of Py:GNS=1:1 contained the overlapping peaks of N-H and C-N components due to the PPy coating on the surface of GNS, Figure 5.76 (c).
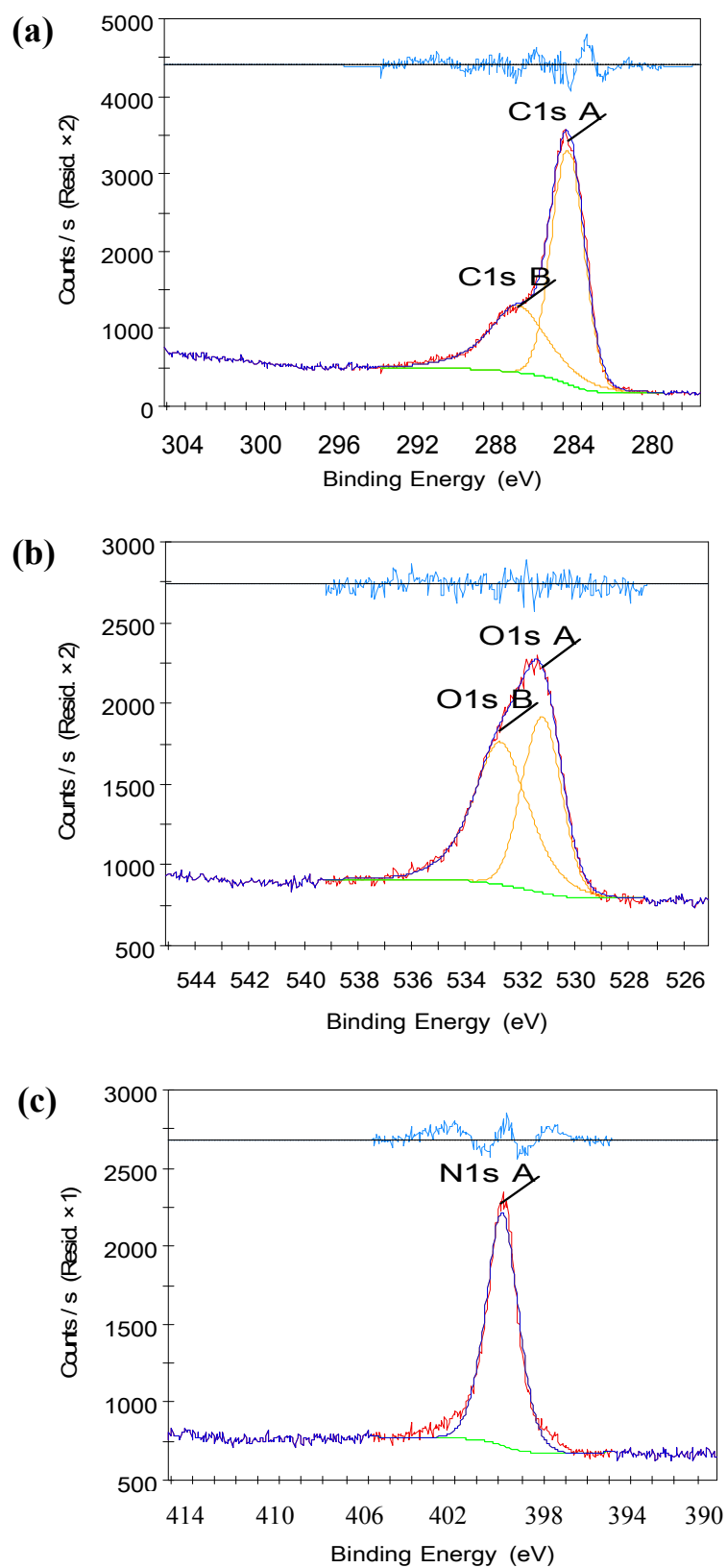
Figure 5.74. Deconvoluted XPS **(a)** C1s spectrum (C1s A= C-C, C1s B: C=O and C=N), **(b)** O1s spectrum (O1s A: C-O, O1s B: C=O) of GNS, and **(c)** N1s spectrum (N1s A: C-N and N-H) of Py:GO=1:1 nanocomposite.
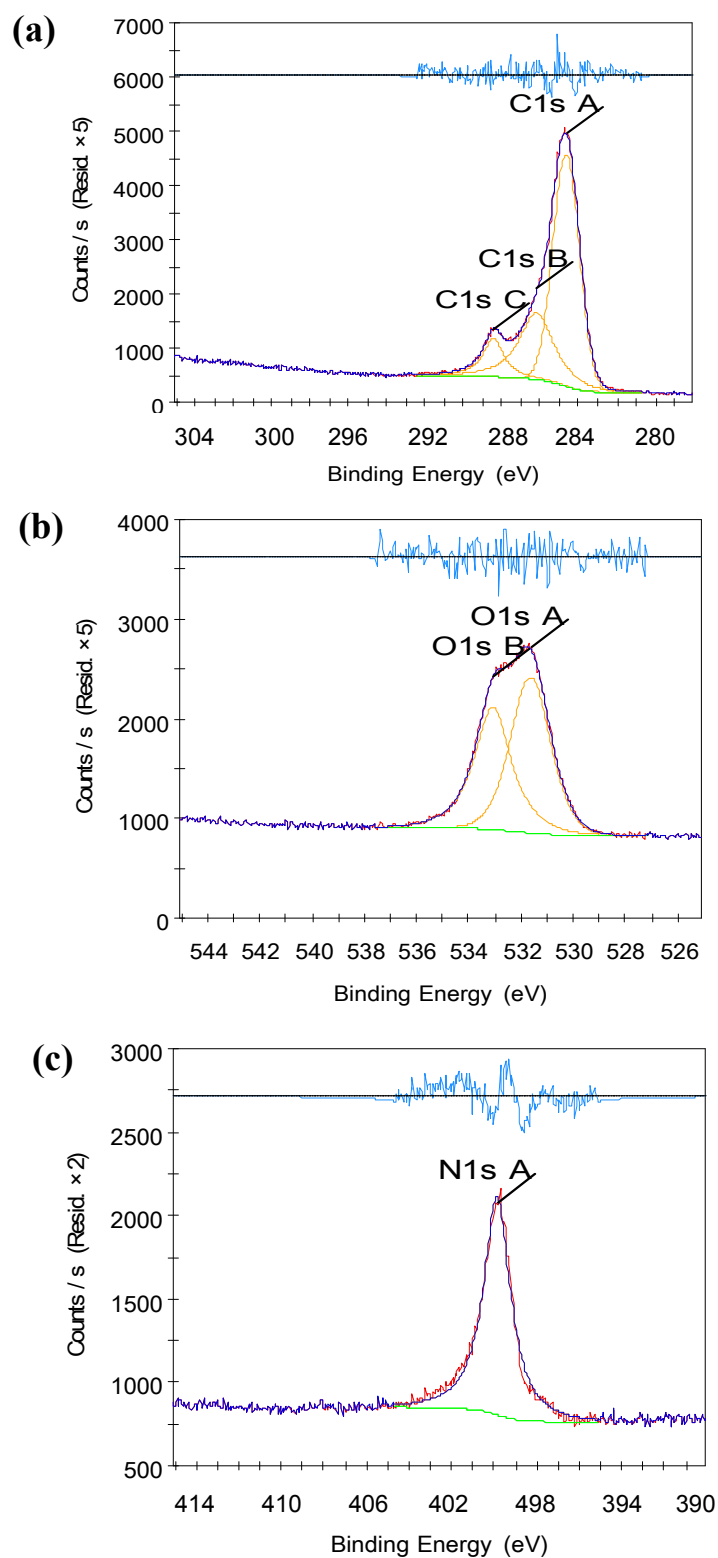
Figure 5.75. Deconvoluted XPS **(a)** C1s spectrum (C1s A= C-C, C1s B=C-O-C, C1s C: C=O, C=N and N=C-O), **(b)** O1s spectrum (O1s A: C-O and C=O, O1s B: HO-C=O) of GNS, and **(c)** N1s spectrum (N1s A: C-N and N-H) of Py:Expanded GO=1:1 composite.
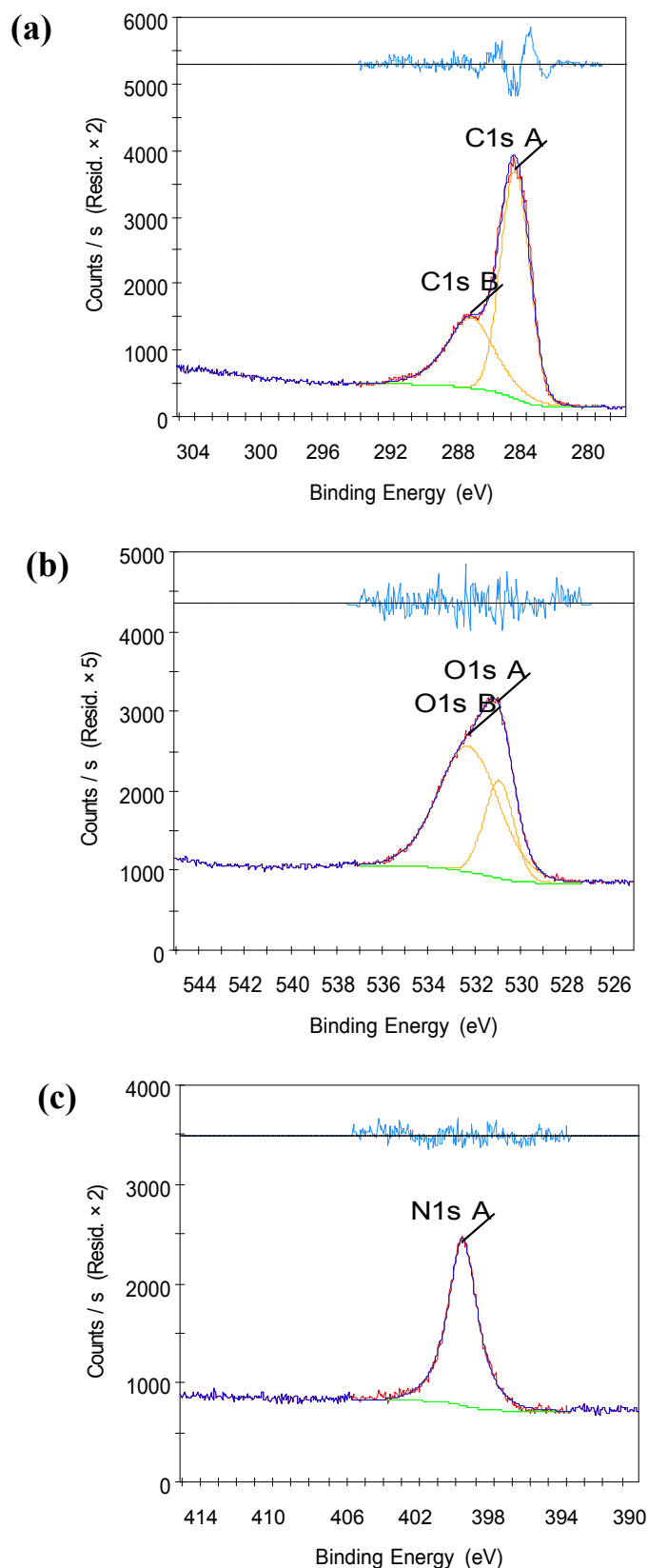
Figure 5.76. Deconvoluted XPS **(a)** C1s spectrum (C1s A= C-C, C1s B: C=O and C-N), **(b)** O1s spectrum (O1s A: C-O, O1s B: C=O) of GNS, and **(c)** N1s spectrum (N1s A: C-N and N-H) of Py:GNS=1:1 nanocomposite.

Table 5.20 and Table 5.21 summarized functional groups, binding energies, FWHM values and atomic percentages which were estimated from the C1s, O1s, and N1s XPS spectra of Py:GO=1:1, Py:Expanded GO=1:1, and Py:GNS=1:1 composites. Py:GNS=1:1 composite with the largest FWHM indicated that different types of carbon-oxygen and carbon-nitrogen containing bonds were superimposed.

Table 5.20.

XPS spectra results for C1s and O1s in the samples of Py:GO=1:1, Py:Expanded GO=1:1, and Py:GNS=1:1 composites

Samples	*C1s*				*O1s*			
	Group	**Binding Energy (eV)**	**FWHM**	**At. (%)**	**Group**	**Binding Energy (eV)**	**FWHM**	**At. (%)**
Py:GO=1:1	C-C	284.8	1.9	46.7	C-O	531.2	1.7	6.0
	C=O, C-N	287.3	3.4	27.0	C=O	532.7	2.4	7.4
Py:Expanded GO =1:1	C-C	284.7	1.6	46.4	C-O, C=O	531.6	1.8	8.0
	C-O-C	286.2	2.1	21.0	HO-C=O	533.1	1.7	6.6
	C=O, C=N, N=C-O	288.4	1.3	7.9				
Py:GNS=1:1	C-C	284.4	2.1	44.0	C-O	530.9	1.5	4.8
	C=O, C-N	287.4	3.4	24.6	C=O	532.3	3.1	13.0

Table 5.21.

XPS spectra results for N1s in the samples of Py:GO=1:1, Py:Expanded GO=1:1, and Py:GNS=1:1 composites

Samples	*N1s*			
	Group	**Binding Energy (eV)**	**FWHM**	**At. (%)**
Py:GO=1:1	C-N, N-H	399.9	1.7	12.9
Py:Expanded GO=1:1	C-N, N-H	399.9	1.5	10.1
Py:GNS=1:1	C-N, N-H	399.7	1.9	13.6

Table 5.22 showed EDX results of GO sheets, expanded GO and GNS. The C/O ratios of GO sheets, expanded GO and GNS were 1.0, 18.1 and 2.6, respectively. Expanded GO had high C/O ratio and thus low amount of oxygen functional groups decreased metal dispersion. Table 5.23 exhibited EDX results of Pt deposited GO sheets, expanded GO and GNS. The results proved that the higher oxygen amount in GO structure hindered agglomeration and promoted Pt dispersion on the surface of sheets.

Table 5.22.

EDX results of GO sheets, expanded GO and GNS

Samples	Carbon (wt%)	Oxygen (wt%)	Other elements (wt%)
GO sheets	46.5	42.8	10.7
Expanded GO	88.9	4.9	6.2
GNS	70.3	27.9	1.8

Table 5.23.

EDX results of Pt deposited GO sheets, expanded GO and GNS

Samples	Carbon (wt%)	Oxygen (wt%)	Platinum (wt%)	Other elements (wt%)
Pt/GO sheets	41.8	44.8	3.5	9.9
Pt/Expanded GO	82.6	10.3	1.2	5.6
Pt/GNS	57.0	31.8	1.4	9.8

The effect of oxygen surface groups on Pt dispersion was also investigated for PPy/GO sheets, PPy/expanded GO and PPy/GNS composites. The EDX analyses of composites were exhibited in Table 5.24. The C/O ratios of Py:GO=1:1, Py:Expanded GO=1:1 and Py:GNS=1:1 were calculated as 1.22, 3.55 and 0.95, respectively. These observations were consistent with the XPS analysis data and also indicated an increase of carbon content after thermal shock. Table 5.25 showed the EDX analyses of Pt deposited composites. The results supported that Pt dispersion increased with increasing amount of oxygen surface groups.

Table 5.24.

EDX results of PPy/GO sheets, PPy/expanded GO and PPy/GNS composites

Samples	Carbon (wt%)	Nitrogen (wt%)	Oxygen (wt%)	Other elements (wt%)
Py:GO=1:1	40.2	16.7	32.9	10.2
Py:Expanded GO=1:1	54.6	23.0	15.4	7.0
Py:GNS=1:1	42.3	7.9	44.3	5.5

Table 5.25.

EDX results of Pt deposited PPy/GO sheets, PPy/expanded GO and PPy/GNS composites

Samples	Carbon (wt%)	Nitrogen (wt%)	Oxygen (wt%)	Platinum (wt%)	Other elements (wt%)
Pt/Py:GO=1:1	37.4	20.2	34.2	6.1	2.1
Pt/Expanded:GO=1:1	46.1	22.8	28.0	0.7	2.4
Pt/Py:GNS=1:1	39.1	3.6	40.9	7.9	8.5

5.6. Fabrication of Fuel Cell Electrodes

All electrodes were fabricated by a drop cast method on Nafion®117 sheet by using 10% Nafion® solution as a binder. SEM image of partially oxidized GO sheets in electrode form indicated that GO sheets were stacked homogeneously during electrode preparation, Figure 5.77 (a). The thickness of electrode was approximately measured as 91 μm. Nonuniform catalyst deposition observed on the surface of GO electrode, Figure 5.77 (b). Some Pt catalysts dispersed seperately and some of them aggregated on the surface. Aggregation of Pt nanoparticles on electrode surface has a significance on the improvement of electrocatalyst film due to a decrease in surface area [158].
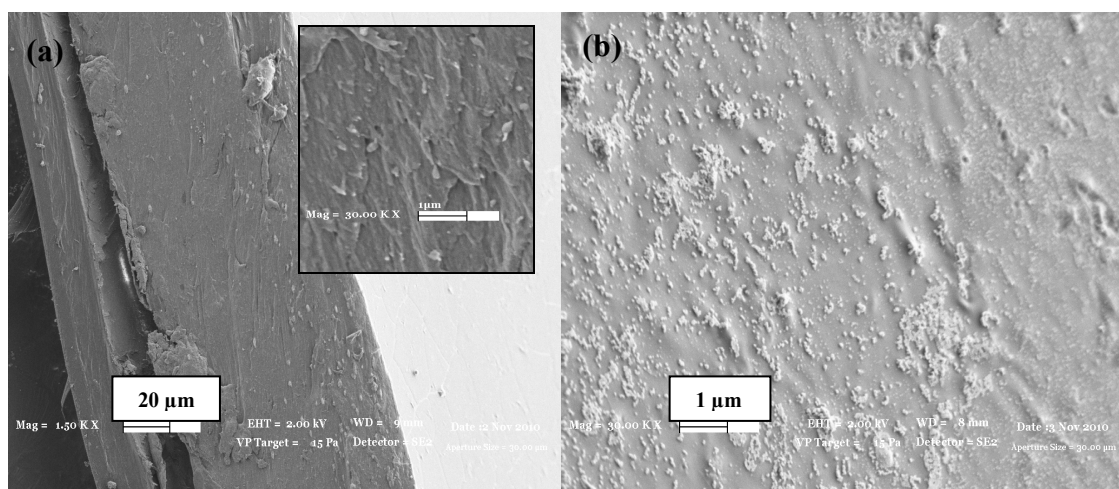
Figure 5.77. SEM images of **(a)** the edge of GO electrode and **(b)** the surface of Pt/GO electrode.

The edge of Py:GO=1:1 electrode was exhibited in Figure 5.78 (a). The inset of Figure 5.78 (a) showed that an electrode has partly porous structure. The thickness of electrode was approximately 36 μm. As Pt particles were spread out on the surface of Py:GO=1:1 electrode, few Pt particles were aggregated and most of them were distributed uniformly with the help of sonication process, Figure 5.78 (b). The diameters of Pt catalysts on the surface of Py:GO=1:1 electrode were in the 30-50 nm range.
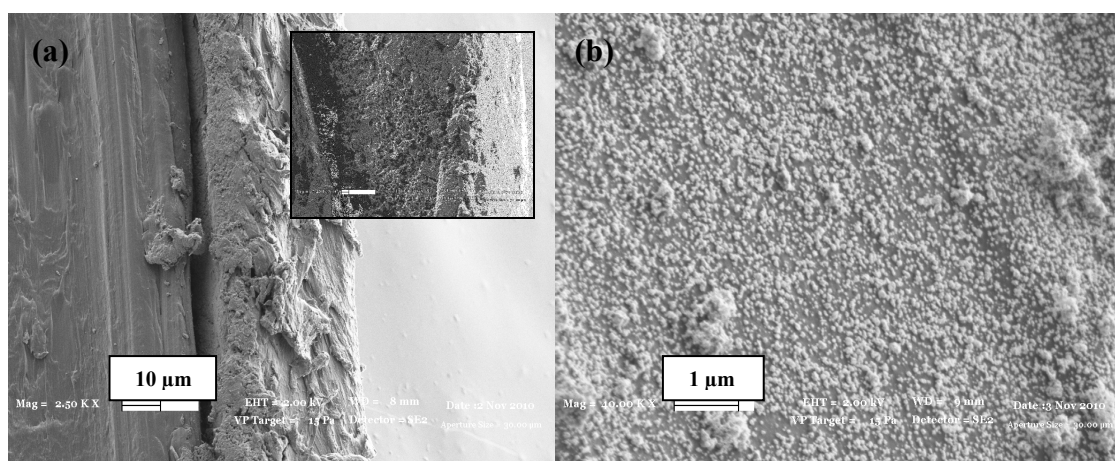
Figure 5.78. SEM images of **(a)** the edge of Py:GO=1:1 electrode and **(b)** the surface of Pt/Py:GO=1:1 electrode.

The edge of Py:GO=2:1 electrode was displayed in Figure 5.79 (a). The thickness of electrode was estimated about 35 μm. Catalysts were dispersed closely each other on the surface, Figure 5.79 (b). The size distribution of Pt catalyst on the surface of Py:GO=2:1 electrode changed from 100 nm to 140 nm. In order to make a more effective catalyst, it is important to control size, make it smaller which gives the catalysts a higher specific surface area [159]. Therefore, Py:GO=1:1 electrode became more advantageous due to narrow particle size distribution and homogeneous catalyst dispersion.
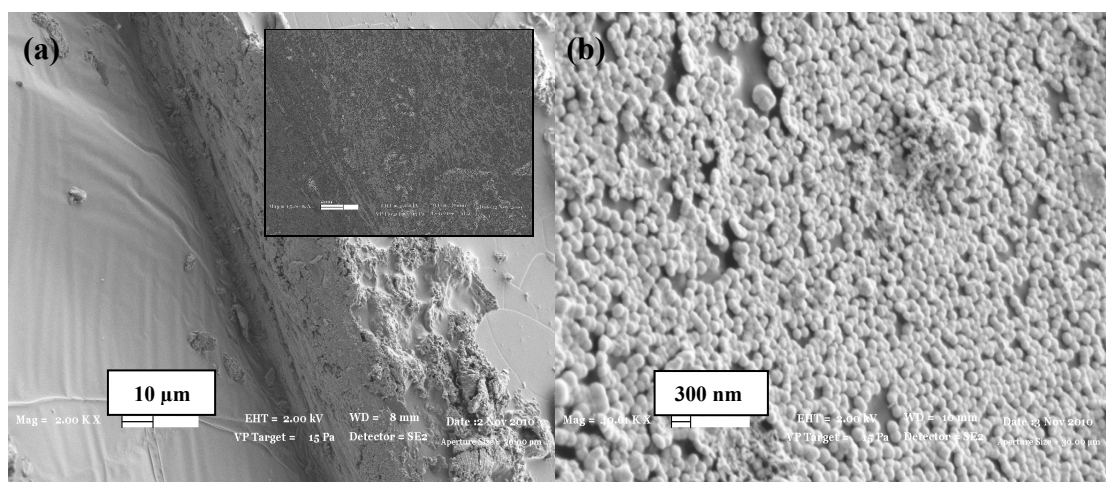
Figure 5.79. SEM images of **(a)** the edge of Py:GO=2:1 electrode and **(b)** the surface of Pt/Py:GO=2:1 electrode.

Photographs of GO, Py:GO=1:1 and Py:GO=2:1 electrodes were presented in Figure 5.80. Electrodes can be obtained as the free standing sheets and seemed to be flexible. In Figure 5.80 (a) and (b), GO sheets and Py:GO=1:1 composite were dispersed homogenously on Nafion® surface and thus smooth electrode surface was obtained. However, Py:GO=2:1 composite were not dispersed uniformly and partly rough surface was observed, Figure 5.80 (c). Herein, hydrophobic nature of PPy might play a role in dispersion because electrode solution was prepared in water.
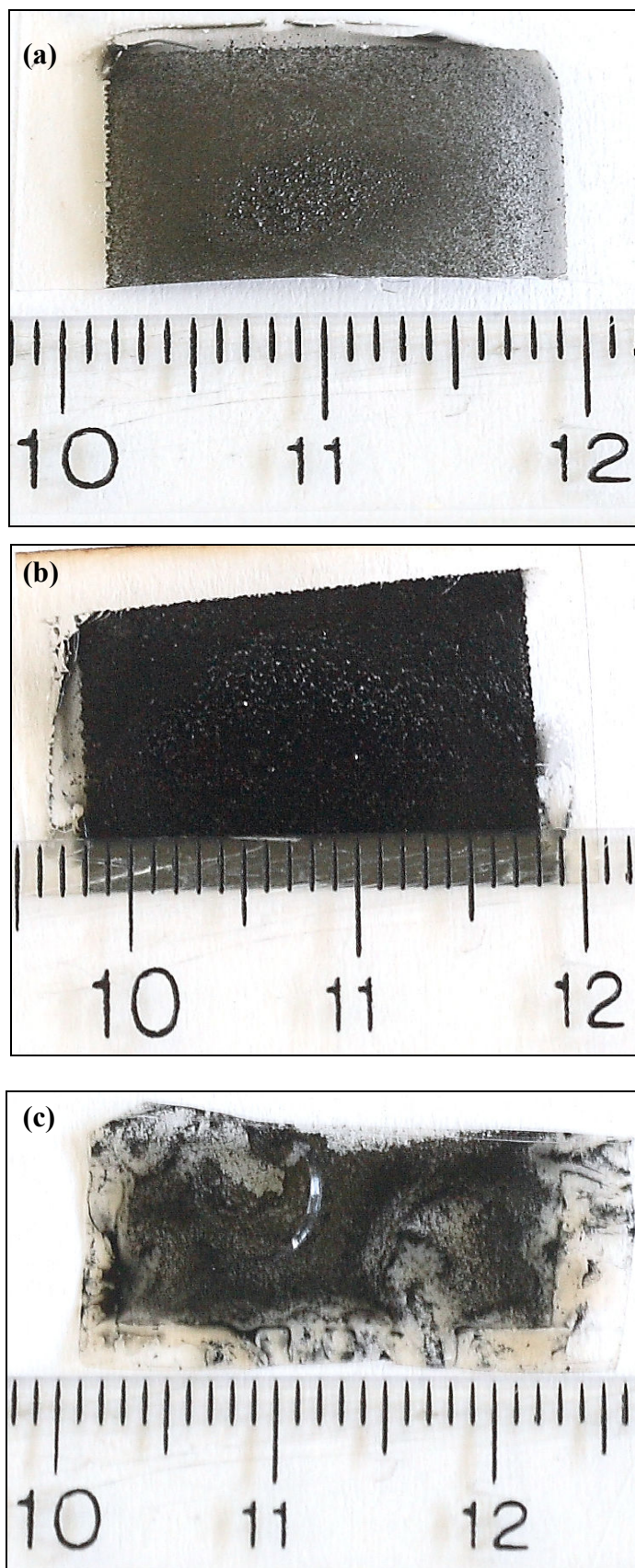
Figure 5.80. Photographs of electrodes **(a)** GO sheets **(b)** Py:GO=1:1 and **(c)** Pt/Py:GO=2:1.

5.7. Fabrication of Membrane Electrode Assembly

Two types of membrane electrode assemblies (MEAs) were fabricated in order to utilize in single fuel cells. One of the MEAs was prepared using the fabricated electrodes (GO, Py:GO=1:1 or Py:GNS=1:1 electrodes) as both the anode and cathode. The other type of MEA was prepared using the fabricated electrode (GO or Py:GNS=1:1 electrodes) as the cathode and commercial carbon cloth electrode as the anode. MEAs were fabricated by combining the electrodes with the commercial Nafion$^®$ membrane by using Nafion$^®$ solution as a binder and then the curing temperature was adjusted to 70°C.

Figure 5.81 (a) showed the photograph of Pt/GO electrode and after Pt deposition. In this case, electrode became thinner and flexible. Ultrasonic treatment before drop-casting provided homogeneous dispersion of GO sheets into Nafion$^®$ solution. Figure 5.81 (b) displayed MEA prepared by Pt/GO sheets at both anode and cathode sides.
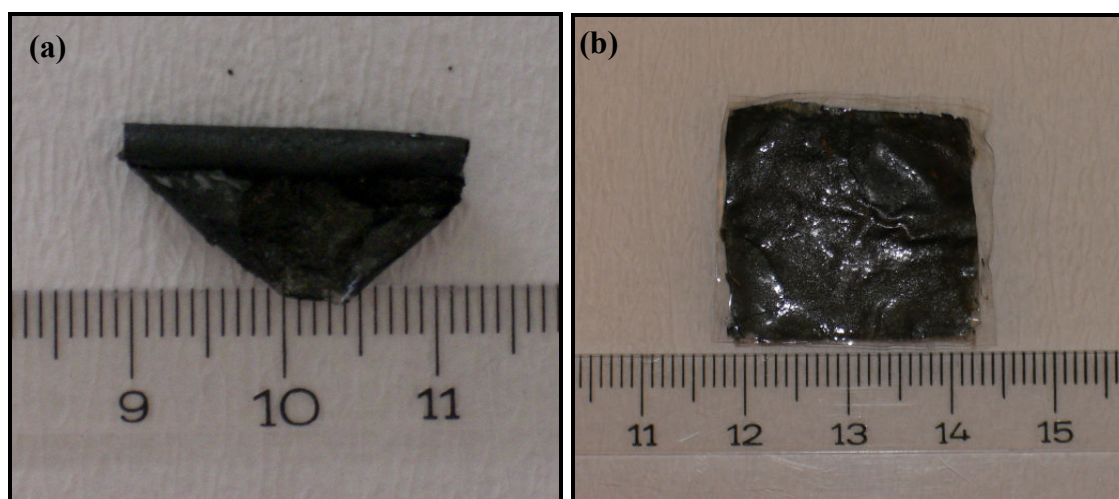
Figure 5.81. Photographs of **(a)** Pt/GO electrode and **(b)** MEA prepared by Pt/GO sheets at both anode and cathode sides.

A photograph of Pt deposited Py:GO=1:1 electrode presented in Figure 5.82 (a). After curing and deposition processes, composites were dispersed partly on the surface of electrode and this might affect the diffusion of each reactant gas to the catalyst on the

MEA. Figure 5.82 (b) showed MEA prepared by Pt/Py:GO=1:1 nanocomposite at both anode and cathode sides.
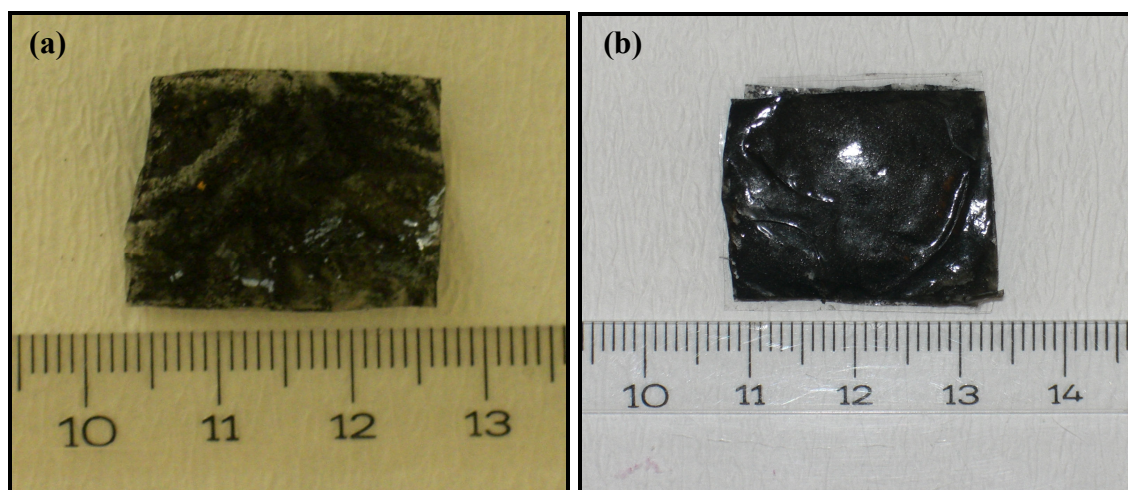
Figure 5.82. Photographs of **(a)** Pt/Py:GO=1:1 electrode **(b)** MEA prepared by Pt/Py:GO=1:1 nanocomposite as both anode and cathode.

A photograph of Pt deposited Py:GNS=1:1 electrode displayed in Figure 5.83 (a). GNS-based electrode was foldable in a free standing state. Figure 5.83 (b) showed a photograph of MEA prepared by Pt/Py:GNS=1:1 nanocomposite as both anode and cathode.
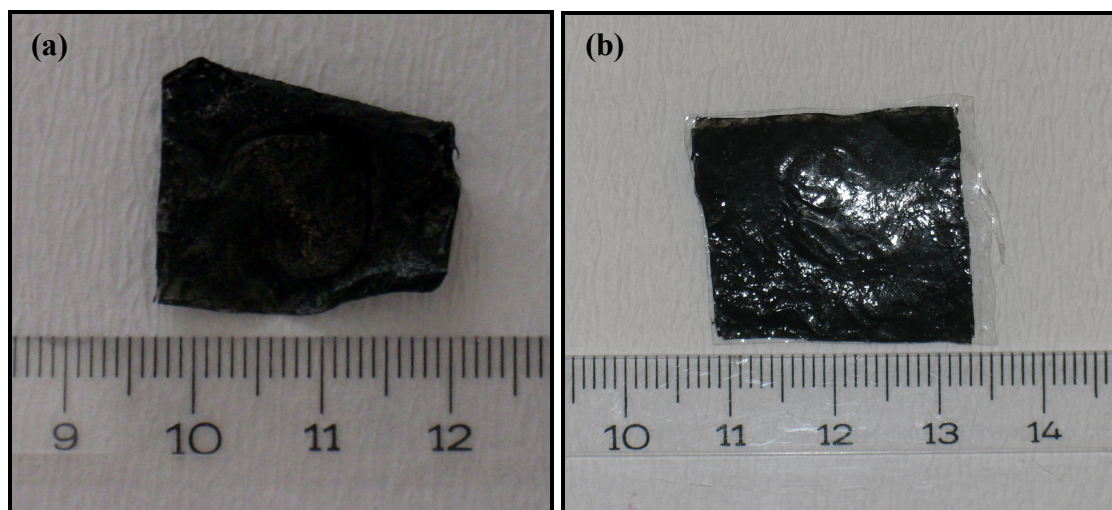
Figure 5.83. Photographs of **(a)** Pt/Py:GNS=1:1 electrode and **(b)** MEA prepared by Pt/Py:GNS=1:1 nanocomposite as both anode and cathode.

Figure 5.84 showed MEA prepared by commercial Pt/carbon cloth (E-TEK) electrode at anode side and Pt/GO sheets electrode at cathode side. The performance of the fuel cells equipped with commercial carbon electrode can be increased and thus fuel cell durability increases [160].
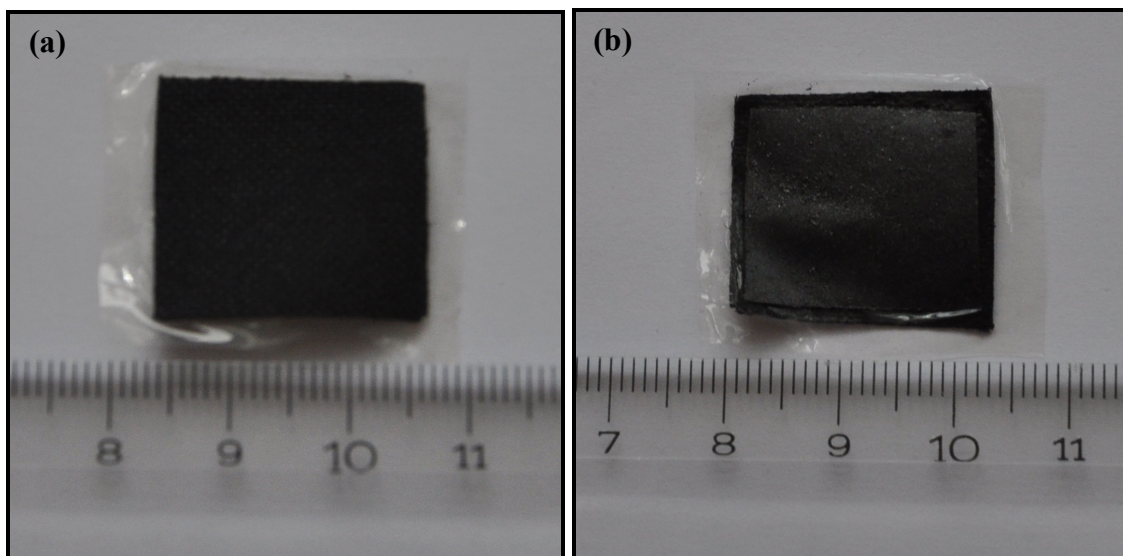
Figure 5.84. Photographs of MEA prepared by **(a)** commercial Pt/carbon cloth as anode and **(b)** Pt/GO sheets as cathode.

Figure 5.85 exhibited MEA prepared by commercial Pt deposited carbon cloth electrode (E-TEK) at anode side and Pt deposited Py:GNS=1:1 nanocomposite electrode at cathode side.
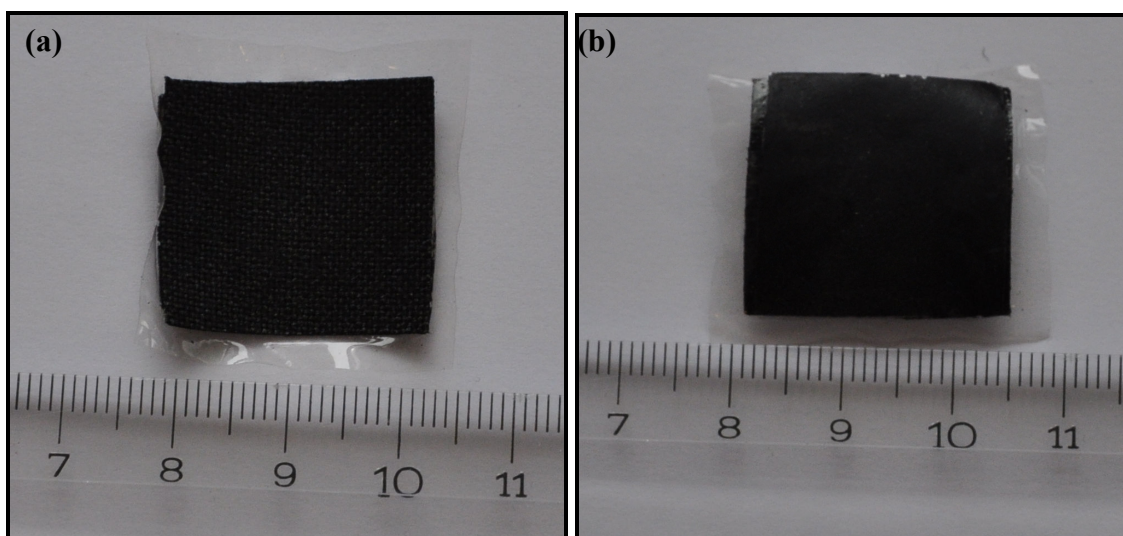
Figure 5.85. Photographs of MEA prepared by **(a)** commercial Pt/carbon cloth as anode and **(b)** Pt/Py:GNS=1:1 nanocomposite as cathode.

5.8. Fuel Cell Testing

The performance of a single cell for MEA with respect of cathode electrodes was evaluated under an atmosphere of hydrogen and oxygen gases with an active area of 5 cm^2 at 60°C. First of all, it was not possible to achieve reasonable current-voltage (I-V) curves or performance in fuel cell when GO-based electrodes and GNS-based electrodes were used as both anode and cathode electrodes. For this reason, GO-based electrodes and GNS-based electrodes were only used as cathode electrodes and commercial carbon cloth (E-TEK) electrodes were employed as the anode. In this case, revealing fuel cell performance curves for both MEAs with commercial Pt/E-TEK, Pt/GO sheet and Pt/Py:GNS=1:1 nanocomposite cathode electrodes was found as shown in Figure 5.86. However, comparably better fuel cell performance was obtained when GO sheet was used as the cathode electrode. This stemmed from the large amount of oxygen surface groups on the surface of GO sheets compared to Py:GNS=1:1 nanocomposite.

In conclusion, the performance of the fabricated electrodes was not as satisfactory as commercial fuel cell electrodes. In order to enhance the utility of Pt on GO sheets, further investigations will be required to establish the optimal condition of Pt/GO sheets electrode fabrication.

159
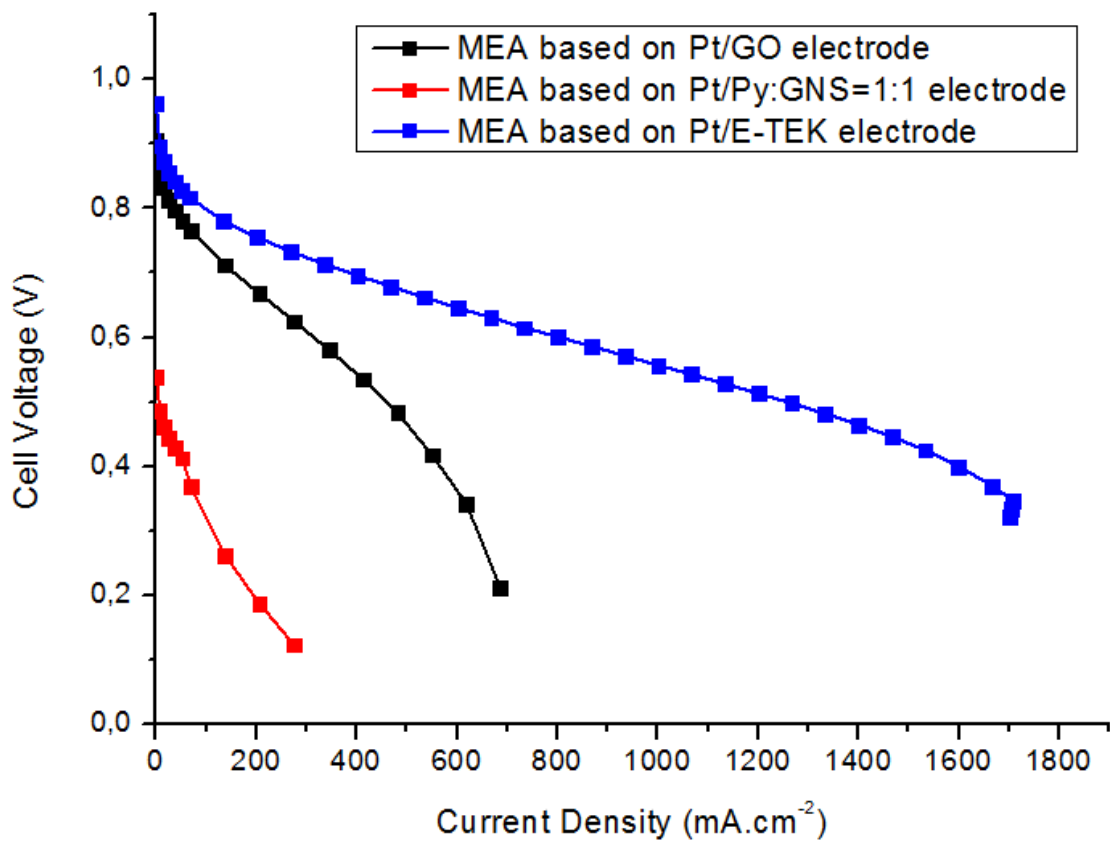
Figure 5.86. I-V performance curves of commercial Pt/E-TEK, Pt/GO sheets and Pt/Py:GNS=1:1 nanocomposite as cathode electrodes in PEMFC at 60°C and fully humidified conditions.

CHAPTER 6. CONCLUSIONS

This study was conducted in seven major steps. The findings for each step can be summarized as follows:

i. *Chemical exfoliation of graphite by an improved, safer and mild method for the large-scale synthesis of graphene nanosheets (GNS):*

In this work, GNS to be used as catalyst support material in PEMFC applications were obtained in moderate quantities by an improved, safer and mild chemical method. With the chemical procedure used, GO was prepared by using concentrated sulfuric acid, acetic anhydride and potassium dichromate from raw graphite. The steps of thermal expansion, ultrasonic treatment and chemical reduction process yielded GNS. The best method for the production of mostly exfoliated (minimum number of layers) GNS is the oxidation of the sonicated graphite flake, ultrasonic treatment of GO, and chemical reduction of sonicated GO samples. Thermal expansion process should be eliminated in the procedure because this step causes stacking the layers in graphitic structure and increasing the layer numbers of GNS. The results from each step were investigated in details by SEM, XRD and Raman spectroscopy. SEM images exhibited that graphene sheets can exist by being rippled rather than completely flat in a free standing state. The XRD results put forward that the number of graphene sheets decreased in each step from 86 (raw graphite) to nine (reduced GO). The analysis of structural changes from raw graphite to GNS in Raman spectra displayed the significant reduction of the graphitic domain sizes after the reduction of GO. The effective surface area of graphene sheets as catalyst support material relies on the layer numbers. When the layer number in graphitic structure decreases, the effective surface area increases and thus increases the metal-support interaction.

ii. *Tailoring characteristic properties of GO sheets and GNS at different oxidation times:*

We have developed a chemical synthesis procedure to tailor the structural properties of GNS. In this study, this procedure was repeated at different oxidation times until the desired graphene sheets were obtained. GO sheets started to exfoliate at longer reaction times. Surface modification with the oxidants led to the distortions in graphite structure and Raman Spectroscopy showed that the regular layered structure of graphite or GO was destroyed. Turbostratic random ordering of GO structure was also supported by XRD analysis. Both the reaction procedures with thermal expansion and without thermal expansion led to the formation of GNS. As the degree of oxidation increased, stacking height of graphene sheets decreased and thus the number of graphene layers decreased. Both SEM and 3D AFM images showed that graphene layers became flattened after each reaction step. It was possible to produce relatively flat graphene clusters with the definite number of layers by controlling the oxidation time. Moreover, TGA results showed that GNS were thermally more stable than GO sheets.

iii. *Graphene based nanocomposite production:*

GO sheets after a mild oxidation of graphite flakes and GNS after chemical reduction of GO sheets were obtained in the present work. Both GO sheets and GNS were coated with conducting PPy by *in situ* polymerization of Py monomer. The characteristic properties of PPy-based nanocomposites were tailored by changing the feeding mass ratio of Py to sheets. The intercalating agent between the graphene layers provided good dispersion in PPy matrix. Therefore, conductivity of nanocomposites increased after polymerization when comparing to pristine PPy. Furthermore, the electrical conductivity of PPy/GO nanosheet based composites slightly decreased with the increase of the feeding mass ratio of Py to GO nanosheets due to the percolative behaviour. A layer by layer polymer coating on individual GNS and GO sheets was clearly observed in SEM images and an increase of polymer thickness in these sheets was also

supported by Raman spectroscopy analyses. PPy/GNS including both characteristic properties of PPy and GNS could be produced in large quantities by the proposed simple and low-cost fabrication technique.

In the chemical exfoliation route, the other product was expanded GO obtained after thermal treatment of GO sheets. Expanded GO was also used as a conductive filler in conducting PPy matrix. During the thermal shock of GO sheets, most of the functional groups eliminated from the surface. Therefore, small amounts of functional groups in the structure of expanded GO combined with PPy, and some PPy chains agglomerated with each other.

Consequently, PPy/graphene nanosheet composites with improved conductivity, thermal stability and high surface area are more advantageous as a catalyst support when comparing with PPy/GO composites in order to achieve higher efficiency of the electrocatalyst in fuel cells.

iv. *Pt deposition on graphene based nanocomposites and the effect of oxygen surface groups on Pt dispersion:*

The impact of physical and chemical aspects of GO sheets and GNS on catalyst size, dispersion and surface chemistry were investigated by applying three different impregnation techniques in order to fabricate novel electrodes for fuel cells. The shortest and most effective impregnation technique was achieved by Pt deposition under ultrasonic vibration about 2 hrs. SEM characterization demonstrated that the deposition of Pt on PPy/GNS nanocomposite by sonication technique was more applicable than on bare GNS. Comparably higher catalyst dispersion on the surface of Py:GO=1:1 composite without the aggregation of Pt catalysts was achieved since few GO layers provided higher specific surface area for a stronger metal-support interaction and thus prevent the aggregation of catalyst particles. In addition, the higher oxygen amount in GO structure hindered agglomeration and promoted Pt dispersion on the surface of nanocomposites. The coverage of PPy on both GNS and GO sheets favored the electronic conduction pathway which is necessary to sink the electrons generated from the chemical reduction of Pt catalysts.

Therefore, as the amount of PPy increased, catalyst dispersion on the surface of nanocomposite could be maximized due to the electronic properties of PPy but catalyst-particle size range increased. On the other hand, as the amount of oxygen functional groups on the surface of GO sheets increased, smaller size catalyst particles dispersed on the surface. Therefore, smaller catalyst size enhanced the specific surface area and thus a more efficient catalyst was provided by tailoring the amount of surface oxygen groups and PPy in nanocomposite structure.

The effect of surface oxygen functional groups on Pt dispersion was investigated by FTIR, XPS and EDX. XPS and EDX results showed that Pt dispersion increased with increasing the amount of oxygen functional groups on the surface of samples. However, the random destruction of graphene layers after thermal treatment and the lack of most of oxygen functional decreased the Pt dispersion on the surface. Since thermal expansion led to the removal of oxygen functional groups on the surface, the C/O ratio increased up to 6.0 in the structure of expanded GO. Therefore, the highest C/O ratio had less hydrophilic carbon surface and this decreased the interaction of Pt catalysts with the support. Consequently, the relationship between surface oxygen functional groups and catalyst particles carries a significant importance on the durability of fuel cells. This comprehensive study will open up new ways for the production of novel catalyst support materials to be utilized in fuel cells.

v. *Fabrication of fuel cell electrodes:*

Fuel cells electrodes made of GO, GNS and their nanocomposites were fabricated by drop casting and Pt deposition was successfully achieved. Pt deposited GO sheets and GNS in the present study were an original attempt for the fabrication of fuel cells electrodes.

vi.   *Fabrication of MEA for fuel cells:*

Two kinds of MEAs were produced to compare their performance in single fuel cells. One of the MEAs was prepared using the fabricated electrodes (GO, Py:GO=1:1 or Py:GNS=1:1 electrodes) as both the anode and cathode. The other type of MEA was prepared using the fabricated electrode (GO or Py:GNS=1:1 electrodes) as the cathode and commercial carbon cloth electrode (E-TEK) as the anode. In this study, the fabricated electrodes were combined with Nafion®212 mebrane successfully.

vii.   *Fuel cell testing:*

If GO-based electrodes and GNS-based electrodes were used as both anode and cathode electrodes, it was not possible to obtain reasonable I-V curves. Therefore, GO-based electrodes and GNS-based electrodes were only utilized as cathode electrodes and commercial carbon cloth (E-TEK) electrodes were employed as the anode. Comparably better fuel cell performance was achieved when GO sheet was used as the cathode electrode. Consequently, better fuel cell performance of GO electrode stemmed from the larger amount of surface oxygen functional groups on its surface since the durability of the catalyst on the support increases with increasing amount of oxygen surface groups.

In summary, the performance of fabricated electrodes was not as satisfactory as commercial fuel cell electrodes. In order to enhance the utility of Pt on GO sheets, further investigations will be required to establish the optimal condition of Pt/GO sheets electrode fabrication.

REFERENCES

[1]   Novoselov KS, Geim AK, Morozov SV, Jiang D, Zhang Y, Dubonos SV, et al. Electric field effect in atomically thin carbon films. Science. 2004;306:666-9.

[2]   McAllister MJ, Li J-L, Adamson DH, Schniepp HC, Abdala A, Liu J, Herrera-Alonso M, Milius DL, Car R, Prud'homme RK, Aksay IA. Single sheet functionalized graphene by oxidation and thermal expansion of graphite. Chem Mater. 2007;19:4396–404.

[3]   Saner B, Okyay F, Yürüm Y. Utilization of multiple graphene layers in fuel cells. 1. An improved technique for the exfoliation of graphene-based nanosheets from graphite. Fuel. 2010;89:1903-10.

[4]   Brodie BC. On the atomic weight of graphite. Philos Trans R Soc London 1859;149:249.

[5]   Staudenmaier L. Verfahren zur darstellung der graphitsaure. Ber Dtsch Chem Ges. 1898;31:1481.

[6]   Hummers WS, Offeman RE. Preparation of graphitic oxide. J Am Chem Soc. 1958;80:1339.

[7]   Karpenko GA, Turov VV, Kovtyukhova NI, Bakai EA, Chuiko AA. Graphite oxide structure and H_2O sorption capacity. Theor Exp Chem. 1990;26:94.

[8]   He HY, Klinowski J, Forster M, Lerf A. A new structural model for graphite oxide. Chem Phys Lett. 1998;287:53-6.

[9]   Chuan X, Chen D, Zhou X. Intercalation of $CuCl_2$ into expanded graphite. Carbon. 1997;35:311-3.

[10]   Shao YY, Liu J, Wang Y, Lin YH. Novel catalyst support materials for PEM fuel cells: current status and future prospects. J Mater Chem. 2009;19:46-59.

[11]   Bao Q, Zhang H, Yang JX., Wang S, Tang DY, Jose R, Ramakrishna S, Lim CT, Loh KP. Graphene–polymer nanofiber membrane for ultrafast photonics. Adv Funct Mater. 2010;20:782-91.

[12]   Pumera M. Electrochemistry of graphene: New horizons for sensing and energy storage. The Chemical Record. 2009;9:211-23.

[13]   Middelman E. Improved PEM fuel cell electrodes by controlled self-assembly. Fuel Cells Bulletin. 2002;2002:9-12.

[14] Vernitskaya TV, Efimov ON. Polypyrrole: A conducting polymer (synthesis, properties, and applications). Uspekhi Khimii. 1997;66:489-505.

[15] Stoller MD, Park SJ, Zhu YW, An JH, Ruoff RS. Graphene-based ultracapacitors. Nano Lett. 2008;8:3498-502.

[16] Katsnelson MI. Graphene: Carbon in two dimensions. Mater Today. 2006;10:20-7.

[17] Sofo JO, Chaudhari AS, Barber GD. Graphane: A two-dimensional hydrocarbon. Phys Rev B. 2007;75:-.

[18] Schadler LS, Giannaris SC, Ajayan PM. Load transfer in carbon nanotube epoxy composites. Appl Phys Lett. 1998;73:3842-4.

[19] Berger C, Song ZM, Li TB, Li XB, Ogbazghi AY, Feng R, et al. Ultrathin epitaxial graphite: 2D electron gas properties and a route toward graphene-based nanoelectronics. J Phys Chem B. 2004;108:19912-6.

[20] Zhang YB, Tan YW, Stormer HL, Kim P. Experimental observation of the quantum Hall effect and Berry's phase in graphene. Nature. 2005;438:201-4.

[21] Chung DDL. Review graphite. J Mater Sci. 2002;37:1475-89.

[22] Ghosh S, Calizo I, Teweldebrhan D, Pokatilov EP, Nika DL, Balandin AA, et al. Extremely high thermal conductivity of graphene: Prospects for thermal management applications in nanoelectronic circuits. Appl Phys Lett. 2008;92:-.

[23] Morozov SV, Novoselov KS, Schedin F, Jiang D, Firsov AA, Geim AK. Two-dimensional electron and hole gases at the surface of graphite. Phys Rev B. 2005;72:-.

[24] Niyogi S, Bekyarova E, Itkis ME, McWilliams JL, Hamon MA, Haddon RC. Solution properties of graphite and graphene. J Am Chem Soc. 2006;128:7720-1.

[25] Subrahmanyam KS, Vivekchand SRC, Govindaraj A, Rao CNR. A study of graphenes prepared by different methods: characterization, properties and solubilization. J Mater Chem. 2008;18:1517-23.

[26] Huc V, Bendiab N, Rosman N, Ebbesen T, Delacour C, Bouchiat V. Large and flat graphene flakes produced by epoxy bonding and reverse exfoliation of highly oriented pyrolytic graphite. Nanotechnology. 2008;19:-.

[27] Shukla A, Kumar R, Mazher J, Balan A. Graphene made easy: High quality, large-area samples. Solid State Commun. 2009;149:718-21.

[28] Park S, Ruoff RS. Chemical methods for the production of graphenes. Nat Nanotechnol. 2009;4:217-24.

[29] Titelman GI, Gelman V, Bron S, Khalfin RL, Cohen Y, Bianco-Peled H. Characteristics and microstructure of aqueous colloidal dispersions of graphite oxide. Carbon. 2005;43:641-9.

[30] Buchsteiner A, Lerf A, Pieper J. Water dynamics in graphite oxide investigated with neutron scattering. J Phys Chem B. 2006;110:22328-38.

[31] Stankovich S, Piner RD, Nguyen ST, Ruoff RS. Synthesis and exfoliation of isocyanate-treated graphene oxide nanoplatelets. Carbon. 2006;44:3342-7.

[32] Wu ZS, Ren WC, Gao LB, Liu BL, Jiang CB, Cheng HM. Synthesis of high-quality graphene with a pre-determined number of layers. Carbon. 2009;47:493-9.

[33] Tkachev SV, Buslaeva EYu, Gubin SP. Graphene: A novel carbon nanomaterial. Inorganic Materials. 2011;47:1-10.

[34] Shioyama H. The interactions of two chemical species in the interlayer spacing of graphite. Synthetic Met. 2000;114:1-15.

[35] Daumas N, Herold A, Seances CR. Chemical properties of the insertion compounds of graphite. Action of oxygen and volatile oxygenated compounds on graphite-potassium compounds. Bulletin de la Societe Chimique de France. 1971;5:1598-604.

[36] Liang C-Y, Che R-C, Tian H-F, Shi H-L, Li J-Q. Structure characterization of $CuCl_2$-$FeCl_3$-H_2SO_4 graphite intercalation compounds. Chinese journal of chemical physics. 2007;20:806-10.

[37] Yan W, Lerner MM. Synthesis and structural investigation of new graphite intercalation compounds containing the perfluoroalkylsulfonate anions $C_{10}F_{21}SO_3^-$, $C_2F_5OC_2F_4SO_3^-$, and $C_2F_5(C_6F_{10})SO_3^-$. Carbon. 2004;42:2981-7.

[38] Herrera-Alonso M, Abdala AA, McAllister MJ, Aksay IA, Prud'homme RK. Intercalation and stitching of graphite oxide with diaminoalkanes. Langmuir. 2007;23:10644-9.

[39] Li XL, Wang XR, Zhang L, Lee SW, Dai HJ. Chemically derived, ultrasmooth graphene nanoribbon semiconductors. Science. 2008;319:1229-32.

[40] Prudhomme RK, Aksay IA, Adamson D, Abdala A. Tire containing thermally exfoliated graphite oxide. US Patent 0054581 A1. 2009.

[41] Ramanathan T, Abdala AA, Stankovich S, Dikin DA, Herrera-Alonso M, Piner RD, et al. Functionalized graphene sheets for polymer nanocomposites. Nat Nanotechnol. 2008;3:327-31.

[42] Gu WT, Zhang W, Li XM, Zhu HW, Wei JQ, Li Z, et al. Graphene sheets from worm-like exfoliated graphite. J Mater Chem. 2009;19:3367-9.

[43] Chen GH, Wu DJ, Weng WG, Yan WL. Preparation of polymer/graphite conducting nanocomposite by intercalation polymerization. J Appl Polym Sci. 2001;82:2506-13.

[44] Berger C, Song ZM, Li XB, Wu XS, Brown N, Naud C, et al. Electronic confinement and coherence in patterned epitaxial graphene. Science. 2006;312:1191-6.

[45] de Heer WA, Berger C, Wu XS, First PN, Conrad EH, Li XB, et al. Epitaxial graphene. Solid State Commun. 2007;143:92-100.

[46] Rollings E, Gweon GH, Zhou SY, Mun BS, McChesney JL, Hussain BS, et al. Synthesis and characterization of atomically thin graphite films on a silicon carbide substrate. J Phys Chem Solids. 2006;67:2172-7.

[47] Camara N, Rius G, Huntzinger JR, Tiberj A, Mestres N, Godignon P, et al. Selective epitaxial growth of graphene on SiC. Appl Phys Lett. 2008;93.

[48] Wang XB, You HJ, Liu FM, Li MJ, Wan L, Li SQ, et al. Large-scale synthesis of few-layered graphene using CVD. Chem Vapor Depos. 2009;15:53-6.

[49] Liu YQ, Wei DC, Zhang HL, Huang LP, Wu B, Chen JY, et al. Scalable synthesis of few-layer graphene ribbons with controlled morphologies by a template method and their applications in nanoelectromechanical switches. J Am Chem Soc. 2009;131:11147-54.

[50] Wang JJ, Zhu MY, Outlaw RA, Zhao X, Manos DM, Holloway BC. Synthesis of carbon nanosheets by inductively coupled radio-frequency plasma enhanced chemical vapor deposition. Carbon. 2004;42:2867-72.

[51] Zhang WJ, Yuan GD, Yang Y, Tang YB, Li YQ, Wang JX, et al. Graphene sheets via microwave chemical vapor deposition. Chem Phys Lett. 2009;467:361-4.

[52] Han MY, Ozyilmaz B, Zhang YB, Kim P. Energy band-gap engineering of graphene nanoribbons. Phys Rev Lett. 2007;98.

[53] Duan XF, Bai JW, Huang Y. Rational fabrication of graphene nanoribbons using a nanowire etch mask. Nano Lett. 2009;9:2083-7.

[54] Graf D, Molitor F, Ensslin K, Stampfer C, Jungen A, Hierold C, Wirtz L. Spatially resolved Raman spectroscopy of single- and few layer- graphene. Nano Lett. 2007;7:238-42.

[55] Ferrari AC, Meyer JC, Scardaci V, Casiraghi C, Lazzeri M, Mauri F, et al. Raman spectrum of graphene and graphene layers. Phys Rev Lett. 2006;97:-.

[56] Shen ZX, Wang YY, Ni ZH, Yu T, Wang HM, Wu YH, et al. Raman studies of monolayer graphene: The substrate effect. J Phys Chem C. 2008;112:10637-40.

[57] Ferrari AC, Robertson, J. Interpretation of Raman spectra of disordered and amorphous carbon. Phys Rev B. 2000;61:14095-107.

[58] Shao YY, Yin GP, Wang HH, Gao YZ, Shi PF. Multi-walled carbon nanotubes based Pt electrodes prepared with in situ ion exchange method for oxygen reduction. J Power Sources. 2006;161:47-53.

[59] Centi G, Perathoner S. The role of nanostructure in improving the performance of electrodes for energy storage and conversion. Eur J Inorg Chem. 2009:3851-78.

[60] Vivekchand SRC, Rout CS, Subrahmanyam KS, Govindaraj A, Rao CNR. Graphene-based electrochemical supercapacitors. J Chem Sci. 2008;120:9-13.

[61] Chen GH, Wu CL, Weng WG, Wu DJ, Yan WL. Preparation of polystyrene/graphite nanosheet composite. Polymer. 2003;44:1781-4.

[62] Grove WR. On voltaic series and the combination of gases by platinum. London and Edinburgh Philosophical Magazine and Journal of Science. 1839;Series 3, 14, 127-130-420.

[63] Barbir F. PEM Fuel Cells: Theory and Practice. Elsevier Academic Press, USA. 2005;ISBN: 0-12-078142-5:1-16.

[64] Penner SS, Appleby AJ, Baker BS, Bates JL, Buss LB, Dollard WJ, et al. Commercialization of fuel-cells. Energy. 1995;20:331-470.

[65] Grupp WT. Fuel Cells. General Electric, US Patent 2 913 511. 1959.

[66] Grot W. Perfluorinated ion-exchange membranes of high chemical and thermal stability. Chemie Ingenieur Technik1972.

[67] Grot W. Perfluorinated cation exchange polymers. Chemie Ingenieur Technik. 1975;47.

[68] Yuan X-Z, Wang H. PEM fuel cell fundamentals. In: Zhang, J. (ed.) PEM fuel cell electrocatalysts and catalyst layers: fundamentals and applications Springer. 2008:22-5.

[69] Wu JF, Yuan XZ, Martin JJ, Wang HJ, Zhang JJ, Shen J, et al. A review of PEM fuel cell durability: Degradation mechanisms and mitigation strategies. J Power Sources. 2008;184:104-19.

[70] Chena S-L, Krishnana L, Srinivasana S, Benzigerb J, Bocarslya AB. Ion exchange resin/polystyrene sulfonate composite membranes for PEM fuel cells. J Membr Sci. 2004;243:327–33.

[71] Gubler L, Gursel SA, Scherer GG. Radiation grafted membranes for polymer electrolyte fuel cells. Fuel Cells. 2005;5:317-35.

[72] Gubler L, Prost N, Gursel SA, Scherer GG. Proton exchange membranes prepared by radiation grafting of styrene/divinylbenzene onto poly(ethylene-alt-tetrafluoroethylene) for low temperature fuel cells. Solid State Ionics. 2005;176:2849-60.

[73] Gursel SA, Yang Z, Choudhury B, Roelofs MG, Scherer GG. Radiation-grafted membranes using a trifluorostyrene derivative. J Electrochem Soc. 2006;153:A1964-A70.

[74] Gubler L, Ben youcef H, Gursel SA, Henkensmeier D, Wokaun A, Scherer GG. Novel ETFE based radiation grafted poly(styrene sulfonic acid-co-methacrylonitrile) proton conducting membranes with increased stability. Electrochem Commun. 2009;11:941-4.

[75] Gursel SA, Sanli LI. Synthesis and characterization of novel graft copolymers by radiation-induced grafting. J Appl Polym Sci. 2011;120:2313-23.

[76] Hickner MA, Pivovar BS. The chemical and structural nature of proton exchange membrane fuel cell properties. Fuel Cells. 2005;5:213-29.

[77] Weber AZ, Newman J. Transport in polymer-electrolyte membranes - II. Mathematical model. J Electrochem Soc. 2004;151:A311-A25.

[78] Litster S, McLean G. PEM fuel cell electrodes. J Power Sources. 2004;130:61-76.

[79] Haile SM. Fuel cell materials and components. Acta Mater. 2003;51:5981-6000.

[80] Gubler L, Beck N, Alkan Gürsel S, Hajbolouri F, Kramer D, Reiner A, Steiger B, Scherer GG, Wokaun A, Rajesh B, Thampi KR. Materials for polymer electrolyte fuel cells. CHIMIA International Journal for Chemistry. 2004;58:826-36.

[81] Borup R, Meyers J, Pivovar B, Kim YS, Mukundan R, Garland N, et al. Scientific aspects of polymer electrolyte fuel cell durability and degradation. Chem Rev. 2007;107:3904-51.

[82] Lizcano-Valbuena WH, de Azevedo DC, Gonzalez ER. Supported metal nanoparticles as electrocatalysts for low-temperature fuel cells. Electrochim Acta. 2004;49:1289-95.

[83] Nallathambi V, Lee JW, Kumaraguru SP, Wu G, Popov BN. Development of high performance carbon composite catalyst for oxygen reduction reaction in PEM Proton Exchange Membrane fuel cells. J Power Sources. 2008;183:34-42.

[84] Yu XW, Ye SY. Recent advances in activity and durability enhancement of Pt/C catalytic cathode in PEMFC - Part I. Physico-chemical and electronic interaction between Pt and carbon support, and activity enhancement of Pt/C catalyst. J Power Sources. 2007;172:133-44.

[85] Pradoburguete C, Linaressolano A, Rodriguezreinoso F, Delecea CS. The effect of oxygen-surface groups of the support on platinum dispersion in Pt/carbon catalysts. J Catal. 1989;115:98-106.

[86] Fraga MA, Jordao E, Mendes MJ, Freitas MMA, Faria JL, Figueiredo JL. Properties of carbon-supported platinum catalysts: Role of carbon surface sites. J Catal. 2002;209:355-64.

[87] Wang X, Hsing IM. Surfactant stabilized Pt and Pt alloy electrocatalyst for polymer electrolyte fuel cells. Electrochim Acta. 2002;47:2981-7.

[88] Frelink T, Visscher W, Vanveen JAR. Particle-size effect of carbon-supported platinum catalysts for the electrooxidation of methanol. J Electroanal Chem. 1995;382:65-72.

[89] Natarajan SK, Hamelin J. Electrochemical durability of carbon nanostructures as catalyst support for PEMFCs. J Electrochem Soc. 2009;156:B210-B5.

[90] Ralph TR, Hogarth MP. Catalysis for low temperature fuel cells. Platinum Metals Rev. 2002;46:3-14.

[91] Matsumoto T, Komatsu T, Nakano H, Arai K, Nagashima Y, Yoo E, et al. Efficient usage of highly dispersed Pt on carbon nanotubes for electrode catalysts of polymer electrolyte fuel cells. Catal Today. 2004;90:277-81.

[92] Yoo E, Okada T, Kizuka T, Nakamura J. Effect of carbon substrate materials as a Pt-Ru catalyst support on the performance of direct methanol fuel cells. J Power Sources. 2008;180:221-6.

[93] Wang Y, Shi ZQ, Huang Y, Ma YF, Wang CY, Chen MM, et al. Supercapacitor devices based on graphene materials. J Phys Chem C. 2009;113:13103-7.

[94] Rodriguez NM. A Review of catalytically grown carbon nanofibers. J Mater Res. 1993;8:3233-50.

[95] Bessel CA, Laubernds K, Rodriguez NM, Baker RTK. Graphite nanofibers as an electrode for fuel cell applications. J Phys Chem B. 2001;105:1115-8.

[96]   Iijima S. Helical Microtubules of Graphitic Carbon. Nature. 1991;354:56-8.

[97]   Oncel C, Yürüm Y. Carbon nanotube synthesis via the catalytic CVD method: A review on the effect of reaction parameters. Fuller Nanotub Car N. 2006;14:17-37.

[98]   Xing YC. Synthesis and electrochemical characterization of uniformly-dispersed high loading Pt nanoparticles on sonochemically-treated carbon nanotubes. J Phys Chem B. 2004;108:19255-9.

[99]   Rajalakshmi N, Ryu H, Shaijumon MM, Ramaprabhu S. Performance of polymer electrolyte membrane fuel cells with carbon nanotubes as oxygen reduction catalyst support material. J Power Sources. 2005;140:250-7.

[100] Sharma AK, Kim JH, Lee YS. An efficient synthesis of polypyrrole/carbon fiber composite nano-thin films. Int J Electrochem Sc. 2009;4:1560-7.

[101] Snook GA, Kao P, Best AS. Conducting-polymer-based supercapacitor devices and electrodes. J Power Sources. 2011;196:1-12.

[102] Santos MJL, Brolo AG, Girotto EM. Study of polaron and bipolaron states in polypyrrole by in situ Raman spectroelectrochemistry. Electrochim Acta. 2007;52:6141-5.

[103] Bredas JL, Street GB. Polarons, bipolarons, and solitons in conducting polymers. Accounts Chem Res. 1985;18:309-15.

[104] Park JH, Kim JH, Lee HK, Lee TH, Joe YI. A novel direct deposition of Pt catalysts on Nafion impregnated with polypyrrole for PEMFC. Electrochim Acta. 2004;50:769-75.

[105] Li L, Drillet JF, Macova Z, Dittmeyer R, Juttner K. Poly(3,4-ethylenedioxythiophene)-modified nafion membrane for direct methanol fuel cells. Russ J Electrochem. 2006;42:1193-201.

[106] Cilingir Dogan HD, Alkan Gürsel S. Preparation and characterisation of novel composites based on a radiation grafted membrane for fuel cells. 2011;11:361-71.

[107] Wang HL, Hao QL, Yang XJ, Lu LD, Wang X. Graphene oxide doped polyaniline for supercapacitors. Electrochem Commun. 2009;11:1158-61.

[108] Wang DW, Li F, Zhao JP, Ren WC, Chen ZG, Tan J, et al. Fabrication of graphene/polyaniline composite paper via in situ anodic electropolymerization for high-performance flexible electrode. ACS Nano. 2009;3:1745-52.

[109] Kou R, Shao YY, Wang DH, Engelhard MH, Kwak JH, Wang J, et al. Enhanced activity and stability of Pt catalysts on functionalized graphene sheets for electrocatalytic oxygen reduction. Electrochem Commun. 2009;11:954-7.

[110] Kim YT, Ohshima K, Higashimine K, Uruga T, Takata M, Suematsu H, et al. Fine size control of platinum on carbon nanotubes: From single atoms to clusters. Angew Chem Int Edit. 2006;45:407-11.

[111] Hirsch A. Functionalization of single-walled carbon nanotubes. Angew Chem Int Edit. 2002;41:1853-9.

[112] Xu CL, Chen JF, Cui Y, Han QY, Choo H, Liaw PK, et al. Influence of the surface treatment on the deposition of platinum nanoparticles on the carbon nanotubes. Adv Eng Mater. 2006;8:73-7.

[113] Yoo E, Okada T, Akita T, Kohyama M, Honma I, Nakamura J. Sub-nano-Pt cluster supported on graphene nanosheets for CO tolerant catalysts in polymer electrolyte fuel cells. J Power Sources. 2011;196:110-5.

[114] Thompson SD, Jordan LR, Forsyth M. Platinum electrodeposition for polymer electrolyte membrane fuel cells. Electrochim Acta. 2001;46:1657-63.

[115] Kuo PL, Chen CC, Jao MW. Effects of polymer micelles of alkylated polyethylenimines on generation of gold nanoparticles. J Phys Chem B. 2005;109:9445-50.

[116] Chen WX, Lee JY, Liu ZL. Preparation of Pt and PtRu nanoparticles supported on carbon nanotubes by microwave-assisted heating polyol process. Mater Lett. 2004;58:3166-9.

[117] Hirano S, Kim J, Srinivasan S. High performance proton exchange membrane fuel cell with sputter-deposited Pt layer electrodes. Electrochim Acta. 2006;42:1587-93.

[118] Li J, Feng L, Jia Z. Preparation of expanded graphite with 160 μm mesh of fine flake graphite. Mater Lett. 2006;60:746-9.

[119] Saner B, Dinc F, Yürüm Y. Utilization of multiple graphene nanosheets in fuel cells 2. The effect of oxidation process on the characteristics of graphene nanosheets. Fuel. 2011;90:2609-16.

[120] Armes SP. Optimum reaction conditions for the polymerization of pyrrole by iron (III) chloride in aqueous-solution. Synthetic Met. 1987;20:365-71.

[121] Ramesh P, Sivakumar P, Sampath S. Phenoxazine functionalized, exfoliated graphite based electrodes for NADH oxidation and ethanol biosensing. Electroanal. 2003;15:1850-8.

[122] Jia YF, Demopoulos GP. Adsorption of silver onto activated carbon from acidic media: nitrate and sulfate media. Ind Eng Chem Res. 2003;42:72-9.

[123] Schniepp HC, Li JL, McAllister MJ, Sai H, Herrera-Alonso M, Adamson DH, Prud'homme RK, Car R, Saville DA, Aksay IA. Functionalized single graphene sheets derived from splitting graphite oxide. J Phys Chem B. 2006;110:8535-9.

[124] Jihui-Li, Huifang-Da, Qian-Liu, Shufen-Liu. Preparation of sulfur-free expanded graphite with 320 μm mesh of flake graphite. Mater Lett. 2006;60:3927-30.

[125] Sakintuna B, Cetinkaya S, Yürüm Y. Evolution of carbon microstructures during the pyrolysis of Turkish elbistan lignite in the temperature range 700-1000 degrees C. Energ Fuel. 2004;18:883-8.

[126] Gurudatt K, Tripathi VS. Studies on changes in morphology during carbonization and activation of pretreated viscose rayon fabrics. Carbon. 1998;36:1371-7.

[127] Gupta A, Chen G, Joshi P, Tadigadapa S, Eklund PC. Raman scattering from high-frequency phonons in supported n-graphene layer films. Nano Lett. 2006;6:2667-73.

[128] Jeong HK, Lee YP, Lahaye RJWE, Park MH, An KH, Kim IJ, Yang CW, Park CY, Ruoff RS, Lee YH. Evidence of graphitic AB stacking order of graphite oxides. J Am Chem Soc. 2008;130:1362-6.

[129] Casiraghi C, Hartschuh A, Qian H, Piscanec S, Georgi C, Fasoli A, et al. Raman spectroscopy of graphene edges. Nano Lett. 2009;9:1433-41.

[130] Wang G, Yang J, Park J, Gou X, Wang B, Liu H, Yao J. Facile synthesis and characterization of graphene nanosheets. J Phys Chem C. 2008;112:8192-5.

[131] Greinke RA, et al. Intercalation of Graphite. US Patent No 4,895,713. 1990.

[132] Zhang XT, Zhang J, Song WH, Liu ZF. Controllable synthesis of conducting polypyrrole nanostructures. J Phys Chem B. 2006;110:1158-65.

[133] Jeong HK, Jin MH, So KP, Lim SC, Lee YH. Tailoring the characteristics of graphite oxides by different oxidation times. J Phys D Appl Phys. 2009;42:-.

[134] Liu YC, Hwang BJ. Identification of oxidized polypyrrole on Raman spectrum. Synthetic Met. 2000;113:203-7.

[135] Han GY, Yuan JY, Shi GQ, Wei F. Electrodeposition of polypyrrole/multiwalled carbon nanotube composite films. Thin Solid Films. 2005;474:64-9.

[136] Sato K, Saito R, Oyama Y, Jiang J, Cancado LG, Pimenta MA, et al. D-band Raman intensity of graphitic materials as a function of laser energy and crystallite size. Chem Phys Lett. 2006;427:117-21.

[137] Sahoo NG, Jung YC, So HH, Cho JW. Polypyrrole coated carbon nanotubes: Synthesis, characterization, and enhanced electrical properties. Synthetic Met. 2007;157:374-9.

[138] Gu Z, Zhang L, Li C. Preparation of highly conductive polypyrrole/graphite oxide composites via in situ polymerization. J Macromol Sci B. 2009;48:1093-102.

[139] Jang JY, Kim MS, Jeong HM, Shin CM. Graphite oxide/poly(methyl methacrylate) nanocomposites prepared by a novel method utilizing macroazoinitiator. Compos Sci Technol. 2009;69:186-91.

[140] Pan DY, Wang S, Zhao B, Wu MH, Zhang HJ, Wang Y, et al. Li storage properties of disordered graphene nanosheets. Chem Mater. 2009;21:3136-42.

[141] Stankovich S, Dikin DA, Piner RD, Kohlhaas KA, Kleinhammes A, Jia Y, et al. Synthesis of graphene-based nanosheets via chemical reduction of exfoliated graphite oxide. Carbon. 2007;45:1558-65.

[142] Zengin H, Zhou WS, Jin JY, Czerw R, Smith DW, Echegoyen L, et al. Carbon nanotube doped polyaniline. Adv Mater. 2002;14:1480-3.

[143] Coloma F, Sepulveda-Escribano A, Rodriquez-Reinoso F. Gas phase hydrogenation of crotonaldehyde over Pt/activated carbon catalyst. Influence of hydrogen surface groups of the support. Appl Catal A Gen. 1997;150:165-83.

[144] Zhamu A, Jang BZ, Shi J. Graphene nanocomposites for electrochemical cell electrodes. US Patent No 0021819 A1. 2010.

[145] Liu R, Her WH, Fedkiw PS. In situ electrode formation on a Nafion membrane by chemical platinization. J Electrochem Soc. 1992;139:15-23.

[146] Sepulveda-Escribano A, Coloma F, Rodriguez-Reinoso F. Platinum catalysts supported on carbon blacks with different surface chemical properties. Appl Catal A-Gen. 1998;173:247-57.

[147] Lee H, Kim J, Park J, Joe Y, Lee T. Performance of polypyrrole-impregnated composite electrode for unitized regenerative fuel cell. J Power Sources. 2004;131:188-93.

[148] Peuckert M, Yoneda T, Dalla Betta RA, Boudart M. Oxygen reduction on small supported platinum particles. J Electrochem Soc. 1986;113:944-7.

[149] Li JH, Li J, Li M. Preparation of expandable graphite with ultrasound irradiation. Mater Lett. 2007;61:5070-3.

[150] Leon CALY, Solar JM, Calemma V, Radovic LR. Evidence for the protonation of basal-plane sites on carbon. Carbon. 1992;30:797-811.

[151] Wang WP, Pan CY, Wu JS. Electrical properties of expanded graphite/poly(styrene-co-acrylonitrile) composites. J Phys Chem Solids. 2005;66:1695–700.

[152] Zhang L, Li Y, Zhang L, Li DW, Karpuzov D, Long YT. Electrocatalytic oxidation of NADH on graphene oxide and reduced graphene oxide modified screen-printed electrode. Int J Electrochem Soc. 2011;6:819-29.

[153] Nguyen ST, Park S, Lee KS, Bozoklu G, Cai W, Ruoff RS. Graphene oxide papers modified by divalent ions - Enhancing mechanical properties via chemical cross-linking. ACS Nano. 2008;2:572-8.

[154] Ventrice CA, Yang D, Velamakanni A, Bozoklu G, Park S, Stoller M, et al. Chemical analysis of graphene oxide films after heat and chemical treatments by X-ray photoelectron and Micro-Raman spectroscopy. Carbon. 2009;47:145-52.

[155] Coloma F, Sepulveda-Escribano A, Fierro JLG, Rodriguez-Reinoso F. Preparation of platinum supported on pregraphitized carbon-blacks. Langmuir. 1994;10:750-5.

[156] Shen W, Li Z, Liu Y. Surface chemical functional groups modification of porous carbon. Recent Patents on Chemical Engineering. 2008;1:27-40.

[157] Zhang JP, Zhang LD, Zhu LQ, Zhang Y, Liu M, Wang XJ, et al. Characterization of ZnO: N films prepared by annealing sputtered zinc oxynitride films at different temperatures. J Appl Phys. 2007;102.

[158] Stankovich S, Piner RD, Chen XQ, Wu NQ, Nguyen ST, Rouff RS. Stable aqueous dispersions of graphitic nanoplatelets via the reduction of exfoliated graphite oxide in the presence of poly(sodium 4-styrenesulfonate). J Mater Chem. 2006;16:155-8.

[159] Herricks T, Chen J, Xia Y. Polyol synthesis of platinum nanoparticles: control of morphology with sodium nitrate. Nano Lett. 2004;4:2367–71.

[160] Chen J, Zhang WM, Swiegers GF, Ma ZF, Wallace GG. Microwave-assisted synthesis of Pt/CNT nanocomposite electrocatalysts for PEM fuel cells. Nanoscale. 2010;2:282-6.

BURCU SANER OKAN

Sabancı University,

Faculty of Engineerings and Natural Sciences,

Orhanlı 34956 Tuzla/İstanbul

Contact: bsaner@sabanciuniv.edu

EDUCATION

2007-2011	Ph.D. in Materials Science and Engineering, Sabancı University/Turkey (3.90 / 4.00)
2005-2007	M.S. in Materials Science and Engineering, Sabancı University/Turkey (3.28 / 4.00)
2000-2005	B.S. in Chemistry, Middle East Technical University /Turkey (3.10 / 4.00)

WORK EXPERIENCE

2005-2011	Teaching Assistant, Sabanci University, Turkey (courses: Nature of Science, Analytical Chemistry, Inorganic Chemistry, Kinetics, Materials Science)
2010-2011	Research assistant in LOREAL supported project (Fabrication of proton exchange membranes for fuel cells).
2009-2011	Research assistant in National Boron Institute supported project (Boron nitride nanotube production and its use in hydrogen storage)
Summer 2004	Research assistant in synthetic polymerization lab at ITU
Summer 2003	GEMSAN/Istanbul - Quality Control Intern

RESEARCH EXPERIENCE

2007-2011   Ph.D. Dissertation, An improved technique for the exfoliation of graphene nanosheets and utilization of their nanocomposites as fuel cell electrodes,
Prof. Dr. Yuda Yürüm (advisor), Sabanci University

2005-2007   M.S. Thesis, Fluorinated nanofibers for potential biomedical applications,
Prof. Dr. Yusuf Z. Menceloglu (advisor), Sabanci University

2003-2005   Undergraduate Final Project, Immobilization of polyphenol oxidase in conducting matrice and determination of phenolics amount in wine with enzyme electrodes,
Prof. Dr. Levent Toppare (advisor), Middle East Technical University

AWARDS & ACHIEVEMENTS

1.   I2CAM Travel Award to attend 2010 Fall MRS Meeting in Boston, MA, USA. "Saner, B., Okyay, F., Yurum,Y., *Fuel*, Vol. 89, Issue 8, pp. 1903-1910 2010)" was ranked in 7th among Top 25 Hottest Articles in Fuel via Sciencedirect in 2010.

2.   Fellowship, CAS (Chemical Abstract Service) Student Information Exchange Program (including visiting research facilities and attending ACS Spring Meeting), August 16-26, 2010, Columbus, OH and Boston, MA, USA.

3.   Oral presentation award, International Conference on Nanomaterials and Nanosystems, 10-13 August 2009, Istanbul, Turkey

4.   Full scholarship, Sabanci University, Turkey, Ph.D. Program of Material Science & Engineering, 2007-2011.

5.   Full scholarship, Sabanci University, Turkey, M.Sc. Program of Material Science & Engineering, 2005-2007.

PUBLICATIONS

1. Saner-Okan, B., Yürüm, A., Gorgülü, N., Alkan-Gürsel, S., Yürüm, Y., Polypyrrole coated thermally exfoliated graphite nanoplatelets and the effect of oxygen surface groups on the interaction of Pt catalysts with graphene-based nanocomposites, *Industrial & Engineering Chemistry Research* (2011), submitted.

2. Saner-Okan, B., Kocabas, Z. O., Nalbant Ergün, A., Baysal, M., Yürüm, Y., Synthesis of boron nitride nanostructures over Fe^{3+} impregnated mesoporous silica MCM-41 by chemical vapor deposition technique and measurement of their hydrogen storage capacity, *International Journal of Hydrogen Energy* (2011), submitted.

3. Saner, B., Yürüm, A., Alkan-Gürsel, S., Yürüm, Y., Fabrication of fuel cell electrodes using Pt deposited polypyrrole coated graphite oxide and graphene nanosheets, *International Journal of Hydrogen Energy* (2011), submitted.

4. Saner, B., Alkan-Gürsel, S., Yürüm, Y., Layer-by-Layer Polypyrrole Coated Graphite Oxide and Graphene Nanosheets as Catalyst Support Materials for Fuel Cells, *Fullerenes, Nanotubes, and Carbon nanostructures* (2011), in press.

5. Saner, B., Dinc, F., Yürüm, Y., Utilization of multiple graphene layers in fuel cells. 2. The effect of oxidation process on the characteristics of graphene nanosheets, *Fuel* Vol. 90, pp. 2609-2616 (2011).

6. Saner, B., Okyay, F., Yürüm, Y., Utilization of multiple graphene layers in fuel cells. 1. An improved technique for the exfoliation of graphene-based nanosheets from graphite, *Fuel*, Vol. 89, Issue 8, pp. 1903-1910 (2010).

7. Saner B., Oncu Bilgin, N., Menceloglu Y.Z., Branched Pentablock Poly(L-lactide-co-ε-caprolactone) Synthesis in Supercritical Carbon Dioxide, *High Performance Polymers*, Vol. 19 (5-6), pp. 649-664 (2007).

8. Müftüoglu, A.E., Saner, B., Demirel, A.L., Yagci, Y., Synthesis and Characterization of Graft and Branched polymers via Type-II Photoinitiation, *Designed Monomers and Polymers*, Vol.8, No.6, pp. 645-658 (2005).

BOOKS

1. Baysal, M., Ergün, A.N., Kocabas, Z.O., Okyay, F., Saner, B., Tas, S., Yürüm, Y. (Editors), Proceedings of 6th Chemical Engineering Conference for Collaborative Research in Eastern Mediterranean Countries, EMCC-6, Atlantis Hotel, Belek, ANTALYA, TURKEY, March 7-12, 2010, ISBN: 9786051250366. (Editor)

2. Saner, B. and Menceloglu, Y.Z. (Authors), Fluorinated Biomaterials: Fluorinated nanofibers for potential biomedical applications, ISBN: 9783639130539, VDM Verlag Dr. Muller Publishing House LTD., Germany, May 2009. (Author)

CONFERENCES

1. B. Saner-Okan, A. Yürüm, S. Alkan-Gürsel, Y. Yürüm, New fuel cell electrodes made from graphene nanosheets and their nanocomposites, *7th Nanoscience and Nanotechnology Conference (NANOTR7)*, Sabanci University, Istanbul, Turkey, June 27-July 1, 2011. *(oral presentation)*

2. B. Saner, S. Alkan-Gürsel, Y. Yürüm, Facile synthesis of polypyrrole/graphene nanosheet based nanocomposites as catalyst support for fuel cells (*MRS Fall Meeting Proceedings* (2011), DOI:10.1557/opl.2011.126), MRS Fall Meeting, Boston, MA, USA, November 29-December 3, 2010. *(oral presentation)*

3. B. Saner, Y. Yürüm, Graphene nanosheet and carbon nanotube based nanocomposites as an electrode support for fuel cells, *International Conference on Clean Energy (ICCE-2010)*, Gazimagusa – N. Cyprus, 15-17 September, 2010. *(oral presentation)*

4. B. Saner, S. Alkan-Gürsel, Y. Yürüm, Application of multiple graphene layers as catalyst support material in fuel cells, *3rd National Catalysis Conference (NCC-3)*, Zonguldak/Turkey, April 28-March 1, 2010. *(oral presentation)*

5.   B. Saner, N. Gorgülü, S. Alkan-Gürsel, Y. Yürüm, Synthesis and characterization of polypyrrole coated graphene nanosheets with enhanced electrical properties, *Carbon Materials for Today and Future Turkish-Japanese Joint Carbon Symposium*, Istanbul Technical University, Turkey, March 18-19, 2010. *(poster presentation)*

6.   B. Saner, N. Gorgülü, S. Alkan-Gürsel, Y. Yürüm, Novel graphene-based electrodes for energy storage devices, *EMCC 6*, Belek, Antalya/Turkey, March 7-12, 2010. *(poster presentation)*

7.   B. Saner, F. Dinc, Y. Yürüm, The effect of oxidation time on the characteristics of graphene oxide nanosheets, *International Conference on Nanomaterials and Nanosystems*, Istanbul/Turkey, August 2009. *(oral presentation)*

8.   B. Saner, F. Okyay, Y. Yürüm, An improved technique for the exfoliation of graphene-based nanosheets, *V. National Nanoscience and Nanotechnology Conference (NANOTR5)*, Eskisehir/Turkey, June 2009. *(oral presentation)*

9.   B. Saner, S. Alkan Gürsel, Y. Yürüm, Graphene: a new approach for the nanostructured electrocatalyst in fuel cells, a preliminary attempt, *2nd National Catalysis Conference (NCC-2)*, Erzurum/Turkey, June 2008. *(poster presentation)*

10.   B. Saner, B.S. Ozdemir, H. Budak, Y. Z. Menceloglu, Biodegradable nanofibrous materials for in-vitro applications, *4th National Nanoscience and Nanotechnology Conference (NANOTR4)*, ITU, Istanbul/Turkey, June 2008. *(oral presentation)*

11.   B. Saner and Y.Z. Menceloglu, Biodegradable nano-fiber webs with oxygen carrying systems for potential biomedical applications, *Plastic, Reconstructive, Aesthetic Surgical, Stem Cell and Tissue Engineering Symposium*, Samsun/Turkey, May 2007. *(oral presentation)*

12.   B. Saner, N. Bilgin, A. Namuslu, E. Piskin and Y.Z. Menceloglu, Poly(L-lactide-*co*-ε-caprolactone) by ring opening polymerization, *ACS Fall Meeting*, San Francisco, USA, September 10-14, 2006. *(poster presentation)*

13.   B. Saner, N. Bilgin, Y.Z. Menceloglu, Linear and four-arm multiblock copolymers by ring opening polymerization in supercritical carbon dioxide, *Polycondensation*, Istanbul/Turkey, August 2006. *(poster presentation)*

14. A.E. Muftuoglu, B. Saner, A.L. Demirel, Y. Yagci, Synthesis and characterization of graft and branched polymers via type-2 photoinitiation, *International Symposium on Advanced Polymers via Macromolecular Engineering APME-6*, Istanbul/Turkey, August 2005. *(poster presentation)*

15. B. Saner, A.E. Müftüoglu, Y. Yagci, Synthesis and characterization of random copolymers possessing H-donating sites for photoinduced grafting, *2nd Mediterranean Meeting on Organic Chemistry*, Spain, November 2004. *(poster presentation)*